

THE MORPHOLOGY OF LOCAL GALAXIES
AND THE BASIS OF THE HUBBLE SEQUENCE

by

Preethi B. Nair

A thesis submitted in conformity with the requirements
for the degree of Doctor of Philosophy

Graduate Department of Astronomy and Astrophysics
University of Toronto

© Copyright by Preethi B. Nair 2009

Abstract

The Morphology of Local Galaxies
and the Basis of the Hubble Sequence

Preethi B. Nair

Doctor of Philosophy

Graduate Department of Astronomy and Astrophysics

University of Toronto

2009

The goal of galaxy classification is to understand the physical basis for the wide range in shapes and structures exhibited by galaxies in the local and high redshift universe. We present a catalog of visually classified galaxies from the Sloan Digital Sky Survey with detailed morphological classifications including bars, rings, lenses, tails, warps, dustlanes, arm flocculence and multiplicity (so called 'fine structure'). This thesis explores the importance of galaxy morphology by probing its relationship to physical properties. Our analysis includes an investigation of correlations between fine structures and AGN activity. This sample defines a comprehensive local galaxy sample which we use to study the low redshift universe both qualitatively and quantitatively.

We find the stellar mass appears to be a defining characteristic of a galaxy. The break in most correlations of physical properties with morphology is due to a lack of late type, massive disk galaxies. Our analysis of the size-mass relations of galaxies as a function of morphology (T-Type) has revealed many interesting connections. We find the size-mass relation of Sa, Sab, Sb, and Sbc galaxies bifurcates into two families of objects as one moves down the sequence such that the high concentration branch exhibits a similar slope to low concentration early type (E) galaxies suggesting a closer than expected physical (possibly evolutionary) connection between the two populations.

We find bar fraction is bimodal with respect to mass (at $3 \times 10^{10} M_{\odot}$) and color (at $g - r \sim 0.55$). The dependence is seen to intimately depend on central concentration such that objects below the transition mass with low concentrations have a higher bar fraction than objects above the transition mass which have high bar fractions for high concentration systems. In

addition we find the presence of an AGN alters the behavior and abundance of barred/ringed galaxies in the high mass peak such that the bar/ring fractions increase with mass in non-active galaxies whereas they decrease with mass in active galaxies. AGN fractions are also decreasing in the same mass range possibly implying a positive correlation between fine structure and ring formation.

Acknowledgements

There are a great many people I need to thank.

First, I offer my sincerest gratitude to my advisor Bob Abraham for his complete support, enthusiasm, inspiration, guidance and faith in my abilities over the years. His ability to see the heart and essence of problems in science and how to move forward is remarkable.

Howard Yee and Ray Carlberg for their patience and many insightful comments, advice and discussions over the years. John Dubinski and my external, Luc Simard, for their discussions and insights.

A special thanks to Kris Blindert for all the amusing and confusing conversations over the past years and for being a great friend.

A special thanks to Marija Stankovic for being a wonderful, caring and supportive friend and office mate. Her dedication to her work, friends and family is truly an inspiration.

Lawrence Mudryk, Kevin Blaggrave, Carrie Bridge, Hy Trac, Vjera Miovic for being great friends and colleagues. My time here would not have been as interesting and enjoyable without them.

Allen Attard, Mark Brodwin, Brian Lee, Colin Borys and Marc Goodman for their help and advice over the years.

Most importantly, this thesis would not have been possible without the confidence and tremendous support of my parents, Balachandran and Prasanna Nair, and my sister, Roopa Nair. Your love, support, guidance and inspiration are constant and inspire me to achieve everything I want.

This thesis is dedicated, with love, to my family.

This research was funded by the University of Toronto.

Contents

1	Introduction	1
1.1	Classification of Galaxies	2
1.1.1	What is the goal of classification?	2
1.1.2	Visual Morphology	2
	de Vaucouleurs extension	3
1.1.3	Other visual classification schemes	4
	Morgan/Yerkes System	4
	DDO luminosity classes	5
	Spiral arm classification	5
	Revision of elliptical classification	6
1.1.4	Summary	6
1.2	Importance of Bars, Rings, and Spiral Arms	7
1.3	Importance of AGNs	9
	Summary	9
1.4	Dissertation Overview	9
2	Observations and Sample Selection: The Sloan Digital Sky Survey	11
2.1	Introduction	11
2.2	Sloan Digital Sky Survey: Overview	11
2.2.1	Imaging	11
2.2.2	Spectroscopic Observations	13
2.3	Supplementary Data : Garching Group	14
2.3.1	Stellar Masses and Ages	14
	Biases	14
2.3.2	Metallicities and Star Formation Rates	14
2.4	Supplementary Data : NYU Group	15
2.5	Catalog	16

3	Classification Schemes	20
3.1	Introduction	20
3.2	Visual Classification Scheme	21
3.3	Representative Examples of T-Types and Fine Classes	23
3.4	Reliability of Classification	32
3.4.1	Comparison of T-Types with Previous Works	32
3.4.2	Comparison of RC3 and PN bar classification	33
3.4.3	Comparison of RC3 and PN ring classifications	37
3.4.4	Caveat: Selection effects due to redshift	41
3.5	Results	41
3.5.1	Sersic Index vs T-Type relation	44
3.5.2	Distribution of T-Types with physical properties	44
3.5.3	Local Statistics	45
3.5.4	Interacting galaxies	47
3.6	Automated Classifications	48
3.6.1	Description of Quantitative Parameters	49
	Concentration	49
	Asymmetry	51
	Gini Coefficient	51
	Moment of light : M_{20}	56
3.7	Catalog of Visual and Quantitative Parameters	57
4	The Morphological Properties of Nearby Galaxy	60
4.1	Introduction	60
4.2	Variation in Galaxy Properties with Visual Morphology: 1D	61
4.2.1	Correlation between size and T-Type	61
4.2.2	Correlation between mass and T-Type	64
4.2.3	Correlation between luminosity and T-Type	67
4.2.4	Correlation between color and T-Type	67
4.2.5	Correlation between surface brightness and T-Type	67
4.2.6	Correlation between surface mass density and T-Type	67
4.2.7	Correlation between mass-to-light ratios and T-Type	68
4.2.8	Summary	68
4.2.9	Statistical Correlations	68
4.2.10	Systematic Effects: Inclinations Effects, Fine structures and AGNs	69
4.3	Variation in Galaxy Properties with Visual Morphology: Bivariate Analysis	72

4.3.1	Correlation between size with T-Type	72
4.3.2	Correlation between mass and T-Type	73
4.3.3	Correlation between luminosity and T-Type	78
4.3.4	Correlation between color and T-Type	78
4.3.5	Correlation between surface brightness and T-Type	79
4.3.6	Correlation between surface mass density and T-Type	79
4.3.7	Correlation between mass-to-light ratio and T-Type	79
4.3.8	Summary	83
4.4	Variation in Galaxy Properties with Quantitative Morphology	83
4.5	Bivariate Statistical Analysis	88
4.6	Summary	89
5	Scaling Relations	90
5.1	Introduction	90
5.2	The Size-Mass relationship along the Hubble Sequence	91
5.2.1	The hidden connection between (some) elliptical and (some) spiral galaxies	94
5.2.2	Implication for dichotomy among bulges	97
5.2.3	A broken connection amongst early-type galaxies	98
5.3	Summary	99
6	Bimodality in Bar Fraction	101
6.1	Introduction	101
6.2	Dependence of bar and ring fraction on axis ratio	102
6.3	Fine Fraction Statistics	103
6.3.1	Optical fraction of Bars, Rings and Lenses with T-Types	103
6.3.2	Optical fraction of Bars, Rings and Lenses with Sersic Index n	109
6.3.3	Optical fraction of Bars, Rings and Lenses with Size	112
6.3.4	Optical fraction of Bars, Rings and Lenses with Mass	112
6.3.5	Optical fraction of Bars, Rings and Lenses with Luminosity	114
6.3.6	Optical fraction of Bars, Rings and Lenses with Color	116
6.4	Origin of Bimodal bar fractions	117
6.5	Variation of fine fractions with morphological parameters	123
6.5.1	Variation of fine fractions with Concentration	123
6.5.2	Variation of fine fractions with Gini	125
6.5.3	Variation of fine fractions with Asymmetry	126
6.5.4	Variation of fine fractions with M20	127
6.6	Implications	128

6.6.1	Redshift evolution of bars	128
6.7	Summary	129
7	Role of AGN	131
7.1	Introduction	131
7.2	Influence of AGN on fine fractions	132
7.2.1	Fraction of Bars, Rings and Lenses with T-Type	132
7.2.2	Optical fraction of Bars, Rings and Lenses with Sersic Index n	133
7.2.3	Optical fraction of Bars, Rings and Lenses with Mass	134
7.2.4	Optical fraction of Bars, Rings and Lenses with Luminosity	135
7.2.5	Optical fraction of Bars, Rings and Lenses with Color	137
7.2.6	Optical fraction of Bars, Rings and Lenses with Size	138
7.2.7	Summary	139
7.3	AGN Fraction Statistics	139
7.3.1	Dependence of AGN fractions on T-Types	139
7.3.2	Dependence of AGN fractions on sersic indices	142
7.3.3	Dependence of AGN fractions on mass	143
7.3.4	Dependence of AGN fractions on magnitude	145
7.3.5	Dependence of AGN fractions on color	146
7.3.6	Dependence of AGN fractions on size	148
7.3.7	Summary	150
7.4	Implications	151
7.5	Summary	152
8	Conclusions	154
8.1	Future Work	156
8.1.1	Study of Quantitative Morphology	156
8.1.2	Quantification of fine parameters	157
8.1.3	Bulge-Disk decomposition	157
8.1.4	Further extensions	158
8.1.5	Spectroscopic follow-up	158
8.1.6	Other work	159
8.1.7	Outlook	159
	Bibliography	160

List of Tables

1.1	Elmegreen Spiral Classification Scheme	5
2.1	Characteristics of the SDSS Fourth Data Release	13
3.1	T-Type Classification Schemes	32
3.2	Summary of Distributions	47
3.3	Summary of Disturbed Objects	48
3.4	T-Type Classification Schemes	59
4.1	T-Type Classification	62
4.2	Summary of Table from Roberts and Haynes 1994	63
4.2	Summary of Table from Roberts and Haynes 1994	64
4.3	Spearman correlation matrix	68
4.4	Spearman correlation matrix	88
6.1	Relative Frequencies of Bars and Inner Rings	107
6.2	Relative Frequencies of Bars, Rings and Lenses	108

List of Figures

1.1	Visual Morphology: Hubble’s Tuning Fork	2
1.2	Visual Morphology: de Vaucouleurs Classification Volume	4
1.3	Visual Morphology: Galaxy Classification Schemes	7
2.1	Distribution on the sky of SDSS DR4 imaging and spectroscopy	12
2.2	Redshift Distributions	17
2.3	Histogram of Absolute Magnitudes.	17
2.4	Local Distributions	19
3.1	Example of Classification Form	22
3.2	Montage of E, S0 and Sa galaxies	24
3.3	Montage of Sb, Sc and Sd galaxies	25
3.4	Montage of Barred galaxies	26
3.5	Montage of Ringed galaxies	27
3.6	Montage of lenses in galaxies	28
3.7	Montage of Interacting Tails	29
3.8	Collisional Ring galaxies	30
3.9	Shells	30
3.10	Comparison of Classifications.	32
3.11	Montage of Barred galaxies common with RC3	34
3.12	RC3 missed face-on Montage of Barred galaxies	35
3.13	Depth Effect on Bar detection	36
3.14	RC3 face-on Montage of Outer Ringed galaxies	38
3.15	RC3 missed face-on Montage of Inner Ringed galaxies	39
3.16	Redshift Variation of T-Type and fine fraction	42
3.17	Local Distributions	43
3.18	Histograms of Sersic index keyed to T-Type	43
3.19	Histograms of mass and size keyed to T-Type	45
3.20	Histogram of g-band absolute magnitude keyed to T-Type	46

3.21	Histograms of T-Types	46
3.22	Concentration Histogram	50
3.23	Gini Histogram	52
3.24	Lorenz Curve	52
3.25	Gini Histogram	54
3.26	Gini vs Concentration in g-band	54
3.27	Gini Histogram	55
3.28	Gini Histogram	56
4.2	Inclination dependence of galaxy parameters with T-Type	70
4.3	AGN and fine-structure dependence of galaxy parameters with T-Type	71
4.4	Size vs T-Type Keyed to physical properties	74
4.5	Mass vs T-Type Keyed to physical properties	75
4.6	Absolute Magnitude vs T-Type Keyed to physical properties	76
4.7	Color vs T-Type Keyed to physical properties	77
4.8	Surface Brightness vs T-Type Keyed to physical properties	80
4.9	Surface Mass Density vs T-Type Keyed to physical properties	81
4.10	M/L vs T-Type Keyed to physical properties	82
4.11	Concentration vs T-Type Keyed to physical properties	84
4.12	Gini vs T-Type Keyed to physical properties	85
4.13	Asymmetry vs T-Type Keyed to physical properties	86
4.14	M20 vs T-Type Keyed to physical properties	87
5.1	Size vs. Mass : All Galaxies Keyed By T-Type Binned In Concentration Panels	92
5.2	Size vs. Mass : All Galaxies Keyed By Concentration Binned In T-Type Panels	93
5.3	FaceOn SB Concentration Below 0.25 Or Above 0.41	95
5.4	Size Mass Keyed to position on Color-Magnitude Diagram	96
6.1	Dependence on Axis Ratio of Fine Fraction	102
6.2	Figure 3 from Sellwood and Wilkinson 1993	104
6.3	T-Type Distributions of Bars, Rings and Lenses	105
6.4	T-Type Distributions of complete and partial Inner and Outer rings	107
6.5	Sersic Distributions of Bars, Rings and Lenses	110
6.6	Size Distributions of Bars, Rings and Lenses	111
6.7	Mass Distributions of Bars, Rings and Lenses	113
6.8	Absolute g-Magnitude Distributions of Bars, Rings and Lenses	115
6.9	g-r Color Distributions of Bars, Rings and Lenses	116

6.10	Bimodality in Bars	120
6.11	Bar fraction vs mass keyed to color and concentration	121
6.12	Ring fraction vs mass keyed to color and concentration	122
6.13	Concentration Distributions of Bars, Rings and Lenses	124
6.14	Mass Distributions of Bars, Rings and Lenses	125
6.15	Mass Distributions of Bars, Rings and Lenses	126
6.16	Mass Distributions of Bars, Rings and Lenses	128
6.17	Bar fraction vs mass keyed to M20	129
7.1	Distributions of Bars, Rings and Lenses with T-Type for AGN and non-AGN samples	133
7.2	Sersic Distributions of Bars, Rings and Lenses for AGN and non-AGN samples	134
7.3	Mass Distributions of Bars, Rings and Lenses for AGN and non-AGN samples	135
7.4	Absolute Magnitude Distributions of Bars, Rings and Lenses for AGN and non-AGN samples	136
7.5	Color Distributions of Bars, Rings and Lenses for AGN and non-AGN sample .	137
7.6	Size Distributions of Bars, Rings and Lenses for AGN and non AGN samples .	138
7.7	T-Type Distributions of Bars, Rings and Lenses	140
7.8	T-Type Distributions of Bars, Rings and Lenses	140
7.9	T-Type Distributions of Bars, Rings and Lenses	142
7.10	T-Type Distributions of Bars, Rings and Lenses	143
7.11	T-Type Distributions of Bars, Rings and Lenses	144
7.12	T-Type Distributions of Bars, Rings and Lenses	144
7.13	T-Type Distributions of Bars, Rings and Lenses	146
7.14	T-Type Distributions of Bars, Rings and Lenses	147
7.15	T-Type Distributions of Bars, Rings and Lenses	147
7.16	T-Type Distributions of Bars, Rings and Lenses	148
7.17	T-Type Distributions of Bars, Rings and Lenses	149
7.18	T-Type Distributions of Bars, Rings and Lenses	149

Chapter 1

Introduction

“Research is to see what everybody else has seen,
and to think what nobody else has thought”

-Albert Szent-Gyorgyi

Galaxies are the building blocks of the visible universe. Understanding their formation and evolution is extremely important to any theory of the origin of the universe and large scale structure. Astronomers have been studying galaxies for a long time, though their extragalactic nature was only verified in the early part of the 20th century (Hubble 1925). Since then tremendous strides have been made in understanding the nature of galaxies, their structure, physical relationships and evolution. Key results include the establishment of a scheme to visually classify galaxies (Hubble 1926; Sandage & Tammann 1981; Morgan 1958; de Vaucouleurs 1959a; van den Bergh 1960c, 1976), the discovery of the fundamental plane of ellipticals (Djorgovski & Davis 1987; Kormendy & Djorgovski 1989), the Tully-Fisher relation for disks (Tully & Fisher 1977), the importance of environment (Dressler 1980), the discovery of super massive black holes at the centers of galaxies (Miyoshi et al. 1995; Genzel et al. 2000), the correlation between black hole mass and the mass of bulges (Ferrarese & Merritt 2000; Gebhardt et al. 2000; Marconi & Hunt 2003), the presence of dark matter etc. At the same time, a number of outstanding problems still remain. What accounts for the wide diversity seen in galaxies? Why are galaxy populations bimodal? What is the role of bar structures and AGNs in galaxy formation? What is the origin of S0 galaxies? How important are mergers in the early universe? And many more. In many cases one of the fundamental tools used to study galaxy populations is their morphology. This thesis undertakes the task of classifying a large sample of SDSS galaxies in detail, including features such as bars and rings, to contribute to these specific topics.

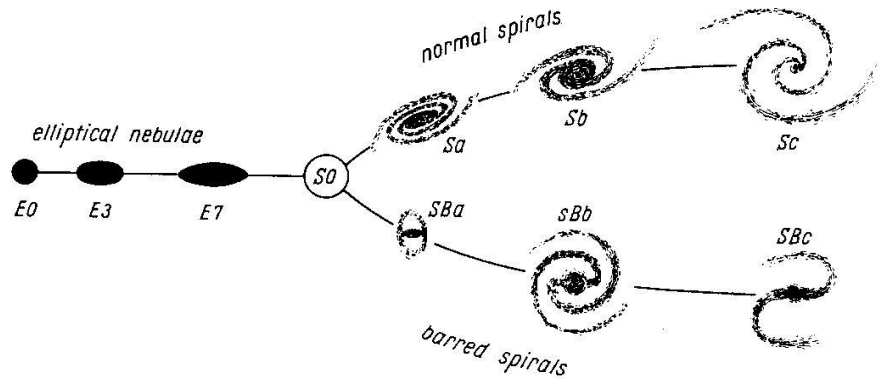


Figure 1.1: The Hubble tuning-fork classification of galaxies (revised 1936 version which includes S0 galaxies, see text).

1.1 Classification of Galaxies

1.1.1 What is the goal of classification?

Galaxies exhibit a wide variety of shapes and structures. The goal of classification is to rank objects in a meaningful way such that objects that are physically different can be distinguished. Ideally the classification scheme must be able to account for all the variations seen in galaxies, and should be reproducible by independent observers. The hope is the classification will help explain how galaxies are related, how they may have evolved and help understand the underlying physics involved. Describing morphology itself can be done by various methods. The most successful has been by visual schemes but quantitative measures are favored in the current era of large data sets. I describe the major schemes in use below.

1.1.2 Visual Morphology

The most successful visual classification scheme is Hubble's tuning fork diagram shown in Figure 1.1 which considers three types of galaxies: ellipticals, spirals and irregulars. Hubble arranged elliptical galaxies in a sequence of increasing ellipticity. The sequence then merged with two tines of spiral galaxies arranged in order of decreasing bulge size, increasing spiral arm pitch angle, and increasing presence of condensates or star formation knots. Normal and barred galaxies occupied separate tines of the fork. Irregular galaxies were a catch all group of objects with patchy structure and no spiral arms and did not fit on either tine.

This original scheme was criticized by (Reynolds 1927) as being too simple (although he himself had binned galaxies similarly by considering the frequency and position of condensates (Reynolds 1920)). Reynolds did not consider Hubble's binning a classification as it over-

looked the wide diversity and variation of galaxies seen within a bin. While acknowledging the importance of some features such as the ‘mass’ of spiral arms, Hubble argued the “spread” of features in a given bin were “reasonably small compared to the length of the sequence” (Hubble 1927). In addition the smooth progression of properties such as mean surface brightness and diameter for a given total luminosity justified the use of the sequence as a tool for statistical studies of galaxies. However Hubble suggested that modifications to account for the strength of arms and other fine features would most probably sub-divide a general class and be taken into account with subscripts and would not alter the continuous nature of the classification. Numerous revisions of Hubble’s scheme along this line were in fact made.

It was recognized early on that the classification bin sizes used were very large. Hubble modified his classification in 1936 to postulate the existence of S0 galaxies at the juncture between ellipticals and spirals. Sandage (1961) further incorporated Hubble’s unpublished revisions to split the Sa type into S0 and Sa galaxies in the Hubble Atlas for a smoother transition between ellipticals and spiral galaxies. The Sc galaxies were sub-divided into Sc and Sd galaxies by Shapley & Paraskevopoulos (1940). Shapley (1941) proposed splitting each class into finer subdivisions which he called Sb^- , Sb^+ , Sc^- , Sc^+ . Holmberg (1958) using a similar scheme was able to show that the classification types correlated strongly to the mean color of the system such that galaxies became monotonically redder from late to early type systems. This was the first confirmation of the physical significance of the Hubble sequence.

de Vaucouleurs extension

The importance of the variation of structures within each class continued to be argued. To better account for the wide diversity of galaxy morphologies de Vaucouleurs (1959b) introduced a three dimensional scheme of classification. The representation is shown in Figure 1.2. de Vaucouleur renamed¹ Hubble’s major classification axis to E-S0-Sa-Sb-Sc-Sd-Sm-Im, where Sm and Im galaxies are amorphous galaxies (with or without spiral structure) originally described by Lundmark (1926) and Holmberg (1958). Elliptical and lenticular galaxies were split more finely and distinguished between by superscripts of ‘-’ or ‘+’, where ‘-’ denotes earlier and smoother varieties while ‘+’ the later varieties of a given type. de Vaucouleur further modified the tines of Hubble’s scheme to introduce the concept of weak bars (SAB), a transition from strongly barred (SB) to no bar(SA). The third dimension added by deVaucouleurs distinguishes between objects with rings (r), without rings (s) and intermediate ring features (rs). It has been argued that the r and s dichotomy ‘may represent only an ephemeral change in morphology due to differences in density wave pattern’ (van den Bergh 1998). However,

¹He also introduced the T-Type parameter in de Vaucouleurs et al. (1976) which are numerical equivalents to the extended Hubble classes where ellipticals are designated -5, S0 -2, Sa 1, Sb 3, Sc 5 and so on.

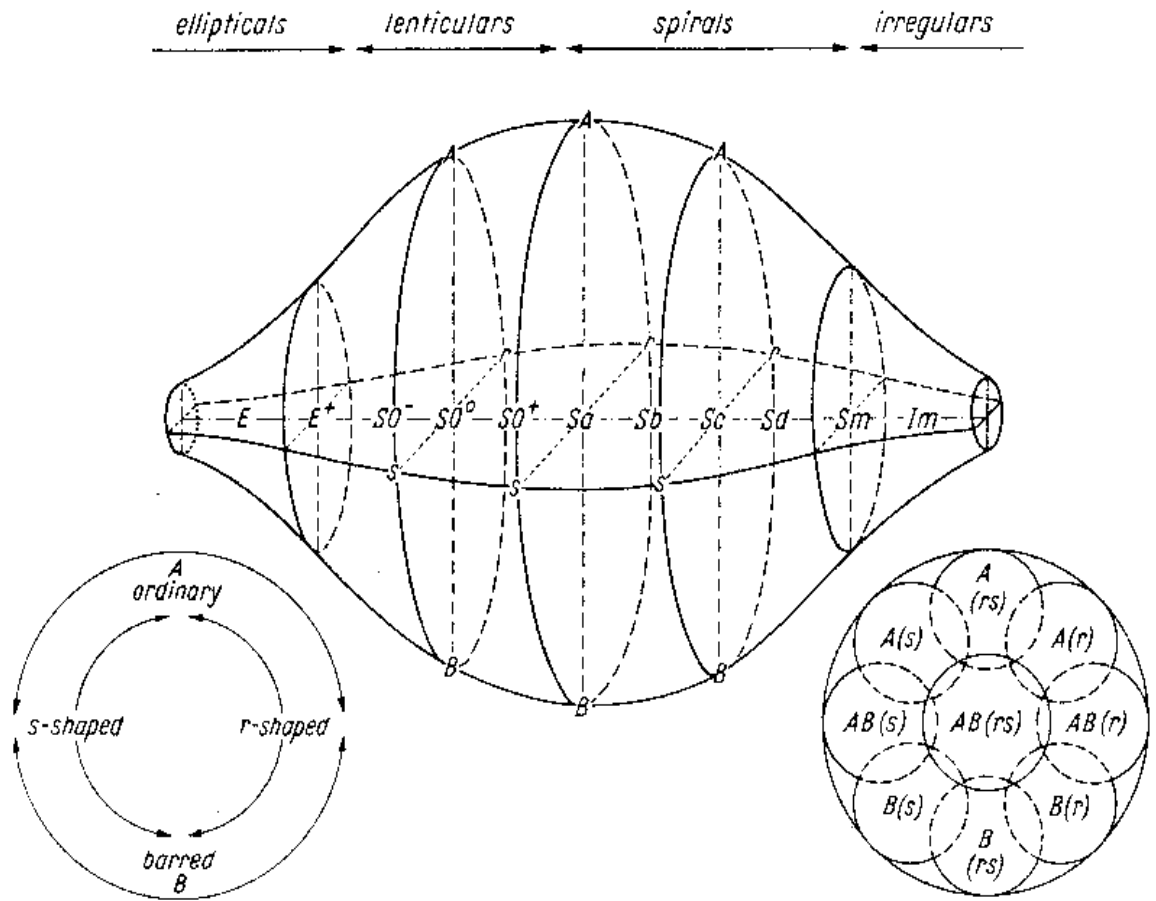


Figure 1.2: de Vaucouleurs modification to Hubble’s classification scheme. The primary classification is the Hubble stage represented by the axis. The second parameter relates to the presence of absence of a bar, while the third distinguishes between (r) and spiral (s) varieties.

correlations have been found between ring frequencies and galaxies with active galactic nuclei (AGN) as I shall describe later.

1.1.3 Other visual classification schemes

Morgan/Yerkes System

Morgan (1958, 1959) proposed a one dimensional classification system based on central concentration. His scheme was based on the observed strong correlation between the dominant spectral type of the galaxy and its concentration (Morgan & Mayall 1957). A scheme based on central concentration of light had previously been suggested by Lundmark (1926) though it was not motivated by correlations seen with stellar populations. Morgan arranged galaxies in increasing order of concentration (a-f-g-k; where the notations are based on the dominant spectral type in the bulge) while recognizing intermediate types. In addition, Morgan clas-

Table 1.1. Elmegreen Spiral Classification Scheme

Arm Class	Description
1.....	Chaotic, fragmented, unsymmetric arms
2.....	Fragmented spiral arm pieces with no regular pattern
3.....	Fragmented arms uniformly distributed around the galactic center
4.....	Only one prominent arm, otherwise fragmented arms
5.....	Two symmetric, short arms in the inner region; irregular outer arms
6.....	Two symmetric inner arms, feathery ringlike outer structure
7.....	Two symmetric, long outer arms, feathery or irregular inner arms
8.....	Tightly wrapped ringlike arms
9.....	Two symmetric inner arms, multiple long and continuous outer arms
10.....	No longer used; previously denoted barred galaxies
11.....	No longer used; previously denoted galaxies with close companions
12.....	Two long symmetric arms dominating the optical disk

sified galaxies into different forms: ellipticals (E), spirals(S), barred spirals(B), irregulars (I), low surface brightness galaxies (L) and objects with bright nuclei (N). The advantage of Morgan's scheme is it is easily applicable to quantitative morphology schemes and is extendable to higher redshifts unlike Hubble's scheme which is only valid for the most luminous galaxies and bins more than a third of the galaxies seen at higher redshifts as irregular(Abraham et al. 1996a; Elmegreen et al. 2005).

DDO luminosity classes

Holmberg (1958) noticed that more luminous galaxies had a higher surface brightness than lower luminosity galaxies. Subsequent work by van den Bergh (1960a) found both the surface brightness of galaxies and their spiral arm structures were dependent on luminosity. van den Bergh (1960a) using Palomar Sky Survey prints devised a classification scheme for the disks of galaxies in analogy to the stellar luminosity classification of Johnson and Morgan 1953. Galaxies were assigned to luminosity classes of I (supergiants), II (bright giants), III (giants), IV (sub giants) and V (dwarfs). In addition galaxies were classified as barred 'b' or not barred '(b)', patchy '*' or smooth 'n' and tidally distorted 't'. The Hubble classes could only be used for supergiants, bright giants and giants.

Spiral arm classification

Even before they were realized as extra-galactic objects, spiral galaxies were known to exhibit a wide diversity in arm structures, from grand design to filamentary (Groot 1925; Reynolds 1925). Although Hubble's classification did account for the differing opening angles of the spiral arms it did not account for this wide diversity. Elmegreen & Elmegreen (1982, 1987) de-

vised a twelve stage classification scheme ² shown in Table 1.1. The classification ranges from flocculent arm structures which are patchy, short and lack symmetry (Type 1) to grand design arm structures which are long, and exhibit symmetry and continuity (Type 12). Elmegreen & Elmegreen found their arm classification was correlated with the DDO luminosity classes such that galaxies with filamentary arm structures were all of lower luminosity whereas objects of Type 12 were of high luminosity. In addition they found all late type galaxies were dominated by lower Type (1-2) arm structures, due most probably to the lower luminosities of these systems. Classical spirals from Sa - Sc showed no correlation with arm type. Further work by Elmegreen & Elmegreen (1990b) showed that flocculent galaxies have nearly flat or rising rotation curves while grand design have falling rotation curves, consistent with the theoretical picture of the mass of long spiral armed galaxies being stellar dominated while late type galaxies are dark matter dominated.

Revision of elliptical classification

Hubble's classification of ellipticals on the basis of apparent axial ratios had no physical significance in comparison to the classification of spirals. Later works showed a dichotomy between low luminosity, fast rotating, isotropic, core-less, disky ellipticals and giant ellipticals that were non-rotating, anisotropic, boxy with a cuspy core (Davies et al. 1983; Bender 1988; Nieto et al. 1988). In addition Kormendy & Bender (1996) suggested a revision to Hubble's classification based on isophote shape. This allowed for a smoother transition from S0's to disky ellipticals.

1.1.4 Summary

A summary of the different visual classification schemes, originally presented in *Galactic Astronomy* by J. Binney and M. Merrifield, is shown in Figure 1.3. Outstanding problems still remain in the extended Hubble classification scheme. S0 galaxies do not fit well as transition objects between the spiral and elliptical tines as their luminosities are not intermediate between the two (van den Bergh 1998). The visual morphology of a galaxy changes in different band passes. The extension to higher redshifts is complicated. HST observations have shown only a modest change in abundance of large disks and spheroids at high redshifts. However, most of the faint galaxy population observed are characterized by a peculiar morphology. Some of these probably represent entirely new classes of galaxies while others may be misclassifications caused by neglecting morphological K-corrections and dust extinction. Also, since the Hubble sequence is defined with respect to bright local galaxies; deeper, magnitude-limited, high redshift surveys may be probing further down the luminosity function. Typical

²Two categories were removed in the later revision so there are 10 stages of arm classification.





	System	Principal criteria	Symbols	Examples
	Hubble-Sandage (Sandage (1961-1995))	barrishness; openness of arms/disk-bulge ratio; degree of resolution of arms into stars	E, S0, S, SB, Irr a, b, c	M87=E1 M31=Sb M101=Sc LMC=Irr I
	De Vaucouleurs (de Vaucouleurs (1959))	barrishness; openness of arms/disk-bulge ratio; rings or s shapes	E, S0, S, SA, SB, I a, b, c, d, m (r), (s)	M87=E1P M31=SA(s)b M101=SAB(rs)cd LMC=SB(s)c
	Yerkes (Morgan (1958-1970))	central concentration of light; barrishness/smoothness	k, g, f, a E, R, D, S, B, I	M87=kE1 M31=kS5 M101=fS1 LMC=afI2
	DDO (van den Bergh (1960-1976))	richness of disk in young stars; barrishness; central concentration of light; quality and length of arms	E, S0, A, S, Ir B a, b, c I, II, . . . , V	M87=E1 M31=Sb I-II M101=Sc I LMC=Ir III-IV

Figure 1.3: The major visual classification schemes. The table is taken from *Galactic Astronomy* by James Binney and Michael Merrifield. The photographs are from google.

high redshift systems may be substantially fainter than L_* and will not be characterized by Hubble's classification. Thus our perceived evaporation of the tuning fork could be due to a redshift dependent evaporation of our local L_* window (Abraham 1999). For local galaxy studies however, Hubble's extended classification scheme is still in use to understand the details of galaxy formation. As I will be focusing on local studies for this thesis I will provide an overview for the extension required for high redshift morphological analysis in the conclusions.

1.2 Importance of Bars, Rings, and Spiral Arms

Although fine structures like rings were not originally included in Hubble's scheme, it was realized that information about the formation physics of a galaxy may be buried in these structures. Both observational and theoretical work has been done over many decades to understand the processes responsible. Stellar bars are now realized to be an important factor in redistributing angular momentum between the gas and disk of a galaxy and therefore are considered to be important in their dynamical and secular evolution (Debattista & Sellwood 1998; Athanassoula 2002). They are also considered to be important to spiral arm structure of galaxies. Spiral arms are believed to be density waves driven by the gravitational field of the galaxy (Toomre 1977; Lindblad 1963). They are believed to be transitional properties which would need replenishment to survive. They can be driven and replenished by interactions with com-

panions (Toomre 1981), excitations by bars (Lindblad 1960; Toomre 1969; Athanassoula 1980) or thirdly, by a swing amplification cycle Toomre (1981).

Ring patterns observed in galaxies are associated with the principal orbital resonances, namely the Inner Lindblad Resonance (ILR), Corotation Resonance (CR) and Outer Lindblad Resonance (OLR). They are also associated with bars in galaxies though the presence of a bar does not guarantee the existence of a ring or *vica versa*. Rings have also been observed in S0 galaxies where there are neither bars nor spiral arm structures. Recent models propose spiral and ring structures are related dynamically in barred galaxies and predict varied results for the age distribution of the different components, when they were formed and which formed first (Romero-Gómez et al. 2007; Wozniak 2007; Gadotti & de Souza 2004). Again the interplay between these different features are complicated by the time-scales of destruction and reformation of the bars, spiral features and rings as well as being influenced by external interactions, environment and the dark matter distribution in galaxies.

Many works in both theory and observation show a correlation between T-Type and the underlying halo dark matter distribution. The theory of galactic spiral waves predicts that galaxies with long, grand design arms are stellar mass dominated with small haloes whereas flocculent, short armed spirals are dark matter dominated. Figure 1 in Elmegreen & Elmegreen (1990b) shows the variation in extended gradients with spiral arm class. Overall the trend implies a decrease in halo size with the strength of the arms. In recent observations, Spano et al. 2008 using 36 nearby spirals from the GHASP survey show late type galaxies ($T > 4$) being dominated by the halo and early types ($T < 5$) by the disk. Seigar et al. (2006, 2008) find spiral arm pitch angles (P) are well correlated with the rate of shear (S) in disk galaxy rotation curves and argue that imaging data alone can provide a powerful probe of galactic mass distributions out to large look-back times. A recent study by Barazza et al. (2008) also confirms an increase in bar fraction for late type objects compared to bulge dominated systems (from $\sim 40\%$ in an absolute magnitude limited sample of objects indicating that the halo might be playing a more important role in bar formation in these systems. Thus there seems to be some evidence of the importance of bars and rings in the evolution of galaxies. However, the roles of bars are further complicated as many studies locally eg., van den Bergh (2007) find no significant difference in global properties between barred or unbarred objects which would imply that the presence or absence of a bar does not strongly effect the evolutionary history of a galaxy. The bars just rearrange the material in the disk of the galaxy. Bar dissolution and re-formation are also not understood and complicate matters.

1.3 Importance of AGNs

Super-massive black holes (SMBH) are thought to be ubiquitous in ellipticals and bulges of spiral galaxies (Kormendy & Richstone 1995), although secure detection and determination of black hole masses are only present for less than a 100 galaxies (Tremaine et al. 2002). The correlation of SMBH masses with host galaxy properties, such as velocity dispersion and the mass of the bulge (Ferrarese & Merritt 2000; Gebhardt et al. 2000), implies a strong correlation between the growth of the SMBH and of the galaxy. Accretion onto SMBH are thought to be responsible for AGN activity (Lynden-Bell 1969) and the detection of high redshift quasars ($z \geq 5$) implies that SMBH were already present when galaxies were forming (Fan et al. 2000, 2001, 2004, 2006). Current theoretical models of galaxy formation invoke the presence of AGN to quench star formation at high redshifts (Silk & Rees 1998) and account for the merging history and observed bimodal distribution of galaxies locally (Wang & Kauffmann 2008; Kauffmann & Haehnelt 2000). However there is still a disconnect between models and observations with Bundy et al. (2008) suggesting AGN feedback may not cause quenching of star formation but is triggered by the same process which does.

In the low redshift universe, AGN are of much lower luminosity than their high redshift counterparts. However, correlations have been found between the presence of an AGN and large scale structures in galaxies, such as an excess of inner rings in Seyfert galaxies or outer rings in LINERs (Hunt et al. 1999b). In addition to their roles as drivers of spiral arm structures and possible role in ring formation, bars have been observed to funnel gas from the outer disk to the inner few hundred parsecs of galaxies (Elmegreen & Elmegreen 1990a; Jogee et al. 1999) and are considered to be related to AGN activity though the exact nature of this is not understood. In part this could be because of the different time-scales of AGN activity and bar lifetimes. The relation between AGN and barred/ringed galaxies is still debated.

Summary

1.4 Dissertation Overview

Considerable progress has been made in developing techniques for automated classification of galaxies. However, the disappointing truth is that, at present, state-of-the-art automated galaxy classification is only capable of delivering crude classifications, albeit very quickly. These classifications have proved useful in their appropriate context, but they are neither as accurate nor as comprehensive as visual classifications made by a trained observer. Perhaps this is not so surprising: after all, no state-of-the-art automated facial recognition systems can presently identify a human face with anything like the accuracy routinely delivered by visual

classifications made by a human child. It may be that a sufficiently large sample of digitally resolved galaxies have not been used to relate visual and quantitative morphology while accounting for fine features.

In this thesis we provide a catalog of g-band visual classifications for an apparent magnitude limited sample of 14034 galaxies obtained from the Sloan Digital Sky Survey (SDSS) Data Release 4. Our catalog is 6x larger than that presented in Fukugita et al. (2007) and attempts to encompass a broad range of morphological features. In addition to T-Types, we record the existence and prominence of bars, rings, lenses, tails, shells, warps and dust lanes. Spiral structure classifications include information on arm flocculence and multiplicity. This catalog is presented with two main goals in mind:

(i) It defines a generally useful comprehensive local sample with highly detailed morphological classifications. We will use this catalog to explore the dependence of galaxy properties on morphology and the local abundance and evolutionary properties of rings, bars, ansae, and tidal features in galaxies.

(ii) It provides a starting point for attempts to improve automated galaxy classification by incorporating detection algorithms for subtle morphological features. With the exception of some simple attempts to automate the detection of galactic bars, to date no automated classification method attempts to characterize the ‘fine structure’ of galaxy morphology.

A plan for this thesis follows. In Chapter 2 we describe the Sloan Digital Sky Survey, the public catalogs used and our sample; we discuss its strengths and limitations. Chapter 3 describes the visual and quantitative classification methodology used and describes the catalog which will be made publicly available. Chapter 4 investigates the correlations seen between galaxy properties and T-Types. Chapter 5 investigates scaling relations and their dependence on morphology in the local universe. Chapter 6 investigates the abundances of bars, rings and lenses in the local universe with Chapter 7 examining their correlations with AGN activity as well as the role of AGN in general. Our results and conclusions are discussed in Chapter 8. Throughout this thesis we assume a flat Λ -dominated cosmology with $h=0.7$, $\Omega_M = 0.3$ and $\Omega_\Lambda = 0.7$.

Chapter 2

Observations and Sample Selection: The Sloan Digital Sky Survey

2.1 Introduction

The Sloan Digital Sky Survey (SDSS; York et al. (2000)) is a comprehensive optical imaging and spectroscopic survey of a quarter of the sky conducted with a dedicated 2.5m telescope (Gunn et al. 2006) at the Apache Point Observatory in New Mexico. The survey provides a large sample of well resolved, digital images of nearby galaxies probing a wide range in luminosities and is ideal for morphological studies in the low redshift universe.

This chapter reviews the imaging and spectroscopic data of the SDSS Fourth Data Release on which this thesis is based. A multitude of work has already been carried out by various groups on the SDSS. We review two public catalogs, by independent groups, which we make use of in this thesis, specifically the stellar masses, ages, metallicities and star formation rates derived by the Garching group (<http://www.mpa-garching.mpg.de/SDSS/DR4/>) and the sersic indices of galaxies derived by the NYU group (<http://sdss.physics.nyu.edu/vagc/>). Finally we describe the selection criterion, characteristics and distributions of the subsample of galaxies from the fourth SDSS Data Release (DR4) used for this thesis.

2.2 Sloan Digital Sky Survey: Overview

2.2.1 Imaging

The SDSS imaging survey is split between the Northern Galactic cap and the three southern/equatorial fields. Most of the imaging survey, around 9000 deg^2 , is above Galactic latitude of 30° centered at $\alpha = 12^h 20^m$, $\delta = +32.5^\circ$. The equatorial stripe covers $\alpha = 20.6^h$ to 4^h , $\delta = 0^\circ$.

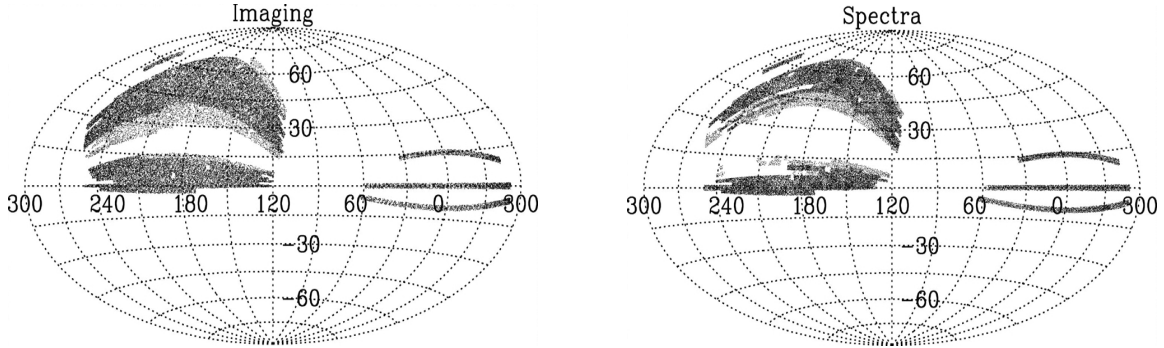


Figure 2.1: Distribution on the sky of SDSS imaging (left) and spectroscopy (right) included in DR4, shown in J2000.0 equatorial coordinates. These cover 6670 and 4783 deg^2 , respectively. The regions of sky that are new to DR4 are shaded more lightly, corresponding to 26% and 28% increments, respectively, over DR3. Figures taken from Adelman-McCarthy et al. (2006).

The other two stripes cover great circles lying between right ascensions and declination of $(20^h.7, -5.8^\circ)$ to $(4^h.0, -5.8^\circ)$ and $(22^h.4, 8.7^\circ)$ to $(2^h.3, 13.2^\circ)$. The fourth data release covers approximately two-thirds or 6670 deg^2 of the total survey area. The distribution on the sky of the imaging and spectroscopy is shown in Figure 2.1.

The SDSS 2.5m telescope uses a large-format CCD camera (Gunn et al. 1998) to image the sky almost simultaneously in five optical bands (u' : 3553 \AA , g' : 4686 \AA , r' : 6166 \AA , i' : 7480 \AA , z' : 8932 \AA). The mosaic CCD camera consists of two sets of arrays: the imaging array and the astrometric array. The imaging array uses 30 2048×2048 SITE Tektronic CCDs ($24\mu\text{m}$ pixels or $0.396''$ on the sky) placed in a grid of six columns and five rows. Each row observes the sky in a different filter, in temporal sequence r', i', u', z', g' . The astrometric array uses 24 400×2048 CCDs with the same pixel size, split into leading and trailing arrays that cover the entire width of the camera. The magnitude range of the array, $r' \sim 8.5\text{-}16.8$, allows measurement of astrometric catalog stars and the brightest unsaturated stars in the photometric array.

The imaging survey is taken in drift scan mode with an effective integration time of 54 seconds per filter. The images are processed through a series of specialized pipelines (Lupton et al. 2002) which flat-field the data, identify and match objects in all five bands, measure properties (Stoughton et al. 2002) and apply the astrometric (Pier et al. 2003) and photometric (Tucker et al. 2006) calibrations from a set of primary stars (Smith et al. 2002) observed on the neighboring USNO 1 m telescope and the 0.5m Photometric Telescope (PT). The photometric calibration is accurate to roughly 2% rms in the g, r and i bands and 3% in the u and z bands while the astrometric calibration is better than $0.1''$ rms per coordinate (Pier et al. 2003). For point sources brighter than $r \sim 20$ the astrometric accuracy when using the USNO Astrometric Catalog is 45 mas rms per coordinate. At the median seeing of the imaging data ($1.4''$), the 95% completeness for a point source is 20.0, 22.2, 22.2, 21.3, 20.5 mags in each of the five bands.

Table 2.1. Characteristics of the SDSS Fourth Data Release

Parameters	Value
Imaging	
Footprint areas (deg^2)	6670 (26% increment over DR3)
Imaging catalog	180 million unique objects
Magnitude limits ^a .	
<i>u</i> (mag)	22.0
<i>g</i> (mag)	22.2
<i>r</i> (mag)	22.2
<i>i</i> (mag)	21.3
<i>z</i> (mag)	20.5
Median PSF width (arcsec)	1.4 in <i>r</i>
Astrometry	$\leq 0''.1$ rms absolute per coordinate
Spectroscopy, Main Survey	
Footprint area (deg^2)	4783 (28% increment over DR3)
Wavelength coverage (\AA)	3800 - 9200
Resolution ($\Delta\Delta$)	1800 - 2100
Number of plates	1052
Number of spectra	673,280
Additional Spectroscopy	
Number of special plates	206
Number of spectra on special plates	121,840
Number of plates, repeat observations	70

2.2.2 Spectroscopic Observations

The main galaxy sample for spectroscopy selects objects with a reddening corrected, *r*-band Petrosian magnitude $^1 \leq 17.77$ and *r*-band Petrosian half-light surface brightness $\mu_{50} \leq 24.5$ mag arcsec⁻² (Strauss et al. 2002). The spectroscopic survey is carried out using two fiber-fed double spectrographs covering the wavelength range 3800-9200 \AA with a resolution between 1850 and 2200. The spectrographs are fed by a total of 640 fibers (each 3'' in diameter) split between the two cameras with a total integration time of 45-60 minutes depending on observing conditions. The spectra are processed through automated pipelines, `spectro2d` and `spectro1d` which reduce the two dimensional spectrograms to flux- and wavelength-calibrated spectra and determine object classifications (galaxy, quasar, star, unknown), redshifts and line measurements. The spectra are calibrated using F-subdwarfs, with a broadband uncertainty of 5% (Abazajian et al. 2004). The wavelength calibration uncertainty is roughly 0.05 \AA . The SDSS spectra are of high enough quality ($S/N > 4$ per pixel) that essentially all targeted galaxies yield a reliable redshift. Table 2.1 summarizes the imaging and spectroscopic characteristics of the DR4 release.

¹defined as the flux within a circular aperture of 2 x the petrosian radius (Petrosian 1976).

2.3 Supplementary Data : Garching Group

We use the derived masses, ages, star formation rates and metallicities from the Garching group (Kauffmann et al. 2003b; Brinchmann et al. 2004; Tremonti et al. 2004) to investigate the relationship between morphology and physical parameters. The reader is referred to the original papers for complete details. A brief summary follows.

2.3.1 Stellar Masses and Ages

Kauffmann et al. (2003b) fitted models based on the population synthesis code of Bruzual & Charlot (2003) to absorption line subtracted, emission line free regions of the spectrum of every galaxy within the spectroscopic main galaxy sample. A library of 39,000 models was created to span the full range of plausible star formations histories, representing bursting and continuous models equally. For each history the predicted values of stellar mass-to-light ratios, ages, colors, $D_n(4000)$, $H\delta_A$ and burst mass fraction were computed. Stellar masses were calculated by multiplying the dust-corrected z-band luminosity with the model predicted stellar mass-to-light ratio. The best estimate mass was obtained by weighting each model by its probability function.

Subtraction of the absorption line features was accomplished by fitting the emission line free regions with a model spectrum. 39 templates spanning a wide range in ages and metallicities were convolved with a gaussian to match the stellar velocity dispersion of each SDSS galaxy and then rebinned to the SDSS dispersion. The best fitting spectra, with dust attenuation modeled as a $\lambda^{-0.7}$ power law (Charlot and Fall 2000) were constructed from a non-negative linear combination of the template spectra.

Biases

The effect of finite aperture size is a worry, but Kauffmann et al. (2003b) showed the bias on mass-to-light ratio measurements is small and is more influenced by variations in luminosity and concentration than effective aperture size. It should be noted that the stellar mass obtained depends on the IMF used in generating the templates. Use of a Salpeter IMF instead of Kroupa's which is used by the Garching group would lead to stellar masses approximately a factor of two larger (Kauffmann et al. 2003b).

2.3.2 Metallicities and Star Formation Rates

Tremonti et al. (2004) and Brinchmann et al. (2004) used a similar method to calculate metallicities and SFRs based on emission line strengths. After continuum subtraction (as described

above) all emission lines were modeled simultaneously, requiring all Balmer lines have the same line width and velocity offset (likewise for the forbidden lines) while accounting for the wavelength dependent instrumental resolution of each fiber. The lines were fit with Charlot and Longhetti (2001) models which combine evolution models from Bruzual and Charlot (1993) with emission line modeling from CLOUDY (Ferland 1996). A model grid of $\sim 2 \times 10^5$ models was generated with different metallicities, ionization parameters, total dust attenuation in V-band and dust-to-metal ratio of ionized gas. The attenuated line ratios from each model were compared directly to the observed spectrum to derive star formation rates and metallicities. Again a likelihood approach was used to define the uncertainty in these parameters. The emission line measure of star formation rate are used only in galaxies without an AGN component. Following the demarcation prescription in Kauffmann et al. (2003a), a galaxy is defined to be an AGN if

$$\log([\text{OIII}]/\text{H}\beta) > 0.61/(\log([\text{NII}]/\text{H}\alpha) - 0.05) + 1.3, \quad (2.1)$$

For AGN and composites the measured D4000 value is used to estimate SFRs from the relationship between emission-line fit SFRs and D4000 for non AGNs. Oxygen abundance were derived from the nebular emission line which has the advantage of greater S/N to absorption features used to measure Lick indices but it restricts the analysis to star-forming galaxies only.

2.4 Supplementary Data : NYU Group

The New York University-Value Added Galaxy Catalog (NYU-VAGC) (Blanton et al. 2005b) is a catalog of local galaxies based on the SDSS public data release. The catalog includes matches to Galaxy Evolution Explorer Survey (GALEX), the Two Micron All Sky Survey (2MASS), IRAS Point Source and Extended Source Catalog, the Two-Degree Field Galaxy Redshift Survey (2df), the Third Reference Catalog of Bright Galaxies (RC3) and Faint Images of the Radio Sky at Twenty cm survey (FIRST). In addition Blanton et al. (2005b) provide one component Sersic fits to the azimuthally averaged radial profiles of each object and use the fit to derive half light sizes r_{50} , 90% light radius r_{90} and the mean surface brightness μ_{50} within r_{50} . Detailed description of the fitting procedure is given in Blanton et al. (2005a). In summary, mean fluxes and errors in annuli output by the SDSS PHOTO pipeline (profMean and profErr ; see Stoughton et al. (2002)) are fit with an axisymmetric Sersic model.

$$I(r) = A \exp[-(r/r_o)^{1/n}], \quad (2.2)$$

where A , r_o and n are free parameters quantifying the amplitude, size and shape of the surface brightness profile. These parameters are determined by minimizing

$$\chi^2 = \sum_i [\text{profMean}_i - \text{seraicMean}_i(A, n, r_o)] / \text{profErr}_i^2, \quad (2.3)$$

where $\text{seraicMean}_i(A, n, r_o)$ is the mean flux in annulus i for the Sersic model convolved with a seeing model. Blanton et al. (2005a) tested the performance of the algorithm by distributing fake stamps (which included the effects of seeing, noise, and sky subtraction) in the SDSS frames and re-extracting them through the PHOTO pipeline. They found a bias in the measurements such that for objects with larger sizes or sersic indices, the algorithm underestimated the sizes and fluxes of the objects by 10% and 15% respectively while the sersic index was itself underestimated by 0.5 for objects with large sersic indices. The bias in measurements is mostly due to the small errors in fitting the sky level by PHOTO. Thus the algorithm provides approximately the right answer for galaxies with a bias not much larger than the uncertainty and where the additional computational expense in fitting the sky is not justified for a small change in χ^2 .

2.5 Catalog

Our goal is to create a large, well defined, morphologically resolved sample of galaxies which can be compared directly to HST images of high redshift objects. It is therefore important that we probe the same physical scales at both high and low redshift. As shown in Abraham et al. (1994), the effects of depth, seeing and resolution are all important in measuring quantitative properties. The effect of seeing is strongest on the smallest objects. Hence we specify all objects in our sample to be a few times the size of the stellar seeing disk in order to measure parameters like concentration reliably. Our objects also have to be fairly bright to sample the objects light profile given signal to noise considerations. We chose an extinction corrected petrosian g' band magnitude brighter than 16 based on visual inspection of the SDSS Atlas images. Our impression with the initial Early Data release was that visual classification could only be carried out in very broad bins. However upon further study of classification schemes we found that we could distinguish between subclasses of spirals. Thus it is possible extend the magnitude cut to fainter limits at lower redshifts. We chose a low redshift cut of $z = 0.01$ to ensure all galaxies are sampled in a single frame. Most objects below this redshift cut are very extended and extraction proves to be very tedious. Unfortunately, given our magnitude considerations this results in an under-representation of late type objects (Sd onwards) in our sample as they are inherently faint. Since mass estimates in this redshift range are also unre-

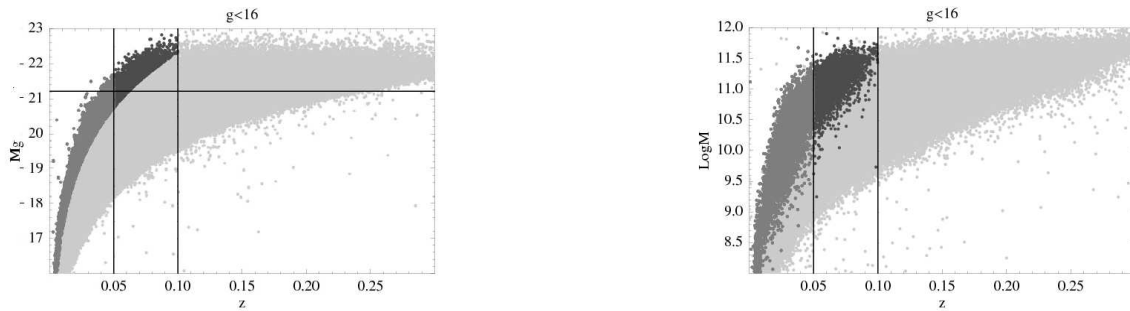


Figure 2.2: Absolute magnitude vs. redshift for our local SDSS sample with $g < 16$. The horizontal line corresponds to $M_* = -20.44 - 5 * \text{Log}_{10}h$ for an $h = 0.7$, $\Omega_M = 0.3$, $\Omega_\Lambda = 0.7$ cosmology. The vertical lines is our redshift cut of $z = 0.05$ and $z = 0.1$. The light grey area shows the distribution of the entire DR4 main galaxy sample up to $z \leq 0.3$. The intermediate grey shows the distribution of the sample with $z \leq 0.05$ while the dark grey area shows the distribution with $z \leq 0.1$.

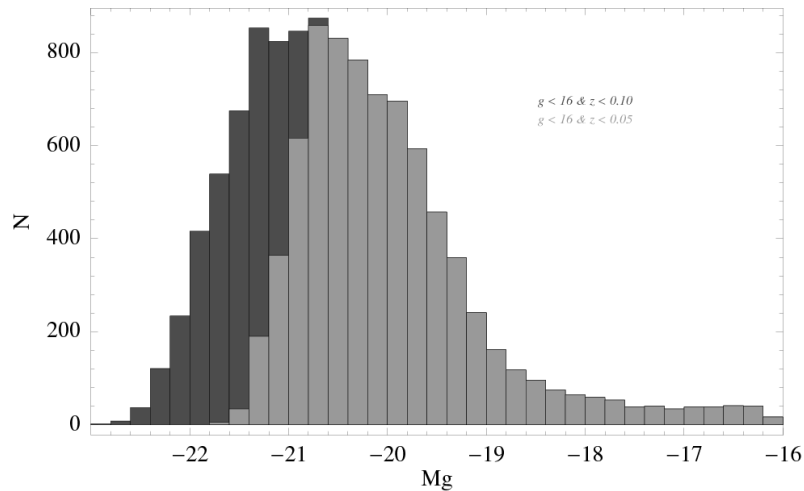


Figure 2.3: Number of Galaxies vs. Absolute g band Magnitude for our sample of galaxies with $g < 16$. The light grey area shows the distribution of the sample with $z \leq 0.05$ while the dark grey area shows the distribution with $z \leq 0.1$. With the initial sample most of the bright galaxies were missed.

liable (Kauffmann et al. 2003b), we have chosen to try to account for this bias at a later date. (This will be discussed further in the next chapter.) Our initial high redshift cut of $z = 0.05$ was based on resolution conditions. Objects imaged with HST at $z \sim 1$ are well matched in physical resolution to SDSS objects below z of 0.05. Figure 2.2 shows the distribution of our

samples' absolute g' -band magnitude and mass with redshift. For an $h = 0.7$, $\Omega_M = 0.3$, $\Omega_\Lambda = 0.7$ cosmology M_* is shown. Beyond $z = 0.05$, only galaxies brighter than M_* are present in our sample. Figure 2.3 shows the distribution of number of galaxies with absolute magnitude for $g \leq 16$. It can be seen that choosing a redshift cut of 0.05, selected to probe the same physical resolution scale as galaxies at $z \sim 1$, results in missing most of the bright, massive galaxy population. To minimize bias at the high mass end we have extended our redshift cut to 0.1 as the lower resolution is compensated by the fact that objects in this redshift regime are brighter and as we will see in the next chapter, predominantly early type.

We use the photometry catalogs from the SDSS Data Release 4, obtained through the online query tool CASJobs, to select all galaxies with an extinction corrected g' band petrosian magnitude brighter than 16 at redshifts between $0.01 < z < 0.1$. This gives us a sample of 14500 galaxies. We chose to re-extract the galaxy images as opposed to using the SDSS provided atlas images as the SDSS 'photo' pipeline did not perform well (as of the DR4 release) for extended objects with star formation knots. The original flat-fielded corrected (fpC) frames for these objects were used for object detection and extraction using SExtractor (Bertin & Arnouts 1996). Each frame was visually inspected to ensure accurate de-blending and segmentation of galaxies and to ensure all non-galaxy contaminants are removed as well as galaxies with a star close enough to distort the image, either because of a diffraction spike or because segmentation was not possible. The final sample size of our catalog is 14034 objects.

Figure 2.4 shows the distribution of (a) axial ratios, (b) size, (c) absolute magnitudes, (d) mass, (e) color and (f) sersic indices for our sample. We find we preferentially select galaxies with large b/a given our apparent magnitude selection criterion. In addition, we find very few objects with sersic indices below 2, which would correspond to pure disk systems. This can also be inferred by the lack of very blue galaxies. The distributions are similar when considering objects with $b/a > 0.6$ only. Thus overall we span a wide range in mass, luminosity, size and structure. In the next chapter we will describe our visual and quantitative classification methodology.

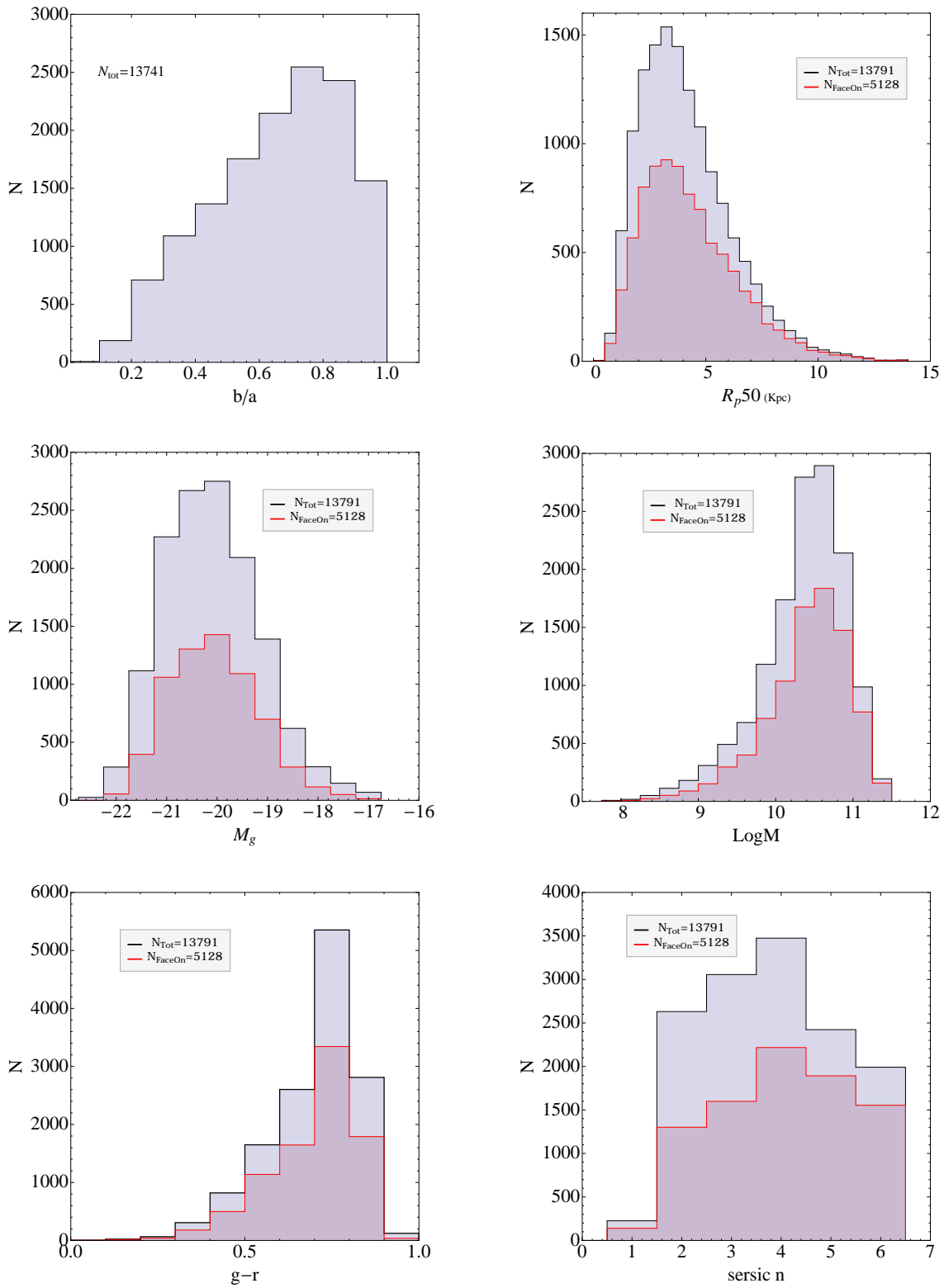


Figure 2.4: Histograms of (a) g-band axis ratios b/a , (b) size R_{p50} , (c) g-band Absolute Magnitude (d) Mass (e) $g-r$ color and (f) g-band sersic index. The gray histogram shows the distribution for the complete sample while the violet histogram shows the distribution for face-on objects defined as $b/a > 0.6$. The distributions for the two samples are similar.

Chapter 3

Classification Schemes

3.1 Introduction

Galaxy morphologies do not take discrete values, rather they exhibit a continuum of features that can be seen in quantitative measures like bulge-to-disk ratio and concentration. This has led to morphology moving from the realm of classification into that of measurement. Nevertheless classification using T-Types (de Vaucouleurs 1963) is very useful in understanding the broader trends in properties of galaxies and studying their evolution. The same cannot yet be said for quantitative measures whose detailed connection to the Hubble Sequence is still unclear (Zamojski et al. 2007). This is in part because a comprehensive comparison between visual and quantitative morphologies in the local universe has not been conducted.

In this chapter we provide a catalog of g-band visual classifications for the sample of ~ 14000 objects defined in Chapter 2. Our catalog is 6x larger than that presented in Fukugita et al. (2007) and attempts to encompass a broader range of morphological features. In addition to T-Types, we record the existence and prominence of bars, rings, lenses, tails, shells, warps and dust lanes. Spiral structure classifications including information on arm flocculence and multiplicity have been carried out but will not be presented in this work as comparison to literature, specifically Elmegreen & Elmegreen (1987) classification scheme, have not yet been carried out. This catalog is presented with two main goals in mind:

- (i) It defines a generally useful comprehensive local sample with highly detailed morphological classifications.
- (ii) It provides a starting point for attempts to improve automated galaxy classification by incorporating detection algorithms for subtle morphological features. With the exception of some simple attempts to automate the detection of galactic bars, to date no automated classification method attempts to characterize the ‘fine structure’ of galaxy morphology.

In this chapter we describe the visual and quantitative methodologies used to classify

galaxies. We investigate the effectiveness of quantitative measures in distinguishing between galaxy types. Parts of this work have already been published in Abraham et al. (2003) and Abraham et al. (2007) We postpone the study of the abundances of bars, rings and interacting objects in the local universe and the correlations seen with AGN activity to Chapter 6 and 7.

3.2 Visual Classification Scheme

The galaxy classification scheme used here is primarily based on the Carnegie Atlas of Galaxies (Sandage & Bedke 1994) in consultation with the Third Reference Catalog of Bright Galaxies (RC3; with images from the IPAC NED webpage). Traditional methods for classification involve printing galaxy images at various contrast ratios and manually inputting the classification back into a table. For the ~ 14000 objects in our sample this would be a very cumbersome and tedious process not to mention an ecological waste. We sought to develop a method of classifying a large number of objects repeatedly and ideally by multiple observers. After investigating a number of on-line methods (including stand alone graphical user interfaces, html based forms and paper-based forms), we decided a web-based html form provided the maximum flexibility to achieve our goals.

We first studied a subsample of objects in all 5 bands to determine the classifications that we could carry out. We classified galaxies by T-Type augmented by other classifications. We find distinction between the various Hubble subclasses is possible for most of our objects. We include flags for doubtful (?), peculiar (p) and unknown (:) in our classification as in the RC3 scheme. In addition to the RC3 scheme, we have additional bins for objects that cannot be classified on the Hubble scheme (clump-clusters, tadpoles, doubles, chains as defined by Elmegreen et al. (2005)) and objects which are possibly peculiar versions of Hubble type objects. We classify 'fine structure' defined to include stellar bars (as strong, intermediate, weak, ansae and peanut), rings (as nuclear, inner, outer, pseudo-outer rings R1/R2, and collisional ring systems), lenses (as inner and outer lenses), arm type (grand design to flocculent as well as length), arm multiplicity, presence of dust lanes, galaxy orientation, interaction features such as tails, warps, shells and bridges, the morphology of the nearest interacting galaxy and the merger orientation. To confirm the presence of some of these features, like bars, we consulted the r and i bands as well as g, though T-Types are based solely on the g-band image. We decided to exclude the u' and z' band images due to poor signal to noise ratio.

Our final visual classification procedure is as follows. The registered SDSS fpC reduced frames are used to re-extract the galaxies in u, g, r, i, z bands with 'SExtractor', using the r band image as the template. The segmentation of each galaxy is checked visually to ensure 'parent' and 'child' objects are correctly separated. Stamps are created for each object in each

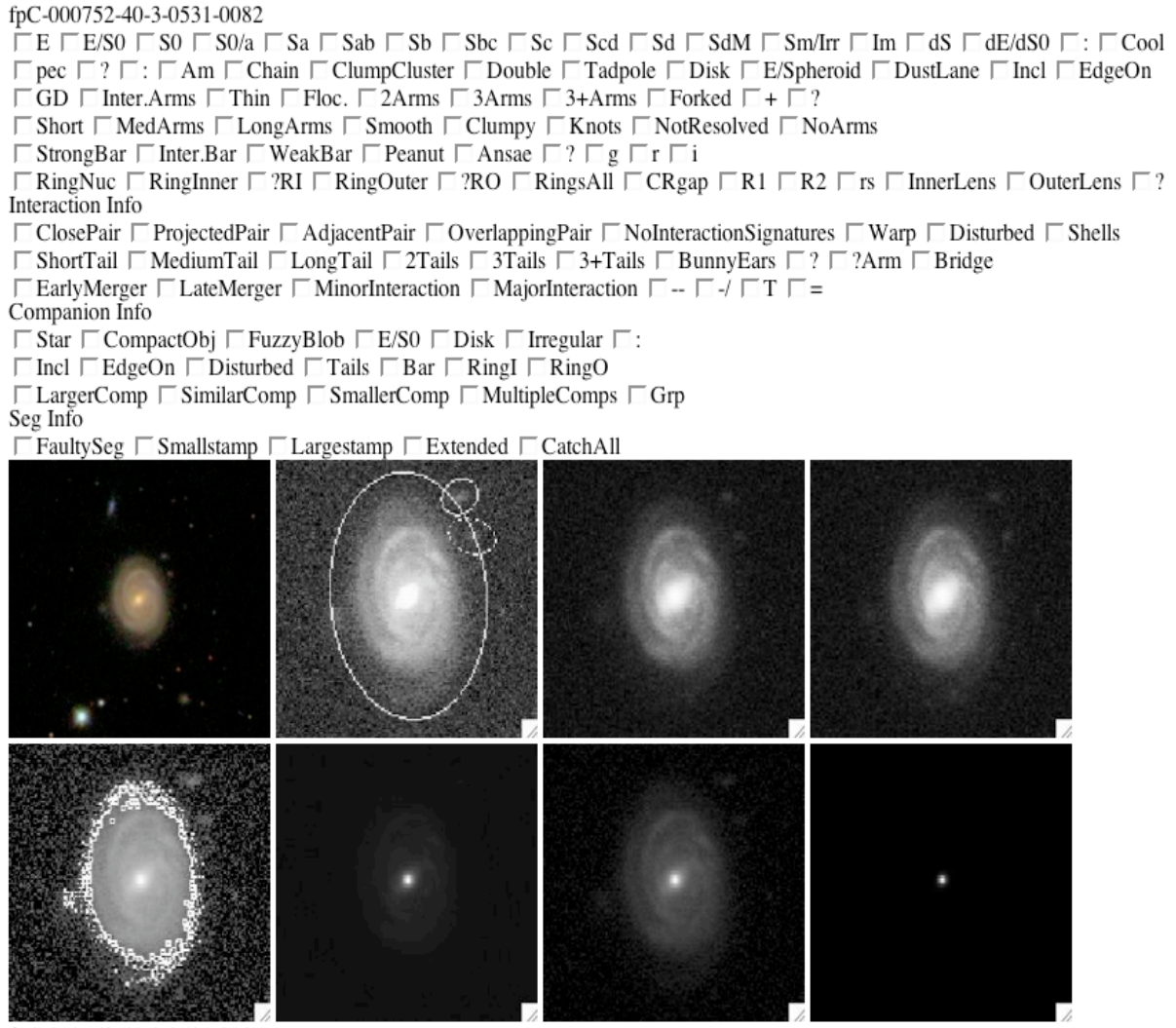


Figure 3.1: An example of the form used for classifying objects in the SDSS. With the exception of the color image, all other stamps are $50 h^{-1}$ kpc on a side. The color image is $100 h^{-1}$ kpc on a side to check for nearby visual companions. The top row shows the g , r and i band images with the sextractor aperture over plotted on the g band image. The second row shows the galaxy at 4 different contrast ratios in the g -band to highlight different parts of the galaxy. The first image in the bottom row shows the quasi-petrosian aperture calculated by our quantitative morph code MORPHEUS. This form is used to classify objects, identify all interaction signatures, identify companions with which our object of interest may be interacting and to check for any segmentation faults. For any object where the set contrast ratios were not appropriate for identification purposes, we used ds9 manually and entered the appropriate check boxes.

band at 5 contrast ratios determined by the flux range spanned by the galaxy. An example of the web form used is shown in Figure 3.1. With the exception of the color image (generated by SDSS), all other stamps are $50 h^{-1}$ kpc on a side. The color image is larger, $100 h^{-1}$ kpc on a side, to check for nearby visual companions. The top row shows the g , r and i band images with the sextractor aperture over-plotted on the g band image. The second row shows the galaxy

at 4 different contrast ratios in the g-band tailored to highlight different parts of the galaxy. The first image in the bottom row shows the quasi-petrosian aperture (Abraham et al. 2007) calculated by our quantitative morphology code MORPHEUS, which will be described later in this chapter. For any object where the set contrast ratios were not appropriate for identification purposes, we used ds9 manually and entered the appropriate check boxes. Results for each galaxy were appended to a master file. An effort was made to assign all peculiar objects to their nearest possible type. Late type mergers, collisional rings and unknowns are assigned to 'bulge-like', 'disk-like' or ': '(unknown). The entire sample was classified twice by the author with a mean deviation of less than 0.5 T-Types.

3.3 Representative Examples of T-Types and Fine Classes

Figures 3.2 and 3.3 show (g,r,i) color¹ composite images of a random sample of E through Sd galaxies with RC3 or Fukugita classifications. Table 3.1 shows the relation between RC3 T-Types², our T-Types, and the T-Types used recently by Fukugita et al. (2007) for classifying 2253 galaxies from the SDSS Data Release Three by three of the authors. For the sake of clarity we have grouped sub-categories of galaxies into the following broad classes: E and E/S0 galaxies, S0 and S0/a galaxies, Sa and Sab galaxies, Sb and Sbc galaxies, Sc and Scd galaxies and galaxies with T-Types later than Sd. The J2000 object identifier is listed at the top with the author's T-Type (PN T-Type) and RC3³/Fukugita classification at the bottom. The objects are arranged in order of decreasing mass. Note the presence or absence of a dust lane is not used as a classification criteria.

For the objects shown, we find our classification agree very well with the RC3 classification though there are some disagreements. For Sd and later objects where only Fukugita classifications exist, the classifications are well matched, with most objects having a Fukugita classification greater than 4 (or Sc and later). The cause of disagreement in some cases appears to be because the central luminous source is attributed to a (pseudo) bulge by Fukugita et al. (2007) and to a bar in our scheme. In the next section we will demonstrate our classifications are consistent with RC3/Fukugita for the complete overlap sample. Overall the figures illustrate the diversity of visual morphologies and fine classes in the SDSS as well as the ability to distinguish between sub-classes with the SDSS images.

¹The color stamps were retrieved from the SDSS Catalog Archive Server (casjobs).

²An easy way to remember the numeric equivalent for a T-Type is to note that all major classes are odd numbers, for example Sa galaxies have T-Type 1, Sb galaxies have T-Type 3. The finer separation Sab has T-Type 2.

³The RC3 short form classification is made up of 7 characters which starting from the left identify (1) peculiarities such as outer rings 'R', (2) Crude class: E for elliptical, L for lenticular or S for spiral (3) bar class: B for strong bar, X for weak bar, A for no bar, (4) inner rings, R or lenses, L, (5) T-Type for example 3 for Sb, (6) flags like unsure(?) and (7) flags.

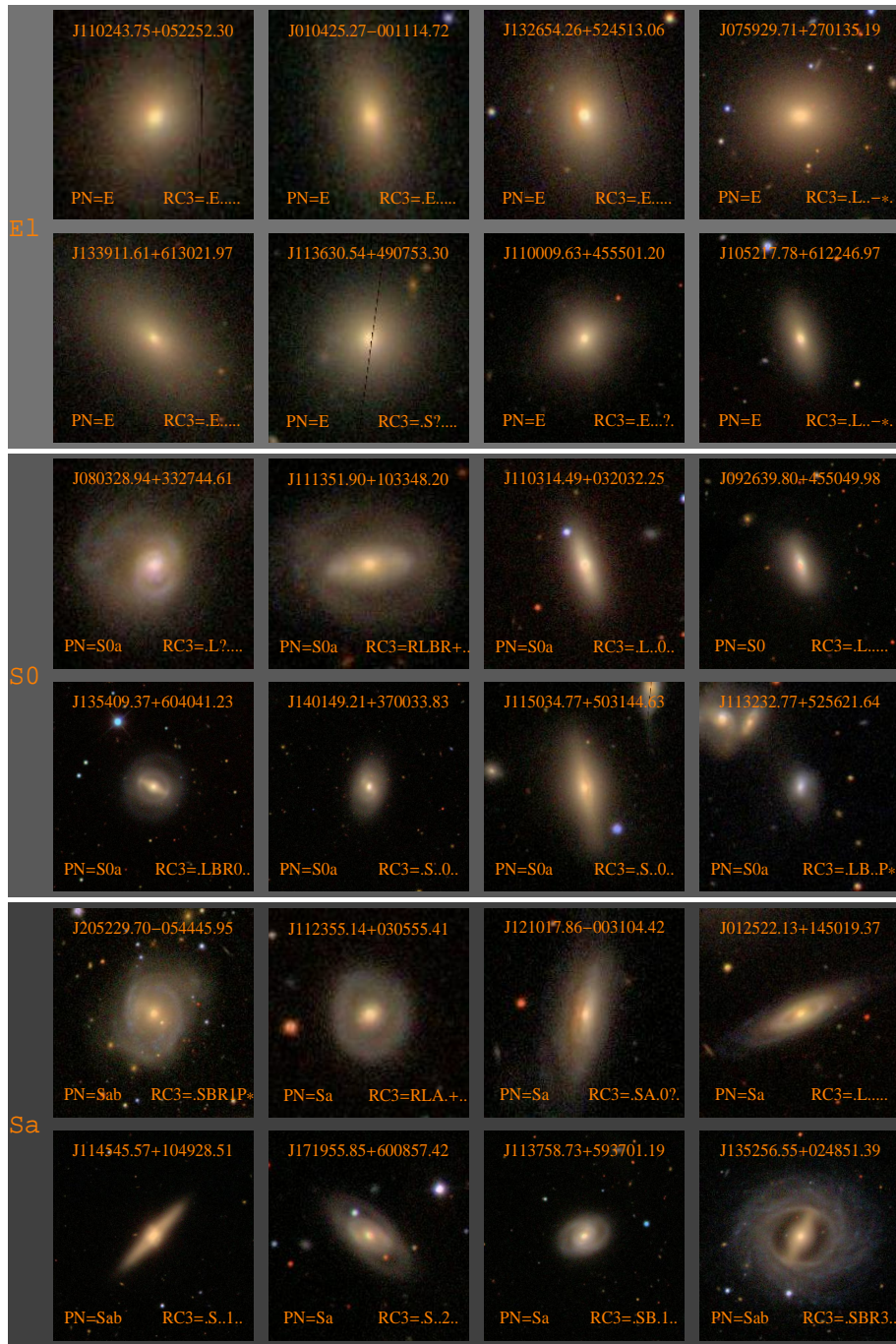


Figure 3.2: A montage of images representing **Top** E + E/So galaxies, **Middle** S0+ S0a galaxies and **Bottom** Sa + Sab galaxies (2 rows for each) as classified by the author. The J2000 object identifier is listed at the top with the redshift and the RC3 classification at the bottom. The seven possible letters starting from the left in the RC3 designation identify (1) peculiarities such as outer rings ‘R’, (2) Type: E for elliptical, L for lenticular or S for spiral (3) bar class: B for strong bar, X for weak bar, A for no bar, (4) inner rings, (5) T-Type eg 3 for Sb (6 and 7) flags like unsure(?). Each stamp is $50 h^{-1}$ kpc on a side. The color images are taken from the SDSS Imaging Server.

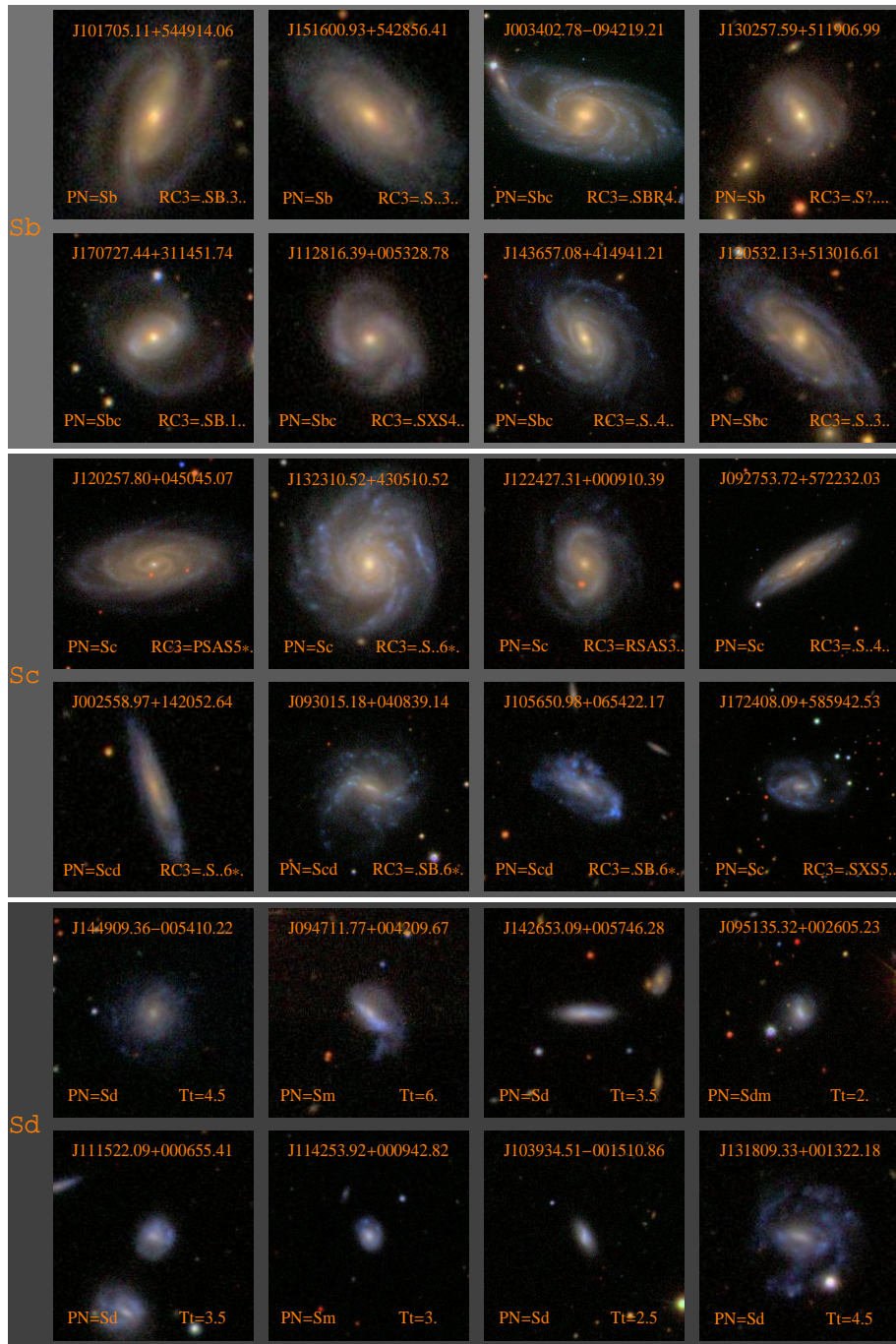


Figure 3.3: A montage of images representing Sb, Sc and Sd galaxies (2 rows for each) as classified by the author. The J2000 object identifier is listed at the top with the redshift and the RC3 classification at the bottom (when available). The seven possible letters starting from the left in the RC3 designation identify (1) peculiarities such as outer rings 'R', (2) Type: E for elliptical, L for lenticular or S for spiral (3) bar class: B for strong bar, X for weak bar, A for no bar, (4) inner rings, (5) T-Type eg 3 for Sb (6 and 7) flags like unsure(?). Each stamp is $50 h^{-1}$ kpc on a side. The color images are taken from the SDSS Imaging Server.

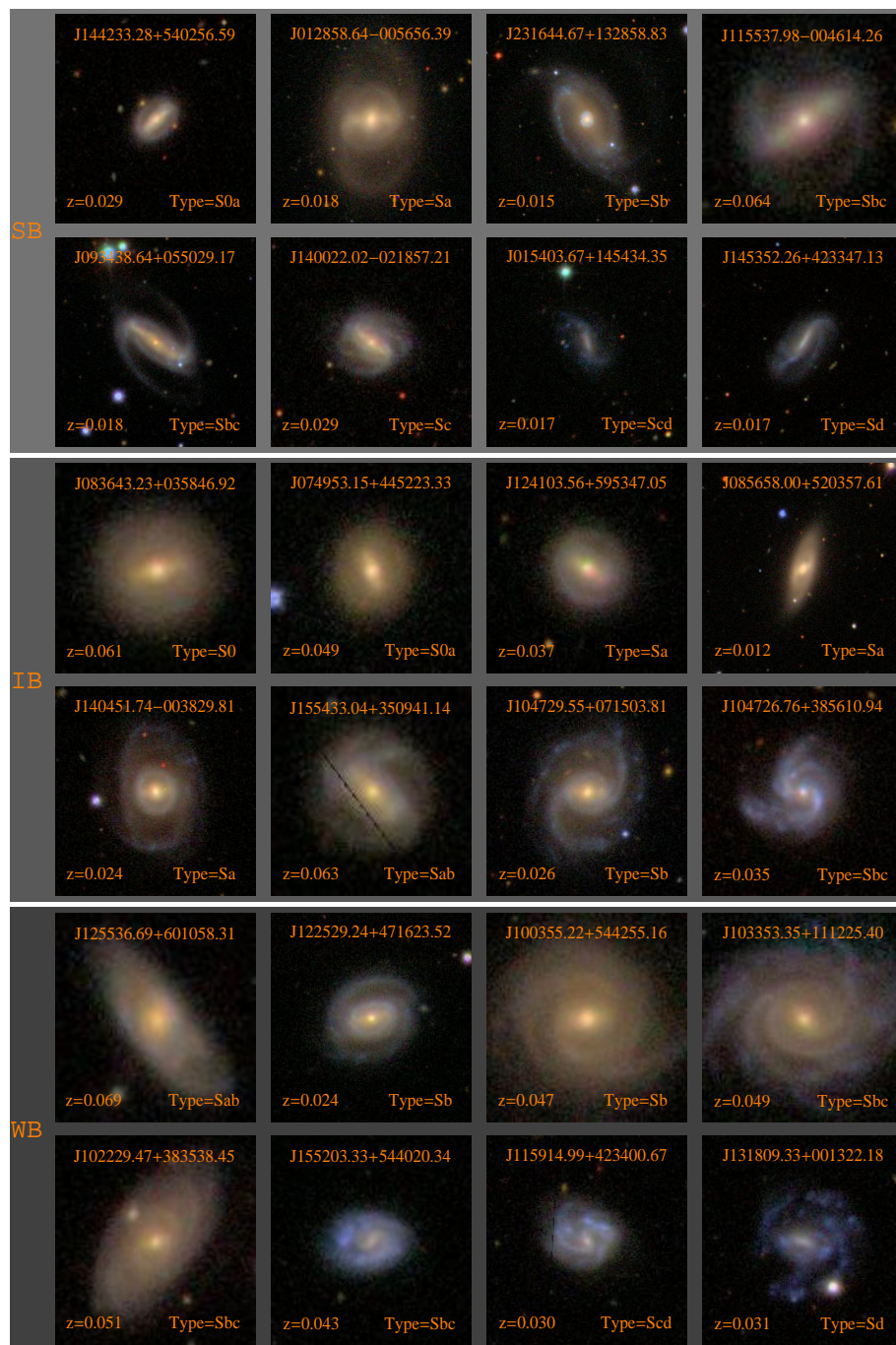


Figure 3.4: A montage of images representing **Top:** Strong bars, **Middle:** Medium bars and **Bottom:** Weak bars (2 rows for each) as classified by the author arranged in order of T-Type. Strong bars are comparable in size to the galaxy and have a significant amount of the total flux of the galaxy. Weak bars are smaller in size and contain a small fraction of the total flux of the galaxy. Intermediate bars span the range between strong and weak bars. The J2000 object identifier is listed at the top with the redshift and the author classification at the bottom. Each stamp is $50 h^{-1}$ kpc on a side. The color images are taken from the SDSS Imaging Server.

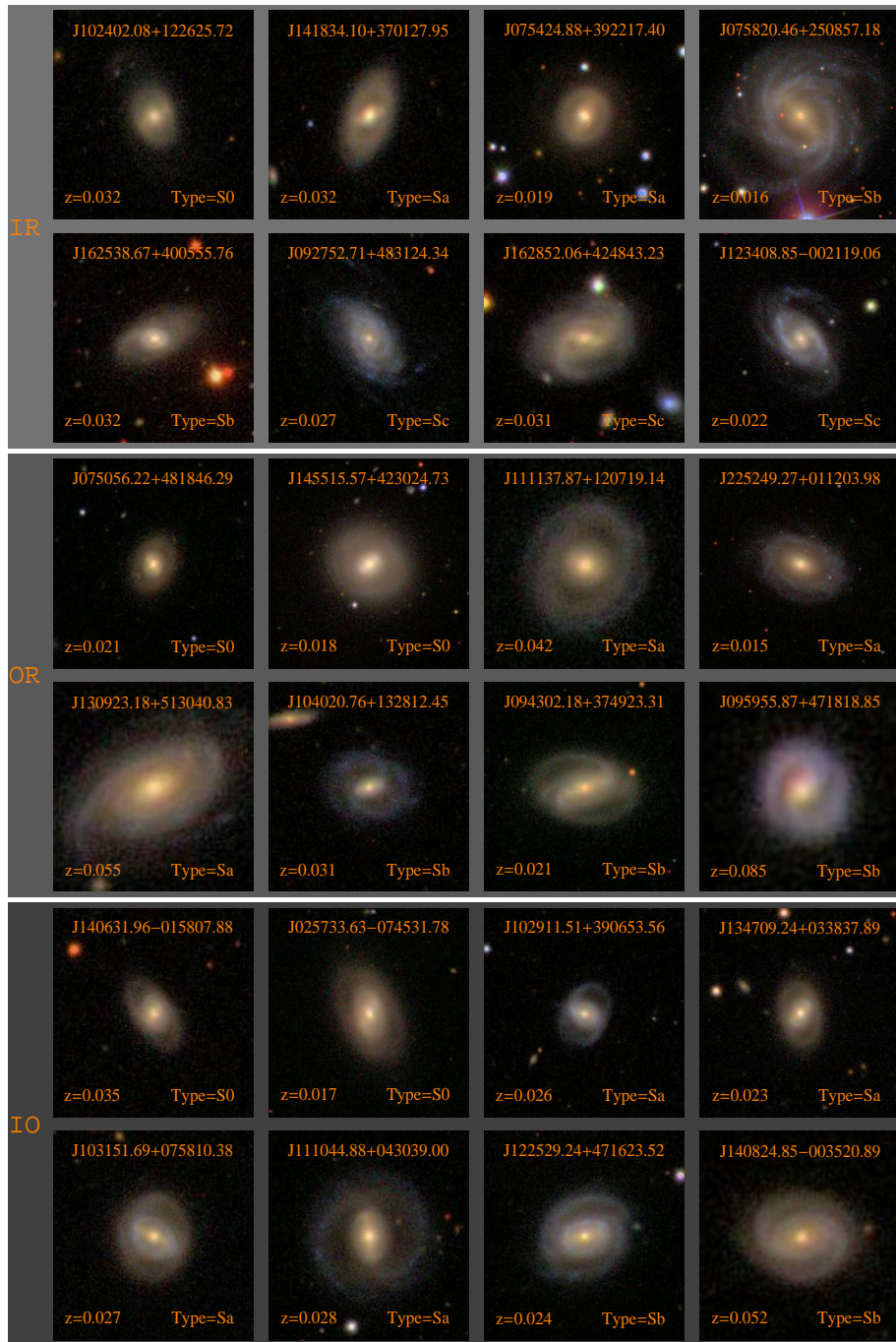


Figure 3.5: A montage of images representing inner rings, outer rings and objects with both (2 rows for each) as classified by the author. Inner rings are more easily identified in barred object where they begin near where the bars end. Partial rings have also been included in this category. Outer rings are fairly easily identified in most systems. Pseudo-rings as defined by Buta (1990) are included in this category. Confusion can arise in systems with no bars and only one ring as well as with collisional ring systems. The J2000 object identifier is listed at the top with the redshift and the author classification at the bottom. Each stamp is $50 h^{-1}$ kpc on a side.

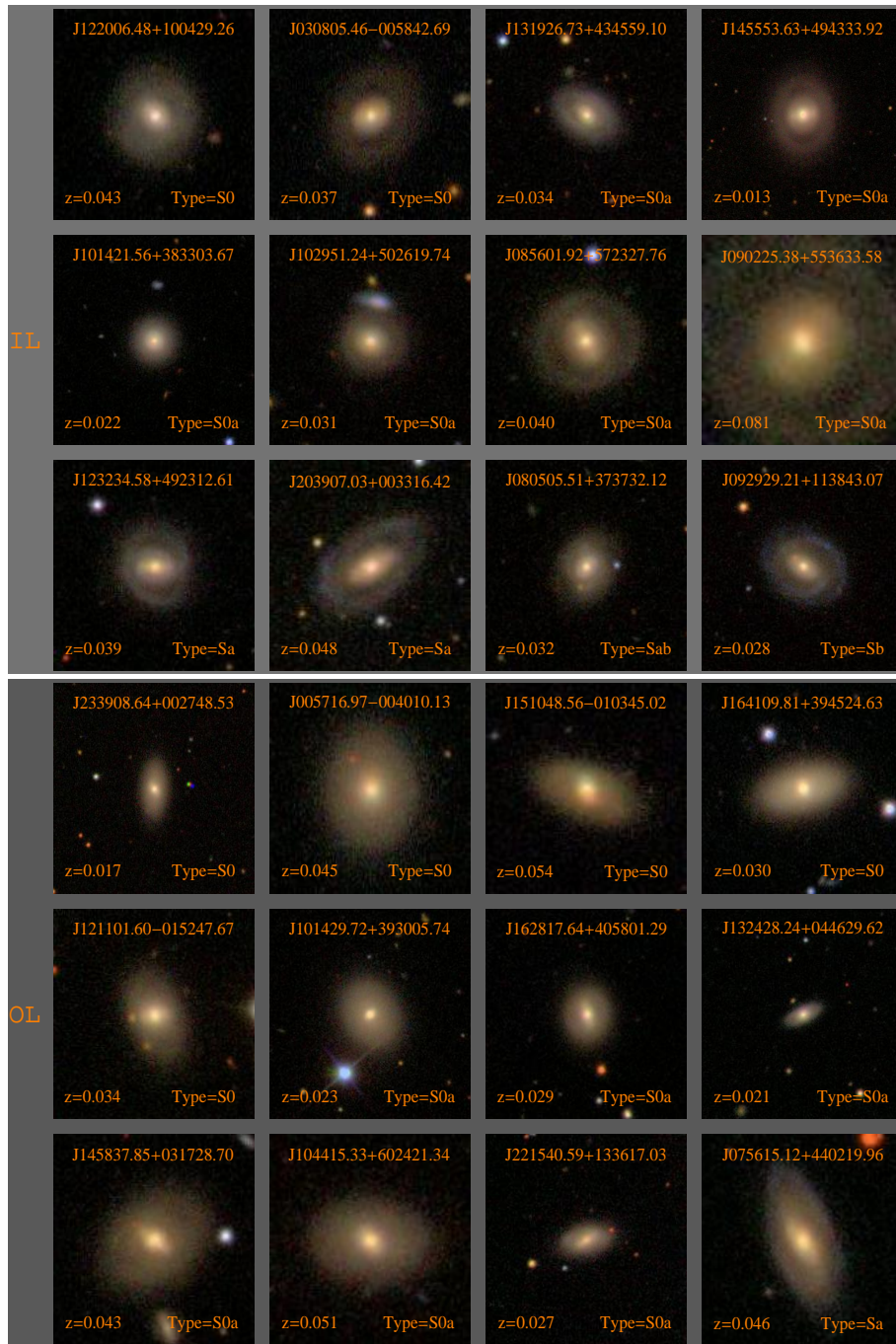


Figure 3.6: A montage of images representing Inner and Outer lenses (3 rows for each) as classified by the author. The lenses are seen as regions of near constant surface brightness with very little variation with radius. Inner lenses are most easily identified when they have an outer ring. Outer lenses can lead to outer rings. The J2000 object identifier is listed at the top with the redshift at the bottom left and the author classification at the bottom right. Each stamp is $50 h^{-1}$ kpc on a side.

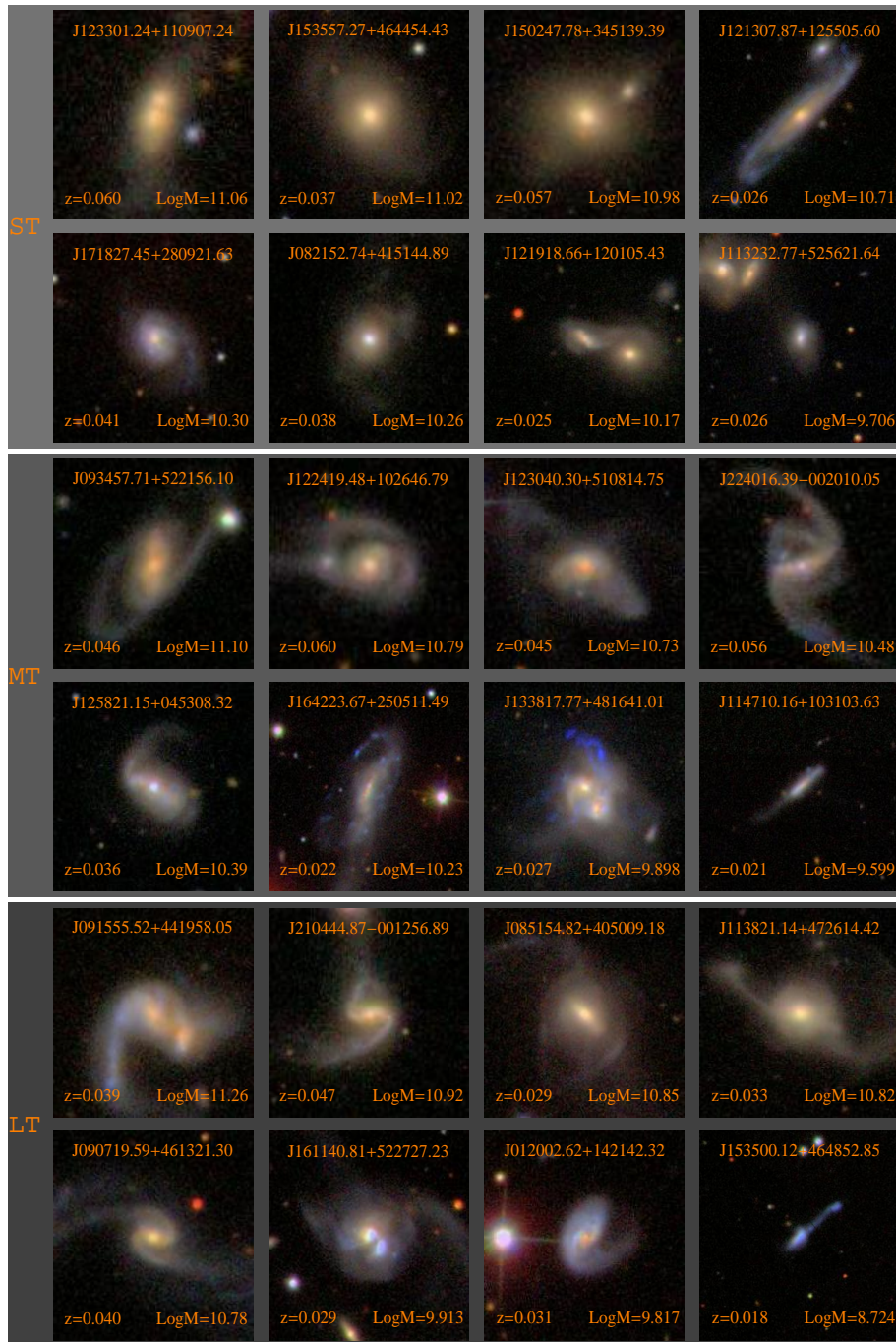


Figure 3.7: A montage of images representing short, medium and long tidal tails (2 rows for each) as classified by the author. Tidal tails are classified into the three categories based on comparison with the host galaxy size. If the tails are much larger than the galaxy, they are classified as long tails. Tails comparable in size to the galaxy are classified as medium tails while those much smaller than the galaxy are classified as short tails. Many objects display multiple tails. The J2000 object identifier is listed at the top with the redshift at the bottom left and the author classification at the bottom right. Each stamp is $50 h^{-1}$ kpc on a side.



Figure 3.8: A mosaic of images representing collisional rings as classified by the author. The J2000 object identifier is listed at the top with the redshift and the author classification at the bottom. Each stamp is $50 h^{-1}$ kpc on a side.

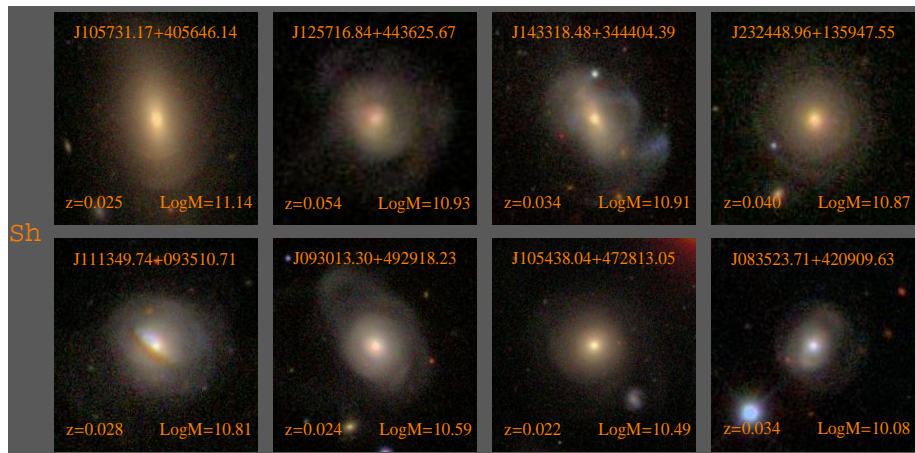


Figure 3.9: A mosaic of images representing shells as classified by the author. The J2000 object identifier is listed at the top with the redshift and the author classification at the bottom. Each stamp is $50 h^{-1}$ kpc on a side.

Figures 3.4 - 3.9 show representative examples of fine-features we have classified in our objects, with the J2000 object identifier listed at the top, the galaxy redshift at the bottom left and our T-Type classification (or mass for disturbed objects) at the bottom right. Our emphasis here is to display our fine classification scheme hence comparison with RC3 classified fine objects will be shown in the next section.

Figure 3.4 shows random samples of strong, intermediate and weak bars. The strength of the bar is defined in terms of the size of the bar compared to the galaxy diameter and its prominence. Bars that dominate that light distribution are strong bars. Weak bars are smaller in size and contain a small fraction of the total flux of the galaxy. Intermediate bars span the range between strong and weak bars. In our scheme all the bar types are definite which is unlike the RC3 fine scheme where weak bars are possible bars. Our classification of bar strength is based on the g band image but the existence is based on all three bands (g,r,i). In nearly every case ($\sim 98\%$), bars observed in the r and i bands are also observed in g. It is also apparent that many of our barred objects have a ring or lens component. We will investigate this further later in the chapter.

Figure 3.5 shows a montage of inner and outer ringed galaxies. Inner rings are more easily identified when bars are present. In galaxies without bars, ring classifications are much harder due to confusion with outer rings. Outer rings and pseudo outer rings as defined by Buta & Combes (1996) are also distinguishable. Confusion can occur with lens galaxies as in Figure 3.6 and collisional ring systems. Lens galaxies (or galaxies with regions of constant surface brightness) can exhibit either an inner or an outer lens. Both lens types can lead to the corresponding rings. So there are galaxies with outer lenses that eventually form outer rings.

We have also classified objects based on interaction signatures. We identify objects with tidal tails, collisional rings, and shells all of which are foolproof signatures of merger activity. Figure 3.7 shows examples of galaxies with short, intermediate and long tails. The strength of the tail is defined in terms of the size of the tail compared to the size of the galaxy. Tails larger than the diameter of the galaxy are classified as large tails. Tails comparable to the diameter of the galaxy are medium or intermediate tails while tails much smaller than the diameter of the galaxy are short tails. Multiple tails can exist in a single system. Figure 3.8 shows a sample of collisional ring systems which are ringed galaxies caused by bulls-eye collisions between two galaxies. The rings formed are bluer than what would be seen in a normal-ringed galaxy and can also be asymmetric. Our classification into collisional rings is based on the color stamp of the galaxy, the shape of the ring, on the presence of spokes (as in the cartwheel galaxy ESO 350G040) and/or the presence of a nearby companion galaxy with which the ringed galaxy may be interacting. Figure 3.9 shows examples of galaxies which have shells and are most probably the end stage of a merger. They are predominantly disturbed E, and S0 galaxies.

Table 3.1. T-Type Classification Schemes

Class	c0	E0	E+	S0-	S0	S0+	S0/a	Sa	Sab	Sb	Sbc	Sc	Scd	Sd	Sdm	Sm	Im	?
RC3	-6	-5	-4	-3	-2	-1	0	1	2	3	4	5	6	7	8	9	10	:
Fukugita	0	0	0	1	1	1	1	2	2	3	3	4	4	5	5	6	6	-1
PN	-5	-5	-5	-3	-2	-2	0	1	2	3	4	5	6	7	8	9	10	99

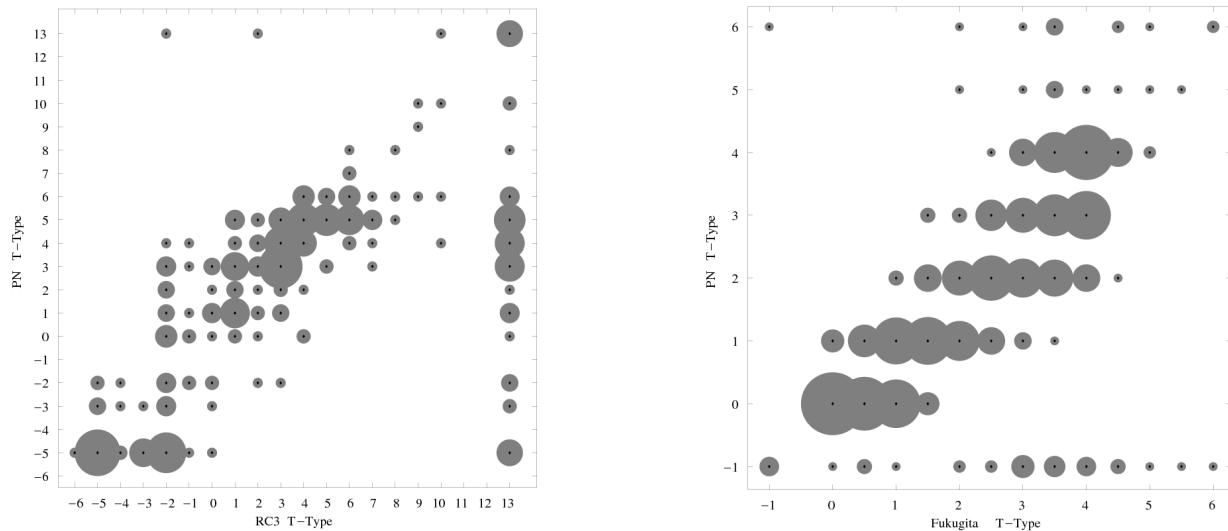


Figure 3.10: Point size is keyed to number of objects. (a) Classification by PN vs RC3 classification for 325 objects. The mean deviation is 1.5 T-Types (b) Classification by PN vs Fukugita et. al 2007 classification for 450 objects. The mean deviation is 0.8 Fukugita bins.

3.4 Reliability of Classification

3.4.1 Comparison of T-Types with Previous Works

Table 3.1 shows the relation between RC3 T-Types, our T-Types, and the T-Types used recently by Fukugita et. al. 2007 for classifying 2253 galaxies from the SDSS Data Release Three. The RC3 T-Types cE and cD (T-Type = -6/-4) and S0- (-1) are incorporated into our T-Types -5 and 0 respectively as we base our classification on the Carnegie Atlas of galaxies which does not have cE or cD types. Figure 3.10(a) shows a comparison of our classification with the 350 objects which overlap with the RC3. There are a number of objects in the RC3 which are not defined explicitly but are stated to be either E (elliptical), L (lenticular) or S (disk) and highly doubtful. Objects classified as E or L alone without any subclass have been assigned to T-Types -5 and -2. Objects assigned an S only have been given a T-Type of 13. Our classification is fairly consistent with the RC3 classification though slightly later overall. The mean deviation in classification between PN and RC3 sample is 1.5 T-Types when excluding objects classified as unknown. Including the unknown objects the mean deviation is 3. We visually inspected all objects for

which discrepancy between our T-Type and the RC3 T-Type was greater than 1. In most cases, the RC3 T-Type is obviously incorrect. For example, there are three objects which we classify as unknown (13) and RC3 as -2, 2 and 10 but they are in fact highly disturbed and/or merging. Figure 3.10(b) shows our classification compared to the 584 objects which overlap with the Fukugita et. al. 2007 sample. Again the agreement between T-Types is fairly consistent but our classifications are slightly earlier than the Fukugita classification scheme. The mean deviation in classification between PN and Fukugita is < 0.8 bins, given their coarse sampling.

3.4.2 Comparison of RC3 and PN bar classification

For objects later than ESO but with no inclination cut, we find bars, rings and lenses are $26\% \pm < 0.5\%$, $25\% \pm < 0.5\%$ and $5\% \pm < 0.5\%$ of our sample population respectively. These fractions are lower limits which do not include objects for which we were not completely confident with the fine-classification. Inclusion of these objects increases the bar and ring fractions by 5%, and the lens fraction by 3%. The bar fractions are still low compared to previous local studies which quote bar fractions of 60% (de Vaucouleurs 1963) or higher.

As stated previously, our bar classification cannot be compared directly to the RC3 bar classification. Our strong, intermediate and weak bar classes can be considered subdivisions of the RC3 strong bar class. To illustrate this, Figure 3.11 shows a montage of SDSS galaxies which are defined as strongly(B) or weakly barred(X) in RC3. In the top panel we show objects which are defined as barred by PN and strongly barred by RC3. Most of the bars are large in scale and there is no confusion in these cases. The middle panel shows objects classified as strong bars by RC3 but as being unbarred by PN. Even after knowing the RC3 classification, only three galaxies could potentially be classified as barred from the SDSS images. Two of the galaxies which do appear barred ($J004746.43 - 095006.18$ and $J092453.21 + 410336.62$) are very weak and appear to be ansae. In the case of $J004746.43 - 095006.18$ the confusion arises due to inclination effects where the object could either be considered to have an inner ring or a weak bar. We opted for an inner ring. The third missed object, $J113536+545655.10$ was classified as a peculiar object by the author as opposed to barred. The bottom panel in Figure 3.11 shows objects considered weakly barred in RC3 (denoted by X in the short designation on the bottom left of the images). In 4 of the 8 cases we classify the galaxy as barred or possibly barred (bar type > 8). With 3 of the galaxies we cannot identify bars. $J142405.96 + 345331.58$ seems more likely to be an inner lens with an inner ring and possibly a nuclear bar. In $J122254.39 - 024008.86$, the bar is difficult to distinguish from the arms in the SDSS image. In $J115458.71 - 582937.27$, the galaxy could have been considered to host an intermediate bar by PN and illustrates that although classifications have been carried out twice, there may be some intermediate/weak bars that have been missed. In summary, of the 71 objects defined as strongly barred in the

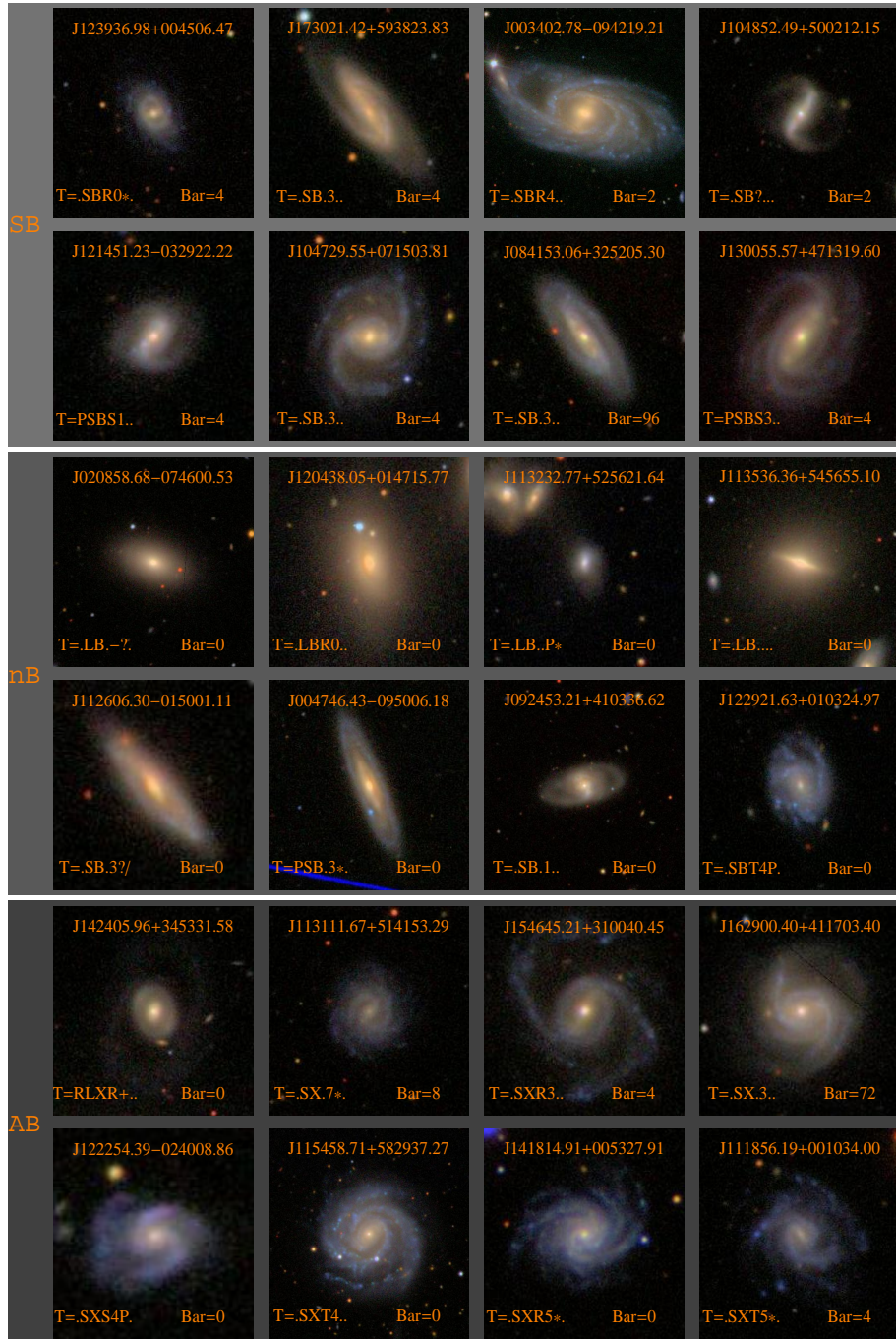


Figure 3.11: A montage of barred RC3 galaxies common with our sample split as follows: **Top Panel:** Strong bars identified by both RC3 and PN. **Middle Panel:** Strong bars identified by RC3 but not by PN and **Bottom Panel:** Weak or AB bars identified by RC3 with PN classification listed. The J2000 object ID is listed at the top. The RC3 classification is listed at the bottom left hand corner and the PN bar flag classification in the right hand corner. 0 corresponds to no bar, 2 to PN strong bar, 4 to PN intermediate, 8 to PN weak bar and any higher number to peanuts+ansae+unsure flags. See Section 3.9 for details. Each stamp is $50 h^{-1}$ kpc on a side.

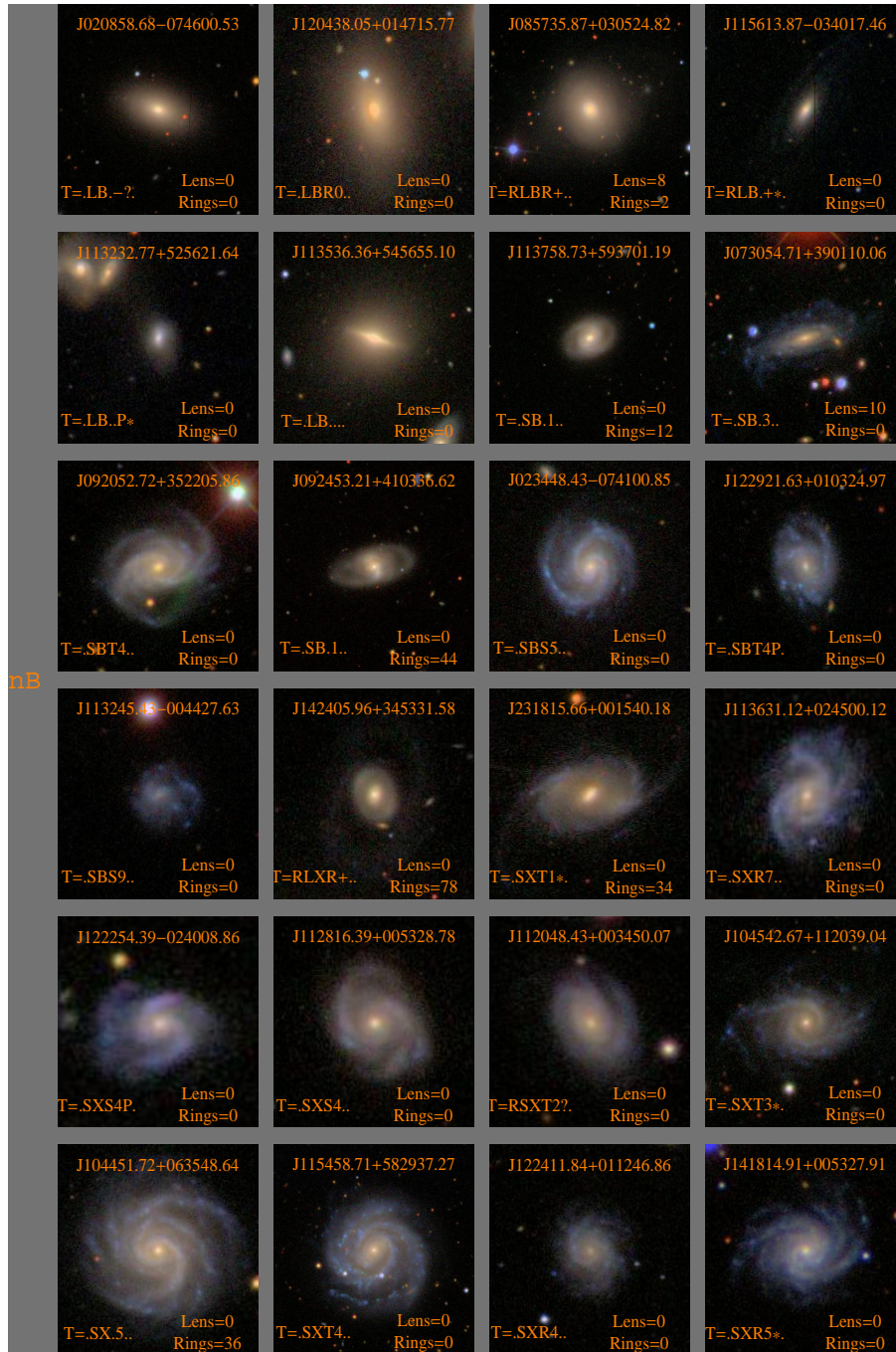


Figure 3.12: A montage of face on ($b/a > 0.5$) galaxies classified as strongly or weakly barred in RC3 but as unbarred in our classification. The J2000 object ID is listed at the top. The RC3 classification is listed at the bottom left hand corner and the PN ring and lens classifications in the right hand corner. 0 corresponds to no ring/lens, 2 to PN inner ring/lens, 4 to outer ring/lens and any higher number to rings or lens with partial, pseudo or unsure flags set. See Section 3.9 for details regarding classification designations. The galaxies are arranged in order of bar strength with the RC3 strong bars first followed by the RC3 weak bars. Each stamp is $50 h^{-1}$ kpc on a side.

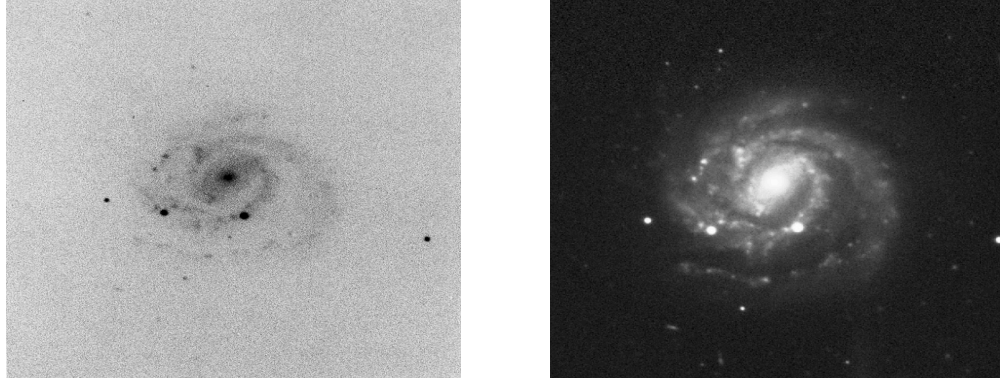


Figure 3.13: Images of NGC 3963 or $J115458.71 - 582937.27$ which is present both in RC3 and in our sample. The left hand image is taken from the Carnegie Atlas of Galaxies while the right hand image is taken from the SDSS image archive.

RC3 sample, we find $\sim 66\% \pm 6\%$ to be barred. Of the 25 objects considered to be weakly barred in the RC3, we find $44\% \pm 10\%$ to be barred. Thus our detection rate of RC3 strong bars is statistically much higher than our detection of RC3 weak bars.

It is apparent from Figure 3.11 that we have missed some bars because of (a) inclination effects, (b) because we may have classified some of the RC3 strong and weak bars as other fine features like lenses or rings, (c) we have missed bars which meet our criterion, (d) our images may be too shallow to detect some bars and (e) our definition of a bar is too conservative. We investigate each effect in turn.

Applying an axial ratio cut of $b/a > 0.5$ to our sample, we find our detection rate increases to $74\% \pm 6\%$ for strongly barred RC3 galaxies and $50\% \pm 11\%$ for weakly barred RC3 galaxies. Figure 3.12 shows the remaining 24 face-on barred RC3 galaxies missed by our classification, arranged in order of RC3 bar strength. The first four galaxies classified by RC3 as strong bars do not appear to show a bar in the SDSS image. The same is true for deeper images of these galaxies taken from NED. There are 5 objects where confusion with an inner ring or lens may cause us to miss a weak bar or ansae. These are $J113758.73+593701.19$, $J073054.71+390110.06$, $J092453.21+410336.62$, $J142405.96+345331.58$, and $J231815.66+001540.18$ which have the 'Rings' or 'Lens' flags set to greater than zero. In three cases, $J113536.36 + 545666.10$, $J113631.12 + 024500.12$ and $J115458.71 - 582937.27$, we have missed possible bars. In the remaining galaxies the weak bars (if present) are better classified as twists in our images. After accounting for incorrect RC3 classifications, our RC3 strong bar detection rate increases to $\sim 80\% \pm 6\%$ while the weak bar fraction detection rate is unchanged.

There are two possible reasons for the lower detection rate of RC3 weak bars; (a) the SDSS exposures are not of sufficient depth or (b) our classifications are too conservative. It must be remembered that bar classifications in RC3 and RSA are done with photographic images

which have greater depth and more information elements while the SDSS exposures are less than a minute on CCD's and have comparatively fewer information elements. This could lead to misclassifications, especially for the weak bars. Figure 3.13 illustrates the effect of longer exposure time with NGC 3963 ($J115458.71 - 582937.27$) classified as an RC3 weak bar which is at a redshift of ~ 0.01 . The detail observed in the SDSS image is comparable to the Palomar 4-minute exposure. Unfortunately no other CAG images of our RC3 weak galaxies were available. However images taken with the 200-inch Palomar telescope are deeper. Exposure time will play a more important effect in galaxies further away. In addition physical resolution will be important for bar recovery and will be discussed in the next section.

Lastly, we need to verify our results and get an understanding of how conservative our classifications are compared to other morphologists. We asked Debra Elmegreen (DB) to independently classify the structures seen in Figure 3.12. In summary, only 3 of the 13 RC3 strongly barred galaxies are reclassified by DB as strongly barred, 5 objects are classified as unbarred and the remaining 5 objects are classified as weakly barred. Specifically, the first 4 objects are classified as 'not-barred'. DB agrees with the RC3 classification of the second row but argues the third galaxy shows ansae but not necessarily a bar while the last galaxy is more uncertain given the 'bar' lies along the major axis and would more likely call it an SAB galaxy. In the third row, the first is reclassified to unbarred while the remaining three are classified as SAB or weak bars. With respect to the RC3 identified weak bars, DB agrees with most of the classifications. Specifically, her classification of the fourth row is the same. In the remaining two rows, the objects are reclassified as weakly barred but with larger uncertainties. $J115458.71 - 582937.27$ is reclassified as a strong bar by DB. Incorporating these reclassifications, our strong bar detection rate for face-on ($b/a > 0.5$) galaxies common with RC3 rises to $\sim 93\% \pm 4\%$ while the weak bar detection rate decreases to $41\% \pm 9\%$. Thus our bar classification can be considered to be predominantly equivalent to RC3 strong bars.

3.4.3 Comparison of RC3 and PN ring classifications

As stated earlier the total, inclination independent, inner plus outer ring fraction for disk galaxies (including lenticulars) in our sample is $25\% \pm 0.5\%$. From Table III in Buta & Combes (1996), the total face-on ring fraction based on 911 disk galaxies in RC3 is $\sim 54\%$, with $\sim 20\%$ for complete rings (r) and $\sim 35\%$ for the partial/pseudo (rs) ring variety. Based on 5247 galaxies in our sample with a similar inclination cut ($b/a > 0.6$) we find a total face-on ring fraction of $30\% \pm 0.5\%$ with $23\% \pm 1\%$ for complete rings (r) and $7\% \pm 1\%$ for partial rings. Thus our total ring fraction estimate is significantly lower than Buta & Combes (1996). Partial rings seem to be significantly underestimated in our classification. It must be remembered that RC3 combines rings and lens classifications. To investigate these differences, we compare our ring

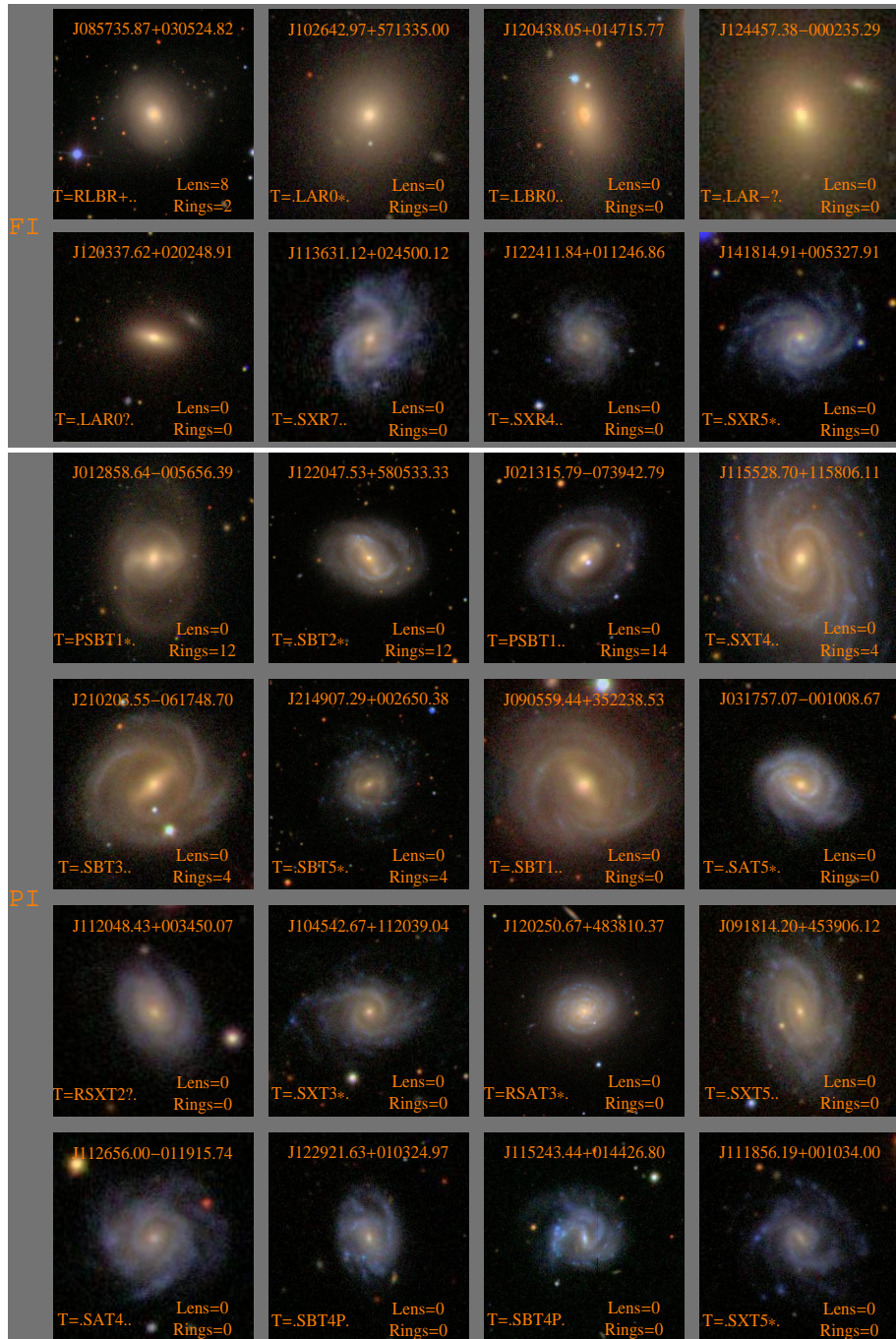


Figure 3.14: A montage of face on ($b/a > 0.6$) galaxies with RC3 classifications of (a) full inner rings and (b) partial inner rings. The J2000 object ID is listed at the top. The RC3 classification is listed at the bottom left hand corner and the PN ring and lens classifications in the right hand corner. See Section 3.9 for details regarding classification designations. The galaxies are arranged in order of ring type. Each stamp is $50 h^{-1}$ kpc on a side.

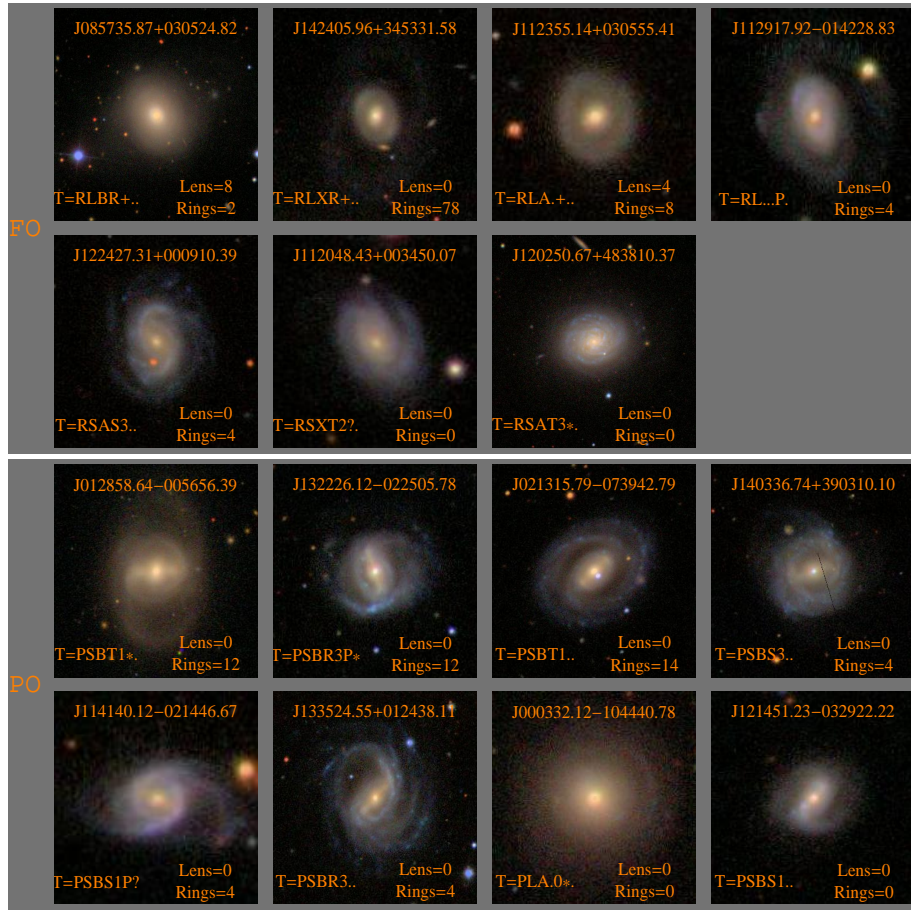


Figure 3.15: A montage of face on ($b/a > 0.6$) galaxies classified as having (a) full outer rings and (b) partial outer rings in RC3. The J2000 object ID is listed at the top. The RC3 classification is listed at the bottom left hand corner and the PN ring and lens classifications in the right hand corner. See Section 3.9 for details regarding classification designations. The galaxies are arranged in order of T-Type. Each stamp is $50 h^{-1}$ kpc on a side.

classifications with RC3 classifications for the 44 face-on ringed galaxies common to both samples. The recovery rate for RC3 full inner rings, partial inner rings, full outer rings and partial outer rings are $62\% \pm 10\%$, $38\% \pm 12\%$, $29\% \pm 17\%$ and $38\% \pm 17\%$ respectively. We miss a large fraction of partial inner-rings and outer rings.

Of the 21 galaxies with full RC3 inner rings, 8 are classified as not having an inner ring in our classification. These galaxies are shown in the top panel of Figure 3.14. In the first row we see no inner rings, though the first galaxy may possess a nuclear ring. In the second row, we again feel no galaxy can be classified as having a full inner ring based on the SDSS images though $J122411.84 + 011246.86$ may have a partial inner ring. It is possible that the reason for disagreement may be because we cannot identify nuclear rings in the SDSS images. Thus our recovery rate of full inner rings is predominantly influenced by misclassifications in RC3 and/or insufficient depth of the SDSS image. Excluding the misclassifications we find an inner ring fraction recovery rate of $81\%(13/16)$.

In the bottom panel of Figure 3.14 we show all the galaxies with RC3 partial inner ring classifications. In the first 6 of 16 galaxies we classify the objects as having inner rings, not partial inner rings. Thus in some cases our classification is more lenient than those listed in RC3. In the remaining 10 galaxies, at least 2 of the galaxies should have been classified as having a partial ring, specifically the last two galaxies in the second row, $J090559.44 + 352238.53$ and $J031757.07 - 001008.67$. In the third row the galaxies may have partial inner rings but they are very doubtful and hard to distinguish based on the SDSS g-band images. In the final row, the first two galaxies may possess a partial ring but the last two galaxies do not appear to host inner rings. Accounting for the two galaxies without partial rings our recovery rate increases to $43\%(6/14)$ and our total inner ring recovery rate increases to $63\%(19/30)$.

Figure 3.15 shows a montage of galaxies with outer rings. In the top panel we show the 7 galaxies classified as having a full outer ring by RC3. Our classifications agree for only 2 galaxies, $J142405.96+345331.58$ and $J112355.14+030555.41$. In the first galaxy we opted to identify the structure as a lens. In two galaxies, $J112917.92-014228.83$ and $J122427.31+000910.39$ we identified the inner rings but not outer rings. We classified the structure seen in $J112917.92-014228.83$ as an inner ring with a tail. The object could also be a collisional ring. $J122427.31+000910.39$ could be considered to have a partial outer ring. RC3 misses the inner ring in this case. In the last two galaxies, partial outer rings may exist though it is highly unsure. Accounting for lenses and misclassifications our full outer ring detection rate increases to $57\%(4/7)$. In the bottom panel, we show the 8 galaxies classified as having psuedo/partial outer rings. We identify the first three objects as outer rings and the next 2 as inner rings while RC3 identifies them as outer rings. The remaining three objects may have psuedo-rings though it seems highly doubtful in the last two cases. The outer structure in $J000332.12-104440.78$ in particular

may be better classified as a shell. Our partial outer ring detection rate increases to 60% (3/5) and our total outer ring detection rate increases to 58% (7/12).

Thus our total ring detection rate is 62% (26/42). The predominant cause for misidentification appears to be a difference in opinion as to what the fine feature is, an inner versus outer ring or outer ring versus outer lens etc. There are only 8 cases out of the 44 galaxies considered here where an objects with an RC3 fine class does not have a fine classification in our scheme. In 4 of those cases (J102642.97+571335.00, J120438.05+014715.77, J124457.38-000235.29 and J120337.62+020248.91 which are supposed to host RC3 inner rings) there is no bar or ring seen in deeper images available on NED in B band. Thus our overall recovery rate of fine structures is $\sim 91\%$.

3.4.4 Caveat: Selection effects due to redshift

Figure 3.16 illustrates the variation of bar, ring and lens fractions for each Hubble type as a function of redshift. In all cases we see the Hubble type fraction decreases with redshift as does the fine-fraction. As we noted in Chapter 2, the galaxies at $z > 0.05$ are predominantly high mass systems. Thus the effect of reduced physical resolution will cause us to underestimate the bar/ring/lens fraction in high mass, predominantly early type systems. We will investigate fine fractions in Chapter 6 though it is interesting to note that S0 galaxies appear to have approximately the same frequency of barred, ringed and lensed objects at all redshifts. Sa galaxies appear to have more ringed galaxies than bars while Sb galaxies have more barred objects. Very late galaxies are restricted to low redshifts as expected.

3.5 Results

Figure 3.17 shows the histogram of (a) T-Types and (b) sersic indices (taken from Blanton et al. (2003)) for our entire sample (in grey) as well as for the face-on sample defined with an axis ratio cut of $b/a > 0.6$ (in blue). The T-Type distribution clearly shows that elliptical and classical spirals are well represented but objects later than Scd are not in comparison. This is mirrored in the distribution of the sersic index where we find very few objects with $n < 2$. Elliptical and S0 galaxies account for 34% of our sample, classical spirals 61% and very late types, including peculiars/mergers approximately 5%. Our face-on sample has a similar distribution.

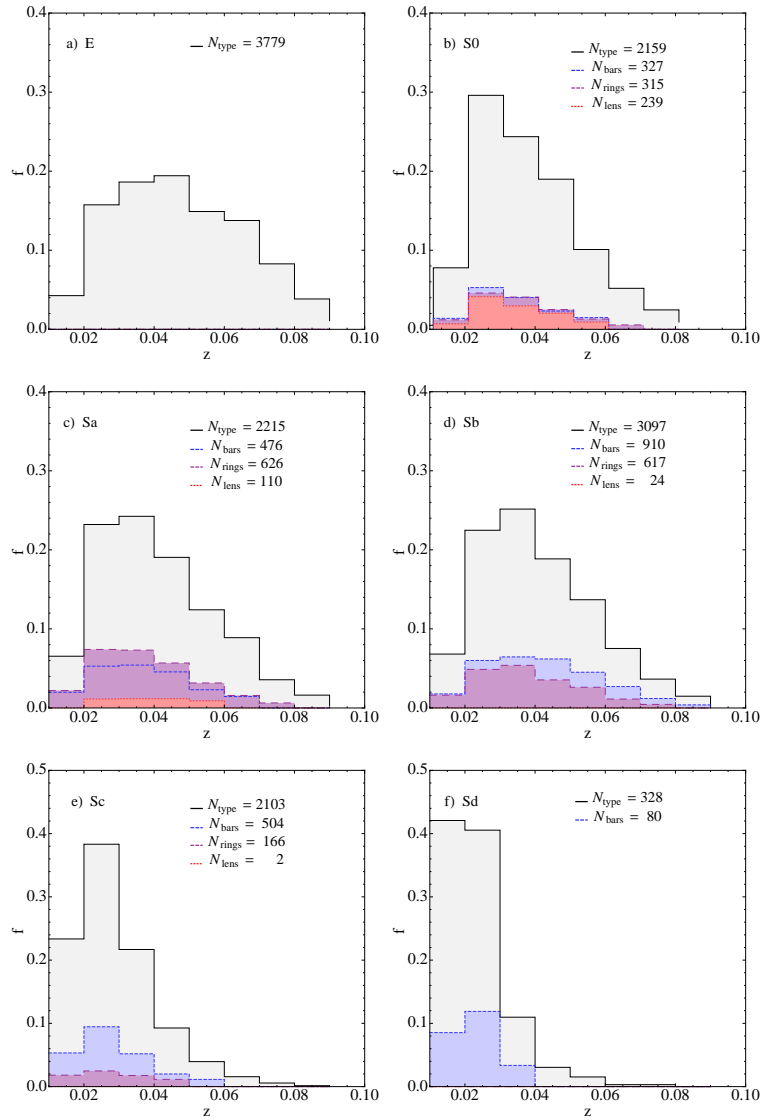


Figure 3.16: Variation of Hubble type fraction with redshift. Each panel also shows the variation of bar (blue), ring (purple) and lens fraction as a function of redshift.

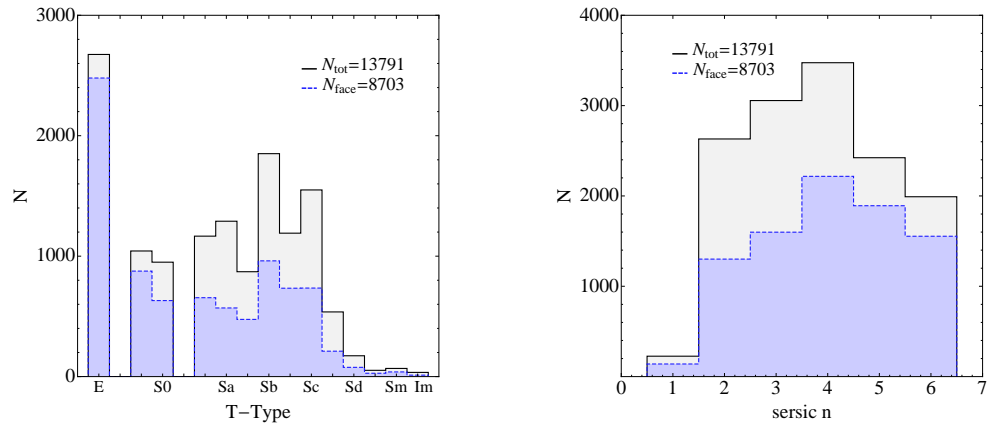


Figure 3.17: Histograms of (a) T-Types, and (b) Sersic indices. The T-Type distribution clearly shows that objects later than Scd are not well represented. This is mirrored in the sersic n distribution which has very few objects at $n=1$. The gray histogram shows the distribution for the complete sample while the blue histogram shows the distribution for face-on objects defined as $b/a > 0.6$.

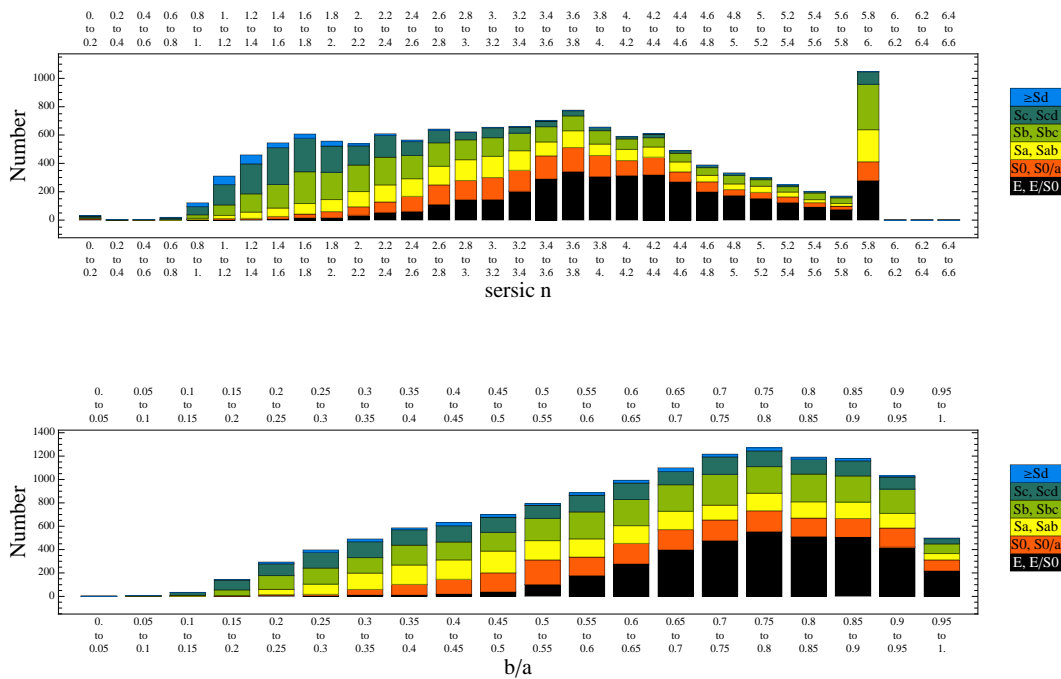


Figure 3.18: Histogram of various Hubble Types as a function of (a) sersic index and (b) axial ratios. The sub-categories of galaxy types have been grouped into the following broad classes: E and E/S0 galaxies (black bars), S0 and S0/a galaxies (orange bars), Sa and Sab galaxies (yellow bars), Sb and Sbc galaxies (light green bars), Sc and Scd galaxies (dark green bars) and galaxies with T-Types later than Sd (blue bars). Sersic index, $n=6$ is a hard limit. See text for details.

3.5.1 Sersic Index vs T-Type relation

Figure 3.18(a) shows the histogram distribution of various Hubble types as a function of sersic index. For the sake of clarity, we have grouped sub-categories of galaxy types into the following broad classes: E and E/S0 galaxies (shown as black bars), S0 and S0/a galaxies (shown as orange bars), Sa and Sab galaxies (shown as yellow bars), Sb and Sbc galaxies (shown as light green bars), Sc and Scd galaxies (shown as dark green bars) and galaxies with T-Types later than Sd (shown as blue bars). We will adopt these bins (and color scheme) throughout the remainder of this thesis unless otherwise stated, and in general will not attempt to subdivide galaxy populations into classes finer than those shown in this figure. In general we find:

(i) *Elliptical and E/S0 galaxies have the highest sersic indices (as expected) and the sersic index of later Hubble types decline smoothly with T-Type.*

(ii) *No single sersic cut isolates a complete sample of E+S0 galaxies which is free from contamination by spiral galaxies.*⁴ As expected, the degree (and nature) of contamination depends on the specific cut chosen.

(iii) *A surprisingly broad range of spiral galaxies exhibit sersic indices which overlap with those of elliptical galaxies.* While most are highly concentrated early spirals (S0,Sa), a significant number of intermediate-late type spirals (Sb,Sbc) have sersic index comparable with those of low- n ellipticals.

A commonly used sersic cut of 2.5 leads to a sample with 80% of the E and E/S0 galaxies but with 43 % contamination by later spirals. Figure 3.18(b) shows the distribution of Hubble types with axis ratio b/a . E+E/S0 galaxies concentrate at higher axis ratios while all other T-Types distribute fairly evenly. Choosing a strict axis ratio cut of $b/a > 0.6$ and $n > 2.5$ yields a sample with 93% of the E+E/S0 galaxies and lower (33 %) contamination by spirals.

3.5.2 Distribution of T-Types with physical properties

Figure 3.19 shows the histogram distribution of Hubble types with (a) mass and (b) petrosian half light radius. We find E+E/S0 have the highest masses as expected, though again they span a wide range. At the highest mass end there are no objects later than S0's. Classical spirals peak in the middle of the distribution, $\text{Log}M \sim 10.7$ with later types dominating the low mass end. The histogram distribution for size shows a very interesting trend. E+E/S0 have small petrosian half light radius and Hubble types Sa onwards have larger sizes on average. However S0's peak earlier than ellipticals. This is most probably because we do not distinguish

⁴In other words, a trade-off always needs to be made between picking a very conservative cut which isolates an *incomplete* sample of early-type galaxies, and a less conservative cut which selects all early-type systems but which has significant contamination by spirals.

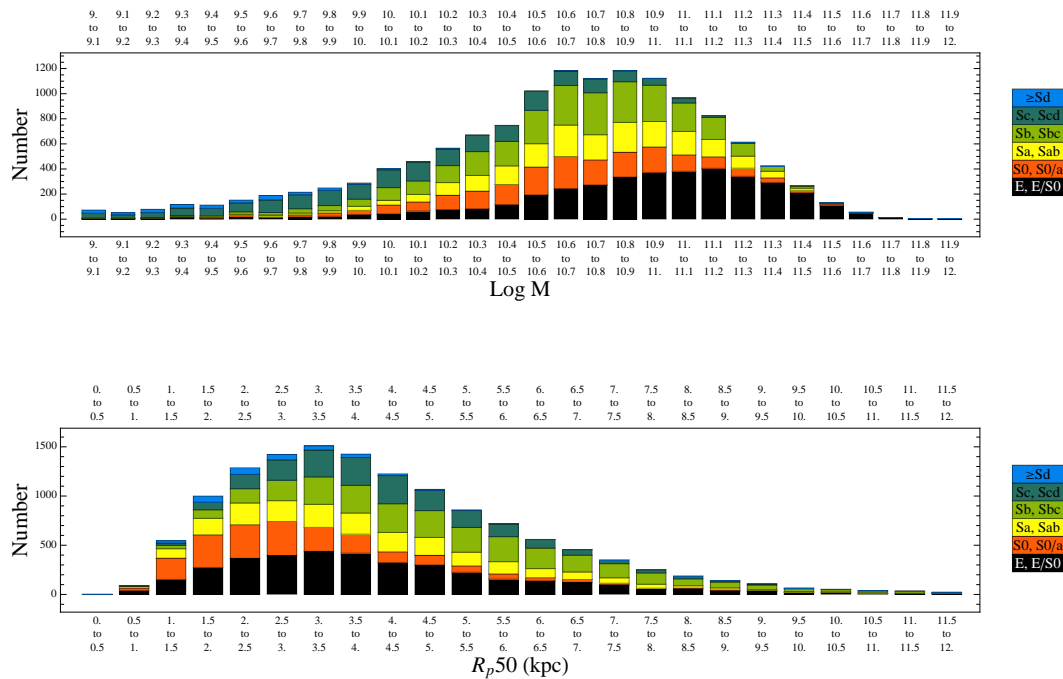


Figure 3.19: Histogram of various Hubble Types as a function of (a) Mass in log units and (b) Petrosian half light radius R_p50 in kpc. The color-coding is the same as Figure 3.18.

between massive cD galaxies or dwarf ellipticals. Hence the range in sizes spanned by E/ES0 is larger than S0's. We will investigate this further in Chapter 4.

Figure 3.20 shows the histogram distribution of Hubble types with (a) g-band absolute magnitude and (b) g-r color. As expected we see elliptical galaxies dominate the bright end of the magnitude distribution, classical spirals dominate the mid-range and late-type spirals dominate the low luminosity end of the distribution. With respect to color, E+E/S0 are the reddest galaxies as expected but have a large tail in their distribution. There is significant overlap with early classical spirals. Late type spirals dominate the blue end of the spectrum. Color cuts are also frequently used to identify ellipticals. Using a g-r color-cut of 0.7, we find the contamination by disk galaxies (Sa and later) is 36%. Using a stringent axis ratio cut of $b/a > 0.6$ reduces the contamination to 19%.

We will conduct a thorough investigation of the relationship between physical properties and T-Types in Chapter 4.

3.5.3 Local Statistics

A summary of the statistics of our sample is given in Table 3.2. We postpone the discussion on abundances of fine classes (bars, rings, lenses) and interacting objects to Chapter 5 along with

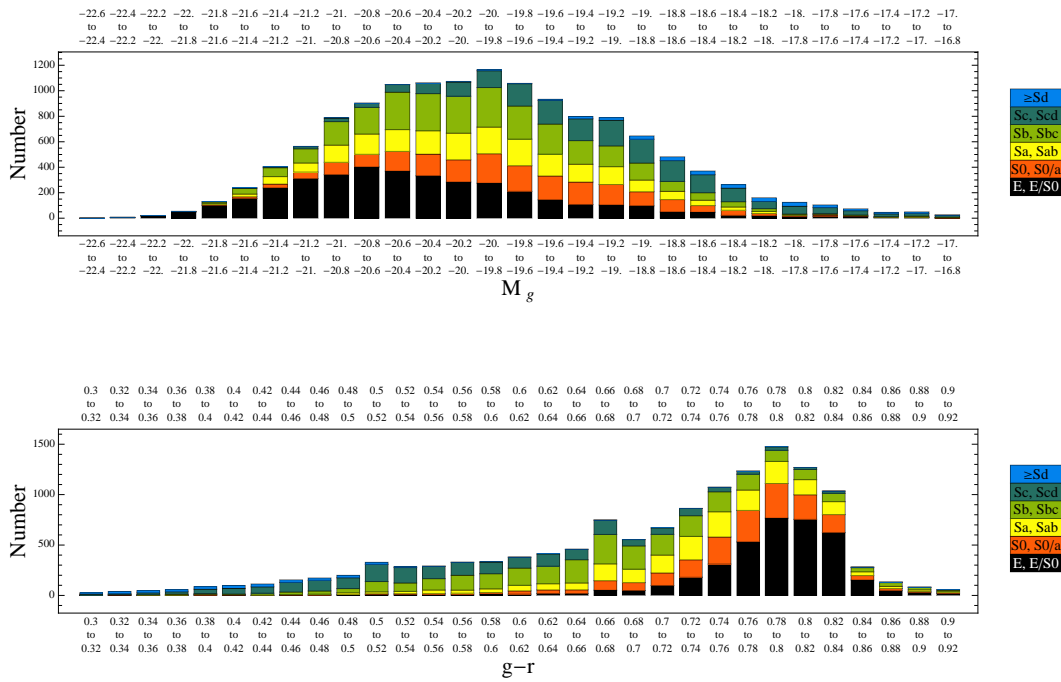


Figure 3.20: Histogram of various Hubble Types as a function of (a) g-band absolute magnitude and (b) g-r color. The color-coding is the same as Figure 3.18.

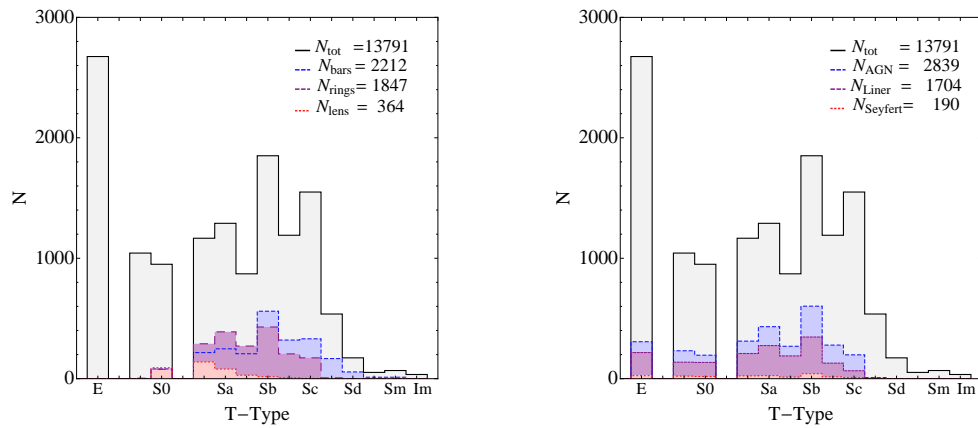


Figure 3.21: Histograms of T-Types for (a) Bars (blue, short dash), Rings (purple, long dash), Lenses (red, dotted), and (b) AGN distribution in blue (short dash), Liner subtype in purple (long dash) and Seyferts in red (dotted). The grey distribution is for the entire sample.

the correlations seen with AGN activity but provide a brief overview here. Figure 3.21 shows the distribution of (a) galaxies with definite bars, rings and lenses and, (b) galaxies defined

Table 3.2. Summary of Distributions

Class	No.	Bars	Rings	Lenses	AGNs	Liners	Seyferts	Dist.
E	2723	0	0	0	307 (11%)	217 (8%)	25 (1%)	90
ES0	1056	0	6	2	232 (22%)	137 (13%)	21 (2%)	164
S0	966	117 (12%)	92 (10%)	127 (13%)	195 (20%)	135 (14%)	18 (2%)	71
S0a	1193	267 (22%)	362 (30%)	190 (16%)	312 (26%)	209 (17%)	23 (2%)	81
Sa	1322	287 (22%)	493 (37%)	107 (8%)	432 (33%)	275 (21%)	25 (2%)	91
Sab	893	243 (27%)	376 (42%)	45 (5%)	269 (30%)	189 (21%)	13 (1%)	78
Sb	1890	649 (34%)	599 (32%)	27 (14%)	602 (32%)	346 (18%)	41 (22%)	93
Sbc	1207	368 (30%)	300 (25%)	19 (2%)	279 (23%)	129 (11%)	15 (1%)	54
Sc	1562	379 (24%)	263 (17%)	13 (1%)	198 (13%)	66 (4%)	9	49
Scd	541	188 (35%)	17 (3%)	0	10 (2%)	0	0	25
Sd	173	72 (42%)	2	0	1	0	0	16
Sdm	52	13 (25%)	1	0	0	0	0	7
Sm	68	18 (26%)	1	0	0	0	0	10
Im	35	0	0	0	1	0	0	6
Un	353	11 (3%)	8 (2%)	1	57 (16%)	29 (8%)	1	134
Total	14034	2612 (26%)	2512 (25%)	531 (5%)	2895 (21%)	1732 (12%)	191 (1%)	969(7%)

as AGNs, seyferts and liners, as in Kauffmann et al. (2003a)⁵. For objects later than ES0 but with no inclination cut, we find bars, rings and lenses are $26\% \pm < 0.5\%$, $25\% \pm < 0.5\%$ and $5\% \pm < 0.5\%$ of our sample population respectively. We find rings and lenses are located nearly entirely in classical spirals (classes earlier than Scd). Bars are distributed through all disk T-Types as expected. Figure 3.21(b) shows the AGNs in our sample are dominated by Liners (12%) with far fewer Seyferts(1.4%). The total AGN fraction is approximately 20% of our sample.

3.5.4 Interacting galaxies

Table 3.3 provides a summary of the different types of disturbed objects in our sample. Galaxies under the ‘general’ column have not been placed into any of the previous categories. Objects listed as pairs are objects with a nearby interacting companion and include both the early and late stages of interaction. There is overlap between some of the columns (shells and tails with pairs). In total, there are 969 (7%) interacting objects in our sample. $23\% \pm 1.5\%$ of the interacting objects host an AGN compared to $20\% \pm 0.5\%$ of non-disturbed galaxies. Split by type, we find objects undergoing an interaction with medium or long tails have a higher AGN fraction ($28\% \pm 5\%$) than other disturbed objects. Galaxies with short tails have a far lower

⁵Seyfert galaxies are defined to have $[OIII]/H\beta > 3$ and $[NII]/H\alpha > 0.6$ while Liners have $[OIII]/H\beta < 3$ and $[NII]/H\alpha > 0.6$

Table 3.3. Summary of Disturbed Objects

Class	Shells	Short Tails	Inter Tails	Long Tails	Pairs	General
E	16	3	0	2	24	44
ES0	30	22	9	7	38	77
S0	7	9	10	7	25	28
S0a	10	10	8	7	13	39
Sa	8	12	6	6	10	50
Sab	1	6	7	8	9	50
Sb	0	4	12	10	13	59
Sbc	1	3	6	7	19	23
Sc	1	4	4	7	17	22
Scd	0	0	0	4	5	15
Sd	1	0	3	2	1	10
Sdm	0	1	1	2	0	3
Sm	0	2	1	3	2	3
Im	1	0	1	0	1	3
Un	3	20	32	33	79	28
Total	79	96	100	105	256	454

AGN fraction ($17\% \pm 4\%$). The results seem to imply that major interactions which yield larger tails are more likely to trigger an AGN than a minor interaction which leads to a short tail. Objects in pairs (which includes both early and late stages of interaction) show an AGN fraction of 23%. Considering only those close pairs which are at an early stage of interaction (171) we find a reduced AGN fraction of $19\% \pm 3\%$. Objects with shells represent the end stage of the merger process and have an AGN fraction of ($17\% \pm 4\%$). Thus our results imply that AGN fractions increase when close pairs are tidally disrupted.

3.6 Automated Classifications

In the previous sections we described our visual classification scheme and some broad results. Our goal is to use this comprehensive local sample with highly detailed morphological classifications to understand the relation between quantitative morphology and T-Types as well as the importance of fine features in quantitative classification.

Quantitative morphological parameters have been calculated for the entire sample using the publicly available code MORPHEUS created by Roberto Abraham with significant contributions from the author, (Abraham et al. 2007). In this section, we describe the parameters used to define a galaxy quantitatively, the effectiveness of these quantities at segregating T-Types and the systematics and biases which are important for morphological classification and its

extensions to higher redshifts.

3.6.1 Description of Quantitative Parameters

Concentration

The central concentration of a galaxy is strongly correlated with bulge-to-disk ratio, which is one of the major indicators of a galaxy's position on the Hubble sequence⁶. (Other important parameters are the presence or absence of a bar, and the pitch angle, length, and degree of resolution of spiral structure). Central concentration is thus a parameter correlated with, but independent from, a galaxy's morphological type. However, because central concentration is so easy to measure, and because bulge-to-disk ratio is so fundamental to our understanding of galaxies, concentration is often used as a simple proxy for morphological type. It is therefore important to consider the effectiveness of central concentration in selecting Hubble Types. The central concentration of a galaxy can be measured in different ways. The two most commonly used definitions are:

(1) The ratio of the radii enclosing 90% of the flux of the galaxy (R90) to the radii enclosing 50% of the flux of the galaxy (R50). In some cases R80/R20 is taken as a more robust measure of concentration (Bershady et al. 2000). R90/R50 is the measure used by the SDSS collaboration, though it should be noted that their measure is based on circular apertures which leads to some systematic effects as described in Blanton et al. (2003).

(2) As defined in Abraham et al. (1994), it is the ratio of flux within an inner and outer elliptical aperture determined from the sky-subtracted, intensity-weighted, second-order moment of the image. The major and minor axes of the outer aperture are normalized so that the total area within the ellipse is the area of the galaxy. The inner aperture is defined by scaling these axes down by a linear factor of 3.

In Figure 3.22 we present two histograms showing the number of galaxies grouped by Hubble type and binned by two measures of central concentration. In the top panel we use the SDSS definition of the ratio of the radii enclosing 90% and 50% of the flux of a galaxy and in the bottom we use the measure defined by Abraham et al. (1994) which is just the ratio of fluxes within two fixed elliptical apertures. Unless stated otherwise, we use the later definition of central concentration for the remainder of the paper. The results are similar when using R90/R50. The overall properties of the galaxies as a function of Hubble type are described

⁶Only in Morgan's Yerkes system (Morgan 1979) does central concentration actually *define* morphological type.

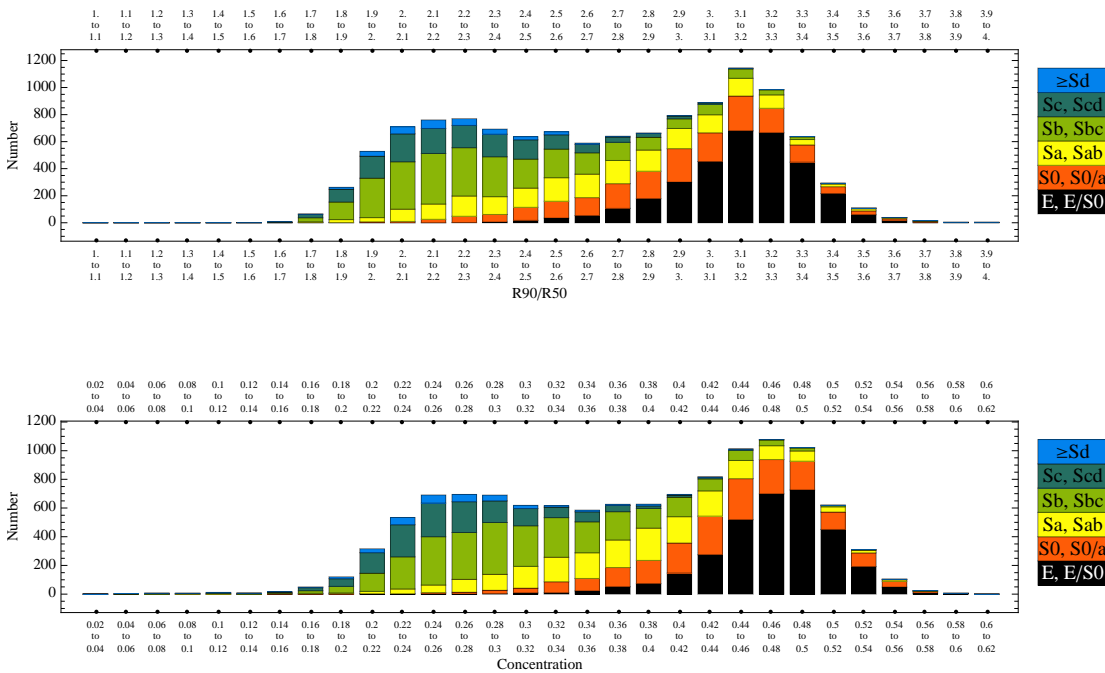


Figure 3.22: Histogram of various Hubble Types as a function of central concentration (a) as defined by Abraham 1994 (top) and (b) $R90/R50$ as used by SDSS collaboration (bottom). The sub-categories of galaxy types have been grouped into the following broad classes: E and E/S0 galaxies (black bars), S0 and S0/a galaxies (orange bars), Sa and Sab galaxies (yellow bars), Sb and Sbc galaxies (light green bars), Sc and Scd galaxies (dark green bars) and galaxies with T-Types later than Sd (blue bars.) See text for details.

in Chapter 4 but for present purposes, it suffices to simply note a few points which can be inferred from Figure 3.22:

- (i) Elliptical and E/S0 galaxies are the most highly centrally concentrated systems (as expected) and the concentration of later Hubble types decline smoothly with T-Type.
- (ii) No single concentration cut isolates a complete sample of E+E/S0 galaxies which is free from contamination by spiral galaxies. As expected, the degree (and nature) of contamination depends on the specific concentration cut chosen.
- (iii) A surprisingly broad range of spiral galaxies exhibit central concentrations which overlap with those of elliptical galaxies. While most are highly concentrated early spirals (S0,Sa), a significant number of intermediate-late type spirals (Sb,Sbc) have central concentrations comparable with those of low-concentration ellipticals. We will have more to say about the nature of these galaxies in this overlapping region in Chapter 5.

Shen et al. (2003) use a $R90/R50$ concentration cut of 2.86 as defined by Nakamura et al. (2003) to distinguish between early type and late type galaxies. As can be seen from Figure 1(bottom), this selects a large range of E, E/S0 and S0 galaxies (85%) but is also significantly

contaminated (22%) by Sa,Sab,Sb and Sbc galaxies. Choosing a concentration cut of $C > 0.44$ selects 88% of the E, E/S0 and S0 galaxies with 25% contamination by later type spirals. Restricting the sample to face on objects $b/a > 0.6$ reduces the contamination to 15%.

Asymmetry

The rotational asymmetry parameter A as defined by Abraham et al. (1996b); Brinchmann et al. (1998) is half the ratio of the absolute value of the total light in the self subtracted image to the total light in the original image (after sky subtraction) or:

$$\mathcal{A} = \frac{\sum_{ij} |I_{ij} - I_{ij}^R|}{2 \sum I_{ij}} - k_A \quad (3.1)$$

where I_{ij} is the intensity in pixel (i, j) , and I_{ij}^R is the corresponding intensity after image rotation by 180° about the centroid of the segmented galaxy image. The k_A term in equation (1) is a small correction accounting for signal introduced into A by noise in the sky background ; k_A is determined by measuring the asymmetry within a rotated and self-subtracted region of sky equal in area to that of the galaxy being analyzed. We have incorporated the suggestion of Conselice et al. (2000) to determine the position of minimum asymmetry in our galaxies.

Figure 3.23 shows the distribution of asymmetry keyed to Hubble type. We find elliptical/lenticular galaxies have the lowest asymmetries but they span a wide range in values such that there is no cut where there will not be significant contamination by disk galaxies. Using asymmetry alone to distinguish between subclasses is not possible. For example, choosing a cut of $\text{Log}A < -1$ yields 93% of the E, E/S0 and S0 galaxies but with 54% contamination by later spirals.

Gini Coefficient

The Gini coefficient (Gini 1912) is a term for measuring the distribution of wealth amongst a population and is commonly used in economics. We introduced this parameter to astronomy in Abraham et al. (2003) as an alternative definition of concentration, applicable to galaxies of arbitrary shape, where the center of the galaxy need not be defined. The reader is referred to Abraham et al. (2003) for complete details. We provide a brief overview here.

The Lorenz curve (Lorenz 1905) is commonly used in economics to describe the inequality in a population's distribution of wealth. In this context the curve is constructed by plotting the cumulative proportion of income as a function of population rank. In a population where all individuals have exactly the same income (where, for example, 20% of the population has 20% of a country's total wealth), the Lorenz curve is a straight diagonal line with a slope of

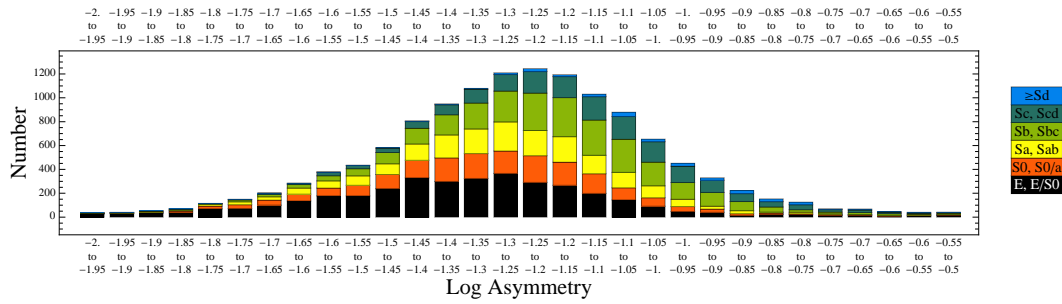


Figure 3.23: Histogram of various Hubble Types as a function of log of Asymmetry The sub-categories of galaxy types have been grouped into the following broad classes: E and E/S0 galaxies (black bars), S0 and S0/a galaxies (orange bars), Sa and Sab galaxies (yellow bars), Sb and Sbc galaxies (light green bars), Sc and Scd galaxies (dark green bars) and galaxies with T-Types later than Sd (blue bars.) See text for details.

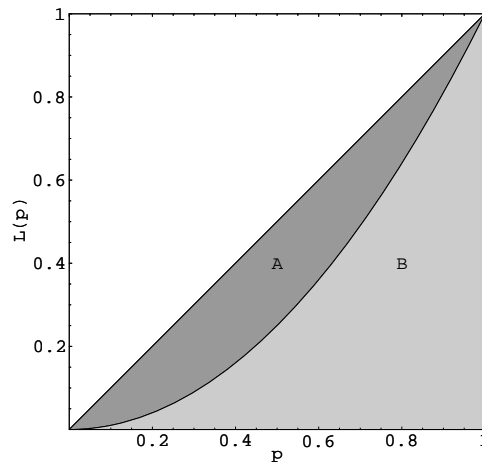


Figure 3.24: Geometric interpretation of the Gini coefficient based on the Lorenz curve. The x-axis corresponds to the quantile distribution and the y-axis to the cumulative distribution. The Lorenz curve for a perfectly equal distribution corresponds to the diagonal line of equality. In the figure, a schematic Lorenz curve divides the area beneath the line of equality into two areas, A and B. The greater the deviation of a measured Lorenz curve from the line of equality, the greater the inequality. The Gini coefficient corresponds to the ratio of area A to the total area under the diagonal $A + B$.

unity, called the line of equality. If there is any inequality in income, then the Lorenz curve falls below the line of equality. For example, in the extreme case where a tiny proportion of the population has nearly all the income, the Lorenz curve is flat and near zero for most of its length until rising precipitously near its end (see Figure 3.24). The total amount of inequality is conveniently parameterized using a summary statistic of the Lorenz curve, the Gini coeffi-

cient G . The geometric meaning of G is illustrated in Figure 3.24. The Gini coefficient is simply the ratio between area A (the area enclosed between the line of equality and the Lorenz curve) and the total triangular area under the line of equality ($A + B$). The Gini coefficient ranges from a minimum value of zero, when all individuals are equal, to a maximum of one in a population where all the wealth is concentrated in a single individual. A more formal statistical description of the Lorenz curve and Gini coefficient complements the intuitive description given above, by highlighting the close connection between the Gini coefficient and the absolute mean difference in a population and showing how the statistic can be computed with trivial computational cost. Let X be a positive random variable with a cumulative distribution function $F(x)$, and let X_i denote one of n random deviates drawn from X . The Lorenz curve is then given by:

$$\mathcal{L}(p) = \frac{1}{\bar{X}} \int_0^p F^{-1}(u) du \quad (3.2)$$

The Gini coefficient is defined as the mean of the absolute difference between all combinations of X_i :

$$\mathcal{G} = \frac{1}{2\bar{X}n(n-1)} \sum_{i=1}^n \sum_{j=1}^n |X_i - X_j|, \quad (3.3)$$

where \bar{X} is the mean value over all X_i . Numerical tests have shown that the estimated error on a measurement of G can be reliably obtained using a statistical bootstrap (Efron and Tibshirani 1993; Dixon et al. 1987), so it is desirable to use a faster algorithm for calculating G than is provided by this formula. A very efficient way to calculate G (Glasser 1962) is to first sort the X_i into increasing order and then do a simple summation:

$$\mathcal{G} = \frac{1}{\bar{X}n(n-1)} \sum_{i=1}^n (2i - n - 1) X_i \quad (n > 2) \quad (3.4)$$

The computational cost of calculating G is therefore dominated by the computational cost of a single one-dimensional sort (which rises as $n \log n$ for an efficient sorting algorithm). In the context of galaxy morphology, G is calculated by applying equation (3) to a list of pixel values sorted by intensity. Can a connection then be made between measures of G as defined above and more conventional visual and quantitative morphological parameters? Figure 3.25 shows the distribution of Gini keyed to Hubble type. We find Gini does a similar job as concentration at segregating the various classes of objects. Elliptical galaxies again dominate at high G 's whereas very late types dominate at low G , though all types show a significant tail in their distributions. Choosing a cut of $G \geq 0.55$ leads to selecting 95% of the elliptical galaxies in our sample with 40% contamination by spirals. With a strict axis ratio cut of $b/a > 0.6$ leads

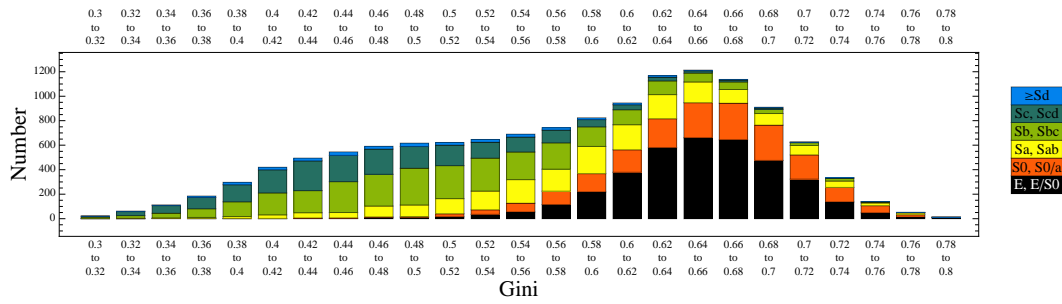


Figure 3.25: Histogram of various Hubble Types as a function of Gini. The sub-categories of galaxy types in Nair & Abraham (2008) have been grouped into the following broad classes: E and E/S0 galaxies (black bars), S0 and S0/a galaxies (orange bars), Sa and Sab galaxies (yellow bars), Sb and Sbc galaxies (light green bars), Sc and Scd galaxies (dark green bars) and galaxies with T-Types later than Sd (blue bars.) See text for details.

to a reduction in contamination to 35%.

(a) g-Band SDSS EDR Sample

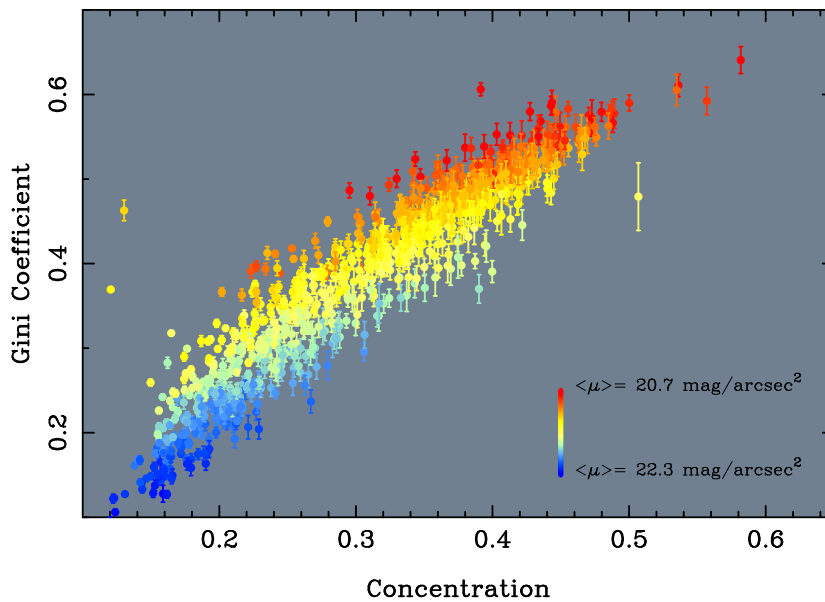


Figure 3.26: Gini coefficient vs. central concentration for the g-band sample. Note that the galaxies span a broad range of morphologies, from pure disk systems at low C to highly centrally concentrated pure R1/4-law elliptical galaxies at high C. Error bars on G ($\pm 1\sigma$) are determined from 100 bootstrap replications (Efron & Tibshirani 1993) of the pixel distribution for each galaxy. Bootstrap replication cannot be used to estimate the errors on C, and no error bars on C are shown. However, on the basis of the Monte Carlo simulations described in Abraham et al. (1994), we expect error bars on C to be approximately similar in size to the error bars on G.

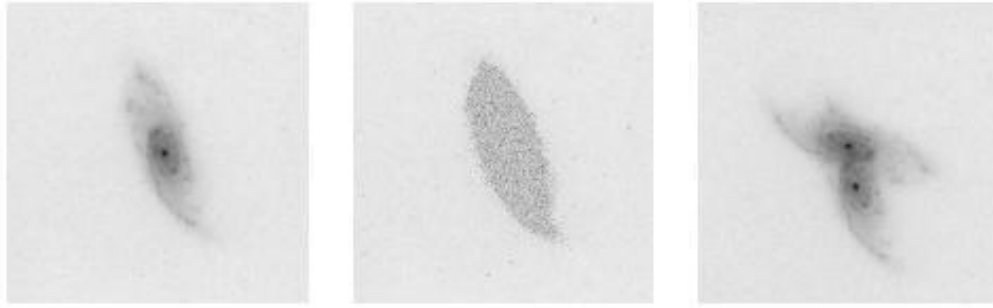


Figure 3.27: Three systems with essentially the same Gini coefficient but very different central concentrations. Left: R-band image of NGC 2715 from the digital catalog of Frei et al. (1996). Middle: Image obtained by jackknife replication of the original NGC 2715 image. Since each pixel in the galaxy’s image is simply a permutation of the original pixel set, G remains unchanged. Right: Image constructed by co-adding the original image of NGC 2715 with a rotated and displaced version of itself. Except within the region of overlap the shape of the pixel intensity distribution is preserved, so G remains nearly unchanged.

Thus to a first approximation, treating G as a sort of generalized concentration index is not too far off the mark. As shown in Figure 3.26, there is a strong correlation between the Gini coefficient and central concentration for local galaxies. The error bars on G ($\pm 1\sigma$) are determined from 100 bootstrap replications (Efron & Tibshirani 1993) of the pixel distribution for each galaxy. Bootstrap replication cannot be used to estimate the errors on C , and no error bars on C are shown. However, on the basis of the Monte Carlo simulations described in Abraham et al. (1994), we expect error bars on C to be approximately similar in size to the error bars on G . We find the scatter in the relation is larger than the errors on individual measurements of G and is in fact correlated with the mean surface brightness of the galaxy. We will have more to say about the nature and significance of this correlation in Chapter 7.

This correlation suggests that G might be a suitable replacement for concentration measures in studies of high-redshift galaxies, as a large fraction of these objects are distorted and peculiar. Measurements of G are completely independent of galaxy shape, do not rely on any kind of aperture photometry, and do not even require that the galaxy image have a single well-defined center. However, the use of G as a straightforward substitute for concentration indices is something of an over-simplification, at least for nearby galaxies where the fraction of peculiar systems is small. As illustrated in Figure 3.27, it is easy to show that galaxy images can be transformed in many ways that preserve G while completely changing measures of concentration. Clearly these two quantities do not simply measure the same thing, and G captures something fundamentally new in the image that is not probed by concentration measures alone.

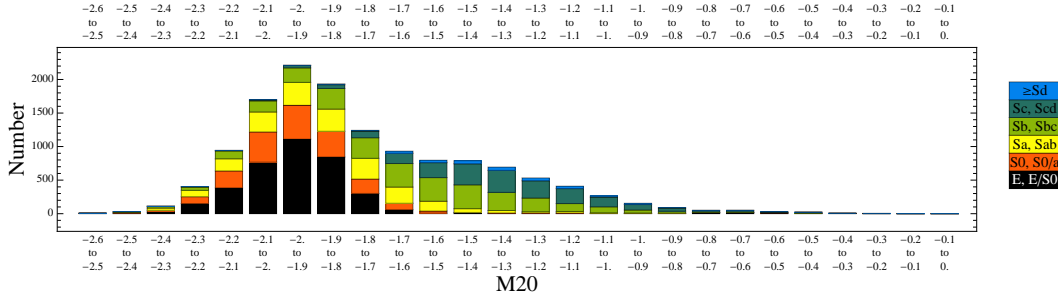


Figure 3.28: Histogram of various Hubble Types as a function of M_{20} . The sub-categories of galaxy types have been grouped into the following broad classes: E and E/S0 galaxies (black bars), S0 and S0/a galaxies (orange bars), Sa and Sab galaxies (yellow bars), Sb and Sbc galaxies (light green bars), Sc and Scd galaxies (dark green bars) and galaxies with T-Types later than Sd (blue bars.) See text for details.

Moment of light : M_{20}

M_{20} , introduced by Lotz et al. (2004), is the second order moment of the brightest 20% of a galaxy's flux. Following the procedure in Lotz et al. (2004), the total second-order moment M_{tot} is the flux in each pixel f_i multiplied by the squared distance to the center of the galaxy, summed over all the galaxy pixels assigned by the segmentation map:

$$\mathcal{M}_{tot} = \sum_i^n M_i = \sum_i^n f_i ((x - x_c)^2 + (y - y_c)^2), \quad (3.5)$$

where (x_c, y_c) is the galaxy's center, computed by finding the position where M_{tot} is minimized. To compute M_{20} , the galaxy pixels are rank-ordered by flux, and then the sum M_i is calculated over the brightest pixels until it equals 20% of the total galaxy flux. This is then normalized by M_{tot} :

$$\mathcal{M}_{20} = \sum_{i=1} M_i / M_{tot} \quad \text{while} \quad \sum_i f_i < 0.2 f_{tot}. \quad (3.6)$$

Note, unlike Lotz et al. (2004) we define M_{20} without taking the log, in line with our other parameters. Here f_{tot} is the total flux of the galaxy pixels identified by the segmentation map and f_i are the fluxes for each pixel i , order such that f_1 is the brightest pixel, f_2 is the second brightest pixels, and so on. The normalization by M_{tot} removes the dependence on total galaxy flux or size.

The definition of M_{20} , although similar to that of C , differs in two important respects. First, M_{20} depends on r^2 and is more heavily weighted by the spatial distribution of luminous regions. Second, M_{20} is not measured within circular or elliptical apertures, and the center of

the galaxy is a free parameter.

Figure 3.28 shows the distribution of M_{20} keyed to Hubble type for our sample. We find M_{20} does a much better job at segregating the various classes of objects than asymmetry. 86% of ellipticals are selected with a selection cut $M_{20} < -1.8$ with 31% contamination by spirals later than S0a. With a strict axis ratio cut of $b/a > 0.6$, roughly 86% of the total elliptical sample is selected but the contamination by spirals reduces to 19%.

Thus far we have considered the usefulness of each parameter individually to distinguish between early and late types. We will not be investigating the distinguishing abilities of these quantities in multi-parameter space in this thesis. We will investigate the relationship between different physical properties, T-Types and quantitative morphology in Chapters 4 and 5.

3.7 Catalog of Visual and Quantitative Parameters

Table 3.4 is a small sample of the entire catalog being released in Nair & Abraham (2009, in prep). The catalog contains 34 columns with the following information.

Column 1 : J2000 ID. The preferred format by SDSS for object identification.

Column 2 : Right Ascension (J2000) in degrees.

Column 3 : Declination (J2000) in degrees

Column 4 : Spectroscopic Redshift

Column 5 : Confidence level in redshift measurement

Column 6 : g' apparent magnitude (extinction corrected)

Column 7 : r' apparent magnitude (extinction corrected)

Column 8 : g' -band absolute magnitude corrected to $z=0$ using the `kcorrect` code of Blanton et al 2003.

Column 9 : Luminosity in g' -band in solar units

Column 10 : Petrosian Radius (Petrosian 1976)

Column 11 : Rp50 in kiloparsec

Column 12 : Rp90 in kiloparsec

Column 13 : Spectra ID made up of the MJD, Plate and Fibre number

Column 14 : Mass in log units (Kauffmann et al. 2003b)

Column 15 : Age in Gigayears (Kauffmann et al. 2003b)

Column 16 : $g'-r'$ color

Column 17 : Total star formation rate (Brinchmann et al. 2004)

Column 18 : Total star formation rate per unit mass (Brinchmann et al. 2004)

Column 19 : Surface Brightness in g , corrected for galactic extinction and internal extinction as prescribed by RC3.

Column 20 : Surface Mass Density

Column 21 : M/L in g

Column 22 : Area of the galaxy in arcsec square

Column 23 : Axis Ratio (b/a)

Column 24 : AGN flag (True/False) as defined by Kauffmann et al. (2003a)

Column 25 : T-Type classification using the modified RC3 classifiers as specified in the previous section.

Column 26 : Bar Type is defined as $\sum_i 2^i$ where i takes the following possible values :

1: strong bar, 2: intermediate, 3: weak bar, 4: ansae, 5 : peanut, 6: nuclear bar 7: bar unsure.

Thus if a large scale strong bar and a nuclear bar is present the bar type will be $2^1 + 2^6 = 66$.

Column 27 : Ring Types defined as $\sum_i 2^i$ where i takes the following possible values- 1: nuclear ring, 2: inner ring, 3: outer ring.

Column 28 : Lens Type, defined as $\sum_i 2^i$ where i takes the following possible values :

1: inner lens is present, 2: outer lens is present

Column 29 : Flags: T-Type flags are 0:No flag set, 1: Doubtful, 2: Highly Doubtful, 3: Unknown, 4: peculiar.

Column 30 : Pair Types defined as $\sum_i 2^i$ where i takes the following possible values :

1: Close Pair, 2: Projected Pair, 3: Adjacent Pair , 4: Overlapping Pair

Column 31 : Interaction Types defined as $\sum_i 2^i$ where i takes the following possible values :

1: NoInteraction Signature, 2: Disturbed, 3: Warp, 4: Shells , 5: Short Tail, 6: Medium Tail, 7: Long Tail, 8: Bridge

Column 32 : Number of tails; 1 Tail, 2 Tails, 3+Tails, Bunny

Column 33 : Rotational Asymmetry (Abraham et al. 1996a; Brinchmann et al. 1997; Conselice et al. 2000)

Column 34 : Concentration (Abraham et al. 1994)

Column 35 : Gini as defined in (Abraham et al. 2003)

Column 36 : M20 (Lotz et al. 2004)

Table 3.4. T-Type Classification Schemes

JID spID T-Type	RA		DEC		z		zconf		g		r		M_g		L_g		Rp		Rp50		Rp90	
	Mass	Bar	Age	Ring	Color	Lens	SFRM	flag	Pairs	SFRM	μ_g	dist	μ_M	tails	M/L	Area	b/a	AGN	b/a	AGN		
J110509.21-004749.10	166.289		-0.796		0.034		1.	1.	14.665	13.856	0.034	1.	-21.268	10.529	11.505	4.829	13.043	False	4.829	13.043	False	13.043
277-51908-2	10.897		999999.		0.764		1.156	1.156	-11.376	22.255	0.374	8.244	8.244	999999.	0.374	449.783	449.783	False	449.783	False	449.783	
1.	8.		36.		4.		0.	0.	0.	0.	0.0510	0.	0.	0.0510	0.396	0.554	0.554	0.01	0.554	0.01	0.554	
J112535.07-004605.66	171.397		-0.768		0.0260		1.	1.	13.774	12.971	0.0260	-21.487	10.57	9.051	9.051	3.471	11.534	False	3.471	11.534	False	11.534
280-51612-5	11.136		999999.		0.815		0.95	0.95	-11.677	22.218	0.834	8.43	8.43	999999.	0.834	508.78	508.78	False	508.78	False	508.78	
-5.	8.		0.		0.		2.	2.	0.	0.	0.02	0.	0.	0.02	0.577	0.671	0.671	0.008	0.671	0.008	0.671	
J115537.98-004614.26	178.909		-0.77		0.065		1.	1.	15.689	15.092	0.065	-21.714	10.666	16.358	6.556	16.144	16.144	True	6.556	16.144	True	16.144
285-51930-309	11.036		3.509		0.563		0.998	0.998	-9.59	22.378	8.362	8.362	8.362	0.218	0.538	471.858	471.858	True	471.858	True	471.858	
4.	2.		0.		0.		0.	0.	0.	0.	0.024	0.	0.	0.024	0.401	0.55	0.55	0.015	0.55	0.015	0.55	
J120127.92-004306.18	180.367		-0.718		0.021		1.	1.	14.304	13.554	0.021	-20.519	10.131	13.297	5.615	10.793	10.793	False	5.615	10.793	False	10.793
285-51930-103	10.416		999999.		0.634		-0.151	-0.151	-10.353	22.999	7.82	7.82	7.82	999999.	0.707	394.235	394.235	False	394.235	False	394.235	
2.	4.		4.		0.		0.	0.	0.	0.	0.0260	0.	0.	0.0260	0.27	0.418	0.418	0.03	0.418	0.03	0.418	
J130855.34-004805.77	197.231		-0.801		0.02		0.997	0.997	15.177	14.287	0.02	-19.465	9.886	5.326	2.087	6.046	6.046	False	2.087	6.046	False	6.046
294-51986-53	10.635		999999.		0.779		0.287	0.287	-10.68	22.271	8.566	8.566	8.566	999999.	0.342	117.207	117.207	False	117.207	False	117.207	
1.	8.		0.		0.		0.	0.	2.	0.	0.063	0.	0.	0.063	0.483	0.646	0.646	0.012	0.646	0.012	0.646	
J130903.63-004557.62	197.266		-0.766		0.0180		1.	1.	14.418	13.623	0.0180	-20.001	10.044	6.4	2.818	6.78	6.78	False	2.818	6.78	False	6.78
294-51986-59	10.539		999999.		0.725		-0.0130	-0.0130	-10.827	22.479	8.223	8.223	8.223	999999.	0.785	207.099	207.099	False	207.099	False	207.099	
0.	72.		12.		0.		0.	0.	0.	0.	0.047	0.	0.	0.047	0.455	0.608	0.608	0.007	0.608	0.007	0.608	
J132234.88-004046.99	200.646		-0.679		0.046		0.999	0.999	15.987	15.331	0.046	-20.609	10.298	6.559	3.168	6.63	6.63	False	3.168	6.63	False	6.63
296-51984-110	10.689		3.484		0.578		0.712	0.712	-10.079	21.904	8.419	8.419	8.419	0.245	0.543	186.289	186.289	False	186.289	False	186.289	
1.	8.		0.		0.		0.	0.	0.	0.	0.084	0.	0.	0.084	0.364	0.587	0.587	0.031	0.587	0.031	0.587	
J135756.80-004000.69	209.487		-0.666		0.07		0.999	0.999	15.932	15.166	0.07	-21.715	10.637	14.991	6.726	17.278	17.278	False	6.726	17.278	False	17.278
301-51942-175	10.941		5.287		0.701		0.874	0.874	-10.224	22.495	8.335	8.335	8.335	0.129	0.621	404.01	404.01	False	404.01	False	404.01	
1.	8.		0.		0.		4.	4.	4.	0.	0.161	0.	0.	0.161	0.295	0.551	0.551	0.016	0.551	0.016	0.551	
J140451.74-003829.81	211.216		-0.641		0.025		1.	1.	14.419	13.649	0.025	-20.783	10.353	9.627	4.097	11.436	11.436	False	4.097	11.436	False	11.436
302-51688-263	10.678		999999.		0.678		0.207	0.207	-10.834	22.665	8.002	8.002	8.002	999999.	0.792	474.826	474.826	False	474.826	False	474.826	
1.	4.		76.		0.		0.	0.	0.	0.	0.041	0.	0.	0.041	0.464	0.613	0.613	0.007	0.613	0.007	0.613	

Chapter 4

The Morphological Properties of Nearby Galaxy

4.1 Introduction

Our fundamental perception of morphology in the local universe has been based on the work of Hubble, Morgan, de Vaucouleurs, van den Bergh, Sandage and many others. Roberts and Haynes (1994; hereafter RH94) reviewed the physical correlations seen in the local universe along T-Types using the Third Reference Catalog of Bright Galaxies (hereafter RC3) supplemented with private HI catalogs. Their work strengthened the correlations seen with T-Type in the local universe, like the color-morphology relation (Holmberg 1958) to which high redshift morphological studies are compared and emphasized the change in properties observed when going from ellipticals to classical spirals to dwarfs.

Conselice (2006; hereafter CO06) built upon the work of RH94 by conducting a statistical analysis on the galaxies in RC3 with $z < 0.05$. Using principal component analysis and a Spearman rank, Conselice showed that color is keyed strongly to mass whether objects are early ($T < 1$) or late ($T > 1$), and postulated that the fundamental parameters in nearby galaxies can be accounted for by eigenvectors dominated by: (i) a scale parameter like stellar mass, (ii) a spectral type measure like star formation or color, and (iii) the degree of dynamical disturbance, interactions/mergers.

Although the works of RH94 and CO06 were based on a much larger sample than previous studies, they were limited in how well they could investigate observed physical correlations due to a lack of measurements of global properties for all objects in their sample. With the advent of large surveys, especially the Sloan Digital Sky Survey (SDSS), we have a vast resource of digitally resolved images with spectroscopic information as well as derived parameters made public by other groups. The only drawback is that a completely automated classifica-

tion scheme still does not reproduce the quantization of the Hubble scheme. We hence use our classifications described in the previous chapter to investigate the correlations of global properties with T-Type and compare our results with RH94 and CO06.

4.2 Variation in Galaxy Properties with Visual Morphology: 1D

Roberts and Haynes, 1994 (RH94) analyzed in total around 12000 galaxies from the RC3 split into 2 samples, a flux-limited sample of objects common to RC3 and the Uppsala General Catalog (UGC) and a second non-overlapping, volume-limited sample common to RC3 and the Local Super Cluster (LSc). These samples were used to investigate the correlations of physical properties of galaxies along the Hubble Sequence. Measures of global properties were not available for all T-Types and in some cases different approaches were used to determine properties. Hence the number of galaxies used in each correlation varies (see RH94).

It is important to note that the properties of the RC3, used by RH94, and the SDSS samples being studied here are not defined the same way. However, we are not interested in absolute values but rather in the trends with T-Type. We study 7 global parameters: the petrosian radius R_p , blue luminosity L_g , stellar mass M , stellar mass-to-light-ratio M/L_g , blue surface magnitude Σ_g , and the surface stellar mass density σ_M . We compare them against the following parameters in RH94: the linear radius R_{lin} , blue luminosity L_B , total mass M_T , total mass-to-light-ratio M_T/L_B , blue surface magnitude Σ_B , and total surface mass densities σ_T . Table 4.1 and 4.2 list the median values and quartiles of these global properties in the SDSS-DR4 and RH94 galaxy samples for the different T-Types. Figures 4.1 shows the variation of these properties with T-Types. Each row compares a similar property from SDSS-DR4 and RH94. Each right hand panel shows the median (filled box) value of the labeled property against T-Type for the SDSS DR4 sample along with a vertical bar indicating the 25% to 75% interquartile range. The left hand panel shows the median values and quartiles for the RC3-UGC (triangle) and the RC3-LSc (box) samples. The RC3 plots are created using the data provided by RH94 which are binned into coarser morphological types. We discuss the relationships as follows.

4.2.1 Correlation between size and T-Type

In RH94, the sizes used are from the RC3 catalog and are the radii to an isophote of 25 B $mag/arcsec^2$. We use the petrosian radius (Petrosian 1976; Stoughton et al. 2002) as a measure of the size of a galaxy for comparison. As seen in Figure 4.1(a) RH94 observe a subtle trend in the change in size from early types to Sc and a sharp decrease beyond T-Type 6 or Scd. Their volume limited sample shows a more pronounced increase in size from Sa to Sc compared to their flux limited sample.

Table 4.1. T-Type Classification

Pr		E0	S0-	S0	S0/a	Sa	Sab	Sb	Sbc	Sc	Scd	Sd	Sdm	Sm	Im
		-5	-3	-2	0	1	2	3	4	5	6	7	8	9	10
R_p	med	4.0	2.9	2.5	2.8	3.2	4.1	4.1	4.3	3.9	3.4	3.1	2.9	2.6	2.1
	25%	2.9	2.0	1.9	2.0	2.2	2.9	3.0	3.2	3.0	2.6	2.4	2.3	2.1	1.6
	75%	5.6	4.2	3.4	3.9	4.6	5.5	5.5	5.6	4.9	4.2	4.0	3.4	3.2	3.1
	num	2877	1024	1073	1130	1427	755	2096	1280	1282	369	143	90	77	71
M	med	10.8	6.5	4.5	4.5	5.0	5.6	5.0	3.9	2.1	0.6	0.3	0.3	0.3	0.2
	25%	5.7	3.2	2.6	2.4	2.7	2.9	2.6	1.7	0.9	0.2	0.1	0.2	0.1	0.1
	75%	18.2	11.8	8.0	7.9	9.3	9.9	8.8	7.2	4.4	1.5	0.7	0.5	0.5	0.4
	num	2877	1024	1073	1130	1427	755	2096	1280	1282	369	143	90	77	71
L_g	med	51.0	34.2	25.3	24.7	26.8	33.1	31.8	29.0	19.0	10.3	8.1	9.0	7.3	8.0
	25%	30.8	18.9	15.3	15.8	15.9	20.0	19.6	17.1	11.5	6.3	4.7	5.5	4.3	4.1
	75%	76.2	53.5	39.1	38.5	44.0	53.3	50.3	47.5	30.2	17.0	13.0	12.0	12.1	14.4
	num	2877	1024	1073	1130	1427	755	2096	1280	1282	369	143	90	77	71
$\frac{M}{L}$	med	2.1	1.9	1.8	1.8	1.8	1.7	1.5	1.3	1.1	0.6	0.4	0.3	0.3	0.2
	25%	1.7	1.4	1.5	1.4	1.3	1.2	1.1	0.9	0.7	0.4	0.3	0.2	0.2	0.1
	75%	2.6	2.5	2.4	2.3	2.4	2.2	2.1	1.8	1.7	1.0	0.6	0.4	0.4	0.4
	num	2877	1024	1073	1130	1427	755	2096	1280	1282	369	143	90	77	71
σ	med	8.7	8.8	8.8	8.6	8.6	8.4	8.3	8.2	8.0	7.6	7.4	7.4	7.5	7.4
	25%	8.5	8.6	8.6	8.4	8.3	8.2	8.1	8.0	7.8	7.4	7.1	7.2	7.1	7.1
	75%	8.9	8.9	8.9	8.9	8.8	8.6	8.5	8.4	8.3	7.9	7.7	7.7	7.7	7.8
	num	2877	1024	1073	1130	1427	755	2096	1280	1282	369	143	90	77	71
Σ_g	med	12.3	12.0	11.8	11.8	11.7	12.2	12.2	12.4	12.3	12.3	12.4	12.6	12.7	12.2
	25%	11.9	11.5	11.3	11.2	11.1	11.5	11.5	11.8	11.5	11.6	11.7	12.1	11.9	11.6
	75%	12.7	12.5	12.3	12.4	12.4	12.7	12.7	12.9	12.9	13.1	13.1	13.2	13.1	12.8
	num	2877	1024	1073	1130	1427	755	2096	1280	1282	369	143	90	77	71
$g-r$	med	0.8	0.8	0.8	0.8	0.8	0.8	0.7	0.6	0.6	0.5	0.4	0.4	0.4	0.3
	25%	0.8	0.8	0.8	0.7	0.7	0.7	0.6	0.5	0.5	0.4	0.4	0.3	0.3	0.2
	75%	0.9	0.9	0.8	0.8	0.8	0.8	0.8	0.7	0.7	0.6	0.5	0.4	0.4	0.4
	num	2877	1024	1073	1130	1427	755	2096	1280	1282	369	143	90	77	71

Table 4.2. Summary of Table from Roberts and Haynes 1994

Parameter	Sample		E,S0	S0a,Sa	Sab,Sb	Sbc,Sc	Scd,Sd	Sm,Im	Total
R_{lin}	UGC	median	21.1	19.8	25.1	22.4	17.7	8.5	7929 4112 12041
		25%	14.0	13.9	18.4	16.4	11.8	4.9	
		75%	28.8	26.5	32.1	29.8	24.0	14.0	
		Number	1362	798	1488	1139	2223	919	
	LSc	median	9.0	9.8	12.0	13.2	9.3	6.0	
		25%	5.8	6.9	8.3	9.5	6.8	4.1	
		75%	13.2	13.6	16.7	17.7	12.2	8.3	
		Number	705	342	454	616	1037	958	
		M_T	UGC	median	-10	22.6	32.4	19.0	
		25%	-10	8.7	17.0	9.5	3.5	0.5	
		75%	-10	49.0	52.5	33.9	16.6	4.0	
		Number	-10	292	808	639	1471	490	
	LSc	median	-10	7.1	11.0	9.1	2.8	1.0	
		25%	-10	3.2	4.9	5.1	1.4	0.4	
		75%	-10	17.4	21.4	16.2	5.1	1.8	
		Number	-10	119	251	389	701	534	
L_B	UGC	median	52.5	43.6	69.2	52.5	25.7	2.7	6426 3379 9805
		25%	21.4	21.4	38.0	29.5	9.8	1.0	
		75%	93.3	79.4	107.2	95.5	53.7	7.1	
		Number	1302	761	1391	1029	1527	416	
	LSc	median	11.0	13.2	19.5	21.9	6.8	1.9	
		25%	4.2	5.4	8.1	9.3	3.2	0.8	
		75%	24.9	23.4	38.0	41.7	13.2	4.1	
		Number	665	315	407	563	834	595	
M/L	UGC	median	-10	4.9	4.4	3.8	3.5	4.2	
		25%	-10	3.1	3.2	2.9	2.6	2.6	
		75%	-10	7.2	6.0	5.4	5.0	6.8	
		Number	-10	278	749	567	1025	245	
	LSc	median	-10	5.1	5.0	4.2	4.1	5.0	
		25%	-10	3.1	3.4	3.2	3.0	3.1	
		75%	-10	8.8	6.9	6.0	6.0	7.9	
		Number	-10	112	238	362	574	342	
σ_T	UGC	median	-10	188.9	154.7	124.2	91.4	74.5	3700
		25%	-10	133.4	115.2	94.5	67.8	49.2	
		75%	-10	249.8	199.9	167.6	119.6	113.2	
		Number	-10	292	808	639	1471	490	
	LSc	median	-10	200.8	178.2	148.5	95.8	81.4	
		25%	-10	121.7	125.4	108.1	69.6	52.1	
		75%	-10	323.1	242.8	194.2	131.8	120	

Table 4.2 (cont'd)

Parameter	Sample		E,S0	S0a,Sa	Sab,Sb	Sbc,Sc	Scd,Sd	Sm,Im	Total
		Number	-10	119	251	389	701	534	1994 5694
Σ_B	UGC	median	14.2	13.98	13.96	14.00	14.02	14.59	
		25%	13.82	13.47	13.44	13.44	13.29	14.08	
		75%	14.62	14.39	14.41	14.48	14.63	15.23	
		Number	1591	977	1694	1154	1663	457	7536
	LSc	median	13.78	13.73	13.55	13.72	14.02	14.73	
		25%	13.51	13.36	13.10	13.23	13.39	14.21	
		75%	14.15	14.10	13.99	14.22	14.65	15.35	
		Number	682	317	412	571	858	649	3489 11025
B-V	UGC	median	0.9	0.78	0.64	0.55	0.48	0.42	
		25%	0.86	0.66	0.55	0.47	0.42	0.35	
		75%	0.94	0.83	0.73	0.62	0.57	0.53	
		Number	484	161	243	320	161	168	1537
	LSc	median	0.89	0.78	0.62	0.52	0.48	0.42	
		25%	0.84	0.65	0.55	0.44	0.42	0.35	
		75%	0.92	0.84	0.71	0.59	0.56	0.51	
		Number	421	156	182	282	180	210	1431 2968

We see a similar trend of decreasing size with T-Type in the SDSS-DR4 sample with a few notable exceptions. Firstly we find a more pronounced trend for S0 galaxies to be smaller in size than either ellipticals or early spirals. We see the same trend in all measures of size (semi-major axis, half-light radius, petrosian R90 radius). This is faintly hinted at in the RH94 plot (Figure 2(a) in the original paper) but the sample size of S0s in RH94 was too small for this to be considered anything beyond scatter. In addition, the RH94 sample under-represented the largest early type galaxies, cDs. Thus size does not monotonically increase from late type to early type galaxies and S0 galaxies cannot be the 'missing link' between ellipticals and early spirals. This fact has already been realized with respect to other properties like luminosity (van den Bergh 1998). This is especially important given the use of the spearman rank, a monotonic measure of correlation, by authors such as CO06 to investigate galaxy properties. We will investigate the sources of scatter in this relation in § 4.3.

4.2.2 Correlation between mass and T-Type

RH94 used a sample of galaxies for which 21 cm line emission was detected to provide an estimate of the circular rotation velocity and hence determined the total masses for all non E-type systems. Their selection criterion brought their sample size down to 5694 galaxies in total, split between the RC3-UGC and RC3-LSc samples. Figure 4.1(b) shows the trend of the DR4 sample is similar to the RH94 sample where there is a small systematic variation in mass earlier than Sb and a sharp decrease for later systems beyond T=4. In RH94, total mass

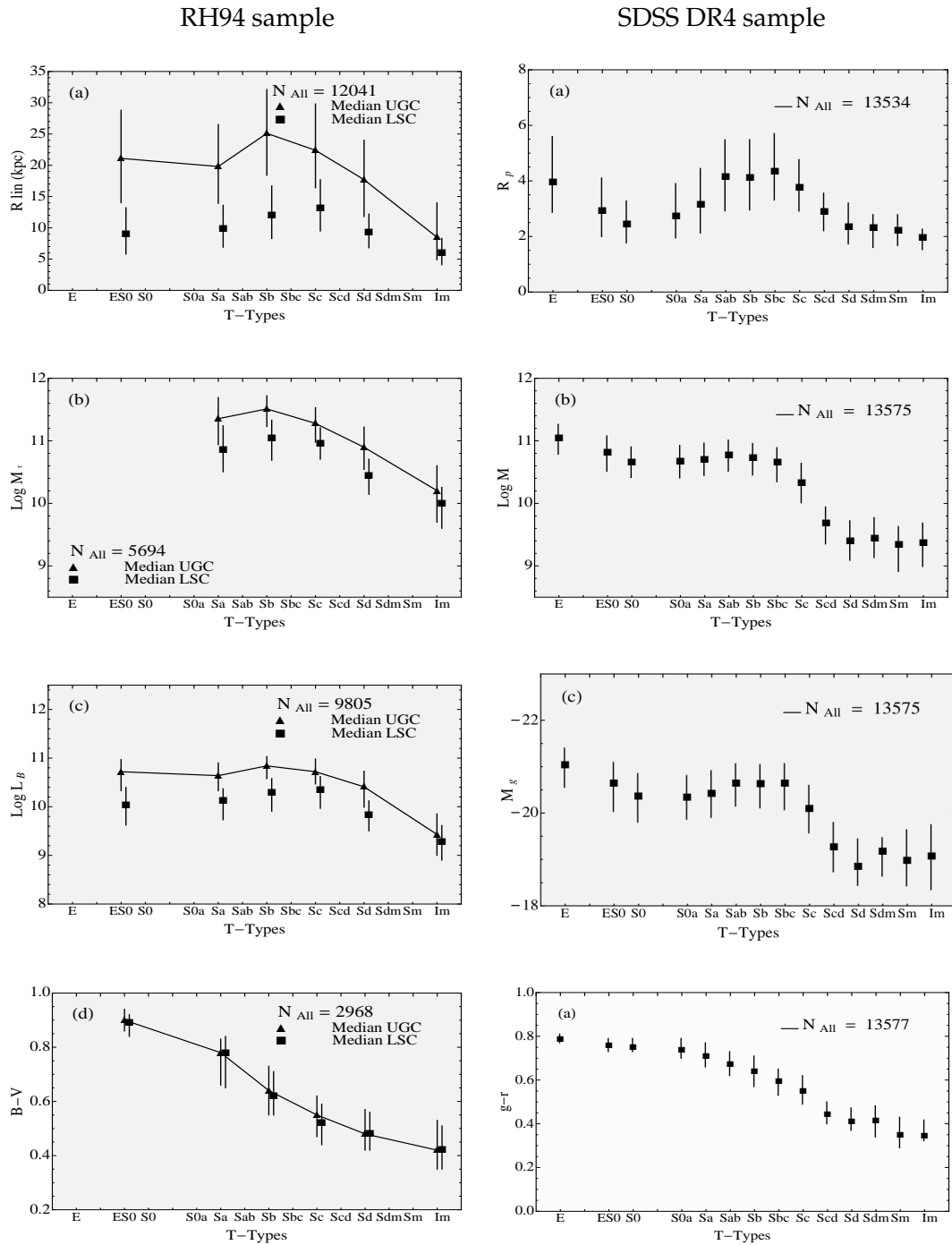


Figure 4.1: Global galaxy parameters vs. morphological T-Type. Each row compares a property from SDSS-DR4 and RH94 samples. (a) log of Mass in solar units (b) log of luminosity L in solar units, (c) mass-to-luminosity-ratio M/L . In the left column, filled triangles represent median values of the RC3-UGC (flux-limited) sample and the filled boxes, the RC3-LSc (volume-limited) sample. In the right column, filled boxes represent median values of the SDSS-DR4 (flux-limited) sample. The lower bar is the 25th percentile; the upper error bar is the 75th percentile.

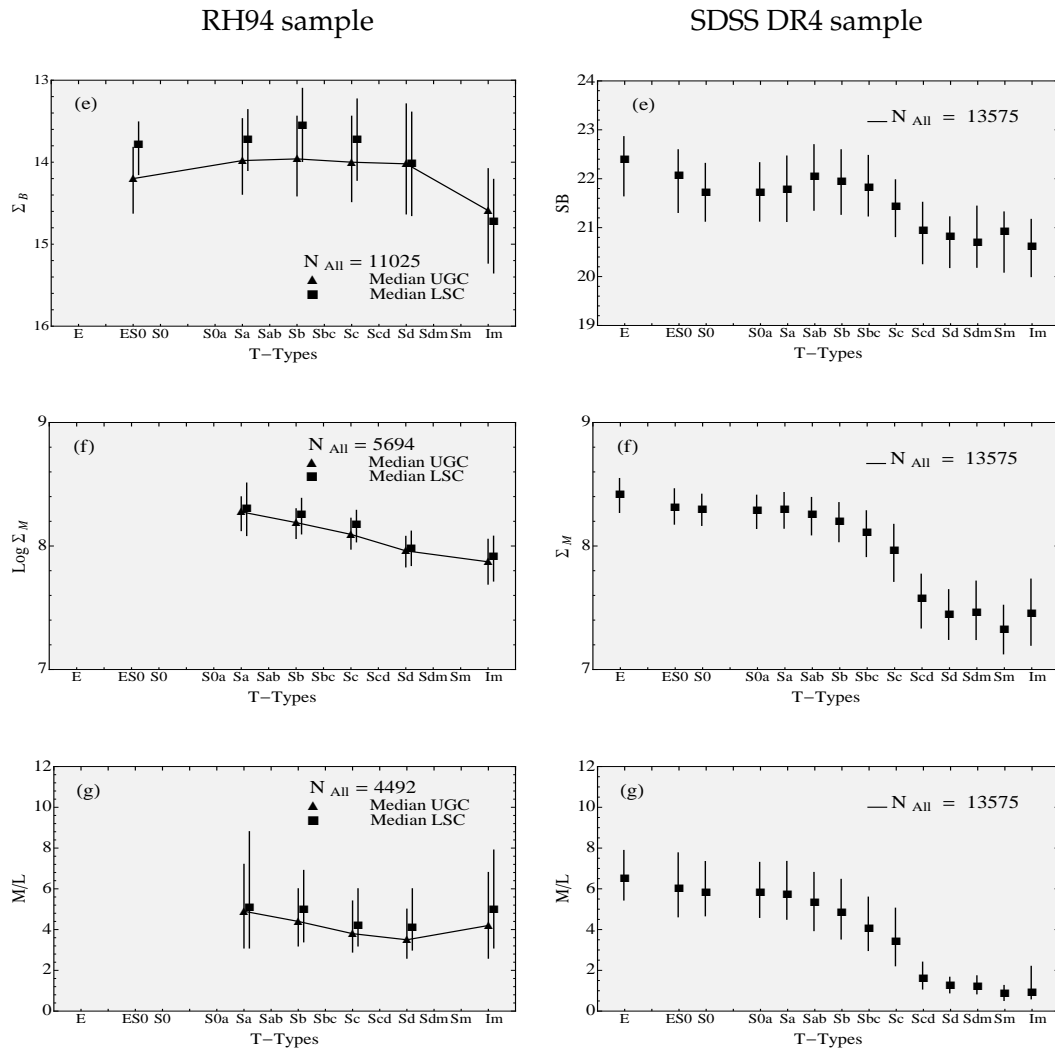


Figure 4.1: Global galaxy parameters vs. morphological T-Type cont.: Each row compares a property from SDSS-DR4 and RH94 samples. (e) optical surface brightness σ , (f) log total surface mass density σ (g) mass-to-light ratio. In the left column, filled triangles represent median values of the RC3-UGC (flux-limited) sample and the filled boxes, the RC3-LSc (volume-limited) sample. In the right column, filled boxes represent median values of the SDSS-DR4 sample. The lower bar is the 25th percentile; the upper error bar is the 75th percentile.

increases slightly from Sa to Sb galaxies, whereas we find a gradual decrease of mass from E to S0a, a near plateau for classical spirals and a sharp drop of mass with T-Type for objects later than Sbc. Our estimates for the mass of late type spirals are much lower than the RC3 measures though it should be realized that we are comparing different mass measures (stellar vs. total). The relation between stellar mass and T-Type is not monotonic.

4.2.3 Correlation between luminosity and T-Type

Figure 4.1(c) shows luminosity as a function of T-Type. RH94 used the total B band luminosity within R_{lin} from RC3 while we use the g-band absolute magnitude within the $1.5 R_p$. Both panels show that luminosity is nearly constant for classical spirals until T-Type 5 after which it decreases gradually for the RH94 sample while dropping sharply for the SDSS sample. Ellipticals and E/S0's show a gradual increase in luminosity in comparison to spirals in the SDSS sample while there is little variation in the RH94 sample. This is most probably due to the under-representation of massive elliptical galaxies in the RH94 sample.

4.2.4 Correlation between color and T-Type

In Figure 4.1(d) we compare the RC3 B-V color ($M_{4400} - M_{5530}$) against the nearest Sloan filters, g-r ($M_{4686} - M_{6166}$). As expected, the best correlation seen between a physical property and T-Type is with color. The variation of color with T-Type is similar for both RH94 and SDSS-DR4 where the early types E's and S0's are redder than later spiral galaxies. The relationship between color and T-Type is clearly monotonic with very small scatter. RH94 noted that the range of colors spanned by Sa's and Sc's were such that some Sa's were as blue as Sc's while some Sc's were as red as Sa's. They explained this scatter as an indication of variation in current star formation rates. We will investigate this further in §4.4.

4.2.5 Correlation between surface brightness and T-Type

In Figure 4.1(e), surface brightness is nearly constant across all T-Types in RH94 with the exception that Sm/Im objects have lower surface brightness. In the SDSS-DR4 sample we find surface brightness initially decreases from E to S0's, gradually increases from Sa to Sc and then falls off again for later types, following similar trends observed with mass, luminosity and size.

4.2.6 Correlation between surface mass density and T-Type

In Figure 4.1(f) both RH94 and SDSS-DR4 show a clear decrease in the overall median values of surface mass density Σ_M with T-Type for classical spirals. SDSS again shows a much stronger break past a T-Type of 5. For classical spirals the surface mass density is nearly constant with very little scatter. Ellipticals have slightly larger surface mass densities.

Table 4.3. Spearman correlation matrix

Family	T-Type	Size	Mass	g-r	M_g
All RC3	1	-0.24	-0.68	-0.80	0.25
All PN	1	-0.24	-0.52	-0.82	0.31
Early RC3	1	-0.09	-0.36	-0.42	0.20
Early PN	1	-0.39	-0.39	-0.40	0.35
Late RC3	1	-0.38	-0.55	-0.63	0.41
Late PN	1	-0.27	-0.46	-0.62	0.30

4.2.7 Correlation between mass-to-light ratios and T-Type

In Figure 4.1(g) RH94 observe a gradually declining M/L ratios though they consider it nearly constant given the scatter in the relation. In the SDSS-DR4 sample we observe a near constant M/L up to $T=5$ and then a sharp decrease in M/L . It should be noted that we measure stellar mass whereas RH94 calculate total mass which is why they observe a higher M/L for late-type galaxies.

4.2.8 Summary

Unlike RH94 we are able to consider variation of properties throughout the entire range of morphologies for our entire sample. All seven properties we have studied show significant dependence on T-Type. Color is by far the quantity most clearly and monotonically correlated with the morphology of a galaxy. All other quantities show a break in their dependence on T-Type at $T \sim 5$. Size and mass are also correlated with T-Type but are not as clearly monotonic. It is for this reason that the interpretation of statistical measures to study correlations must be considered carefully.

4.2.9 Statistical Correlations

CO06 used the spearman rank to analyze the correlations between physical properties and T-Type. Table 4.3 shows the spearman ranks for the RC3 data used by CO06 and our sample (PN) for the 4 quantities we have in common. CO06 find mass and color are significantly correlated with T-Type but size and magnitude are not. CO06 attribute the weak correlation as an indication that the size/luminosity of a galaxy are secondary scale characteristics. We find the more likely reason is because the spearman rank averages over the non-monotonic, physically important, variations seen with T-Type. Similar results are obtained with our data if we use a spearman rank as a metric of correlation. When split between early and late types, we find no significant dependence of any quantity with T-Type for E or S0 galaxies and a strong

dependence of color (and possibly mass) on T-Type for spiral galaxies. Thus the correlations of physical properties with T-Type are mainly driven by spiral galaxies.

4.2.10 Systematic Effects: Inclinations Effects, Fine structures and AGNs

Although we find strong correlations between T-Types and physical properties there is a large scatter in these relations, much larger than the errors associated with the terms. We would like to understand the causes of the scatter but it is important to account for biases which may be introduced by inclination effects, fine structures or AGNs. Figure 4.2 shows the variation of each of the seven physical parameters we investigated in the previous section with T-Type for different axis ratio cuts in galaxies without AGNs or bars. The solid black line shows the variation for the entire sample, the red, dashed line shows the variation for the sample with $b/a > 0.4$ and the blue, dotted line for $b/a > 0.6$. We find sizes are over-estimated for all spiral galaxies with the strongest overestimation for the latest T-Types. The mass of the galaxies are not influenced by inclination cuts. The magnitudes are under-estimated for spiral galaxies while color is redder for more inclined systems as expected. Surface brightness and surface mass densities are slightly over-estimated for spirals while mass-to-light ratios are significantly over-estimated for classical spirals (Sa-Sc) when including face on systems. The general trends however remain the same for all plots and the scatter in points is roughly comparable for all inclination cuts.

Figure 4.3 shows the variation of physical properties with T-Type for face-on objects with a fine component (blue/ring/lens; blue, dashed) or AGN (red, dotted) compared to the distribution of normal face-on galaxies (purple) with no fine component or AGN. The black line is for normal galaxies with no-inclination cut. We find the size of galaxies with a fine component or AGN is over-estimated for spirals but slightly under-estimated for early type galaxies. The masses and luminosities of classical spiral galaxies with AGN or fine components are slightly larger than normal (non-AGN, non-fine) galaxies. Galaxies with fine components are redder than galaxies with AGN which are in turn redder than normal galaxies for all T-Types. The surface mass densities are comparable for all three populations. The mass-to-light ratios are larger for AGN and galaxies with a fine component compared to normal, non-active galaxies. The trends for all distribution are nearly the same with the exception of the variation of surface brightness with T-Type. For galaxies with AGN the surface brightness is larger for classical spirals compared to fine structured and normal galaxies. We will not be studying this effect specifically for this thesis but will be investigating it separately.

As we have shown, accounting for inclination effects and the presence of an AGN will be important for studying mass-to-light ratios and surface brightness variations. For all other properties, inclination and the presence of a bar or AGN do not account for the scatter in the

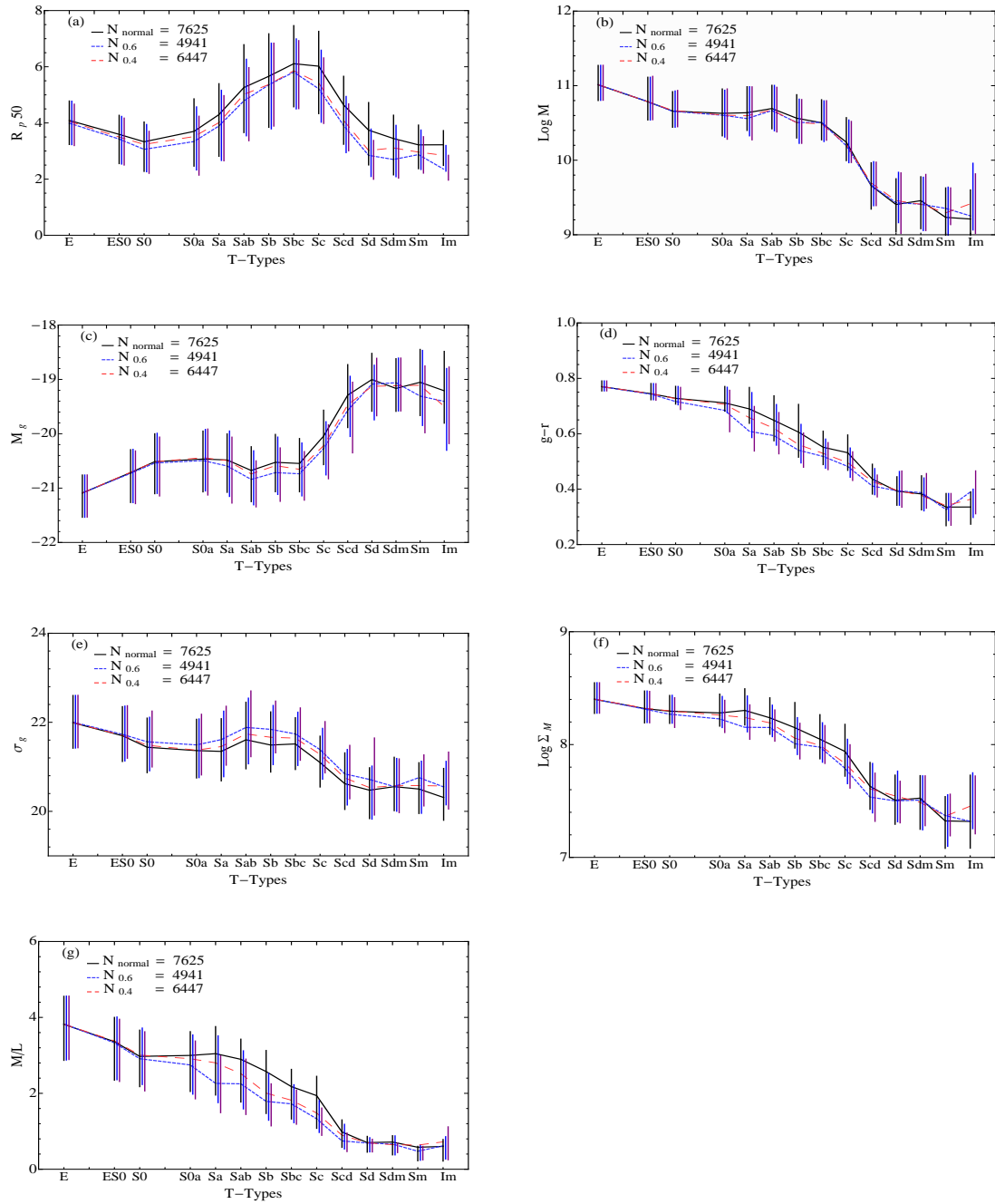


Figure 4.2: Global galaxy parameters vs. morphological T-Type. Each panel compares the effect of axial ratio cuts on the variation of a physical property with T-Type for the SDSS-DR4 sample. The solid black line is the complete, non-AGN, non-fine component sample. The dashed red line is for the sample with $b/a > 0.4$ and the dotted blue line is for $b/a > 0.6$ sample. The lower bar in each case is the 25th percentile while the upper error bar is the 75th percentile.

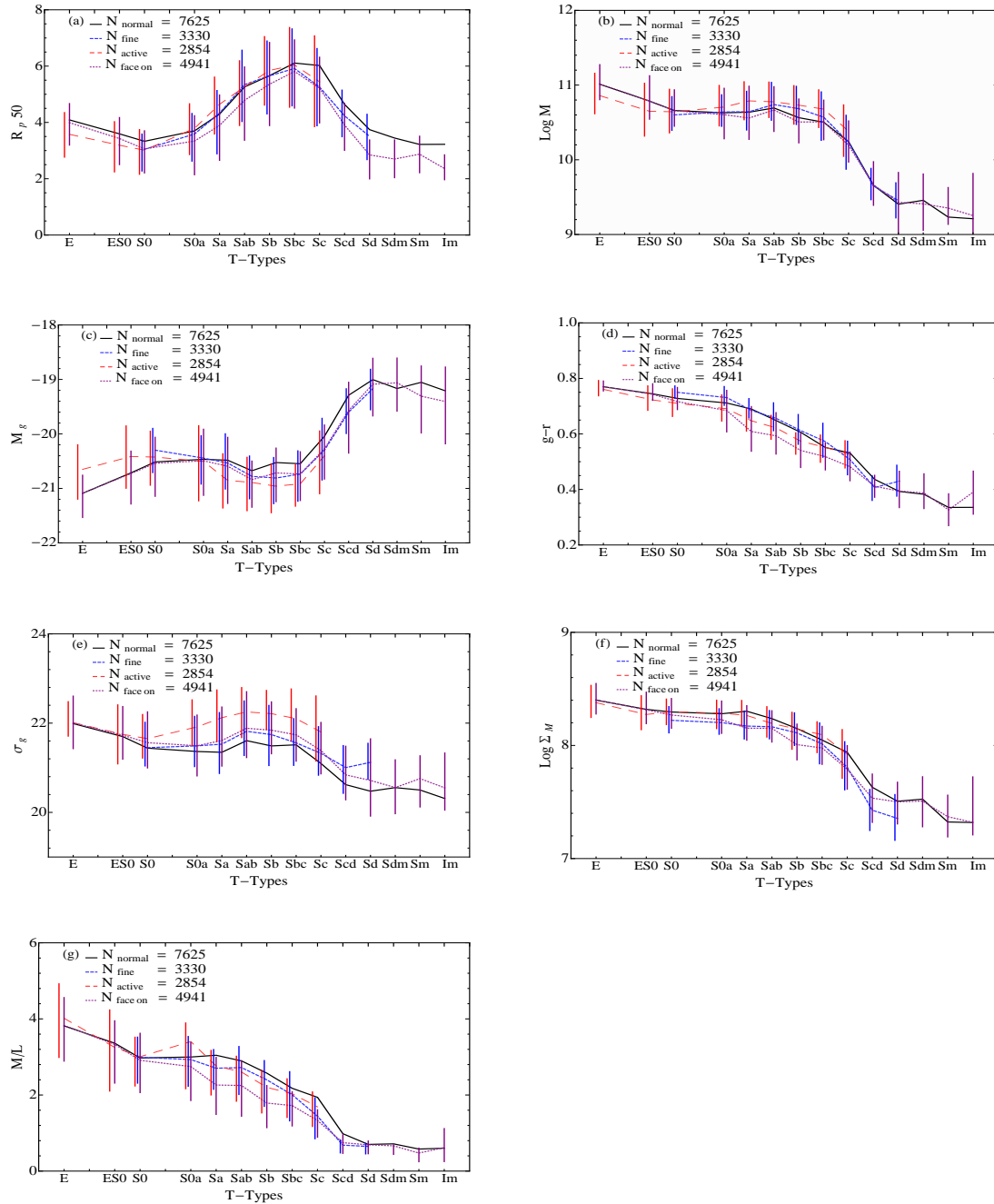


Figure 4.3: Global galaxy parameters vs. morphological T-Type. Each panel compares the effect of the presence of an AGN or fine-structure on the variation of a physical property with T-Type for the SDSS-DR4 sample. The solid black line is the complete, non-AGN, non-fine component sample with no inclination cut. The dashed red line is for galaxies with AGNs only and no fine-component, the small dashed blue line for galaxies with either a bar, ring or lens but no AGNs while the dotted purple line is for the normal sample. All three samples have an inclination cut of $b/a > 0.6$. The lower bar in each case is the 25th percentile while the upper error bar is the 75th percentile.

various relations.

4.3 Variation in Galaxy Properties with Visual Morphology: Bivariate Analysis

To better understand the causes of the scatter in the relationship between the seven physical properties studied in the previous section with T-Type, we now investigate the dependence of each relation on the following 10 properties split into three bins each:

- (a) Size in kpc: $0 < R_{p90} < 3$, $3 < R_{p90} < 5$, $5 < R_{p90} < 15$;
- (b) Mass in M_{\odot} : $M < 10.2$, $10.2 < M < 10.8$, $M > 10.8$;
- (c) Absolute Magnitude: $-20 < M_g < -16$, $-21 < M_g < -20$, $-24 < M_g < -21$;
- (d) Color: $g - r < 0.6$, $0.6 < g - r < 0.75$, $g - r > 0.75$;
- (e) Surface brightness (per square arc second): $18 < SB < 21$, $21 < SB < 22$, $22 < SB < 25$;
- (f) Surface mass density (per square arc second) : $5 < SMD < 8.35$, $8 < SMD < 8.35$, $8.35 < SMD < 10$;
- (g) Mass-to-light ratio: $0 < M/L < 4$, $4 < M/L < 6$, $M/L > 6$;
- (h) Age in Gy: $0 < Age < 3$, $3 < Age < 6$, $Age > 6$;
- (i) Total star formation rates in M_{\odot}/yr : $-5 < SFRT < 0.3$, $0.3 < SFRT < 0.8$, $0.8 < SFRT < 3.0$ and
- (j) Star formation rates per unit mass in yr^{-1} : $-15 < SFR/M < -11$, $-11 < SFR/M < -10$, $-10 < SFR/M < -7$.

4.3.1 Correlation between size with T-Type

Figure 4.4 shows the variation of size with T-Type keyed to various property bins. The first panel shows the overall variation of size with T-Type for the complete sample. We find the scatter in the size T-Type relation is predominantly related to mass, luminosity, surface brightness and total star formation rate. For example panel (c) shows that at a given Hubble stage there is a strong correlation between size and absolute magnitude. The median size of a galaxy changes by a factor of three over a change in absolute magnitude of four magnitudes. Secondary influences are related to color, surface mass density, age and star formation rate per unit mass. It is apparent that the skew of the size vs. T-Type relation towards smaller sizes at later T-Types in the overall distribution is due partially to the fact that there are very few late type objects with large masses, luminosities or redder colors. For each mass bin, the overall trend shown by the black line is repeated where S0 are of smaller size than their neighboring T-Types and the sizes decrease beyond T-Type 6. As mass decreases the median sizes of all ob-

jects decreases. It is interesting to note that only in the highest mass bins are elliptical galaxies comparable in size to classical spirals. In the lowest and intermediate mass bins classical spirals have larger median petrosian radii than early types. This trend is seen in all measures of size (half-light radius, R_{90}) though the trend is weakest with semi-major axis. A similar scatter is seen with luminosity which is as expected. For the lowest absolute magnitude bin, spirals are larger than ellipticals whereas in the highest luminosity bins ellipticals are as large as spirals. Thus S0 galaxies could be considered the 'missing link' between ellipticals and spirals for low mass, low luminosity objects but not for high mass, high luminosity galaxies.

Figure 4.4 also shows there is no obvious dependence of the scatter in the size-T-Type relation to color for classical spirals though for ellipticals, the bluest galaxies are smaller than the reddest elliptical galaxies. A similar trend is observed for surface mass density. It is interesting to realize that while mass and luminosity explain much of the scatter in the size vs T-Type relation in a similar way, mass/area and luminosity/area show very different behavior.

There is no significant dependence on mass-to-light ratio or the age of the galaxy though larger galaxies at all T-Types have slightly higher mass-to-light ratios and are slightly older. The scatter seen with respect to total star formation rate mirrors that seen with mass. This is emphasized by noting there is no dependence of the scatter on star formation rate per unit mass. Thus the largest objects tend to be more massive, slightly older and have lower total star-formation rates and the size of a galaxy depends on both its T-Type and mass. We will study the size-mass relationship in the next chapter.

4.3.2 Correlation between mass and T-Type

Figure 4.5 shows another projection in our bivariate analysis. This figure shows the scatter in the mass vs. T-Type relation. Mass is correlated most strongly with size, luminosity and surface mass density. For any size or luminosity bin there is very little variation of mass with T-Type earlier than 5. However moving from classical spiral to late type galaxies, or from bulge dominated to no bulge systems, the stellar mass of galaxies drops off steeply with T-Type because there are no massive late type galaxies. There are strong correlations with surface brightness, mass-to-light ratio, age and the total star formation rate. There is only a slight dependence on the color of the galaxy for classical spirals (Sa-Sc) but a stronger dependence on early type galaxies such that the highest mass galaxies are redder. It is interesting to note that for the bluest color bin (corresponding to the blue cloud) E and S0 galaxies are less massive than classical spiral galaxies but more massive than late type disks. In general, the highest mass objects across all T-Types have larger petrosian radii, are older and have the lowest total star-formation rates. This can be seen as a natural result of the downsizing scenario where massive objects formed first. For a given absolute magnitude, size, or total star formation rate,

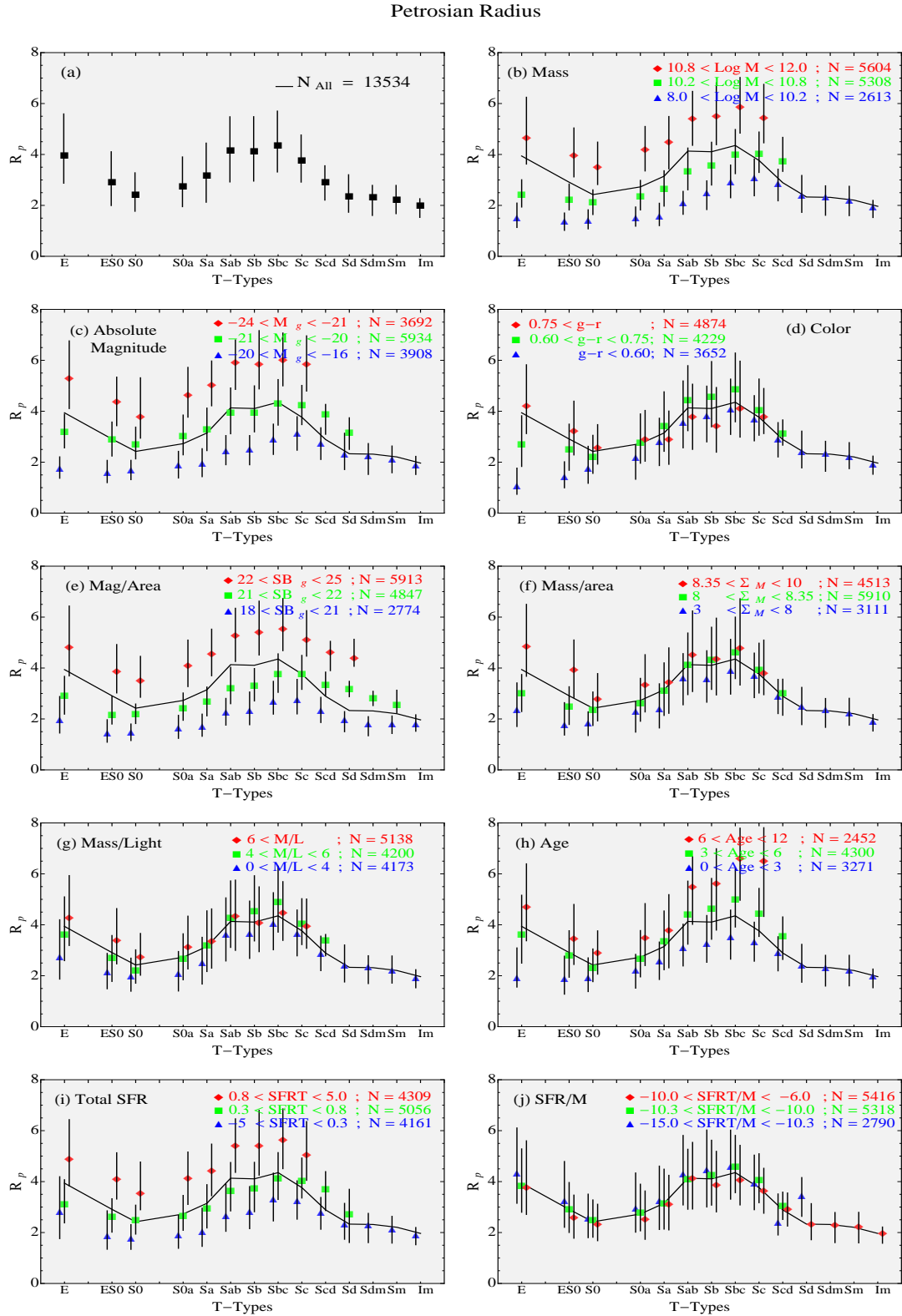


Figure 4.4: Each panel shows Size versus T-Type keyed to bins of (a) R_p 90 (b) mass, (c) g-band absolute magnitude, (d) g-r color, (e) surface brightness, (f) surface mass density, (g) stellar Mass-to-Light ratio, (h) Age of the galaxy (i) total star formation rate SFRT, and (j) star formation rate per unit mass SFRT/M.

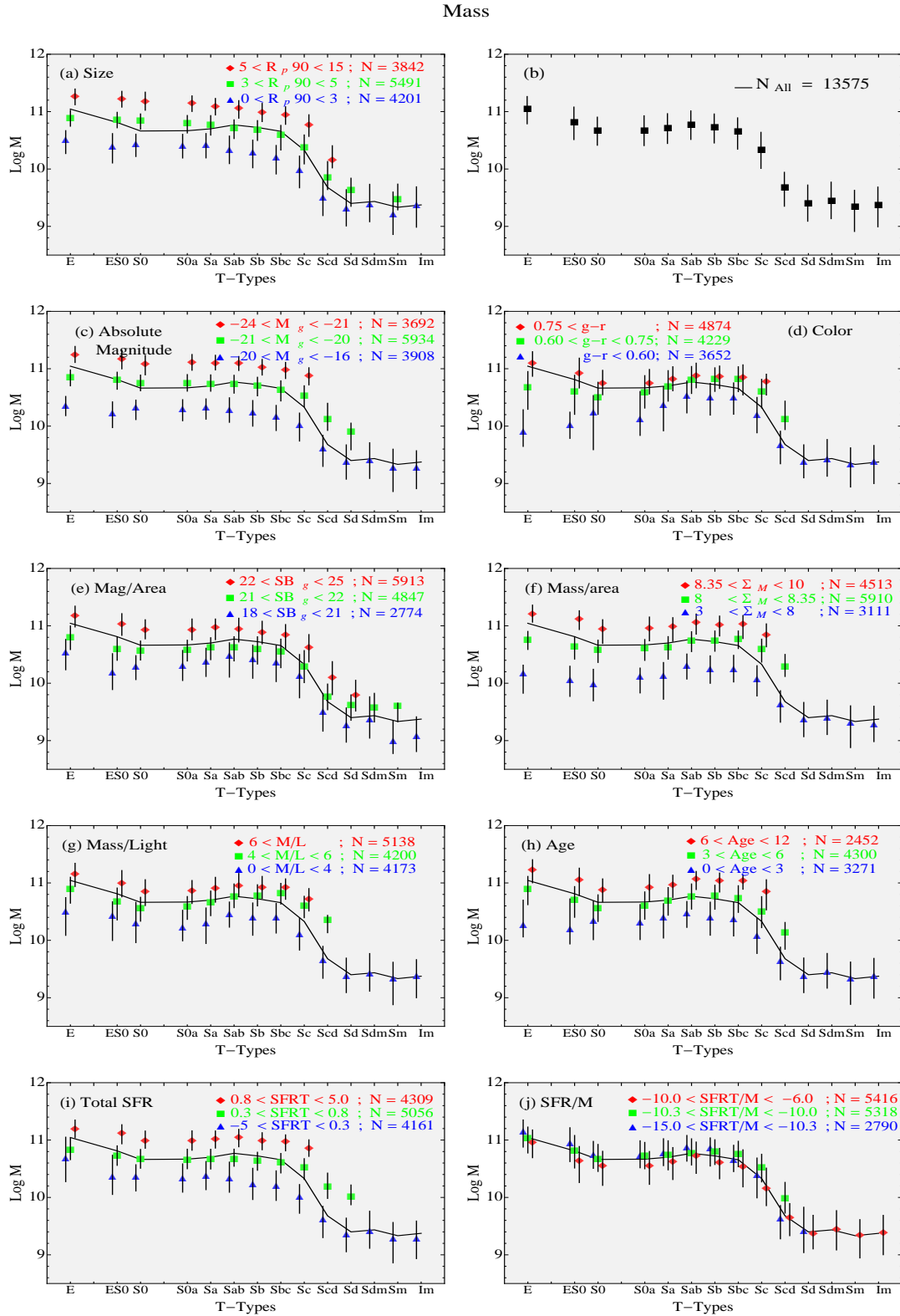


Figure 4.5: Each panel shows Mass versus T-Type keyed to bins of (a) $R_p 90$ (b) mass, (c) g-band absolute magnitude, (d) g-r color, (e) surface brightness, (f) surface mass density, (g) stellar Mass-to-Light ratio, (h) Age of the galaxy (i) total star formation rate SFRT, and (j) star formation rate per unit mass SFRT/M.

Absolute Magnitude

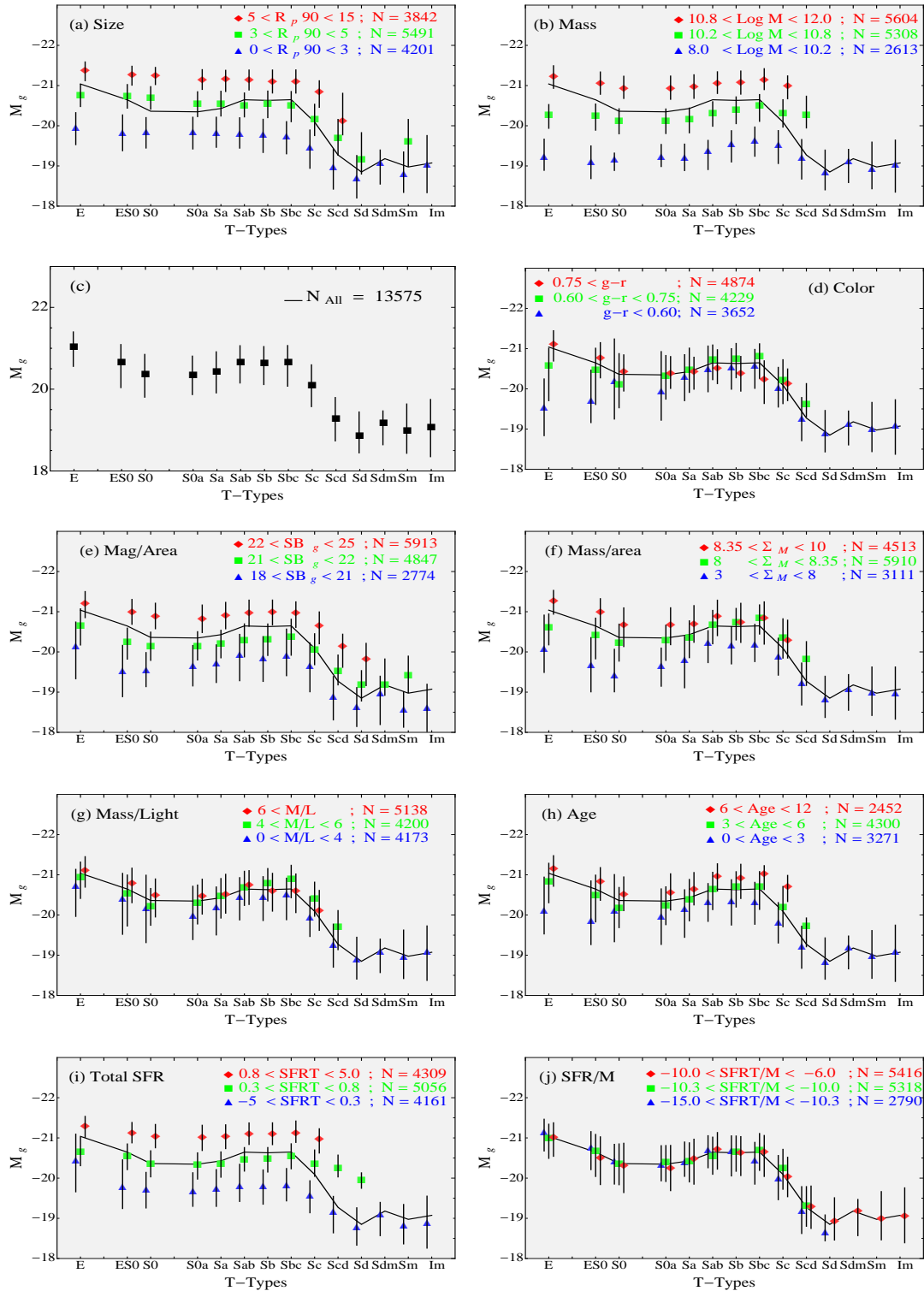


Figure 4.6: Each panel shows g-band Absolute Magnitude versus T-Type keyed to bins of (a) $R_p 90$ (b) mass, (c) g-band absolute magnitude, (d) $g-r$ color, (e) surface brightness, (f) surface mass density, (g) stellar Mass-to-Light ratio, (h) Age of the galaxy (i) total star formation rate SFRT, and (j) star formation rate per unit mass SFRT/M.

Color

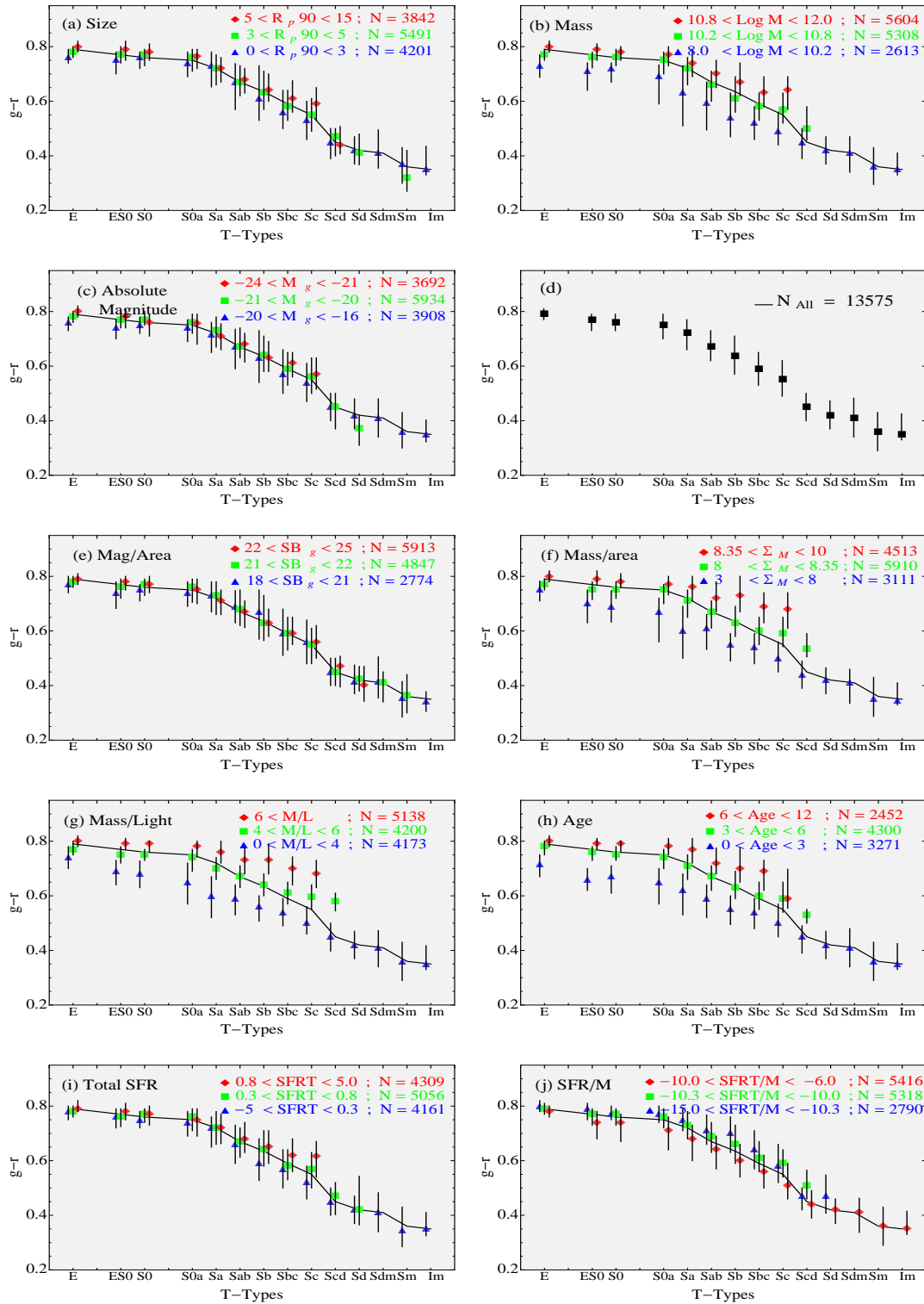


Figure 4.7: Each panel shows $g-r$ color versus T-Type keyed to bins of (a) $R_p 90$ (b) mass, (c) g -band absolute magnitude, (d) $g-r$ color, (e) surface brightness, (f) surface mass density, (g) stellar Mass-to-Light ratio, (h) Age of the galaxy (i) total star formation rate SFRT, and (j) star formation rate per unit mass SFRT/M.

the median absolute magnitude appears to be only weakly dependent on morphology for $T < 5$ or Sc galaxies. We will investigate this further in the next chapter. Thus 'current mass' appears to be one of the fundamental parameters determining galaxy properties.

4.3.3 Correlation between luminosity and T-Type

Figure 4.6 shows how the scatter in the absolute magnitude versus T-Type plane. Again we find the scatter in the relation is predominantly due to the mass and size of the galaxy and their related parameters. There is little dependence of magnitude on morphology for T-Types less than 5 for a given mass or size bin. As mass or size decreases, the average luminosity of the galaxy decreases. Again the color of the galaxy only influences early types, where the bluest elliptical galaxies are also the faintest. Mass-to-light ratio and age show weak trends where the youngest and lowest M/L objects at each T-Type are slightly fainter. There is no dependence on the star formation rate per unit mass. Thus for a given mass, size, or total star formation rate, the median absolute magnitude is only weakly dependent on morphology for $T < 5$ or Sc galaxies.

4.3.4 Correlation between color and T-Type

Figure 4.7 shows the scatter in the color vs T-Type plane as a function of different properties. There is no dependence of the scatter in the color of a galaxy at a given T-Type on the size, luminosity, surface brightness, total star formation rate or star formation rate per unit mass. As an example, a galaxy can have either a high star formation rate (total or per unit mass) or a low star formation rate but what determines its color is its morphology. The scatter is weakly dependent on the mass, surface mass densities, mass-to-light ratio and age of a galaxy. For the most massive galaxies and objects with the largest mass-to-light ratios, the slope of the color vs T-Type relation is less steep than the averaged relation showed by the black line implying a weaker dependence of color on the T-Type of an object. There are spiral galaxies nearly as red as ellipticals because they have higher surface mass densities or mass-to-light ratios. Since $g - r \sim 0.55$ is the transition between the blue cloud and the red sequence, it implies spiral galaxies on the red sequence have mass-to-light ratios 1.5 times or larger compared to galaxies in the field and have larger surface mass densities. Overall we find that the reddest objects have higher masses, higher mass-to-light ratios and are older. Environment and metallicities will be playing a more important role in these systems which we cannot properly address in the current work.

4.3.5 Correlation between surface brightness and T-Type

Figure 4.8 shows the scatter in the surface brightness vs. T-Type relation is predominantly due to the scale of a galaxy, mass, size and luminosity. There is very little variation in the surface brightness of a galaxy with star formation rate per unit mass or surface mass density or color.

4.3.6 Correlation between surface mass density and T-Type

Figure 4.9 shows the scatter in the relation is dependent on the mass, color, mass-to-light ratio and age of the galaxy. There is a very weak dependence on the luminosity of the galaxy where the brightest objects have slightly larger surface mass densities. There is very little dependence of the scatter in the surface mass density (SMD) vs T-Type relation with mass for $T < 5$ in the highest mass bins. In the lowest mass bin, there is a gradual dependence of SMD with T-Type where late type galaxies have low surface (stellar) mass densities. The reddest and oldest objects have the highest surface mass densities and the bluest/younger objects have lower SMDs. There is little to no dependence of the surface mass density of the galaxies with size, surface brightness or SFR/M across all T-Types.

4.3.7 Correlation between mass-to-light ratio and T-Type

Figure 4.10 shows the scatter in the relationship between mass-to-light ratios and T-Type depends on the mass, color, SMD, and age of the galaxy. It is important to note that if we consider face on systems only, the dependence of mass-to-light ratio with T-Type of the reddest bin does not depend on T-Type, or rather M/L does not increase with T-Type but is flat. From §4.2, we have seen there is no difference in the estimate of mass with different inclination cuts. Thus the errors (if that) must arise from the estimate of the luminosities and dust corrections. However it should be noted that no other trends change when using a face on sample and the inclination dependence of luminosity with T-Type is fairly small and in no way accounts for the scatter in the relation.

When split into mass bins, M/L for the intermediate and high mass bins are nearly constant for $T < 2$ above which they decline slowly with T-Type. However for the lowest mass bin, the later T-types have a much lower M/L and there is an overall trend of decreasing M/L with T-Type. The scatter in M/L can also be accounted for by variation in surface mass densities. The scatter in M/L does not depend significantly in surface brightness, star formation rate or star formation rate per unit mass. Thus over, high mass-to-light galaxies are older, redder, more massive and have a higher surface mass density.

Physical Surface Brightness

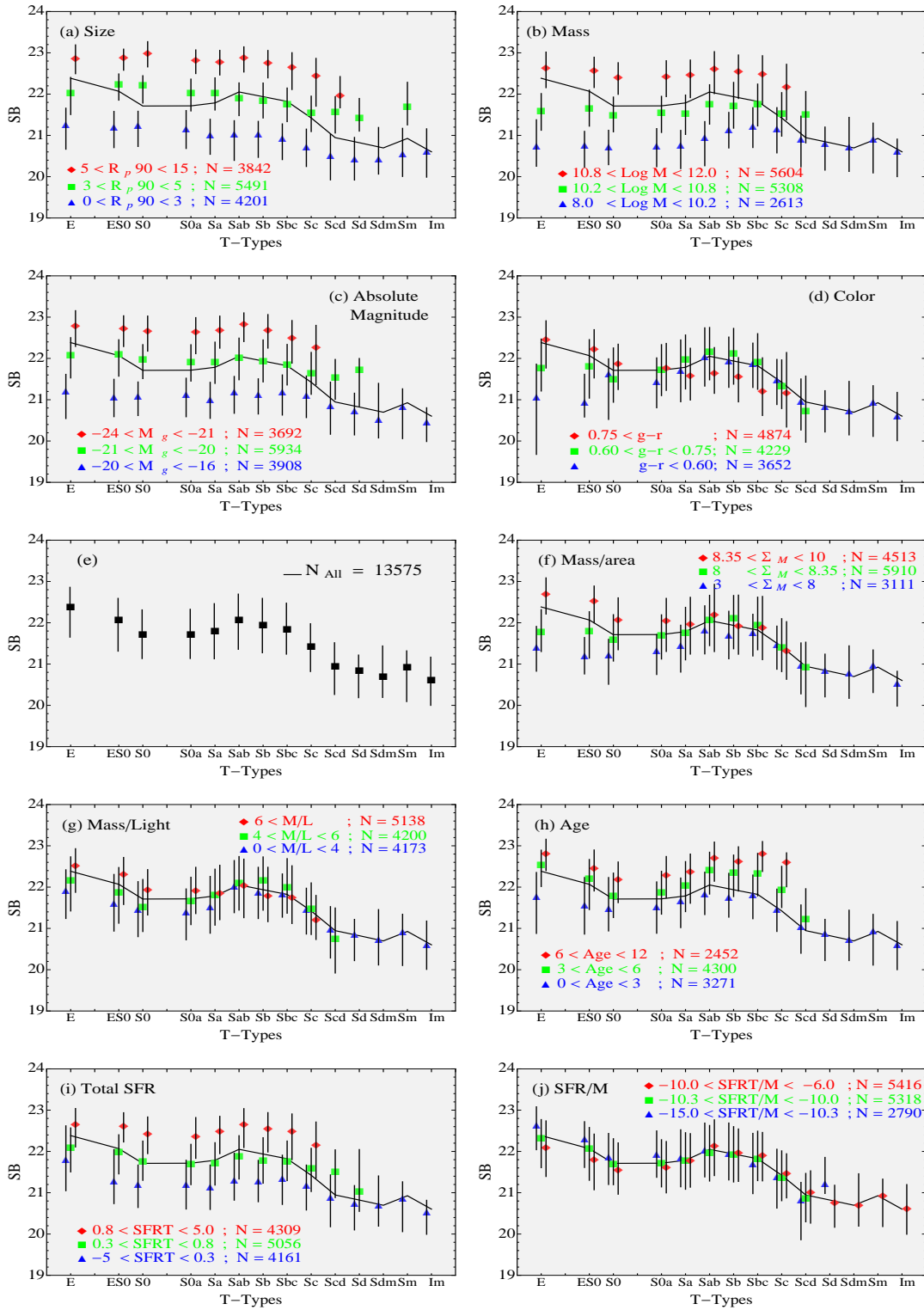


Figure 4.8: Each panel shows Surface Brightness versus T-Type keyed to bins of (a) $R_p 90$ (b) mass, (c) g-band absolute magnitude, (d) g-r color, (e) surface brightness, (f) surface mass density, (g) stellar Mass-to-Light ratio, (h) Age of the galaxy (i) total star formation rate SFRT, and (j) star formation rate per unit mass SFRT/M.

Surface Mass Density

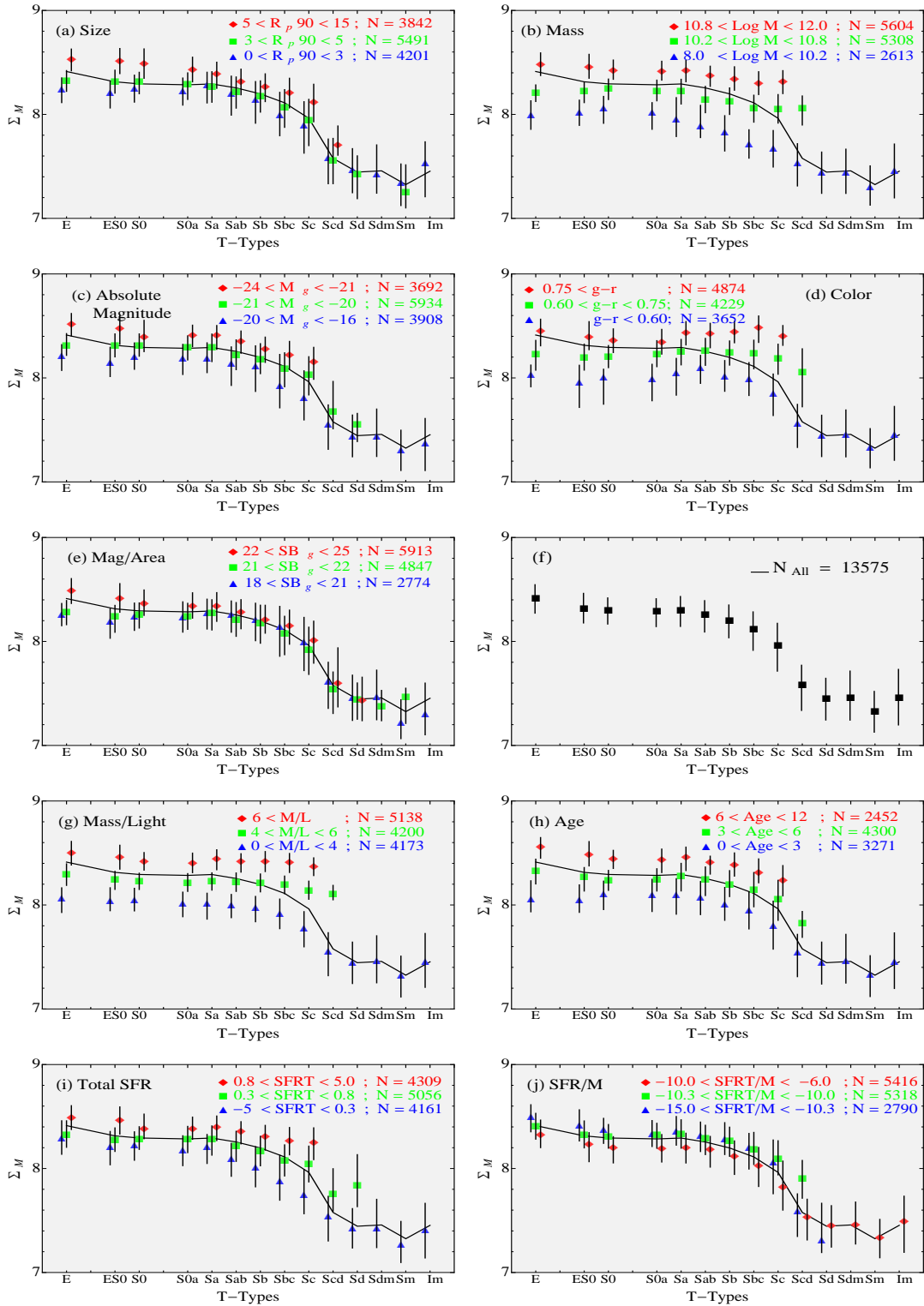


Figure 4.9: Each panel shows Surface Mass Density versus T-Type keyed to bins of (a) $R_p 90$ (b) mass, (c) g-band absolute magnitude, (d) g-r color, (e) surface brightness, (f) surface mass density, (g) stellar Mass-to-Light ratio, (h) Age of the galaxy (i) total star formation rate SFRT, and (j) star formation rate per unit mass SFRT/M.

Mass-to-Light Ratio

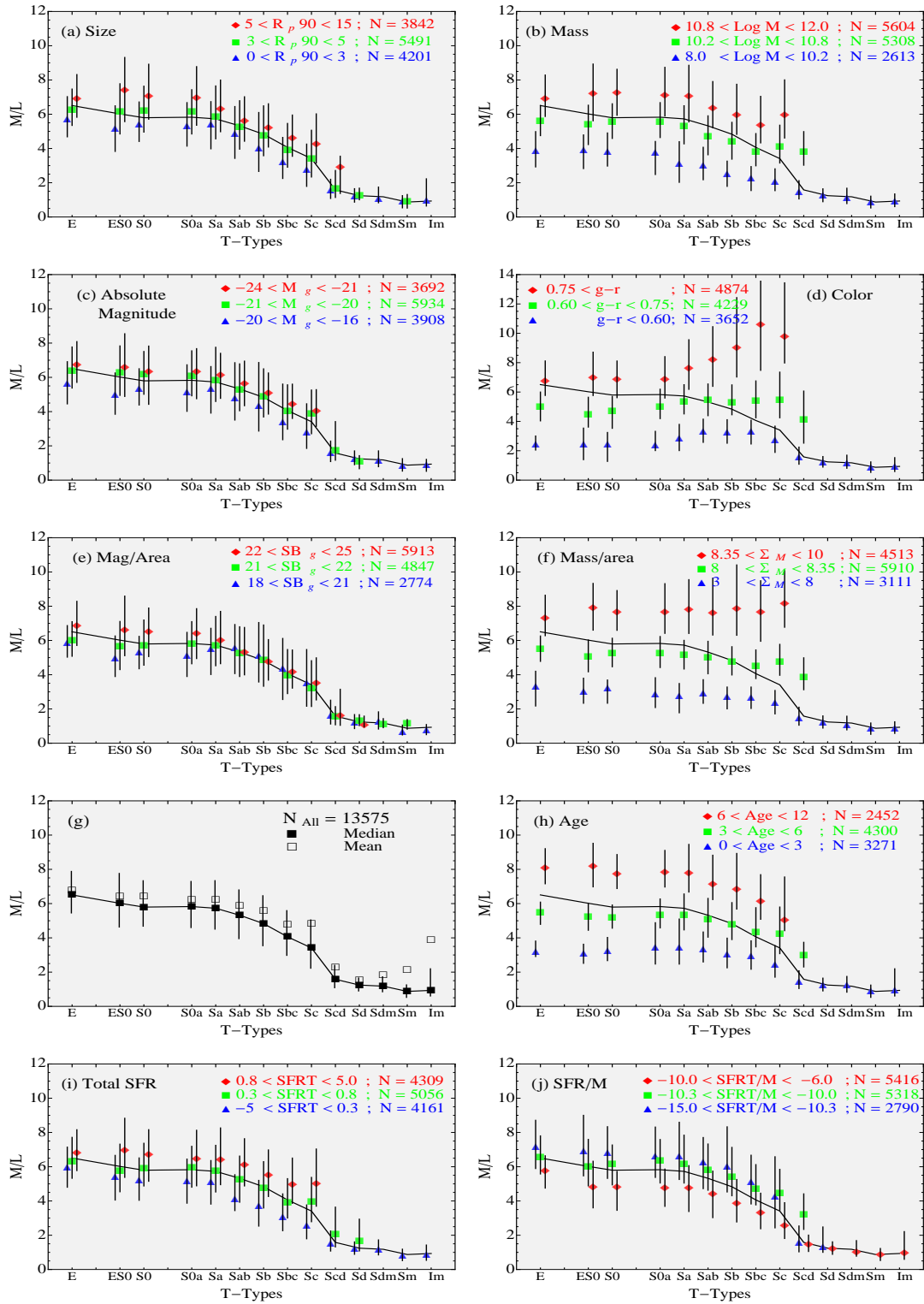


Figure 4.10: (a) The first panel shows absolute magnitude vs T-Type for the entire sample. Every other panel shows absolute magnitude versus T-Type keyed to bins of (b) $R_p 90$ (c) g-band absolute magnitude, (d) g-r color (e) total star formation rate SFRT, (f) star formation rate per unit mass SFRT/M, (g) Mass-to-Light ratio and (h) Age of the galaxy.

4.3.8 Summary

The scatter in the relation of physical properties with T-Types is complex in many cases. There are dependencies between physical properties and understanding which is most important is difficult, for example the color of a galaxy is more important in early type galaxies with respect to luminosity. It is clear that the relations are not necessarily monotonic but we can identify which relations are not from the plots. We can thus use a spearman correlation matrix to compare results between different parameters. We first investigate the correlations between T-Type and quantitative morphological parameters.

4.4 Variation in Galaxy Properties with Quantitative Morphology

So far we have only looked at the variation of physical properties with T-Type. In this section we consider how well the morphological quantities we introduced in Chapter 3 correlate with T-Types and the dependence of the scatter on other physical properties.

From Fig 4.11 and Fig 4.12, Concentration and Gini both show strong correlations with T-Type with both decreasing from early types to late types. Concentration flattens out past a T-Type of 6 whereas Gini shows an increase in median values. This is because Gini is sensitive to inequality in flux distribution and the later T-Types are more asymmetric in their flux distribution. Concentration shows little or no dependence on size, mass, luminosity or SFRs. In other words, a more concentrated object isn't more massive, or older or larger. But a more concentrated object is likely to be an early type. There is a slight dependence of concentration on color where redder galaxies are slightly more concentrated. Gini shows similar trends as concentration. Concentration values of $C > 0.4$ and $G > 0.5$ should isolate early type galaxies.

Fig 4.13 shows asymmetry gradually increases with T-Type. When split into three mass bins little or no dependence on mass is seen on the median values. The same applies to variations with size and SFRs. There is a slight variation seen with age where the most asymmetric objects are slightly younger. This is especially valid for later T-Types. Overall, the scatter in the relation cannot be accounted for by any physical property currently studied.

M20 in Fig 4.14 also shows a pronounced trend with T-Type though its value is nearly constant for E-type systems up to S0a and then gradually increases until T=6. After that M20 again decreases though the trend is very small and consistent with constant given the error bars. The scatter in M20 is dependent on the color of a galaxy such that the redder the galaxy, the smaller M20 will be. This has been seen by other groups (Zamojski et al. 2007). The scatter is also slightly correlated with mass, age and mass-to-light ratio. At every T-Type, the galaxies with higher M20 values are slightly bluer, less massive, younger, with lower mass-to-light ratio.

Concentration

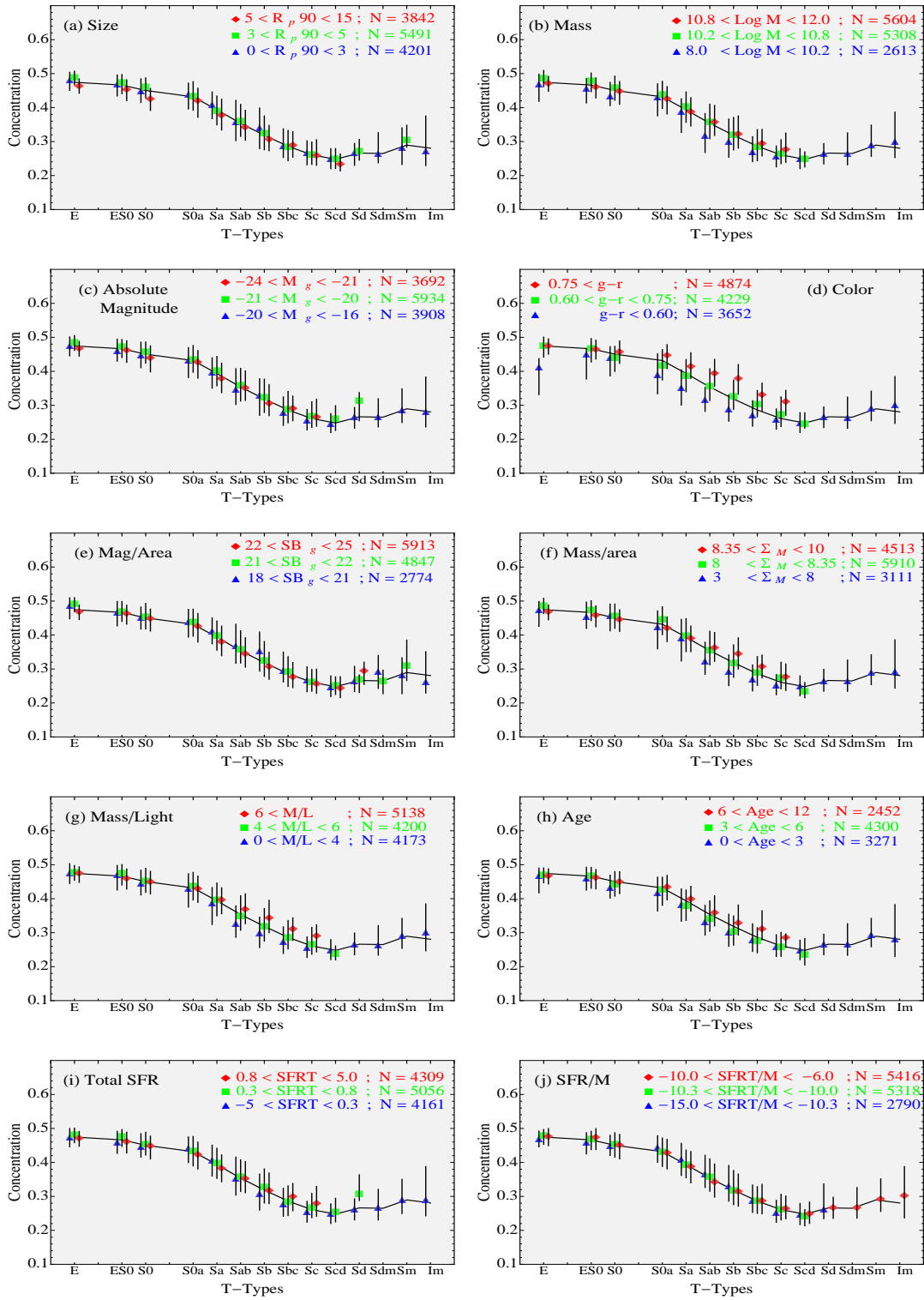


Figure 4.11: Each panel shows Concentration versus T-Type keyed to bins of (a) $R_p 90$ (b) mass, (c) g-band absolute magnitude, (d) g-r color, (e) surface brightness, (f) surface mass density, (g) stellar Mass-to-Light ratio, (h) Age of the galaxy (i) total star formation rate SFRT, and (j) star formation rate per unit mass SFRT/M.

Gini

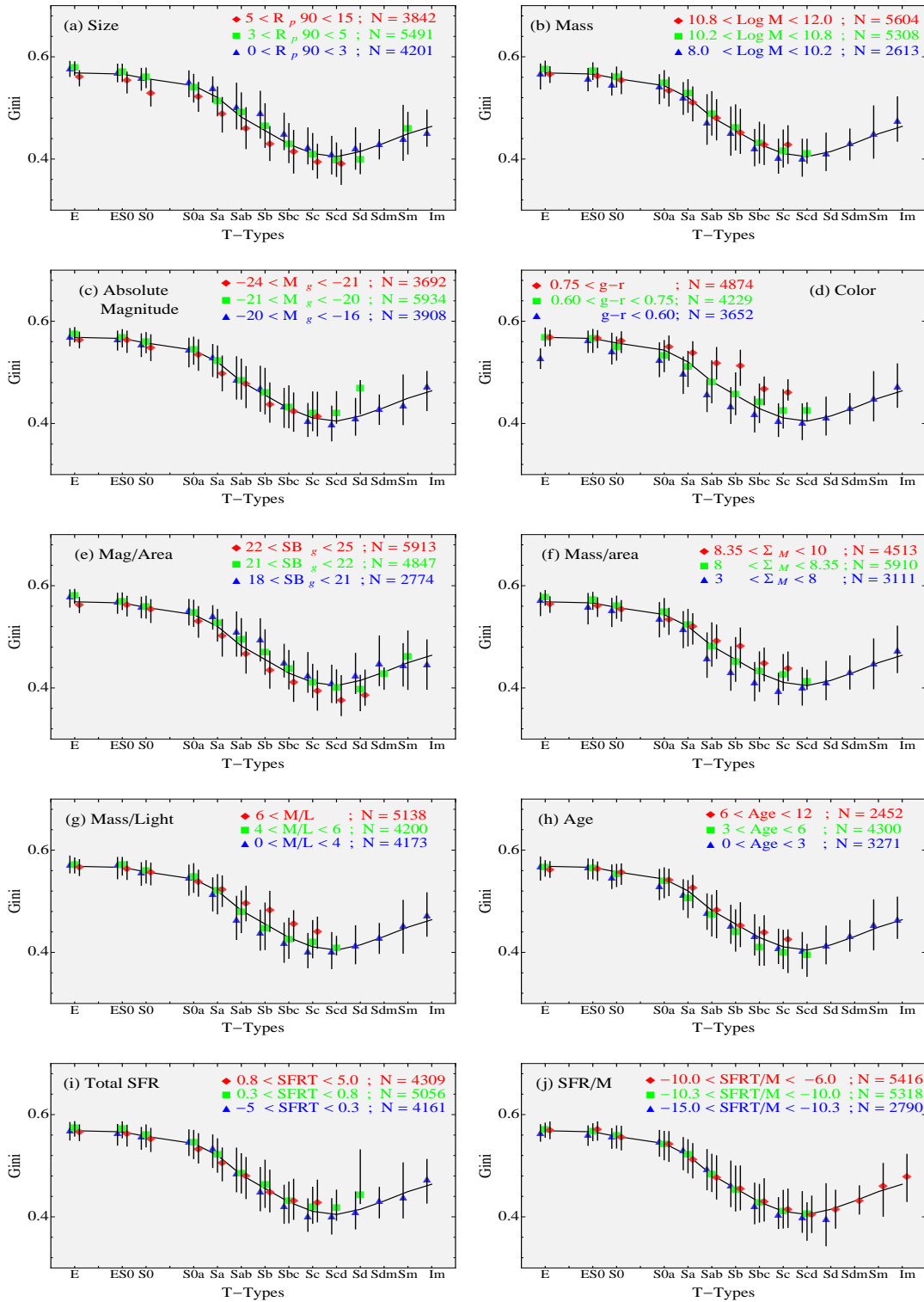


Figure 4.12: Each panel shows Gini versus T-Type keyed to bins of (a) $R_p 90$ (b) mass, (c) g-band absolute magnitude, (d) g-r color, (e) surface brightness, (f) surface mass density, (g) stellar Mass-to-Light ratio, (h) Age of the galaxy (i) total star formation rate SFRT, and (j) star formation rate per unit mass SFRT/M.

Rotational Asymmetry

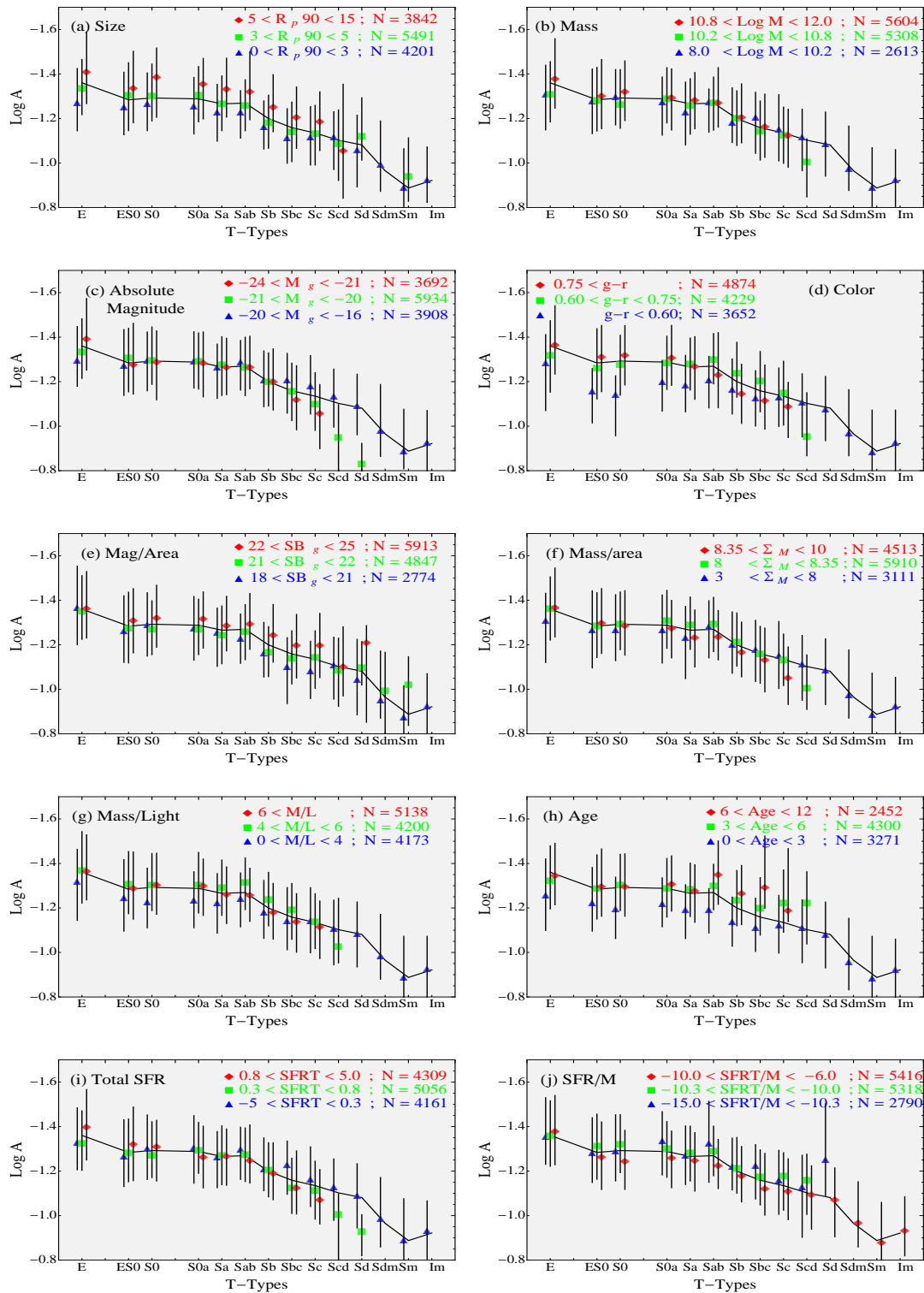


Figure 4.13: Each panel shows Asymmetry versus T-Type keyed to bins of (a) $R_p 90$ (b) mass, (c) g-band absolute magnitude, (d) g-r color, (e) surface brightness, (f) surface mass density, (g) stellar Mass-to-Light ratio, (h) Age of the galaxy (i) total star formation rate SFRT, and (j) star formation rate per unit mass SFRT/M.

M20

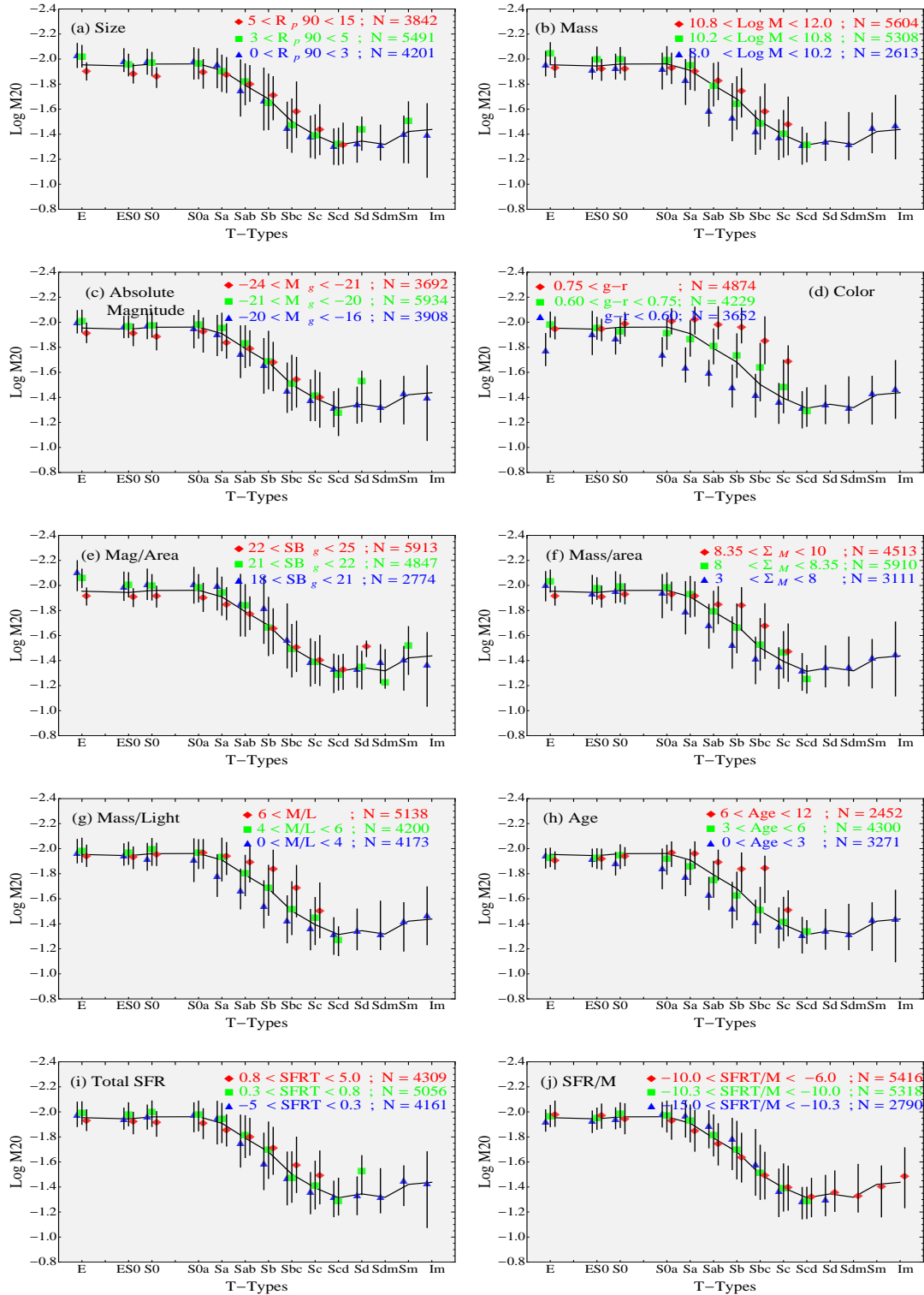


Figure 4.14: Each panel shows $M20$ versus T-Type keyed to bins of (a) $R_p 90$ (b) mass, (c) g-band absolute magnitude, (d) g-r color, (e) surface brightness, (f) surface mass density, (g) stellar Mass-to-Light ratio, (h) Age of the galaxy (i) total star formation rate SFRT, and (i) star formation rate per unit mass SFRT/M.

Table 4.4. Spearman correlation matrix

Family	T-Type	Size	Mass	g-r	M_g	M/L	SB	SMD	SFRT	SFR/M	Asy	Conc	Gini	M20
T-Type	1.00	-0.21	-0.50	-0.82	0.30	-0.64	-0.19	-0.63	-0.26	0.37	0.36	-0.71	-0.67	0.64
Size	-0.21	1.00	0.79	0.36	-0.81	0.50	0.80	0.48	0.61	-0.21	-0.27	-0.18	-0.30	0.03
Mass	-0.50	0.79	1.00	0.64	-0.87	0.81	0.67	0.87	0.71	-0.38	-0.27	0.21	0.13	-0.23
g-r	-0.82	0.36	0.64	1.00	-0.35	0.83	0.29	0.75	0.31	-0.49	-0.42	0.6	0.54	-0.62
M_g	0.30	-0.81	-0.87	-0.35	1.00	-0.45	-0.67	-0.60	-0.72	0.18	0.10	-0.06	0.00	0.05
M/L	-0.64	0.50	0.81	0.83	-0.45	1.00	0.43	0.91	0.45	-0.52	-0.37	0.37	0.30	-0.41
SB	-0.19	0.81	0.67	0.29	-0.67	0.43	1.00	0.42	0.51	-0.19	-0.19	-0.12	-0.20	0.12
SMD	-0.63	0.48	0.87	0.75	-0.60	0.91	0.42	1.00	0.54	-0.46	-0.25	0.41	0.38	-0.34
SFRT	-0.26	0.61	0.71	0.31	-0.72	0.45	0.51	0.54	1.00	0.27	-0.09	0.08	0.03	-0.09
SFR/M	0.37	-0.21	-0.38	-0.49	0.18	-0.52	-0.19	-0.46	0.27	1.00	0.26	-0.24	-0.20	0.26
Asy	0.36	-0.27	-0.27	-0.42	0.10	-0.37	-0.19	-0.25	-0.09	0.26	1.00	-0.19	-0.07	0.27
Conc	-0.71	-0.18	0.21	0.60	-0.06	0.37	-0.12	0.41	0.08	-0.24	-0.19	1.00	0.95	-0.79
Gini	-0.67	-0.30	0.13	0.54	0.00	0.30	-0.20	0.38	0.03	-0.20	-0.07	0.95	1.00	-0.70
M20	0.64	0.03	-0.23	-0.62	0.05	-0.401	0.12	-0.34	-0.09	0.26	0.27	-0.79	-0.70	1.00

Overall the quantitative morphological parameters studied here are strongly keyed to T-Type with little or no dependence on a second parameter, though it is interesting to note that color is the property that seems to induce the worse scatter. The quantitative parameters can only be used to broadly separate early types from classical spirals and dwarf galaxies.

4.5 Bivariate Statistical Analysis

Although the relationship between T-Type and physical and quantitative morphological properties studied here may not be monotonic, the relationship between parameters like size and mass do appear to be monotonic. Table 4.4 shows the spearman rank correlations between various properties including the quantitative morphological parameters. Again we see the strongest correlations are between mass and nearly every other physical property. van den Bergh (2008) has suggested that ‘reconciling the conclusion that galaxies are essentially a one parameter family defined by their initial mass is challenging in the context of hierarchical merging scenario’. This in fact may not be the case as it appears galaxy properties depend on their final mass. Merging may lead to the quick build up of galaxies and may account for some variation seen within T-Types but it may bode well that the wide variety of galaxy interactions does not, to first order, influence overall properties. However, mass does not correlate with any of the quantitative morphological parameters. We find the concentration, gini and M20 of a galaxy strongly correlates with T-Type, color and each other (Abraham et al. 2003; Zamojski et al. 2007; Lotz et al. 2004). Asymmetry does not correlate with any galaxy property. CO06 does find that asymmetry correlates with disturbed morphologies. Any object which could not be assigned to a regular T-Type from -5 to 12 was assigned to T-Type 99, for

example collisional rings, and are hence excluded from the current analysis. We have very few objects (<200) classified as 99 and hence this should not affect our overall results. However asymmetry is expected to correlate strongly with some of these disturbed systems.

4.6 Summary

Thus we find many of the trends observed with T-Type are due to variations in the relationship of mass with other physical properties or rather mass appears to be the defining characteristic of a galaxy (Disney et al. 2008; van den Bergh 2008). The break in most of the correlations occurs due to a lack of massive late type ($T > 5$) galaxies. Strong correlations are observed between size, luminosity, color and star formation rate with mass. Color is the quantity most strongly correlated to T-Type where the scatter does not depend on any other parameter with the exception of mass (and related quantities). S0 galaxies are smaller in size than either ellipticals or spirals but this may be a mass dependent effect because in the lowest mass bin S0 galaxies are the same size as ellipticals. Although there are a number of correlations we can study, we will restrict our investigation in this thesis to the relationship between size and mass in the next Chapter.

Chapter 5

Scaling Relations

5.1 Introduction

The size distribution of galaxies places important constraint on theories of galaxy formation and evolution. Recent studies using the Sloan Digital Sky Survey (SDSS; York et al. 2000) have found the galactic size-mass relationship to be dependent on morphology. Shen et al. (2003) and Kauffmann et al. (2003) showed that early type galaxies follow a steeper size-mass relation than late types. Particular interesting is the identification of a characteristic mass $\sim 10^{10.5-10.6} M_{\odot}$, where the size of late type galaxies shows a transition. Below this characteristic mass, where less concentrated disk systems dominate, $R \propto M^{0.18-0.15}$ whereas above it, in more concentrated bulge dominated systems the increase is more rapid with $R \propto M^{0.3-0.55}$. This break in the size mass relationship reflects the bimodality seen with mass (Kauffmann et al. 2003b), one of many parameters where the bimodal nature of galaxies has been observed for eg., the color-magnitude plane (Baldry et al. 2004a, 2006), concentration (Blanton et al. 2003; Kauffmann et al. 2003c), luminosity, surface brightness, stellar mass densities (Kauffmann et al. 2003c,b) and star formation rates (Brinchmann et al. 2004). The bimodality observed in these quantities are related but the outstanding question remains; what is the physical basis for the observed bimodality and which relation is more fundamental?

The problem is complicated and various underlying evolutionary mechanisms are probably involved like hierarchical merging (White & Rees 1978; Fall & Efstathiou 1980), gas infall (Blumenthal et al. 1986), secular evolution (Kormendy & Kennicutt 2004), AGN feedback as well as environmental effects like ram pressure stripping (Gunn & Gott 1972), harassment (Moore et al. 1996), minor mergers and cannibalism (Ostriker & Hausman 1977). Galaxy morphology and features such as bars, rings and lenses may also contribute to or obscure the nature of bimodality. With large data sets like the SDSS, where visual classification of the entire sample is not usually attempted, an important selection effect is introduced by the method

which isolates early or late type galaxies, specifically a concentration cut (Shen et al. 2003; Kauffmann et al. 2003b) or a color cut (Trujillo & Pohlen 2005). The effects of these simplistic cuts needs to be determined to better understand the nature of bimodality. In this chapter, we use the sample of ~ 14000 , visually classified bright galaxies from this thesis to investigate the size-mass relation in the local universe. To simplify this analysis, we select a clean sub-sample of 12670 objects with no projection effects by smaller satellites, foreground objects or nearby stars.

5.2 The Size-Mass relationship along the Hubble Sequence

Figure 5.1 shows the distributions of galaxy size vs. stellar mass in panels which segregate galaxies into different concentration ranges. The six panels subdivide the total distribution into six quantiles of concentration. The colors of symbols within each panel are keyed to T-Type using the same color scheme adopted in Figure 5.1. E and E/S0 galaxies are shown as black points, S0 and S0/a galaxies as orange points, Sa and Sab galaxies as yellow points, Sb and Sbc galaxies as light green points, Sc and Scd galaxies as dark green points, and galaxies with T-Types later than Sd as blue points. The concentration ranges which define the samples shown in the individual panels are shown at the top-left of each panel.

The first panel in Figure 5.1 shows the distribution in size vs. mass of galaxies in the top sixth quantile of concentration. As expected, this population is dominated by early-type galaxies, most of which are E and S0 systems, although there is some contamination by early-type spirals (systems classed as Sa and S0/a). It is interesting to see that the S0 galaxies do not subtend the full mass range of the sample. At a given concentration, the most massive objects are elliptical galaxies, and there are essentially no S0 galaxies more massive than $10^{11.2} M_{\odot}$. To 'guide the eye' a dark gray band on Figure 5.1 encompasses the region of the figure occupied by S0 systems, and this band is replicated on all remaining panels of the figure. The second panel in Figure 5.1 resembles the first though with a slightly larger scatter. Combining the first two panels to compare with the concentration cut used by Shen et al. (2003), we find a slope in the size-mass relation of 0.5 which is in excellent agreement with the canonical relationship (slope of 0.55) found by Shen et al. (2003).

The remaining panels in Figure 5.1 begin to isolate interesting trends as the concentration bins begin to encompass a richer variety of Hubble types. Inspection of the last two panels (systems with the lowest concentrations), shows that, over a broad range of concentration levels, spirals with Hubble types Sc and Sd (and later) exhibit a tight relation on the size-mass diagram. As expected, the very late-type spiral systems dominate the very low-mass ($< 10^{10} M_{\odot}$) population. These systems define the bulk of the objects in the late-type (i.e. low-

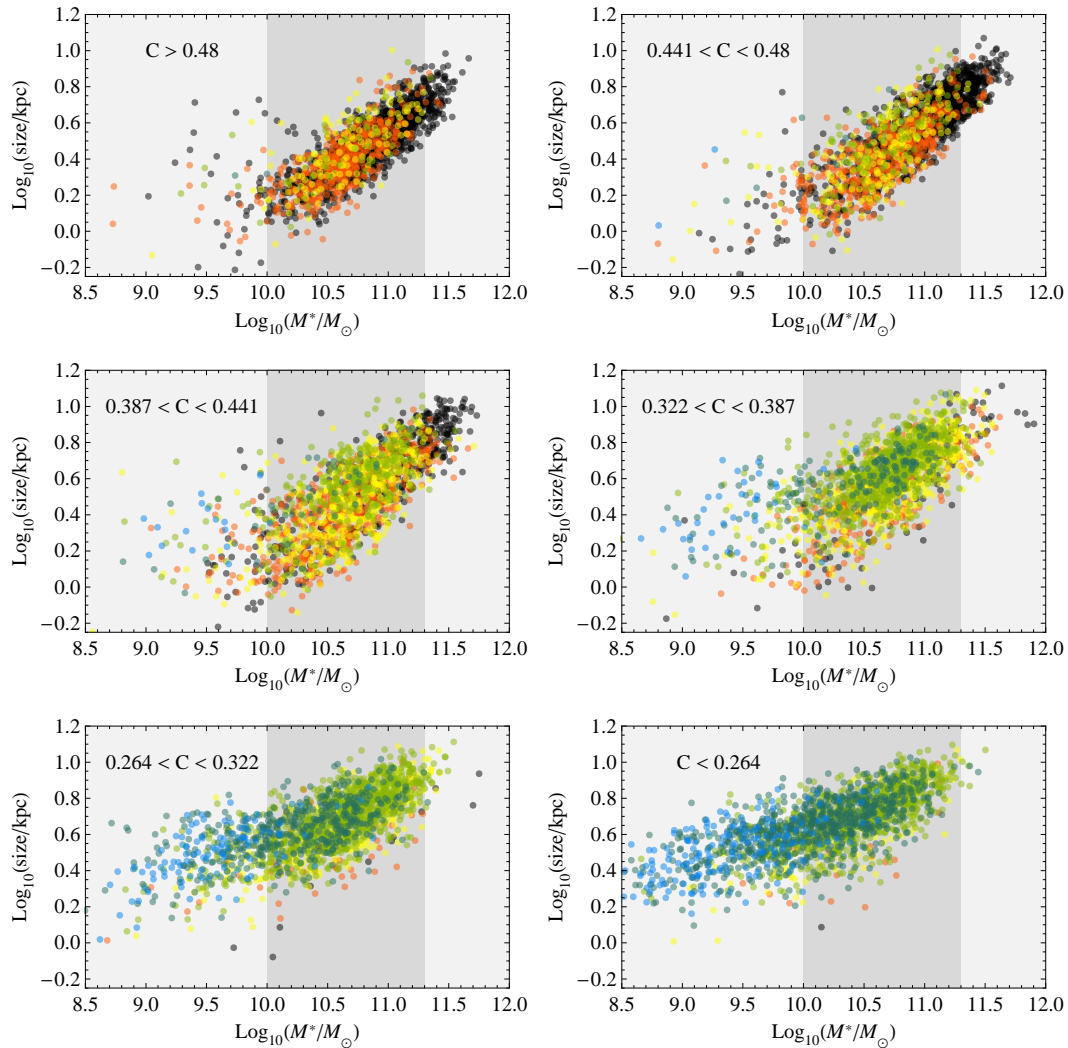


Figure 5.1: Distributions of galaxy size vs. stellar mass in panels which segregate galaxies into different concentration ranges. Each panel contains 1/6th of the total data. Symbol colors correspond to different T-Types, keyed according to the following color scheme: E and E/S0 galaxies (black points), S0 and S0/a galaxies (orange points), Sa and Sab galaxies (yellow points), Sb and Sbc galaxies (light green points), Sc and Scd galaxies (dark green points) and galaxies with T-Types later than Sd (blue points). A dark gray band on each panel denotes the region of this figure occupied by S0 galaxies.

concentration) component of Shen et al. (2003)'s analysis of the size-mass relation. The slope and normalization of the relation for these late-type spirals is in excellent agreement with that found by Shen et al (2003). The curvature in the relation for low-concentration systems found by Shen et al. (2003) led them to identify $10^{10.6} M_{\odot}$ as a characteristic mass beyond which the slope steepens. A similar effect is seen in Figure 5.1, but the origin of this effect now becomes clearer: the size-mass relation is very sensitive to the concentration of objects and this characteristic mass is simply the upper envelope of the mass distribution of the Sc and Sd

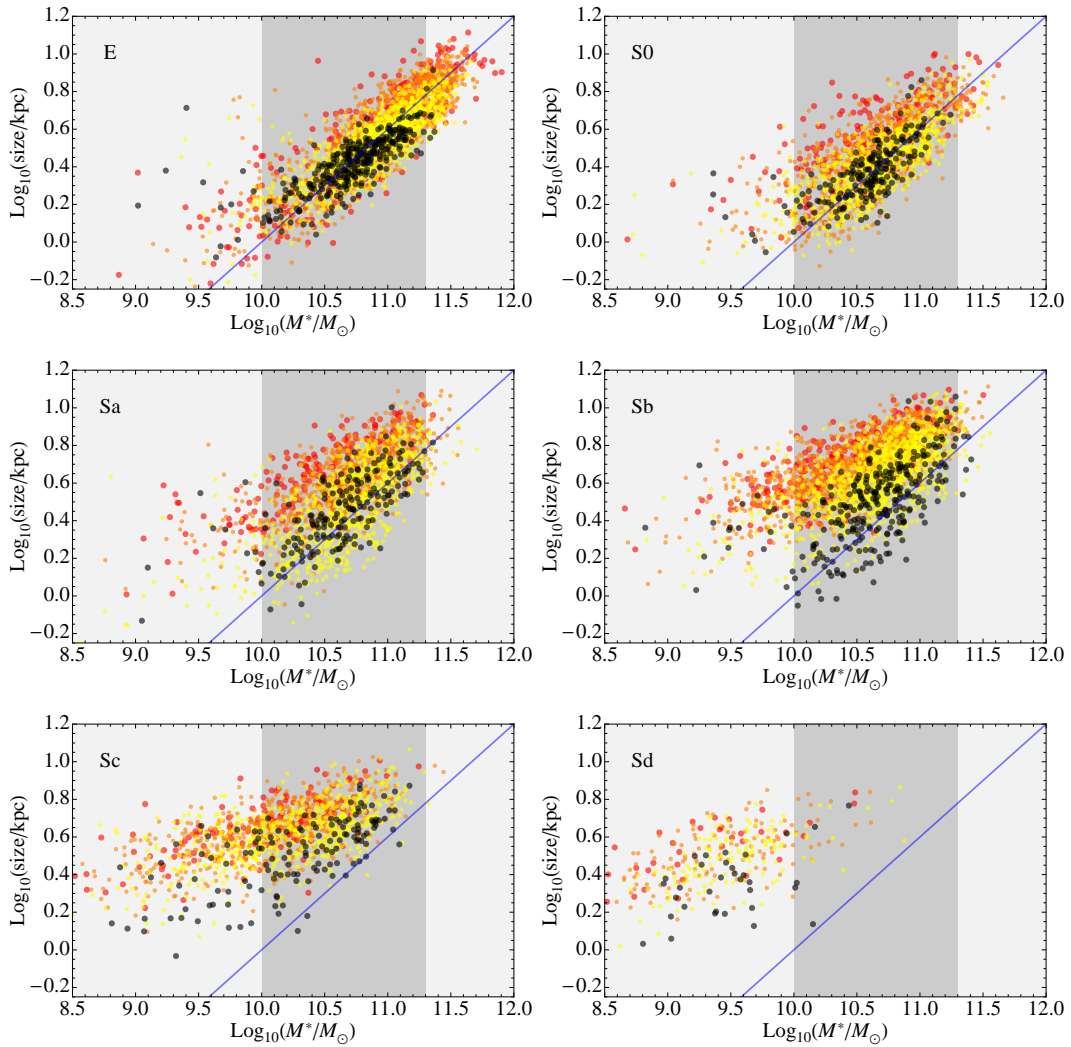


Figure 5.2: Distributions of galaxy size vs. stellar mass in panels which segregate the galaxies into different morphological types. Colors are keyed according to quantiles of the distributions in each panel. Black points correspond to the 10% most concentrated points, and red points to the 10% least concentrated. Yellow and Orange points comprise the central 80% of the distribution.

galaxies which increasingly dominate the galaxy population as the concentration decreases. Spirals more massive than this characteristic mass are the Sa and Sb systems which dominate the middle two panels and correspond to concentration values around the median of the histogram shown in Figure 3.22. Inspection of the middle two panels in Figure 5.1 shows that the distribution in size at a given mass for spirals of type Sa and Sb is broader than that which defines the relation for systems at lower and higher concentrations (dominated by the ellipticals and for the very late-type spirals). This is shown most clearly by comparing the fourth and sixth panels, in which we see that early-type spirals have nearly twice the dispersion about the size-mass relationship compared to late-type spirals.

5.2.1 The hidden connection between (some) elliptical and (some) spiral galaxies

It is interesting to consider whether the overlap in the properties of high concentration spirals and late-type ellipticals is telling us something fundamental about their nature. Figure 5.2 shows the size-mass relationship of our sample. Each panel in this figure corresponds to a single Hubble type. Within each panel most concentrated objects (top 10th percentile) are shown in black, and the least concentrated objects (bottom 10th percentile) are shown in red. As for Figure 5.1, a solid line delineates the size-mass relationship found for early-type galaxies, based on a fit to the top left-panel. This same fit is then replicated in all panels.

Most of the trends inferred from Figure 5.1 can also be noted in Figure 5.2, but a rather striking new trend now emerges more obviously. *The most concentrated spiral galaxies at each Hubble stage share a common size-mass relationship with elliptical galaxies.* This relationship remains true for Hubble stages out to at least type Sbc, before weakening strongly at type Sc, and then disappearing for later type spirals.

The structural connection between highly concentrated late-type spirals and weakly concentrated elliptical galaxies is a surprise, and hints at an evolutionary connection between these systems. The nature of this connection is shown more clearly in Figure 5.3. At the top of this figure we re-plot the size vs. mass distribution of Sb + Sbc galaxies but restrict our sample to only those objects in the bottom 10th percentile of concentration (in red) and top 10th percentile of concentration (in black). We emphasize that fully 80% of the Sb + Sbc galaxies in our sample are *not* shown. We have also only plotted those-objects whose axial ratios are greater than 0.5, in order to display their morphologies more clearly in the bottom two panels of the figure. These two panels show a montage of randomly-chosen galaxies from each of the high and low-concentration populations. The low-concentration objects are shown in the middle panel (bordered in red) and the high-concentration objects are shown in the bottom panel (bordered in black).

A number of interesting conclusions emerge from an inspection of Figure 5.3. Firstly, by

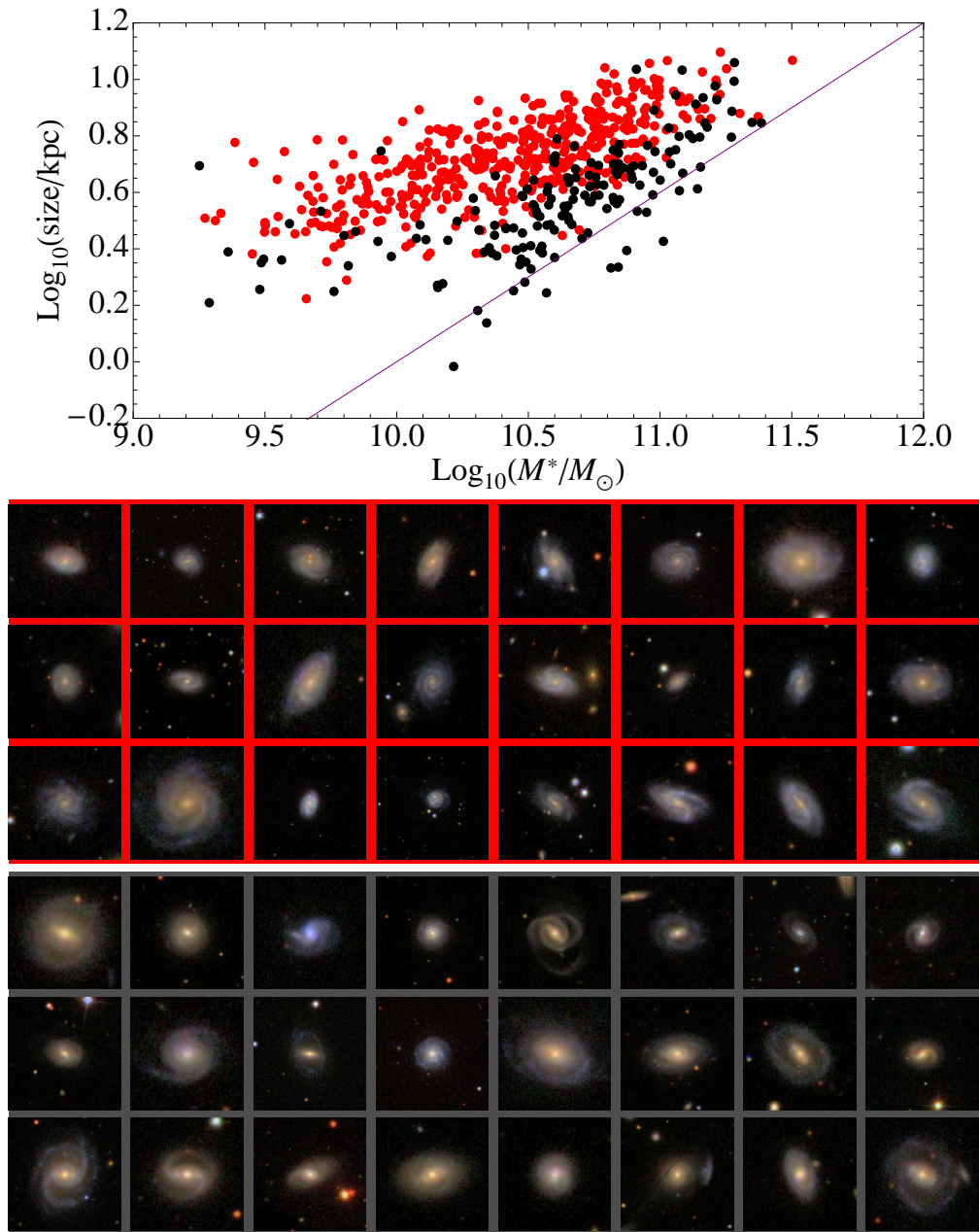


Figure 5.3: A comparison of the morphologies of Sb galaxy populations which lie on the top and bottom loci of the size-mass relationship. The top panel shows the size-mass distribution of all low-inclination (axial ratio > 0.5) Sb galaxies with $C < 0.25$ (shown in red) and $C > 0.41$ (shown in black). The lower two panels illustrate the morphologies of 24 randomly-chosen galaxies from each of these populations. Low-concentration galaxies are shown in the middle montage, and high-concentration galaxies in the bottom montage.

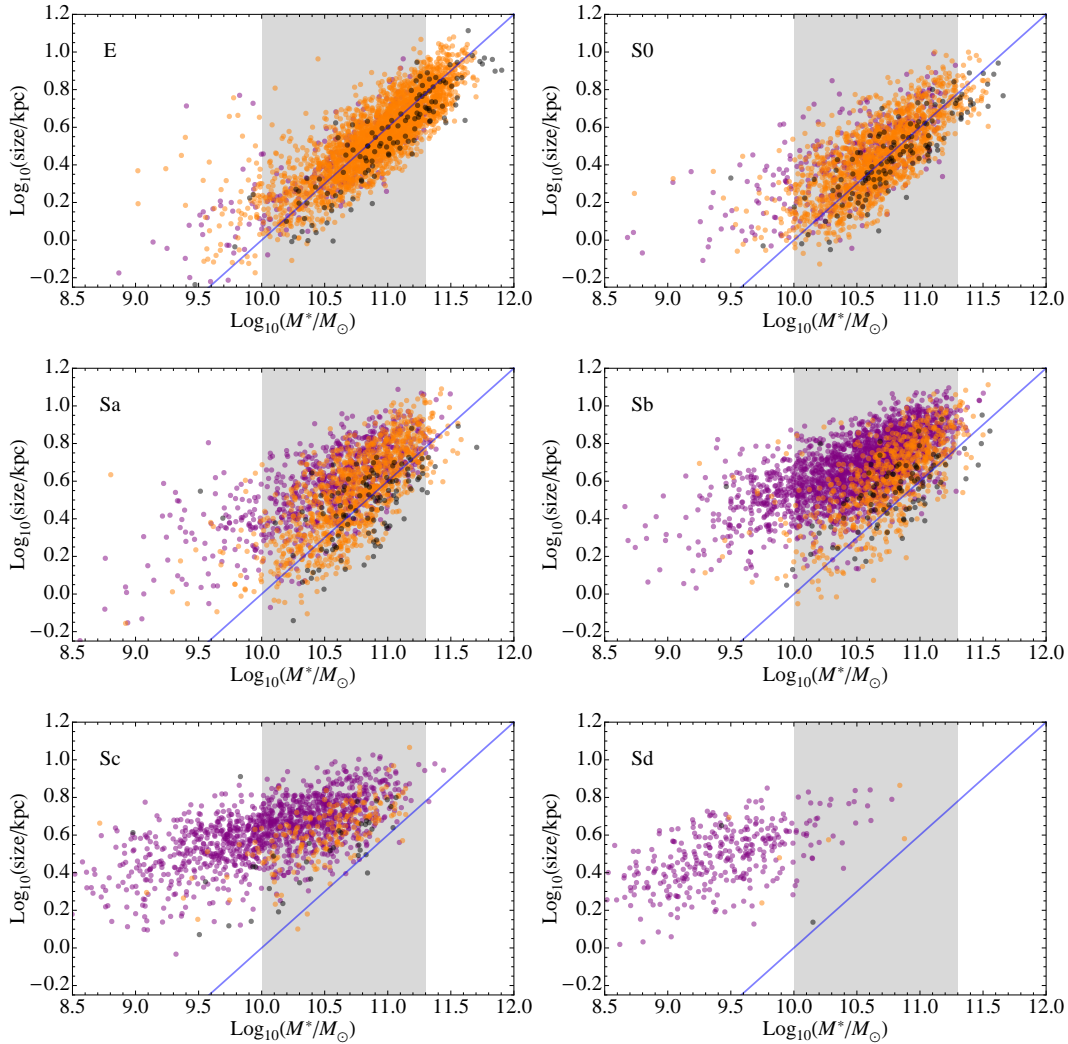


Figure 5.4: Distributions of galaxy size vs. stellar mass in panels which segregate the galaxies into different morphological types. Colors are keyed according to their position on the C-M diagram as defined by Baldry et al. 2004. Orange are galaxies defined to be in the red sequence. Purple are galaxies defined to be in the blue cloud. Black points are the most concentrated objects.

comparing this Figure with the corresponding Sb panel in Figure 5.1, it is clear that by eliminating the most highly-inclined systems we remove many objects which are under-sized for their mass. We attribute this simply to a numerical aperture effect introduced by the SDSS pipeline, which uses circular apertures to compute galaxy sizes even for highly inclined systems. By eliminating such highly-inclined systems we see that the size-mass relationship of highly-concentrated Sb + Sbc still has the same slope as that seen in the relationship for elliptical galaxies, but the distribution is now displaced so that a typical Sb spiral of a given mass is actually somewhat larger than an elliptical of the same mass. An inspection of the images in Figure 5.1 shows that (as expected) the main difference between the low and high

concentration Sb + Sbc galaxies is that the latter have larger bulge-to-disk ratios. A more subtle difference is that the high-concentration Sb systems appear to have a greater fraction of rings. Quantitatively 41% of the high concentration Sa+Sb galaxies have rings (inner + outer) in comparison to 24% in the lowest concentration bin. The Sb galaxies also appear to be at earlier stages in the luminosity classification system proposed by van den Bergh (1960a,b). This suggests that at a given stage in the Hubble sequence a galaxy's van den Bergh's luminosity classification might also be useful for distinguishing the subset of systems whose size-mass relationship has the slope defined by elliptical galaxies.

5.2.2 Implication for dichotomy among bulges

Figures 5.1 and 5.2 also make an important statement regarding the characteristic mass as defined by Kauffmann et al. (2003) and Shen et al. (2003). It seems that this is the mass at which the bimodal nature of galaxies is most clearly observed but may not physically motivated, i.e. objects of this characteristic mass are not transition galaxies between the two bimodal populations. In fact, galaxies above $\sim 10^{10} M_{\odot}$ display a bimodal nature in the size-mass plane. An important caveat is that we cannot say if this is a lower limit because our sample is magnitude-limited and we do not have very many low mass ($< 10^{10} M_{\odot}$) ellipticals or classical spirals.

We would expect the bimodal nature of the color-magnitude plane to be reflected in the size-mass plane. Figure 5.4 shows the size-mass relationship of our sample, keyed to position in the C-M diagram of Baldry et al. (2004b) so as to distinguish red galaxies from 'blue cloud' galaxies. Each panel corresponds to a single Hubble type. Even with the scatter, it can be seen that the red-sequence predominantly follows the steeper size-mass relation of concentrated objects, whereas the blue cloud has a shallower slope corresponding to the least concentrated objects. This implies that the shift from the blue cloud to the red sequence is in part due to increasing central concentration or B/T in galaxies. This conclusion is fairly consistent with a recent paper by Driver et al. (2006) which shows that objects with redder 'core' colors and more concentrated sersic profiles are predominantly in the red-sequence. It is interesting to consider this result in context of recent work by Drory & Fisher (2007). In a sample of 39 objects spanning T-Types from ellipticals to late types, they find visually identified pseudo-bulges predominantly lie in the blue cloud whereas classical bulges always lie on the red-sequence. The bulge type also predicts where the galaxies lie in other bimodal structural parameters; specifically global sersic index and the central surface brightness. Given the different evolutionary histories of these two types of bulges (major mergers vs. secular evolution), Drory & Fisher (2007) interpret the red-blue sequence transition as not due to changing B/T alone but also dependent on the evolutionary histories of the two populations.

Identifying psuedo-bulges vs. classical bulges in this sample is beyond the scope of this thesis but in light of this result, it is worthwhile to revisit the changing size-mass slopes in Figure 5.2. In all the classical spiral galaxies, there are two sequences. As we move up the Hubble Sequence from late types to early types, the distribution evolves from the blue cloud onto the size-mass relation for early types. If evolutionary histories are (partly) responsible for this transition, then the transition population should have undergone a significant merger event in the past, though not strong enough to push the galaxy onto the red-sequence. Thus the opening angle between the size-mass relations for the minimum and maximum concentration populations in each Hubble type should be related to their past merger rate and hence star-formation histories. It should be noted that environment has not been taken into consideration and should play an important role.

5.2.3 A broken connection amongst early-type galaxies

The structural homology of early-type galaxies a source of considerable debate, since non-homologies may go a considerable way toward explaining the “tilt” (with respect to canonical relationships predicted by the virial theorem) of the fundamental plane, and also the scatter around the tilted fundamental plane. In this section we consider the implications our results for explaining the tilted fundamental plane.

At present the two most likely explanations for tilt (and the scatter) in the fundamental plane are structural (or kinematic) non-homology in the early-type galaxy population, and a range of star-formation histories in the population. (The latter manifests itself as a changing stellar mass-to-light ratio as a function of age.)¹ Do our results suggest that non-homology or stellar mass-to-light ratio variations are the the major contributor to the tilt?

Figure 5.2 clearly shows that the most concentrated early-type galaxies have a size-mass relationship that is different from that of the less concentrated population. The mass range spanned by highly concentrated systems is truncated and the slope of the size-mass relationship appears to be shallower. On the other hand, it is important to emphasize that Figure 5.2 has been (deliberately) constructed to emphasize the characteristics of the extremes of the population distribution, and the systems shown in black and red in Figure 5.2 together comprise only 20% of all E+E/S0 galaxies in our sample. The size-mass distribution of the yellow and orange systems, which comprise 80% of all E+E/S0 galaxies, appear quite similar. We therefore suggest that one should be cautious in interpreting Figure 5.2 as strong evidence for non-

¹In principle stellar mass to dark matter mass variations could also play a role in tilting the fundamental plane, but since baryonic matter dominates inside the effective radius of massive early-type galaxies, this seems unlikely to be a major contributor to the tilted fundamental plane, at least for galaxies as massive as those in the present paper.

homology being responsible for the bulk of the tilt in the fundamental plane. On the other hand, the differing size-mass distributions at the extremes of the concentration distribution does suggest to us that non-homology may be a rather significant source of the scatter about the tilted fundamental plane.

This (tentative) conclusion seems fairly consistent with recent papers which use resolved kinematics and lensing to argue for inhomogeneities in the stellar populations playing the dominant role in defining the tilt of the fundamental plane. For example, Cappellari et al. (2005) investigated a sample of early-type systems using the SAURON integral-field unit and conclude that tilt of the fundamental plane is “almost exclusively due to a real M/L variation, while structural and orbital non-homology have a negligible effect”. Similarly, Bolton et al. (2007) use lensing to claim that “a systematic variation in the total (i.e., luminous plus dark matter) mass-to-light ratio as the origin of the ‘tilt’ of the fundamental plane (FP) scaling relationship between galaxy size, velocity dispersion, and surface brightness.” Interestingly, the same paper reports a correlation between the mass-to-light ratio and residuals about the fundamental plane. In the same context, our present results suggest that it would be interesting to determine whether the correlations between mass-to-light ratio and residuals about the fundamental plane are stronger than those between central concentration and scatter in the fundamental plane.

5.3 Summary

Our analysis of the galactic size-mass relationship has revealed both hidden connections and broken connections. The most striking hidden connection is that between spirals and ellipticals. We find that the size-mass relationship for Sa, Sab, Sb and Sbc galaxies bifurcates into two families of objects as one moves down the sequence from Sa to Sbc, and that objects along the high-concentration branch of the size-mass relationship are distributed with a similar slope (and span a similar mass range) to that exhibited by low-concentration elliptical galaxies. This suggests a closer-than-expected physical (even possibly evolutionary) connection between the most highly-concentrated spiral galaxies and low-concentration early-type galaxies.

The main broken connection highlighted by our analysis is that exhibited internally within the family of elliptical galaxies. We find that elliptical galaxies exhibit strikingly different size-mass relationships as a function of central concentration, strongly suggesting a non-homologous population of objects. Over the whole of the mass range studied, the size-mass relationship for the most centrally concentrated elliptical galaxies is displaced to lower masses. In other words, the more concentrated an elliptical galaxy is, the more likely it is to be under-sized and under-massive. The most massive early-type galaxies are all low-concentration systems.

This trend appears to extend to cD galaxies, though we emphasize that the objects we have analyzed are not (on the whole) central cluster galaxies. This presents a worrisome selection effect that should be allowed for in analyses of the size evolution of early-type galaxies seen at high-redshifts (Trujillo et al. 2004b,a; Damjanov et al. 2008).

Chapter 6

Bimodality in Bar Fraction

6.1 Introduction

Understanding the role of bars in galaxy formation is central to understanding the evolution of galaxies. Bars are important structures that help to redistribute angular momentum between baryonic and dark matter components in disk galaxies (Weinberg 1985; Debattista & Sellwood 1998, 2000; Athanassoula 2002) thereby driving their secular and dynamic evolution. Bars are thought to drive spiral arms (Lindblad 1960; Toomre 1969; Sanders & Huntley 1976) and ring structures (Schwarz 1981, 1984, 1985; Martinez-Valpuesta et al. 2006). They transport gas/matter to the centers of galaxies (Knapen et al. 1995; Hunt & Malkan 1999) and help to build bulges (Laurikainen et al. 2007) and possibly trigger AGN activity (Laine et al. 2002; Knapen et al. 2000; Laurikainen et al. 2004).

Early work on bar fractions suffered from poor sample sizes which limited the study of correlations between bar fraction and physical properties. Recent large surveys like the SDSS and COSMOS have helped rectify this deficiency. Sheth et al. (2008) (hereafter SE08), using a sample of ~ 2000 galaxies from COSMOS, have shown conclusively that bar fractions decrease with redshift as claimed by Abraham et al. (1999) and van den Bergh et al. (2002). In addition they find the bar fraction of spiral galaxies is a strong function of stellar mass, color and bulge prominence such that more massive, redder, concentrated galaxies have a larger bar fraction than less massive, bluer, diskier galaxies. This result points to connections between bar formation and galactic downsizing and re-emphasizes the importance of understanding the origins of bars.

Barazza et al. (2008) (hereafter BJ08) have characterized the bar fractions of ~ 2000 galaxies from the Sloan Digital Sky Survey. Their study is restricted to redshifts between 0.01 and 0.03 which causes them to miss the most luminous and massive objects in the local universe (see Chapter 2). It is important to note that the mass range spanned by the SE08 and BJ08

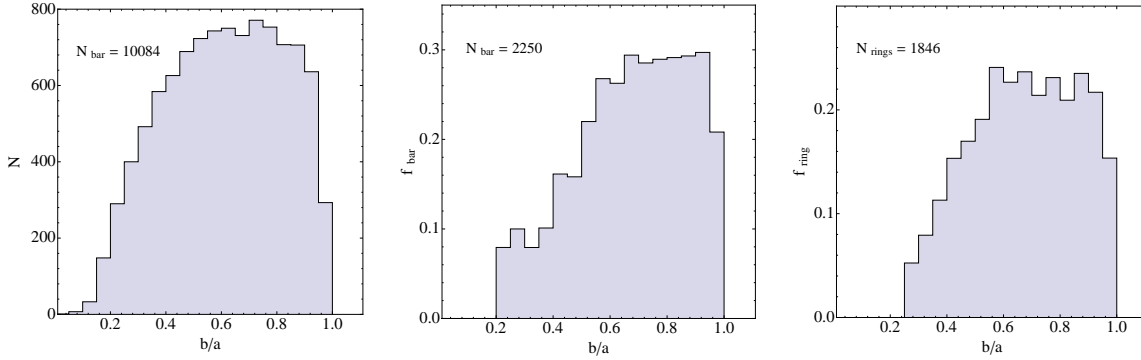


Figure 6.1: Axis Ratio Dependence of Fine Fraction: (a) the histogram distribution of axis ratios, (b) bar fraction as a function of axis ratio and (c) ring fraction as a function of axis ratio

samples only partially overlap. SE08 is not sensitive to masses < 10.2 (M_{\odot} in log units) while BJ08 is not sensitive to galaxies above 10.5 (M_{\odot} in log units). It is possibly for this reason that BJ08 find results counter to SE08, i.e. bar fractions increase with decreasing mass and bluer colors (corresponding to late type galaxies). In addition BJ08 find their bar fraction estimates in the local universe are consistent with no change in bar fraction with redshift (Elmegreen et al. 2004; Jogee et al. 2004). Reconciling the two results requires a larger sample which spans nearly the entire range in masses. Our sample of ~ 10000 disk galaxies with more than 2500 barred objects represents the ideal sample to investigate the dependence of bar fractions on the physical properties of galaxies in the local universe. Although we have fewer late type galaxies in comparison to classical spirals, the numbers are still greater than previous studies. In addition to bars we have recorded the frequency of rings and lenses which are related to bar activity (Buta & Combes 1996) and hence will be able to probe the dependence of fine-classes with physical properties as well as AGN activity.

6.2 Dependence of bar and ring fraction on axis ratio

From Table 3.2 in Chapter 3, we find the inclination-independent bar fraction of our sample is 26%. With a moderate inclination cut of $i < 0.65$ or $b/a > 0.4$, our bar fraction is $\sim 30\%$, much lower than what has been observed in the optical or near-infrared in the local universe. In Section 3.4 we showed using galaxies common with RC3, a strong bar recovery rate of $\sim 93\%$ and a weak bar recovery rate of $\sim 40\%$ for face on galaxies. Thus our bar classification is equivalent to RC3 strong bars which is $\sim 34\%$ in the local universe (Sellwood & Wilkinson 1993).

We did not study the effect of an axial ratio cut specifically in Chapter 3 or determine the

ideal axial ratio cut. Figure 6.1 illustrates the effect of axial ratios on bar and ring fractions. In Figure 6.1(a) we show the histogram distribution of axis ratios. We find using an apparent-magnitude limited sample preferentially selects more face-on objects. Hence we are under-represented in inclined objects. Figure 6.1(b) shows the bar-fraction as a function of axis ratio is nearly constant for $b/a > 0.6$ but decreases steeply below this threshold. The same applies for the ring fraction shown in Figure 6.1(c). Thus orientation effects lead to a decrease in the observed optical bar/ring fraction in the local universe. However we are interested in the variation of bar/ring fractions with different properties. We choose a stringent axis ratio cut of $b/a > 0.6$ which yields a sample of 1518 barred galaxies and 1177 ringed galaxies. If we made a less rigorous cut of $b/a > 0.4$ we would have ~ 2100 barred and ringed galaxies. The trends we describe below are similar for both samples.

6.3 Fine Fraction Statistics

6.3.1 Optical fraction of Bars, Rings and Lenses with T-Types

Depending on the samples used, previous results for the dependence of bar fraction with T-Type vary. Figure 6.2 taken from Sellwood & Wilkinson (1993) (Figure 3 in their paper) shows the fraction of strong and intermediate bars from the Revised Shapley-Ames Catalog (RSA: Sandage & Tammann 1981, 987 galaxies), the Second Reference Catalog (RC2: de Vaucouleurs et al. 1976, 1339 galaxies) and the Uppsala General Catalog (UGC: Nilson 1973, 4169 galaxies). In all three cases, the strong bar fractions peak around type Sa/Sb and falls off at earlier or later types. The RSA and RC2 show a further increase in bar fractions for Sd and later (Sd+) galaxies whereas UGC shows no such trend. Considering the total bar fraction, inclusive of intermediate bars, the same result holds for RSA and UGC samples while the RC2 shows a near constant bar fraction for Sa to Sc galaxies with a decline in bar fraction for S0 and Sd+ galaxies. Given the associated counting errors and difficulty identifying weak bars, the trends at early and late Hubble types were not considered significant (de Vaucouleurs 1963; van den Bergh 1998). Using RC3 data, Odewahn 1996 showed that total bar fractions does increase past Scd with nearly 78% of the 246 Magellanic type galaxies being strongly barred and 19% weakly barred. Ho et al. (1997) using ~ 500 local galaxies also find a near constant total bar fraction between Sa to Sc galaxies with a rising bar fraction past Sc to Sm galaxies. More recent results from BJ08 also find similar results for late type galaxies. Thus overall, late type galaxies show a higher bar fraction than classical spirals or early type galaxies.

Studies on the distribution of rings in the local universe are well established for inner rings. de Vaucouleurs (1963) and de Vaucouleurs & Buta (1980) find inner rings are most

common in early type and classical spiral galaxies while pseudo-rings are most common in late type galaxies. Buta & Combes (1996) (hereafter BC96) using RC3 data find inner ring fractions are nearly uniform between S0 and Sc galaxies while pseudo inner rings are again most common in late types. They find a face-on full inner ring fraction in the local universe of $\sim 20\%$ while the partial ring fraction is $\sim 35\%$. Statistics on nuclear rings and outer rings are not as well established as they are prone to more serious selection effects related to the depth of the available images. With nuclear rings, the problem is related to over-exposure of photographic plates and poor resolution. Thus very little is known about the variation of nuclear ring fraction with T-Type. In the case of outer rings, lack of depth to sample the wide range in surface brightnesses of outer rings affects known statistics. BC96 find outer rings are most common in the S0/a stage while psuedo-outer rings are most common at slightly later stages. Overall, outer rings are predominantly found in classical spirals with very few past a Hubble type of Sc. The total outer ring fraction in RC3 is 10% over all disks.

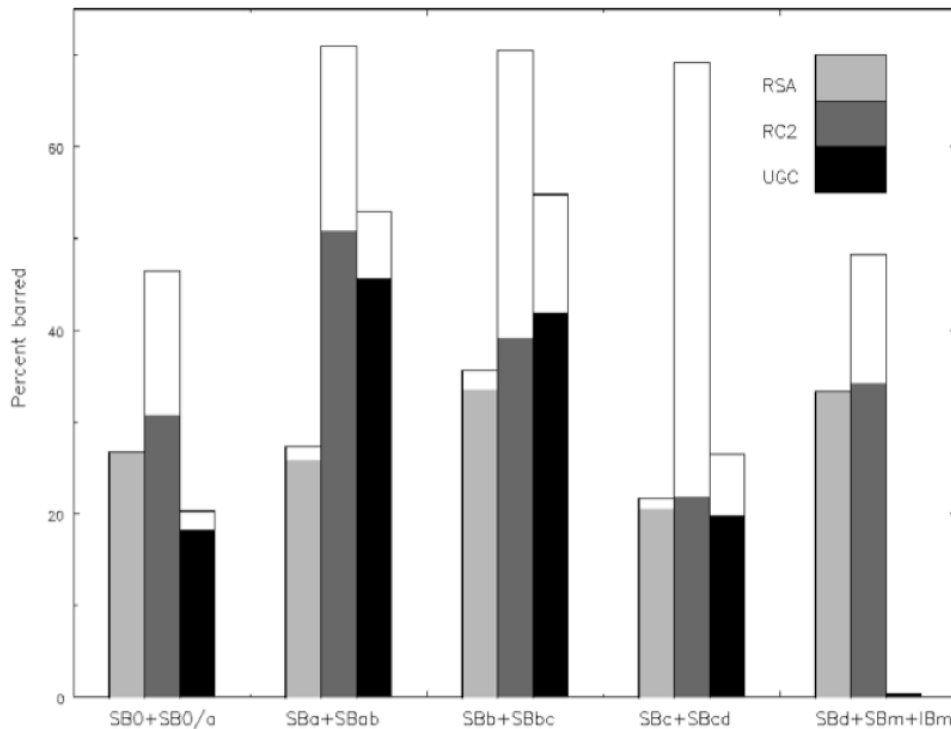


Figure 6.2: This figure is taken from Sellwood & Wilkinson (1993) and shows : “The fractions of barred (SB,shaded) and intermediate (SAB, unshaded) types at different stages along the Hubble Sequence of spiral galaxies identified in three independent morphological classifications. The statistics from RSA are based upon 987 objects. The RC2 sample contains 1339 objects after excluding peculiar, uncertain and ‘spindle’ types, edge-on objects and those with diameters less than 1 arcmin - unless large-scale plate material was available. The UGC sample contains 4169 galaxies when selection criteria similar to those for the RC2 were applied. The statistics are insensitive to the selection criteria, provided they remain within sensible ranges.”

Statistics on lenses in galaxies are not well known because they have normally been included as rings in many catalogues like RC3. Kormendy (1979) introduced specific designations for inner and outer lenses when studying a subsample of 129 barred galaxies from RC2. He found 54% of S0/Sa barred spirals have lenses with none beyond type SBab - SBc. In addition he found a very 'intimate connection' between bar and lens sizes and postulated that lenses possibly originate as bars. We have not characterized the sizes of fine structure in our sample (which is beyond the current scope of this thesis) and cannot make any comments in this respect. We restrict our analysis on the dependence of fine fractions with global physical properties.

Figure 6.3 shows the distribution of bars, rings and lenses with T-Type in our sample of face-on, disk objects only. The sample sizes for each fine class are 1508 bars, 1177 rings and 246 lenses. The top row, shows the histogram distribution for each fine-class while the bottom row

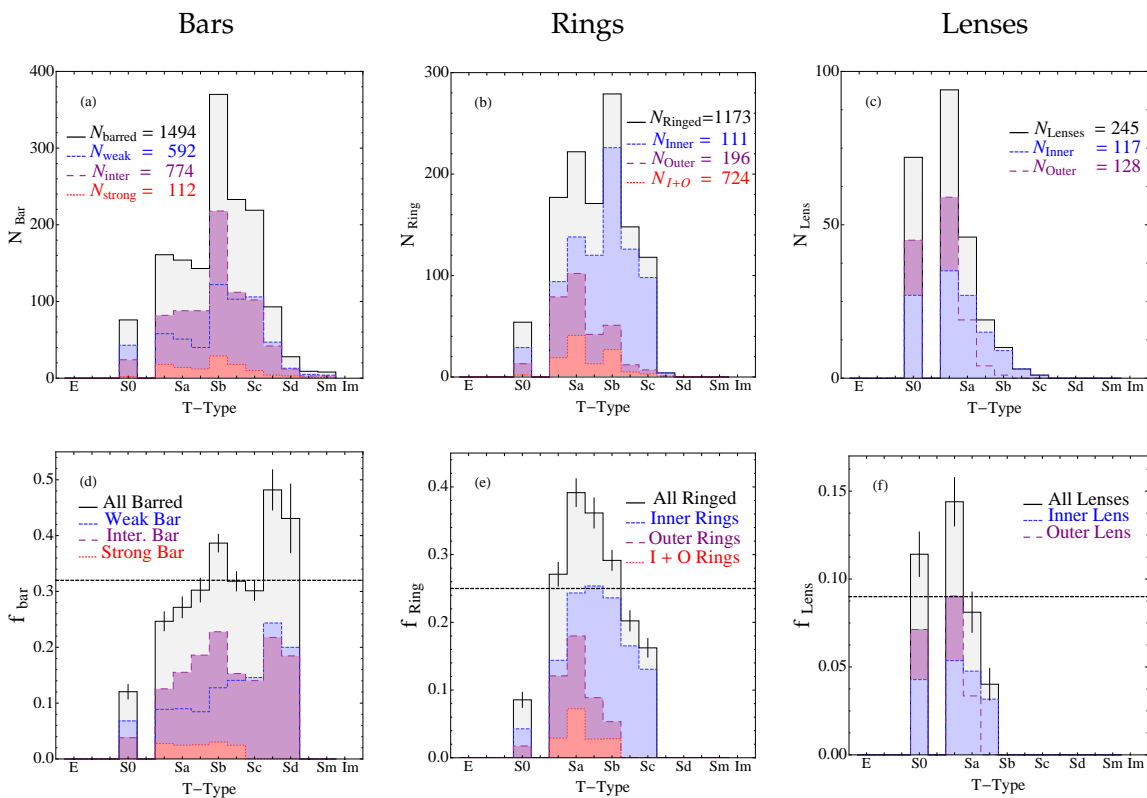


Figure 6.3: **Top Row**: T-Type Histograms for (a) Bars, (b) Rings and (c) Lenses in face-on disks. **Bottom Row** : Fractional histogram per T-Type for (d) Bars, (e) Rings and (f)Lenses. For Barred galaxies, the distribution of strong(red), intermediate(purple) and weak(blue) bars are shown. For Ringed galaxies, inner (blue), outer (purple) and combination (red) ring distributions are shown. In galaxies with lenses, inner (blue) and outer (purple) lens distributions are shown. The grey region shows the total distribution. The horizontal line in each panel is the average fraction of each fine type. Error bars are shown for the total fractional distribution.

shows the fractional distribution. For barred galaxies we show the distribution of strong (red), intermediate (purple) and weak (blue) bars. For ringed galaxies, we show the distribution of inner rings (blue), outer rings (purple) as well as objects with both inner and outer rings (red). Partial rings are included within the inner and outer ring fractions. Lenses are split into inner (blue) and outer (purple) lenses. We only show data points with a minimum of 20 barred/ringed/lens object in each bin and 10 objects in each sub-class (eg inner lens or outer lens) per bin.

Figure 6.3(d) shows the variation of bar fraction with T-Type for our sample of ~ 10000 galaxies. The overall bar fraction gradually decreases from late types to early types with a significant dip around a T-Type of Sc where the RSA and UGC also see a dip in bar fraction. We find the bar fraction gradually decreases from $\sim 40\% \pm 2\%$ for Sb galaxies to $12\% \pm 2\%$ for S0's. The bar fraction from Sb to Sc galaxies falls by $10\% \pm 4\%$ after which it again rises to $45\% \pm 4\%$ for Scd+Sd galaxies. (The bar fractions of Scd and Sd galaxies are consistent within the error bars). The RSA and RC2 (strong) also show increasing bar fractions past Sc. Thus our overall distribution is similar in shape to the RSA distribution but with 10 times the number of objects. Our average bar fraction is 31% consistent with RC3 strong bar fraction estimates in the local universe. The source of the break in bar fraction between T-Types Sb to Sc will become clearer as we investigate the relationship of bar fraction with other physical properties. For bar sub-classes, we find strong bars are restricted to classical spirals. Intermediate bars show similar trends to the overall distribution while weak bars seem to show a gradual increase in bar fraction past morphological type Sb. It should be kept in mind that our characterization of strong, intermediate or weak bars does not relate directly to the RC2/RC3 scheme. All bars classified as weak in our classification are definitely barred but are small or have lower luminosity.

Unlike BC96 who find no significant variation of ring fraction with T-Type, we find the ring fraction in Figure 6.3 (e) increases steeply with T-Type, from $\sim 15\%$ for Sc galaxies to 36% for Sa galaxies. For objects earlier than Sa the ring fraction decreases sharply to $\sim 6\%$ for S0 galaxies. There are very few rings observed past Sc and most are inner rings. Both inner rings and outer rings show a similar trend, though the outer ring fraction peaks earlier than the inner ring fraction. There are very few outer rings past a morphological type of Sb. Though not shown in the figure, we have 91 nuclear rings in our sample, many with a higher degree of uncertainty. They show no significant dependence on T-Type with an average fraction of $\sim 2\%$ from S0 to Sc galaxies.

We have considered inner and pseudo-inner rings as a single group for both inner and outer rings. Figure 6.4 shows the distribution of complete and partial rings for (a) inner rings and (b) outer rings relative to the variation of total ring fraction with T-Type. We find partial

Table 6.1. Relative Frequencies of Bars and Inner Rings

Family	f(r)%	f(rs)%	f(s)%	N
SB	24.5 (23.2)	8.9 (32.4)	55.0 (38.4)	1370 (336)
SA	9.6 (15.8)	2.5 (32.1)	73 (46.7)	2426 (165)
All S	15.0 (18.8)	4.8 (38.8)	66.8 (37.1)	3796 (773)
LB	25.3 (36.1)	1 (19.4)	59 (25)	276 (36)
LA	5.8 (21.5)	0.5 (7.7)	83.0 (32.3)	1008 (65)
All L	9.9 (23.2)	0.6 (13)	77.0 (31.2)	1284 (138)
All	14 (19)	4 (35)	70 (36)	5080 (911)

inner rings (rs) are mainly found in later type galaxies and their fractions are approximately constant from Sab to Sc galaxies. Complete inner rings (r) follow the distribution of the overall ring fraction over the whole range of T-Types. Pseudo &/or partial outer rings (P) again show very little dependence on T-Type. They show a slight preference for later T-Types compared to complete outer rings (R) but both peak around T-Type Sa. Thus we will continue to consider inner and psuedo-inner rings as a single group with the same for outer and outer-pseudo rings.

The average full+partial ring fraction in our face-on sample is 23% much lower than the combined 55% reported by BC96. This is partially because lenses are included as rings in RC3. If we consider rings and lenses as a single class the average fraction rises to 32%. The most significant reason for the difference though is a dearth of partial rings in comparison to RC3. Table 6.1 shows a comparison of inner rings frequencies, $f(r)$, partial inner ring frequencies, $f(rs)$, and no ring frequency, $f(s)$, between our sample and BC96 (in brackets) as a function of broad T-Types (spiral S or lenticular L) and bar presence (B). It is apparent that we are missing a

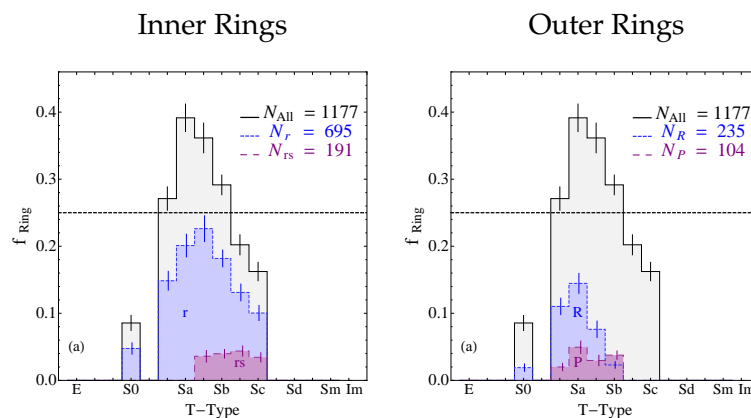


Figure 6.4: **Left**: Fractional histogram per T-Type for inner full (blue,r) and partial (purple,rs) rings and **Right**: Fractional histogram per T-Type for outer full (blue,R) and pseudo (purple,P) rings. The variation of total ring fraction with T-Type is shown in black. Error bars are shown for each distribution.

Table 6.2. Relative Frequencies of Bars, Rings and Lenses

Family	S0	Sa	Sb	Sc	Sd	All
$f_{r/b}(\%)$	41 ± 3	70 ± 3	48 ± 2	22 ± 2	0	44 ± 1
$f_{b/r}(\%)$	40 ± 3	44 ± 2	54 ± 2	43 ± 4	0	47 ± 1
$f_{l/r}(\%)$	18 ± 2	11 ± 2	3 ± 1	0	0	8 ± 1
$f_{r/l}(\%)$	24 ± 3	60 ± 5	61 ± 9	0	0	37 ± 3
$f_{l/b}(\%)$	22 ± 3	8 ± 2	~ 0	0	0	5 ± 1
$f_{b/l}(\%)$	29 ± 3	29 ± 5	~ 0	0	0	27 ± 3

large number of partial rings in both lenticular and spiral galaxies irrespective of the presence or absence of a bar. However it should be noted that our sample size is a factor of 5 larger than BC96 and our recovery rate for partial inner rings from Chapter 3 is $\sim 43\%$ with a strong caveat that the objects which RC3 considers partially ringed are either very doubtful or hard to distinguish in the SDSS g-band image. Thus overall, we find 14% of all disks have a full inner ring, only 4% have partial inner rings and 70% have no rings (inner or outer).

We find the overall outer ring fraction is 8% without including outer lenses and 11% with outer lenses. This is consistent with the fraction of 10% quoted by BC96. It should be noted that we are more prone to missing outer rings especially low surface brightness rings given the short exposure time of SDSS images but this affects many of the images used in the RC3 classifications as well.

Considering lens fraction independently, Figure 6.3 (f) shows a rapid decline from $\sim 14\% \pm 2\%$ for S0a galaxies to $\sim 4\% \pm < 1\%$ for Sab's. There is a slight drop in lens fraction from S0a to S0 galaxies. This trend is mirrored in both inner and outer lenses although inner lenses are more common in later types than outer lenses. We find very few lenses past the morphological type Sab and no inner lenses past Sc. Thus lenses are predominantly restricted to early type bulge dominated galaxies. We do not include nuclear lenses in our classification scheme as described by Buta (1995). The overall lens fraction of our sample is 8%. The major cause of uncertainty is the smaller sample size of lenses (N=246).

So far, we have considered each fine structure independently. However, both simulations and observations suggest a very strong link between bars, rings and lenses. In Table 6.2 we consider how fine features affect each other as a function of T-Type. The fraction of rings in barred galaxies ($f_{r/b}$) shows a very strong dependence with T-Type (binned over subclasses). It gradually rises from 22% for Sc's to peak at 70% for Sa galaxies and then drops to 40% for S0 galaxies. Considering the frequency of bars in ringed galaxies ($f_{b/r}$) we find a fairly high fraction of 47% over all disks with a peak around Sb galaxies. It is important to consider this in the context of the life times of bars and rings. Bars are thought to have shorter lifetimes of $\sim 1\text{Gyr}$ in comparison to rings (Buta & Combes 1996). Thus if the sequence from Sd to Sa is an age

sequence, the frequency of rings would be higher in early classical spiral galaxies as we have seen previously in Figure 6.3(e) and would account for the trend of $f_{r/b}$. As ring frequency increases from Sb to Sa galaxies by 10%, the overall bar frequency actually decreases with T-Type from Sb to Sa by 10% as shown in Figure 6.3(d). This could account for the 10% decrease of $f_{b/r}$ from 54% for Sb to 44% for S0 galaxies. Though it is hard to interpret, there does seem to be a strong correlation between the decrease in bar frequency with a corresponding increase in ring frequency between Sb to Sa. It could also be that whatever process causes bar destruction takes longer to affect rings. It should be noted that from Sa to S0 galaxies, both bar and ring fractions decrease.

When considering the relationship between rings and lenses we find 60% of lensed galaxies host rings ($f_{r/l}$) in Sa and Sb galaxies. The fraction is lower for S0 galaxies where both lens and ring frequencies decrease. Thus the presence of a lens is strongly related to the presence of a ring. Conversely the presence of a ring does not imply the presence of a lens. We find 8% of ringed galaxies host lenses with a slight trend with T-Type such that the fraction gradually increases from Sb to S0 galaxies. It may be possible that some rings are dissolving to form lenses.

Considering the interplay between bars and lenses we find nearly 30% of lenses host bars in S0 and Sa galaxies with no dependence on T-Type. Conversely, the frequency of lenses in barred galaxies increases from 8% for Sa's to 22% for S0's. It should be noted again that our fractions are predominantly a strong bar fraction measure and miss a number of weak bars, specifically ansae. This could account for the difference between our results and Kormendy (1979) who finds 54% of galaxies with bars have lenses in S0 and Sa galaxies.

In summary, we find bar, ring and lens fractions are strongly dependent on the T-Type of an object. In addition there are strong correlations between fine classes which are also dependent on T-Type.

6.3.2 Optical fraction of Bars, Rings and Lenses with Sersic Index n

Previous work on variation of fine fractions with sersic index is fairly limited to smaller samples and specifically to barred galaxy samples e.g. BJ08. This is in part because determining the sersic index for galaxies with fine components is tricky. Some methods ignore the presence of the fine component and fit a 1 component or a bulge + disk component model to the galaxy. More recent work (Laurikainen et al. 2005; Gadotti 2008) attempt to remove the multi-component structure before fitting and find bulge-to-total light ratios are over estimated (by 5% - 10%) if bars are not accounted for. We are using the sersic indices from Blanton et al. (2003) where no attempt is made to profile fine structure. The largest work with which we can compare, BJ08 also uses single component 2D profile fitting with *GALFIT* to estimate the

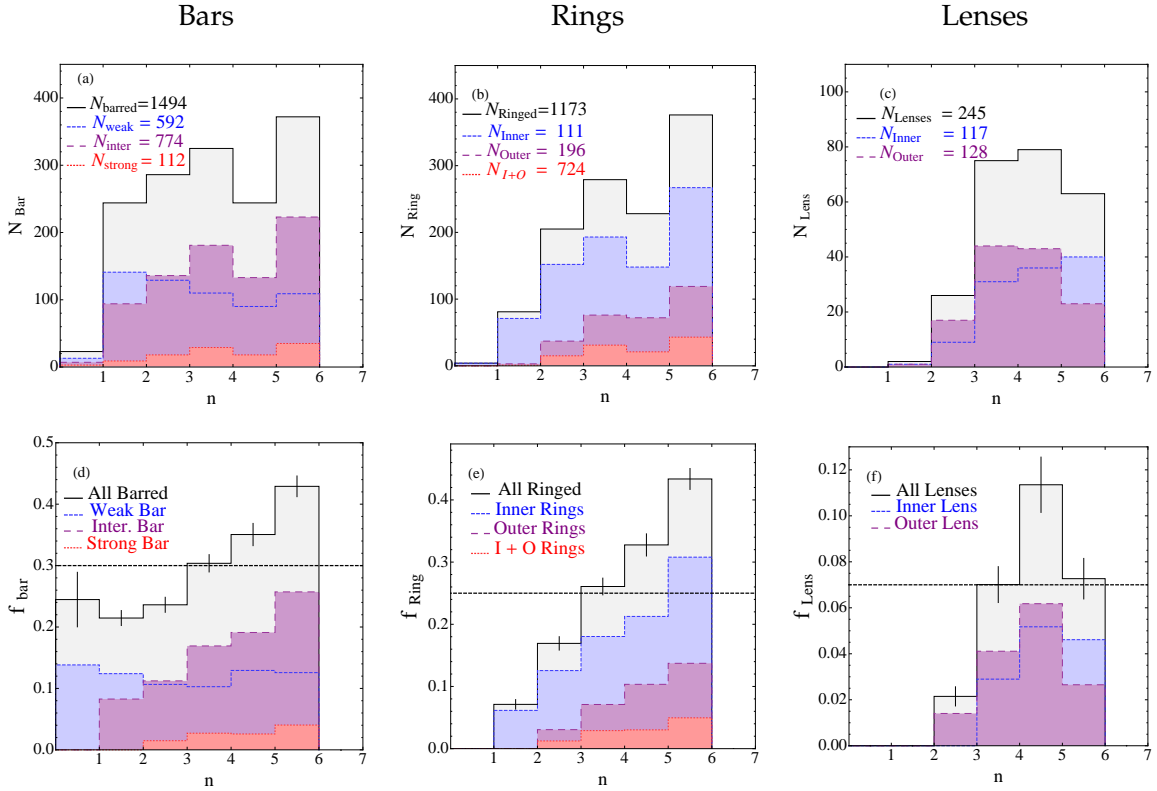


Figure 6.5: **Top Row:** Sersic index Histograms for (a) Bars, (b) Rings and (c) Lenses in face-on disks. **Bottom Row :** Fractional histogram per Sersic index for (d) Bars, (e) Rings and (f) Lenses. For Barred galaxies, the distribution of strong (red), intermediate (purple) and weak (blue) bars are shown. For Ringed galaxies, inner (blue), outer (purple) and combination (red) ring distributions are shown. In galaxies with lenses, inner (blue) and outer (purple) lens distributions are shown. The grey region shows the total distribution. The horizontal line in each panel is the average fraction of each fine type. Error bars are shown for the total fractional distribution.

Sersic index and half light radii of their galaxies.

Figure 6.5 shows the distribution of bars, rings and lenses with Sersic index in our sample of face-on, disk objects only. The color coding is the same as in Figure 6.3. Figure 6.5(a) shows we have very few galaxies with $n < 1$. Considering the variation of bar fraction with Sersic index in Figure 6.5(d) we find the bar fraction is nearly constant at $\sim 20\%$ for $n < 3$ but gradually increases as Sersic index increases. In contrast, BJ08 finds the bar fraction initially drops as n increases and is then constant at $\sim 52\%$ for $1 < n < 3$ before falling off at higher n . This directly contradicts our results. It should be noted that we have only ~ 20 galaxies in lowest n bin and this could account for the lower bar fraction at low n in comparison to BJ08. In the high- n region, we have over 200 galaxies in each bin while BJ08 have fewer than 40 hence our results are more robust. BJ08 attributes their decrease in bar fraction for $n > 2.5$ to contamination by blue spheroids. For bar sub-classes, we find strong bars are restricted to high- n galaxies. Intermediate bars show similar trends to the overall distribution while weak

bars seem to show little variation in bar fraction with sersic index.

Figure 6.5(e) shows that ring fraction is strongly correlated with sersic index. As sersic index increases, the ring fraction increases from 6% at $n = 1$ to 42% for $n > 5$. Both inner and outer rings also follow a similar trend though outer rings have a preference for slightly higher n galaxies than inner rings. The average ring fraction is 25%. Figure 6.3(f) shows the lens fraction initially increase with sersic index from 2% at $n = 2$ to $\sim 12\%$ for $n = 5$ before dropping off to 7% for $n > 5$. There are no galaxies with lenses below $n = 2$. The trend is seen in both inner and outer lenses. The effect of multi-component fitting of galaxies profiles may be important for the variation of ring and lens fractions but it is beyond the scope of the current thesis. Overall, the more bulge dominated galaxies have higher bar, ring and lens fractions.

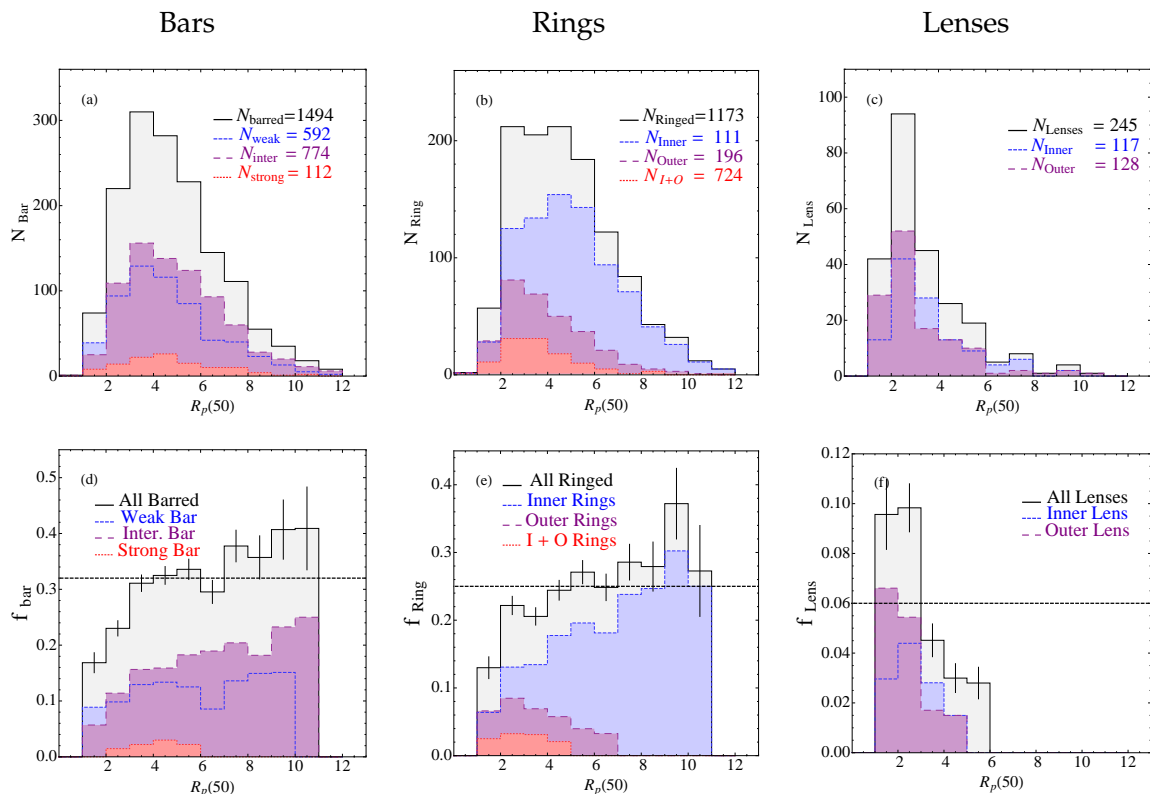


Figure 6.6: **Top:** Petrosian half-light radius ($R_p(50)$) Histograms for (a) Bars, (b) Rings and (c) Lenses in face-on disks. **Bottom :** Fractional histogram for (d) Bars, (e) Rings and (f) Lenses as a function of sersic index. Color coding is the same as Figure 6.3. The horizontal bar shows shows the average fraction for bars, rings and lenses respectively. Note that scales are different in each figure.

6.3.3 Optical fraction of Bars, Rings and Lenses with Size

Most work related to the size of galaxies with fine features focuses on the variation of the size of the bar or ring with the variation in size of the galaxy. We have not characterized the sizes of our fine features and hence we restrict ourselves to the overall variations of fine fraction with size. A good review of the variation of bar and ring sizes can be found in de Vaucouleurs (1963), de Vaucouleurs & Buta (1980), and Buta & Combes (1996).

BJ08 finds bar fractions increase with half light radius from 40% for $R_{50} \sim 2kpc$ to 60% for $R_{50} > 6kpc$, beyond which the bar fraction is fairly flat. SE08 finds similar results (Figure 12 in their paper) with total bar fraction rising from 40% for $R_{50} \sim 1kpc$ to 65% for $R_{50} > 4kpc$ in their lowest redshift bin. For $R_{50} > 4kpc$ the bar fraction is constant with size within error bars.

Figure 6.6 shows the histogram and fractional distribution of the petrosian half light radius (in kpc) of galaxies with bars, rings and lenses. The color coding is the same as in Figure 6.3. From Figure 6.6(d) we see the bar fraction increases steadily with the size of the galaxy, going from 20% for $R_{p50} \sim 2kpc$ to 40% for $R_{p50} \sim 10kpc$. This is consistent with the results of BJ08 and SE08. Strong and weak bars follow the same trend. Figure 6.6 (e) shows the ring fraction increase steadily with size as well. Inner rings follow a similar trend while outer rings gradually decrease with the half light size of the galaxy. This is because objects with larger half light radii are more disky and have a later T-Type and hence are less likely to have an outer ring as we see in Figure 6.3(e). The lens fraction shows a steep decrease with the half light radius for very much the same reason as with the outer rings.

6.3.4 Optical fraction of Bars, Rings and Lenses with Mass

To date, the only studies that have investigated the bar fraction as a function of mass are SE08 and BJ08. As stated earlier, SE08 finds the bar fraction of galaxies is a strongly increasing function of mass at high redshifts (Figure 3 in their paper). As the mass of a galaxy increases from $\text{Log } M \sim 10.3$ to 11.2, the bar fraction increases from 10% to 50% for all bars (including weak bars) and 5% to $\sim 18\%$ for strong bars. As redshift decreases, the strength of the dependence of bar fraction on mass decreases but is still present. In the lowest redshift bin, SE08 finds the bar fraction is nearly constant at higher masses and may decrease at lower masses. BJ08 on the other hand finds the bar fraction strongly decreases as mass increases from $\text{Log } M \sim 9.5$ to 10.5.

Figure 6.7 shows the histogram and fractional distribution of mass for galaxies with bars, rings and lenses. The color coding is the same as in Figure 6.3. We find most of our galaxies are between $10 < \text{Log } M < 11$. There are very few rings or lenses below $\text{Log } M \sim 10$ but we do

have a large number of low mass barred galaxies. Figure 6.7(d) shows the bar fraction gradually decreases from $\sim 40\%$ for low mass galaxies ($10^9 M_\odot$) to $\sim 20\%$ for intermediate mass galaxies ($2 * 10^{10} M_\odot$). It then gradually increases and plateaus at 30% before truncating at $4 * 10^{11} M_\odot$. This high mass cut-off is most likely due to a lack of massive disks. For individual bar types, we find strong bars are restricted to high mass galaxies. Weak bars are similar to the overall distribution with a more apparent plateau at the high mass end while intermediate bars show a similar break in bar fraction at $M \sim 2 * 10^{10} M_\odot$.

The decrease of bar fraction from low to intermediate masses is also seen by BJ08 (where they have > 100 objects in each bin compared to < 100 in our low mass bins). However in BJ08, the bar fraction continues to decrease with increasing mass (from 10^{10} to $5 * 10^{10} M_\odot$) while we see a slightly increasing/constant bar fraction. This is because BJ08 have fewer than 100 high mass data points in total whereas we have more than a 100 in each bin. The break in the bar fraction occurs around the characteristic mass where bi-modality in galaxy proper-

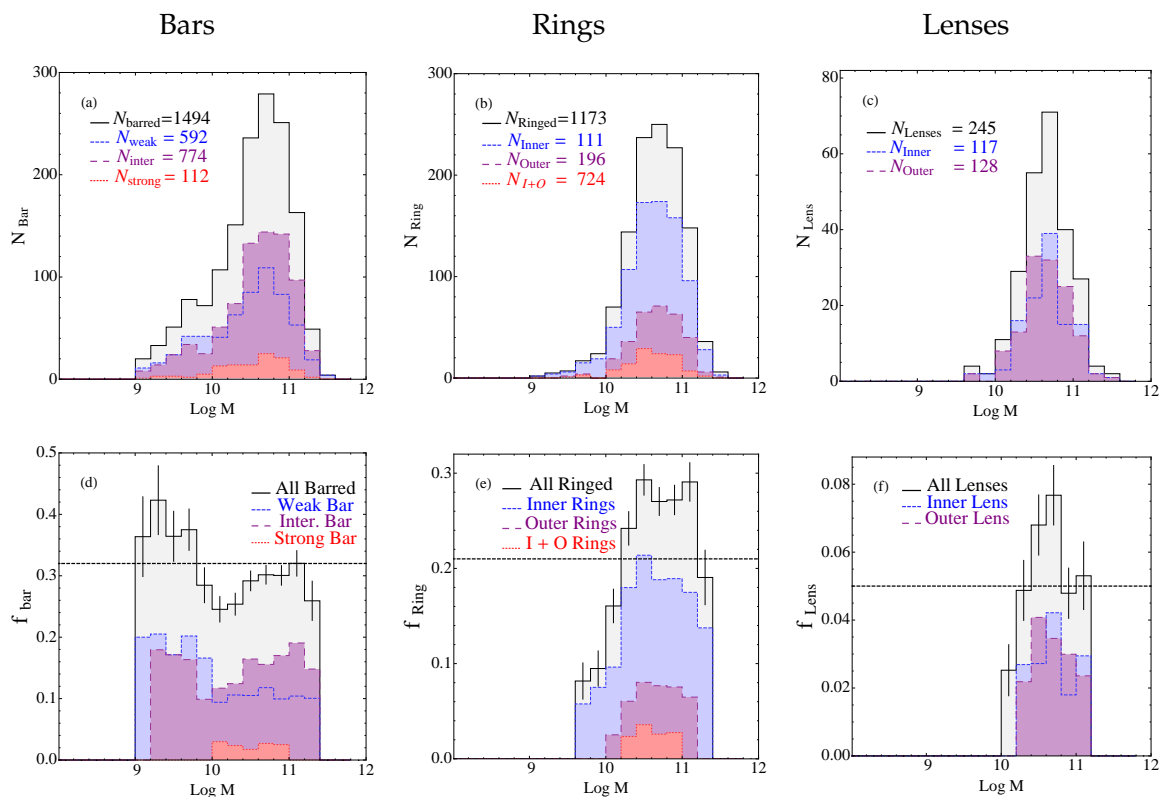


Figure 6.7: **Top:** Mass Histograms for (a) Bars, (b) Rings and (c) Lenses in face-on disks. **Bottom:** Fractional histogram per T-Type for (d) Bars, (e) Rings and (f) Lenses. Color coding is the same as Figure 6.3. We find the bar fraction falls steeply from low masses to intermediate masses, $M \sim 10.2$, and rises slowly thereafter. Bar fractions fall off again past $M \sim 11$ where elliptical galaxies tend to dominate. It is interesting to note that the ring and lens fractions increase with mass while the bar fraction is decreasing in the same range.

ties has been observed. Kauffmann et al. (2003b) found AGN of all luminosity reside almost exclusively above this mass threshold. This could indicate that AGN are playing a role in the bar formation/destruction process or different types of bars are dominant in low-mass vs. high-mass galaxies (Elmegreen & Elmegreen 1985). We postpone this analysis to the next chapter.

The ring fraction in Figure 6.7 (e) is seen to increase steeply with mass, from 10% at $10^{10}M_{\odot}$ to 30% at $5 * 10^{10}M_{\odot}$ where it plateaus. Both inner rings and outer rings show a similar trend. The lens fraction in Figure 6.7 (f) peaks sharply at $M \sim 5 * 10^{10}M_{\odot}$ and then falls off. Inner and outer lenses also follow the overall distribution. Thus the processes responsible for ring and lens formation dramatically depend on mass between $6 * 10^9M_{\odot}$ and $5 * 10^{10}M_{\odot}$. It is interesting to note that when bar fraction stays constant, the ring fraction is also approximately constant. When considered with our results from the previous sections, it indicates a strong connection between bar and ring formation.

Overall we find bar and ring fractions are strongly dependent on the mass of the galaxy. *The apparent discrepancies in the analysis of SE08 and BJ08 is probably due to bar fractions being bimodal.*

6.3.5 Optical fraction of Bars, Rings and Lenses with Luminosity

The high redshift sample from SE08 shows a strong dependence of bar fraction on absolute magnitude (Figure 2 in their paper). As the luminosity decreases, the total bar fraction decreases from $\sim 55\%$ at $M_V = -24$ to $\sim 20\%$ at $M_V = -21.5$ in the redshift bin ($0.6 < z < 0.84$). For each lower redshift bin the strength of the decrease (gradient) reduces. In their lowest redshift bin ($0.14 < z < 0.37$), SE08 find the bar fractions are nearly constant at 60% for $M_V > -22$. Similar trends are observed with the strong bar sample with a decrease in bar fraction from 18% to 5% as galaxies become fainter in the highest redshift bin and a constant bar fraction of $\sim 25\%$ for $M_V > -22$ in the lowest redshift bin. BJ08 finds the optical bar fraction is fairly constant between at 50% for $-20.6 < M_g < -19.6$ and increases as magnitude decreases going to 58% for $M_g = -18.5$ (Figure 13(c) in their paper). It should be noted that the magnitude range spanned by the two samples are different but both SE08 and BJ08 see a region of near constant bar fraction with magnitude.

Figure 6.8 shows the histogram and fractional distribution of absolute magnitudes in g-band for galaxies with bars, rings and lenses in our sample. The color coding is the same as in Figure 6.3. We have very few objects fainter than $M_g \sim -19$ a reflection of our lack of low mass, late T-Type objects. Thus a complete comparison with BJ08 will not be possible. In Figure 6.8 (d) we find the bar fraction is fairly constant at $\sim 30\%$ for $M_g < -18.5$. At the brightest magnitudes the bar fraction decreases sharply as is also seen by BJ08 and possibly by

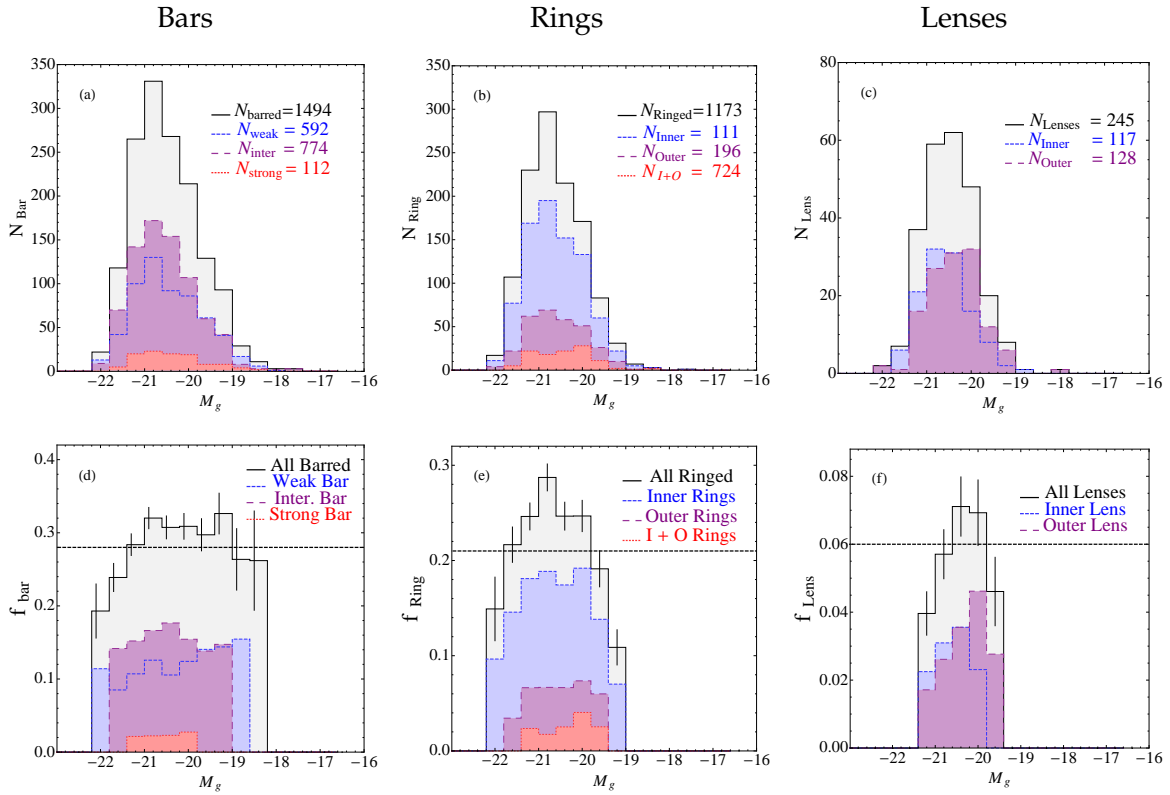


Figure 6.8: **Top**: Absolute Magnitude Histograms for (a) Bars, (b) Rings and (c) Lenses in face-on disks. **Bottom**: Fractional histogram per magnitude bin for (d) Bars, (e) Rings and (f) Lenses. Color coding is the same as Figure 6.3.

SE08 though the counting errors are much larger. Our results are consistent with no increase in bar fraction at fainter magnitudes mainly because we lack bulge-less disk galaxies, which BJ08 find are nearly 70% barred and dominate fainter magnitudes. If we were to consider our $b/a > 0.4$ sample, we do see a slight increase in bar fraction with $M_g > -19$ but again, this is consistent with no change within the counting error bars. Strong and intermediate bars display a near constant bar fraction whereas weak bars show a gradual increase in bar fraction with decreasing magnitude.

Figure 6.8 (e) shows the ring fraction sharply increases with absolute magnitude from 8% at $M_g \sim -18.6$ to 28% at $M_g \sim -21$, and then starts to decrease past $M_g \sim -21$. This is consistent with the increasing of ring fraction with decreasing T-Type (Sc through S0a, which dominates the intermediate magnitude range). The ring fraction may also be considered to be fairly constant between $-21 < M_g < -19.6$ given the error bars. The inner rings follow the overall distribution with a definite plateau at intermediate magnitudes while the outer rings show no variation with magnitude. The average ring fraction is 21%. The lens fraction in Figure 6.8 (f) is seen to decrease strongly with increasing magnitude with both inner and

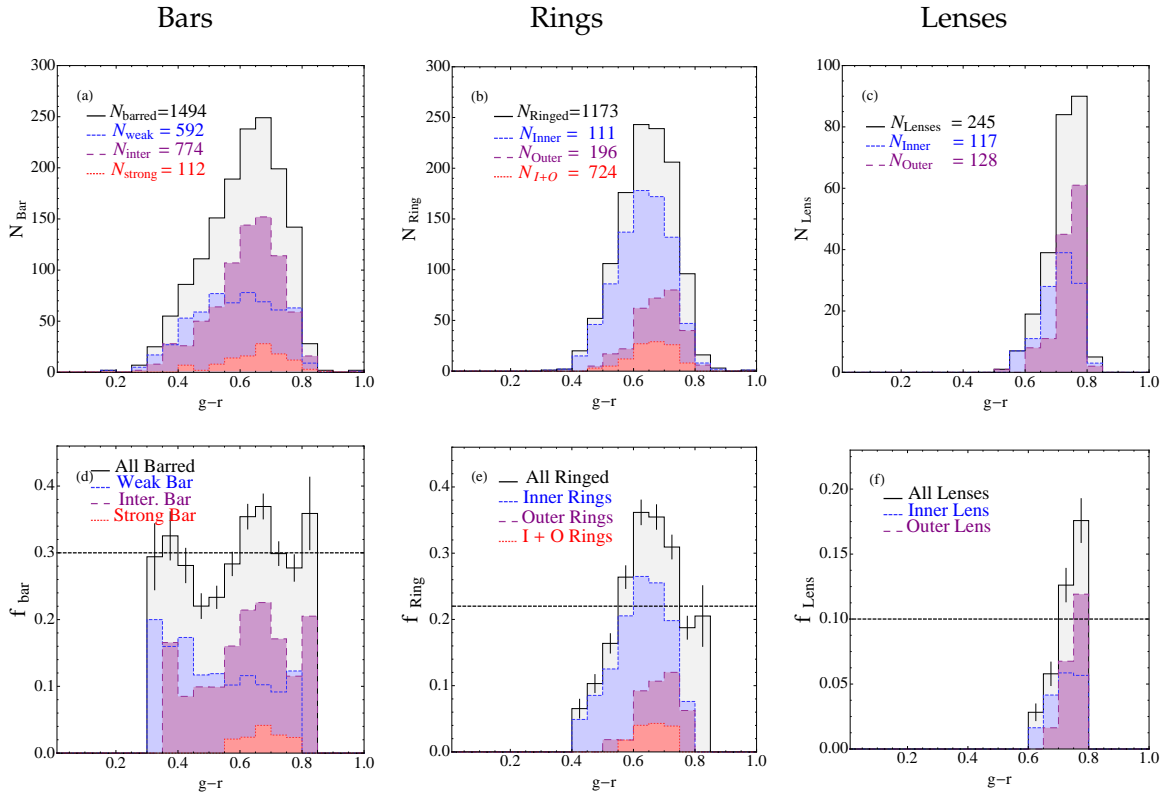


Figure 6.9: **Top**: $g-r$ Color Histograms for (a) Bars, (b) Rings and (c) Lenses in face-on disks. **Bottom** : Fractional histogram per magnitude bin for (d) Bars, (e) Rings and (f) Lenses. Color coding is the same as Figure 6.3. We find the bar fraction decreases from bluer colors to intermediate colors, $g-r \sim 0.5$, and rises slowly thereafter. It is interesting to note that the ring and lens fractions increase with color while the bar fraction is decreasing in the same range. Ring fractions decrease past $g-r \sim 0.7$

outer lenses following the trend. Over the range where ring fractions are increasing and lens fractions are decreasing, the bar fraction is fairly constant as can be seen in Figure 7.4(d). For the very brightest objects though the bar, ring and lens fractions are a strongly decreasing function of absolute magnitude.

6.3.6 Optical fraction of Bars, Rings and Lenses with Color

BJ08 finds the bar fraction gradually decreases from 58% for $g-r \sim 0.2$ to 50% for $g-r \sim 0.55$ before plummeting to 30% for $g-r \sim 0.65$. SE08, using SED type as a proxy for color, find bar fractions are nearly constant with SED type within the error bars though it could possibly be decreasing as an object becomes redder.

Figure 6.9 shows the number and fractional histogram distribution of $g-r$ color for galaxies with bars, rings and lenses. The color coding is the same as in Figure 6.3. Bar fractions show a

clear bimodal nature with respect to color. The bar fraction initially decreases as the galaxies become redder from 33% at $g - r \sim 0.4$ to 22% at $g - r \sim 0.5$. Above $g - r \sim 0.5$ the bar-fraction transitions and starts to increase again as the galaxies become redder. This reflects the break seen in the mass histogram in Figure 6.7(d). The bar fraction starts to decrease again past $g - r \sim 0.7$ (ignoring the increase in reddest data point which has a large error bar and is not seen when choosing a less strict axis ratio cut). BJ08 find similar results for the bluest bins, while SE08 find similar results for the bar fractions in the reddest bins. For bar subclasses, we find weaker bars tend to prefer bluer galaxies and strong bars are preferentially redder. Intermediate bars span the whole range of colors but exhibit a stronger red peak.

The ring fraction in Figure 6.9(e) increases dramatically as the galaxies become redder from 4% at $g - r \sim 0.4$ to $\sim 36\%$ at $g - r \sim 0.7$. As galaxies become redder the ring fraction decreases sharply. The trends are repeated in inner and outer rings with outer rings being in redder galaxies than inner rings. The peak of the distribution for outer rings is slightly to the red in comparison to the distribution of inner rings. This ties in with the variation seen with T-Type where outer rings peak at earlier T-Types compared to inner rings. Interestingly, most of the rings in our sample lie in the red peak. In the range where bar fractions are increasing ($g - r > 0.5$), ring fractions also increase thus indicating a positive correlation between bar and ring fractions. Thus the appearance of the red sequence appears to be correlated with an increase in bar and ring fractions.

The lens fraction in Figure 6.9(f) sharply increases with color, from 1% at $g - r \sim 0.6$ to $\sim 20\%$ at $g - r \sim 0.82$. Lenses occur in the reddest galaxies in our sample. Outer lenses are in redder galaxies than inner lenses. Comparing the ring and lens fractions, in the region where the ring fraction decreases with color by $\sim 20\%$ the lens fraction increases correspondingly. Thus rings and lenses are intimately linked in the range $0.7 < g - r < 0.9$ while bars and rings are intimately linked in the range $0.5 < g - r < 0.7$.

Thus bimodality in galaxy properties has a direct morphological signature. Bar fractions are bimodal in both mass and color. Understanding the direction of causality will be important to understanding the evolution of galaxies. We discuss possible origins in the next section.

6.4 Origin of Bimodal bar fractions

A number of galaxy properties like color, magnitude (Strateva et al. 2001; Balogh et al. 2004; Baldry et al. 2004) mass, surface mass density (Kauffmann et al. 2003), luminosity, size and concentration (Shen et al. 2003, Blanton et al. 2003, Driver et al. 2006b) exhibit a bimodal distribution. The fact that bimodality is manifested in many parameters is not surprising given the strong correlations between them. A consensus on the cause of bimodality is appearing,

specifically that it is due to the two component nature of galaxies (bars + disk) as opposed to two distinct galaxy populations (Allen et al. 2006). To this list of bimodal properties a morphological signature, bar fraction, can be added. Whatever process is causing the creation of the red and blue sequence is either influencing or being influenced by structural changes in the galaxies, specifically the change in bar fraction and/or the nature of bars.

Theoretically the effects of stellar disk mass on bar fractions are not well understood. The only conclusion common to most theories of bar formation is that bars disappear more quickly in the presence of gas. However if dark matter is dominant then bars may not be as easily destroyed. Aside from this, theories vary in complexity, physics considered, numerical resolution and results. This is because understanding the behavior of bar fractions in low mass galaxies is tricky as there are a number of factors to consider specifically, the interaction of gas, stellar matter and dark matter, the instabilities and triggers which cause bar formation, the lifetimes of bars and the effect of a central mass concentration and bulge build up on the stability of the bar. All of these issues are highly debated. The determining factor in most of these processes are the methods and rate of transfer of angular momentum between halo, gas and disk. The halo and gas are playing a very important role in low concentration, low mass galaxies where they dominate the dynamics. Unfortunately we have no measure of gas fraction in our galaxies and so we will try to draw inferences based on previous works.

Numerical simulations show that low mass, gas dominated galaxies are very prone to instabilities and bar formation. This could explain why the bar fraction is higher in the low mass, blue peak as opposed to the high mass peak. A possible trigger could be minor satellite impacts (10:1 ratio) which have been shown to cause bar instabilities in axisymmetric disks (Dubinski et al. 2008). In addition asymmetries in the dark matter distribution or internal instabilities have also been considered as mechanisms for triggering bar instabilities (Curir et al. 2008). However the bars can form at any time during the lifetime of the disk (Widrow et al. 2008) and the bars which do form in low mass disks have a short lifetime (~ 1 Gyr) because gas can destroy the bars, though again this is debated. Curir et al. (2008) find bars in low mass dark matter dominated disk galaxies can live for a very long time in Λ CDM cosmology. According to simulations when bars first form in a disk they are long and thin with very little spiral structure in the disk. As the disks evolve the bars become smaller and the disks develop more spiral patterns. Thus our average bar fraction in low mass galaxies would most likely be averaged over different stages in the life of a bar. On the other hand for high mass, bulge dominated galaxies, which have very little gas, it has been found that once a bar forms they are not easily destroyed and are strengthened by buckling instabilities which may cause the bar to shrink in size but will not destroy it. Thus in massive galaxies in the local universe the bars are most likely long lived. Thus gas fractions are more important in low mass galaxies. The effect

of gas on low concentration galaxies with respect to mass can be argued in two ways. First it is reasonable to suppose that if galaxies are evolving secularly, the mass of the galaxy increases as gas fraction decreases due to star formation. Thus the galaxies are less prone to instabilities and bar formation triggers such as satellite collisions and this would cause the bar fraction to decrease as mass increases. This approach considers the role of gas in the creation of bars. However, the problem can be inverted. Bar-gas interactions can destroy bars thus as the gas fraction decreases it is not unreasonable to suggest that the bars which already formed in low mass disks should be more stable as the galaxy mass increases. But this implies bar fractions should not decrease with increasing mass. Thus some other process may be responsible for the decrease in bar fractions as mass increase. Unfortunately, this is where the life time of exponential bars may come into play and requires detailed numerical modeling. If mass is built up by major mergers then bar formation, especially in a galaxy without a bulge, can be disrupted. However in the case of mergers a central bulge component is normally built up and thus mergers would not account for the decrease in bar fraction with mass for a given concentration.

There is a running debate on whether central mass concentrations (CMC) are capable of destroying bars, and if so what mass concentrations are required and how prone bars are to destruction (Shen & Sellwood 2004; Bournaud et al. 2005). The central mass concentration can be due to stellar mass but also due to the build up of gas and dust. It has been shown that barred galaxies do have a larger concentration of CO (Sheth et al. 2005; Sakamoto et al. 1999) and PAH emission (Regan et al. 2006) than unbarred galaxies. It has been suggested that if the growth of the CMC does not completely dissolve a bar (Shen & Sellwood 2004) the gas flow to the center aided by the bar is itself responsible for bar destruction (Friedli & Benz 1993). Bournaud et al. (2005) suggests the transfer of angular momentum between the infalling gas and the bar can severely weaken the bar. However according to the simulation this can only occur if the disk is not dominated by dark matter in which case angular momentum is transferred to the dark matter and the bar is not destroyed. These two processes, the build up of a central concentration and the transfer of angular momentum from infalling gas to bars in stellar mass dominated systems could account for the decreasing bar fraction trends we observe at a given mass.

How do our observations constrain scenarios for bar growth /destruction? It has been shown by Elmegreen & Elmegreen (1985, 1989) that the nature of bars change along the Hubble Sequence. Bars in early type galaxies are longer, stronger, show a flatter light profile and a strong correlation with grand design 2-spiral arm structures compared to bars in late type galaxies which show an exponential light profile and more multiple armed or flocculent arm structure. This bimodality in bar type may be directly related to the bimodality in bar fractions

which we have shown exists with mass and color. To illustrate this, Figure 6.10 shows representative examples of bars below and above the transition mass threshold of $\text{Log}M \sim 10.2$ sorted in increasing mass. The first noticeable difference between the two panels is the color of the galaxy, where the lower mass galaxies are blue while the higher mass galaxies are red as expected. Galaxies in the higher mass bin have definite bulges while those in the lower mass bin have no bulge or a very tiny bulge and more flocculent arm structure. There is a possible indication of increasing bulge presence with mass in the low-mass barred galaxies. If this is the case we would expect bar fraction to be keyed to concentration.

Figure 6.11 shows the fractional histograms relating the bar fraction to mass keyed to concentration (left) and color (right) for objects without AGNs. With respect to bar fractions keyed to color (right) we see that blue objects occupy the low mass peak and redder objects occupy the high mass peak as expected. As mass increases, the fraction of blue galaxies with bars

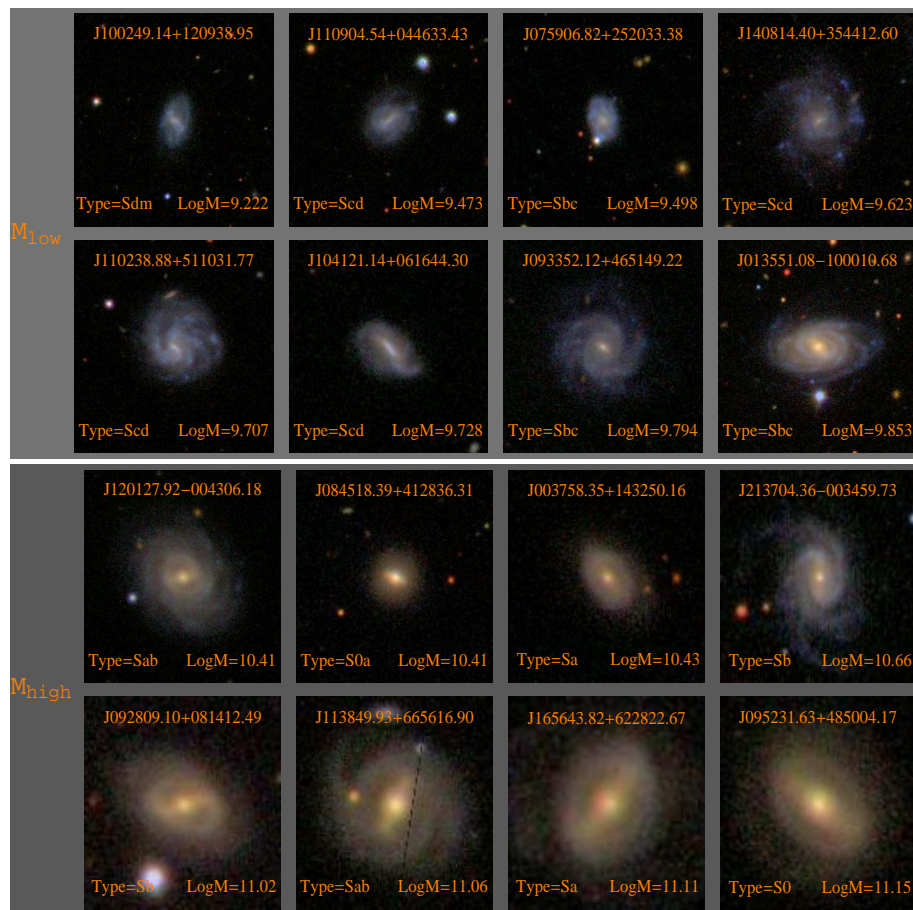


Figure 6.10: Bimodality in Bars: The top two rows shows a random sample of bars below the transition mass of 10.2 while the bottom two rows show barred galaxies above the transition mass. The J2000 objects identifier is listed at the top, the type in the bottom left corner and the mass on the right. Objects are arranged in order of increasing mass.

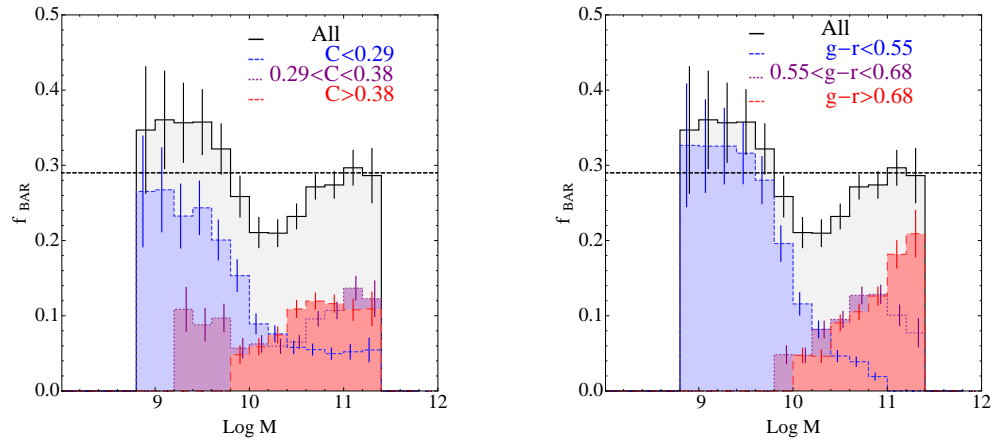


Figure 6.11: Bar fraction as a function of Mass keyed to concentration (left) and color (right) in three quantile bins. Blue indicates the lowest quantile, purple the intermediate range and red the highest quantile. For improved statistics we use $b/a > 0.4$ and restrict the sample to non-AGNs.

decreases. Interpreting this result is easier when considering concentration in the left hand panel.

The first thing we notice with bar fraction keyed to concentration (left) is that the low mass peak is dominated by low concentration galaxies but low concentration galaxies span the whole range in mass. Secondly, as concentration increases the bar fraction drops in the low mass peak and increases in the high mass peak. Nearly all of the most concentrated galaxies reside in the high mass peak but have a very weak dependence on mass above $\text{Log}M \sim 10.4$. The third and most important point to note is that in the lowest concentration bin, bar fraction decreases steeply with increasing mass. Or in other words, although low concentration galaxies are significantly more barred than higher concentration galaxies, their bar fraction is very sensitive to the mass of the galaxy. Thus the larger the stellar mass of the galaxy is in comparison to the central concentration (which should be related to the central mass concentration), the more prone a bar is to being destroyed. For the higher concentration bin $0.29 < C < 0.38$, although the overall bar fraction is lower in the low mass peak, the decrease of bar fraction with mass is less steep compared to the lowest concentration bin. Thus the greater the central concentration, the less prone the galaxy is to bar destruction in the $\text{Log}M < 10.4$ regime. Above $\text{Log}M \sim 10.4$ the bar fraction for the lowest concentration bin does not depend on the stellar mass of the galaxy. For the intermediate concentration galaxies, the bar fraction starts to increase above $\text{Log}M \sim 10.6$ and for the highest concentration galaxies, the bar fraction starts to increase above $\text{Log}M \sim 9.8$ and is nearly constant for $\text{Log}M > 10.4$. Thus low mass, low concentration galaxies are more likely to contain bars. However bars are more easily destroyed in intermediate mass, low concentration galaxies. Intermediate concentration galaxies

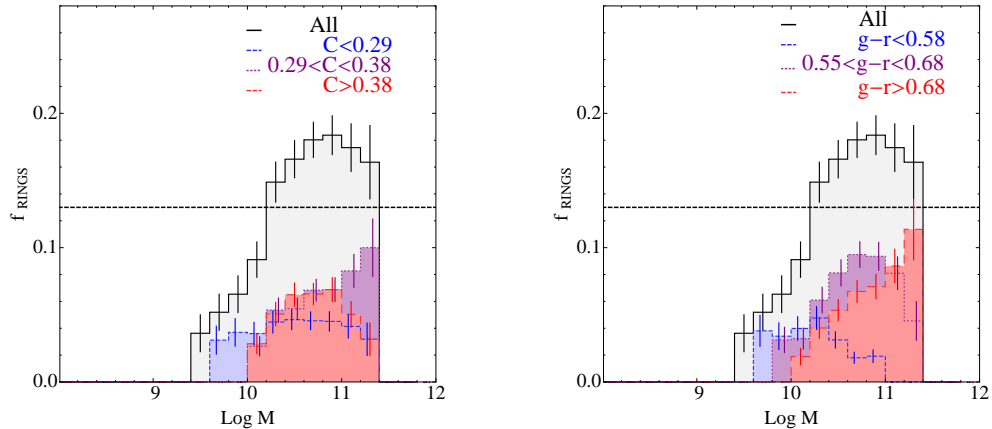


Figure 6.12: Ring fraction as a function of Mass keyed to concentration (left) and color (right) in three quantile bins. Blue indicates the lowest quantile, purple the intermediate range and red the highest quantile. For improved statistics we use $b/a > 0.4$ and restrict the sample to non-AGNs.

have far fewer low mass bars but they are less prone to bar destruction by whatever process influences low concentration galaxies. Galaxies with large concentrations on the other hand are more likely to have bars above $LogM \sim 10$ and are not affected by the bar destruction processes of low mass, low concentration galaxies, possibly because the central mass concentration stabilizes the bar (Athanasoula et al. 2005).

Thus there appears to be two methods of bar destruction in low mass galaxies which may be dependent on each other. The first is related to increasing galaxy mass and the second to increasing central concentration. Numerical simulations have shown that exponential bars common in low mass galaxies are prone to bar destruction as the central concentration increases while flat surface density strong bars which occupy high mass galaxies are not destroyed by a central mass concentration but may have their bars shortened (Athanasoula et al. 2005). Our results are consistent with the former point but we cannot test the latter point as we have not measured the sizes of the bars in our sample. It should be noted that the central mass concentrations predicted to destroy bars are much larger (5% of disk mass) than what seems to be observed in low mass galaxies.

Numerical simulations also show that the formation of an inner Linblad resonance (ILR) or inner rings can cause bar destruction. However from Figure 6.12 we find the increase of inner ring fraction with mass in the regime $9.4 < LogM < 10$ is much smaller than the decrease in bar fraction. When keyed to concentration there is no variation of inner ring fraction with mass for the lowest concentration bin. So although, inner rings may be having an effect in destroying low mass bars, they do not appear to be the dominant cause. In addition we find that in high mass galaxies both bar and ring fractions increase implying a possible positive

correlation between their formation mechanisms.

For high mass galaxies, we find the bar fraction is roughly the same for any high concentration bin and is nearly constant with respect to mass. The cause of the initial increase in bar fraction with mass may be due to bars forming in bulge dominated systems due to some external trigger. However once a bar forms they are not easily destroyed. This could be why at the high mass end, the bar fractions are fairly constant. It is interesting to consider that high mass galaxies are formed further back in time and most likely by major mergers. Thus even if a merger destroys the bar, they do reform in less than a Hubble time. This is especially interesting considering the results of SE08. Sheth finds that bar fraction strongly decreases as a function of redshift but shows an interesting redshift-dependent trend with mass. Bar fraction is a strongly increasing function of mass at high redshifts, $z \sim 0.8$. The most massive galaxies would have formed earlier and would have had time to reform their bars by some triggering process. The intermediate mass bulge-dominated galaxies have not had enough time to form bars again at $z \sim 0.8$. But in the next redshift bin, more intermediate mass bulge-dominated galaxies have bars. Thus it seems in high mass galaxies bars gradually evolve by some triggering mechanism and once formed are stable excluding major mergers.

6.5 Variation of fine fractions with morphological parameters

In the previous section we showed that barred galaxies above and below the transition mass threshold of $M \sim 3 * 10^{10}$ exhibit different structural properties. Galaxies in the blue cloud have smaller bulges, and more flocculent spiral structure than objects in the red cloud which are more bulge dominated and have larger bars. We would expect this difference in structure to manifest in the variation of bar fraction with morphological quantities. We have already seen a dependence on central concentration with low concentration galaxies populating the blue cloud while high concentration galaxies predominantly populate the red cloud. However the interpretation of the dependence is not clear and begs further study.

6.5.1 Variation of fine fractions with Concentration

Figure 6.13 shows the histogram and fractional distribution of galaxies with bars, rings and lenses as function of central concentration. We find bars and rings span the whole range in concentrations while lenses occur predominantly in high concentration galaxies. In Figure 6.13(d) bar fractions show a subtle variation with concentration. For $C < 0.35$, bar fractions increase slowly with concentration. Beyond $C \sim 0.35$ bar fractions fall with increasing concentration. It should be noted that this transition value is the separation between the bimodal populations in concentration as can be seen in Figure 3.22. It should also be noted that our weak and

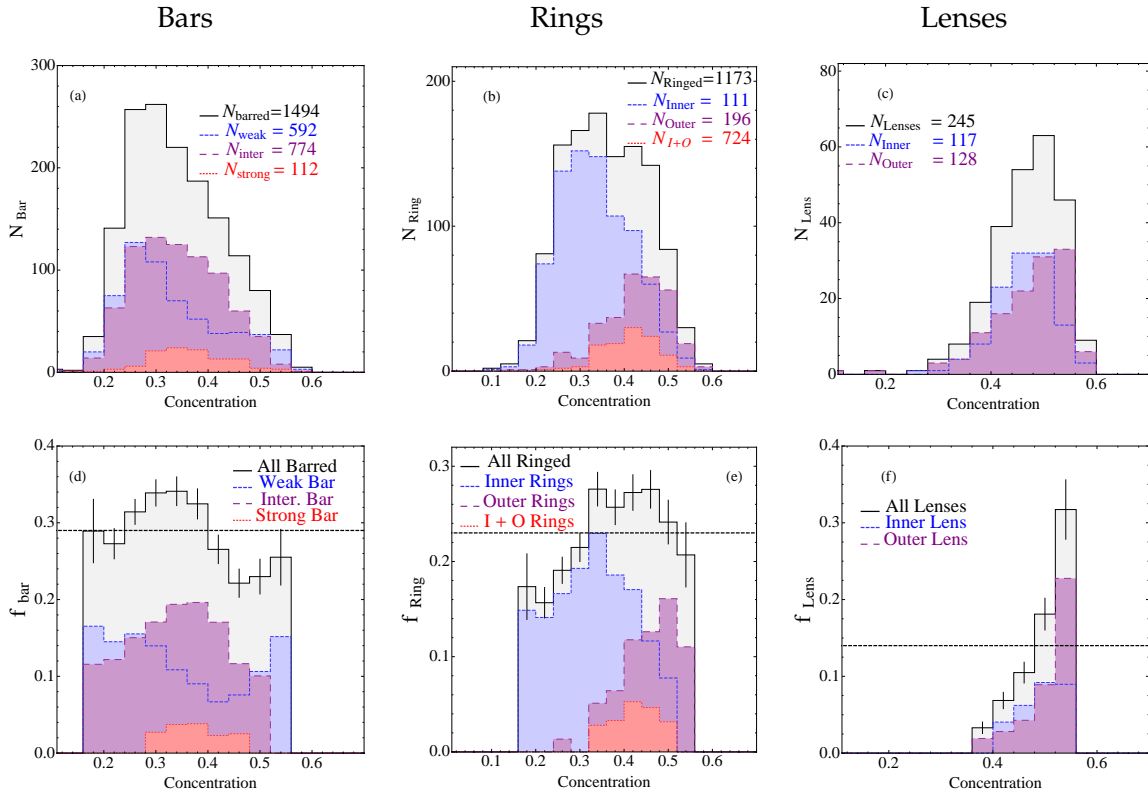


Figure 6.13: **Top:** Concentration Histograms for (a) Bars, (b) Rings and (c) Lenses in face-on disks. **Bottom :** Fractional histogram per T-Type for (d) Bars, (e) Rings and (f) Lenses. The distributions of each fine type are shown : Bars(blue), Rings (Purple), Lenses (Red). The horizontal line in each panel is the average total fine-fraction.

intermediate bar fractions behave slightly differently. Our weak bar fraction decreases with concentration until $C \sim 0.45$ beyond which the fraction starts to increase again. Intermediate bar fractions follow the overall distribution but peak at higher concentrations. Considering figures 6.13(d) and 6.7(d) we find the increase in bar fraction at higher masses and higher concentrations are predominantly due to intermediate strength bars.

It is interesting to note that although bar fractions decrease for $C < 0.30$, it is these very galaxies which dominate the low mass peak and have a larger bar fraction compared to intermediate concentration objects (with respect to mass). This is because the relation of concentration to bar fraction critically depends on mass. Considering just the variation of bar fraction with concentration averages over the mass ranges spanned by the galaxies.

Figure 6.13(b) and (e) show that inner rings are preferentially located in low concentration systems while outer rings are preferentially located in higher concentration systems as expected from the variation of ring fraction with T-Type. We find the ring fraction initially increases with concentration until $C \sim 0.35$ beyond which inner ring fraction starts to de-

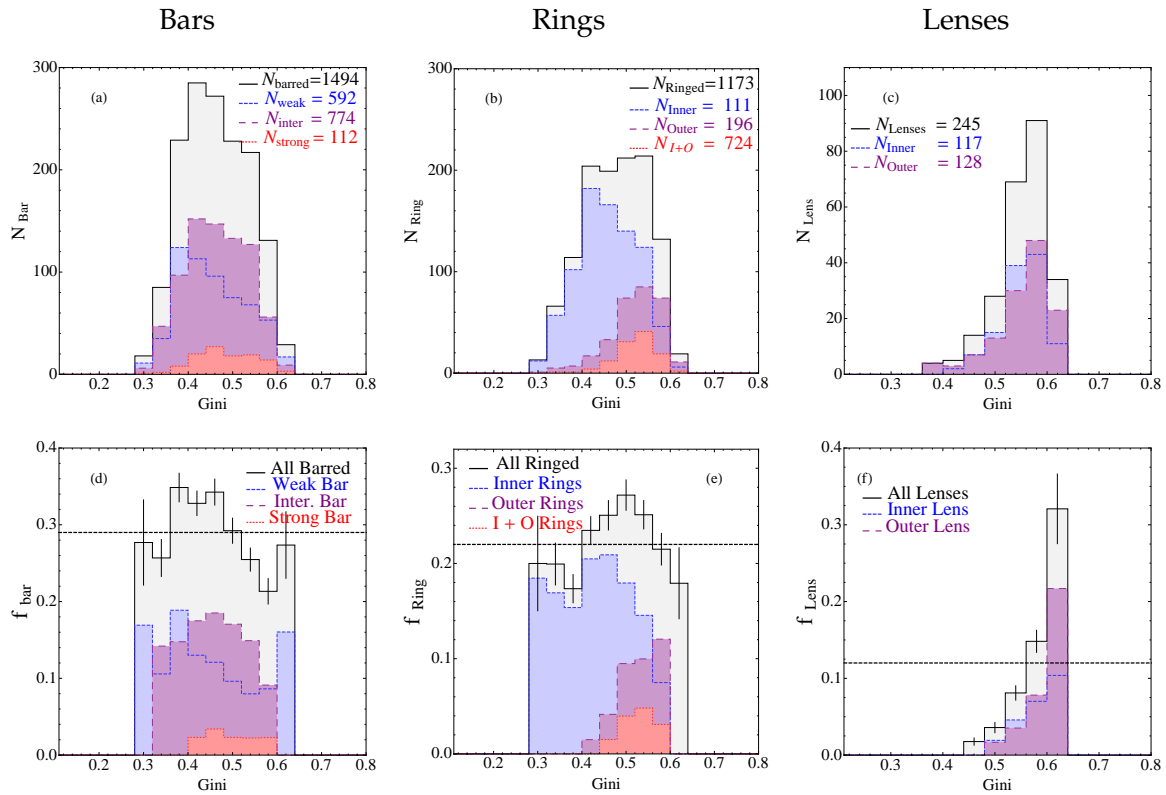


Figure 6.14: **Top:** Gini Histograms for (a) Bars, (b) Rings and (c) Lenses in face-on disks. **Bottom :** Fractional histogram per T-Type for (d) Bars, (e) Rings and (f) Lenses. The distributions of each fine type are shown : Bars(blue), Rings (Purple), Lenses (Red). The horizontal line in each panel is the average total fine-fraction.

crease but the outer ring fraction continues to increase. Thus the overall ring fraction between $0.35 < C < 0.5$ is fairly constant and starts to drop for $C > 0.5$. Inner and outer lenses are both located in high concentration galaxies as can be seen in Figure 6.13(c) and (f) with the lens fraction increasing sharply with C .

6.5.2 Variation of fine fractions with Gini

Figure 6.14 shows the variation of fine fraction with Gini and shows a similar trend as concentration. The bar fractions in panels (a) and (d) show weak and intermediate bars span the whole range in gini while strong bars are predominantly in high gini galaxies. Bar fraction initially increases with gini before turning over and decreasing with G . Weak and intermediate bars show slightly different variations with weak bar fraction decreasing with gini while the intermediate bar fraction follows the overall distribution more closely. As seen with concentration there is possibly an increase in bar fraction for very high gini values.

Figure 6.14 (b) and (e) show inner and outer rings can be clearly distinguished in gini

space. Inner rings predominantly have low G 's while outer rings and galaxies with both inner and outer rings have a high gini coefficient. The lens fraction in panel (f) shows lenses mainly occupy galaxies with high G and again their fraction increases sharply as gini increases. Inner and outer lenses follow the overall distribution. Unlike concentration, gini does not depend on the choice of aperture or a defined center.

6.5.3 Variation of fine fractions with Asymmetry

Figure 6.15 shows the variation of fine fractions with rotational asymmetry. Bars (a), rings (b) and lenses (c) span the whole range in asymmetries. The overall bar fraction is initially constant with asymmetry (within error bars) and then drops from 30% at $\text{Log}A \sim -1.5$ to 20% at $\text{Log}A \sim -1$. Thus as asymmetry increases bar fraction decreases. In the most asymmetric objects, the error bars are fairly large and it is uncertain if the increase in bar fraction is real. We do expect very late type and irregular galaxies with high A to be barred (Barazza et al. 2008). Considering bar sub-classes we find strong bars occupy the middle of the distribution, while

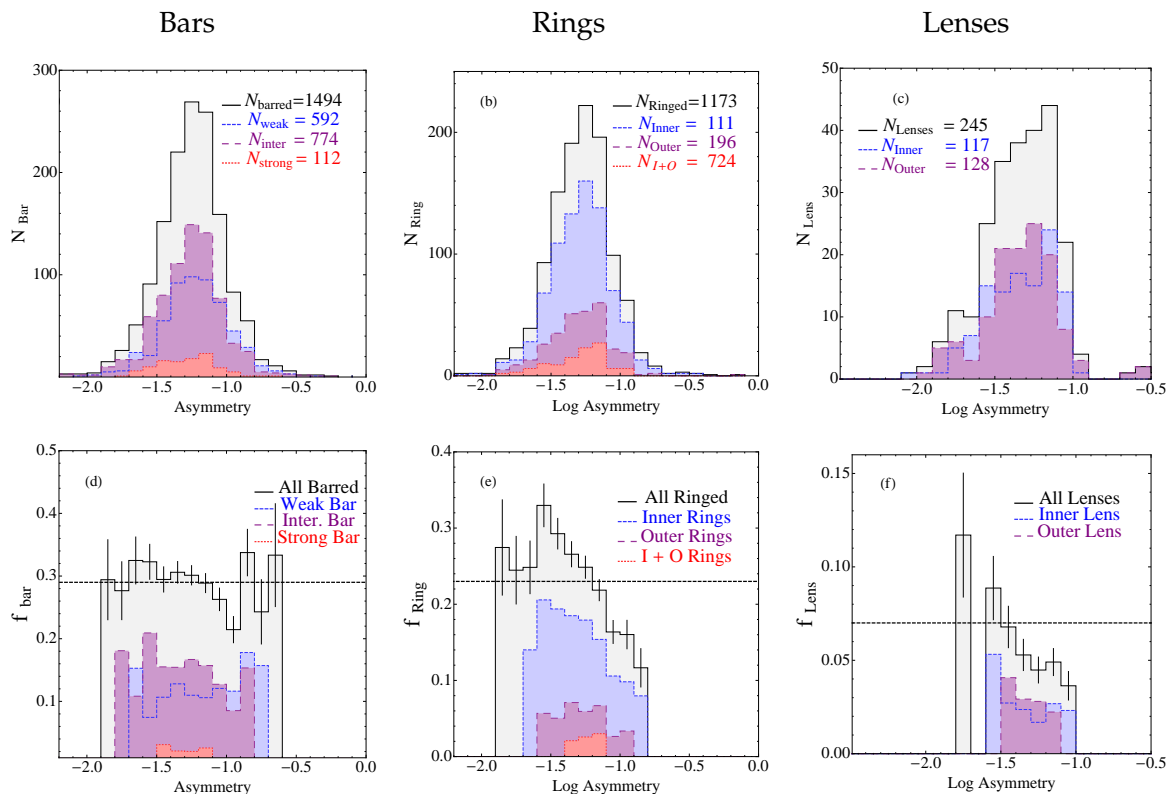


Figure 6.15: **Top:** Asymmetry Histograms for (a) Bars, (b) Rings and (c) Lenses in face-on disks. **Bottom** : Fractional histogram per T-Type for (d) Bars, (e) Rings and (f) Lenses. The distributions of each fine type are shown : Bars(blue), Rings (Purple), Lenses (Red). The horizontal line in each panel is the average total fine-fraction.

weak and intermediate bars span the whole range of possible asymmetries. No clear trend is discernible with weak and intermediate bars with their fractions being nearly constant with asymmetry.

With rings it is clear that as asymmetry increases (ignoring the first 3 points) the ring fraction decreases from 35% at $\text{Log} A \sim -1.6$ to 10% at $\text{Log} A - 0.8$. The overall trend is followed by inner rings but not as tightly by outer rings. Inner rings span the range of asymmetries while outer rings are in the middle of the distribution. The ring fraction decreases when objects become very symmetric dropping from 35% at $\text{Log} A \sim -1.6$ to $\sim 25\%$ at $\text{Log} A - 2$ though the error bars are large. This is indicative of the falling ring fractions for S0/S0a galaxies in our sample.

Both inner and outer lenses in Figure 6.15 (f) show a decrease in lens fraction with increasing asymmetry as expected. Lenses occupy the middle of the distribution of asymmetry though it should be noted that there are a few at either extreme.

6.5.4 Variation of fine fractions with M20

Figure 6.16 shows the variation of fine fractions with M20. Bars (a) and rings (b) span the whole range in M20 values. Lenses are predominantly located in low M20 galaxies. Figure 6.16 (d) shows that as M20 increases the bar fraction plummets from 55% at $\text{Log} M20 \sim -2.3$ to 24% at $\text{Log} M20 \sim -1.6$. As M20 continues to increase the bar fractions starts to increase again. Thus bar fractions show a clear bimodal nature with respect to M20. Intermediate and weak bars follow the overall distribution, with intermediate bars showing a stronger low M20 peak. Strong bars are predominantly in low M20 galaxies. Choosing a less rigorous axial ratio cut of $b/a > 0.4$ yields similar results except the low M20 peak is at 45% not 55%.

Figure 6.16 (b) and (e) shows that M20 clearly distinguishes between inner and outer rings as do concentration and gini. There are very few outer rings above $\text{Log} M20 > -1.7$ and most which are present appear to be in systems with both inner and outer rings. The overall ring fraction drops from 50% for $\text{Log} M20 \sim -2.3$ to 14% for $\text{Log} M20 \sim -1.5$ before hitting a plateau and slowly rising again at high M20's. M20 is the only quantity to show a clear break in the overall ring fraction though this can be attributed to the fact that it seems to be very good at distinguishing between ring types. The inner ring fraction follows the overall distribution but within error bars could be nearly flat. Outer rings show a strong increase in ring fraction as M20 decreases. Figure 6.16 (f) shows that inner and outer lens fractions strongly increase as M20 decreases. They also occupy galaxies with the lowest M20 or early type galaxies.

Thus M20 shows the most striking results out of the quantitative morphological parameters we have investigated. We find both bar and rings fractions to be bimodal with respect to M20. This is actually not so surprising given that M20 shows a very strong correlation with

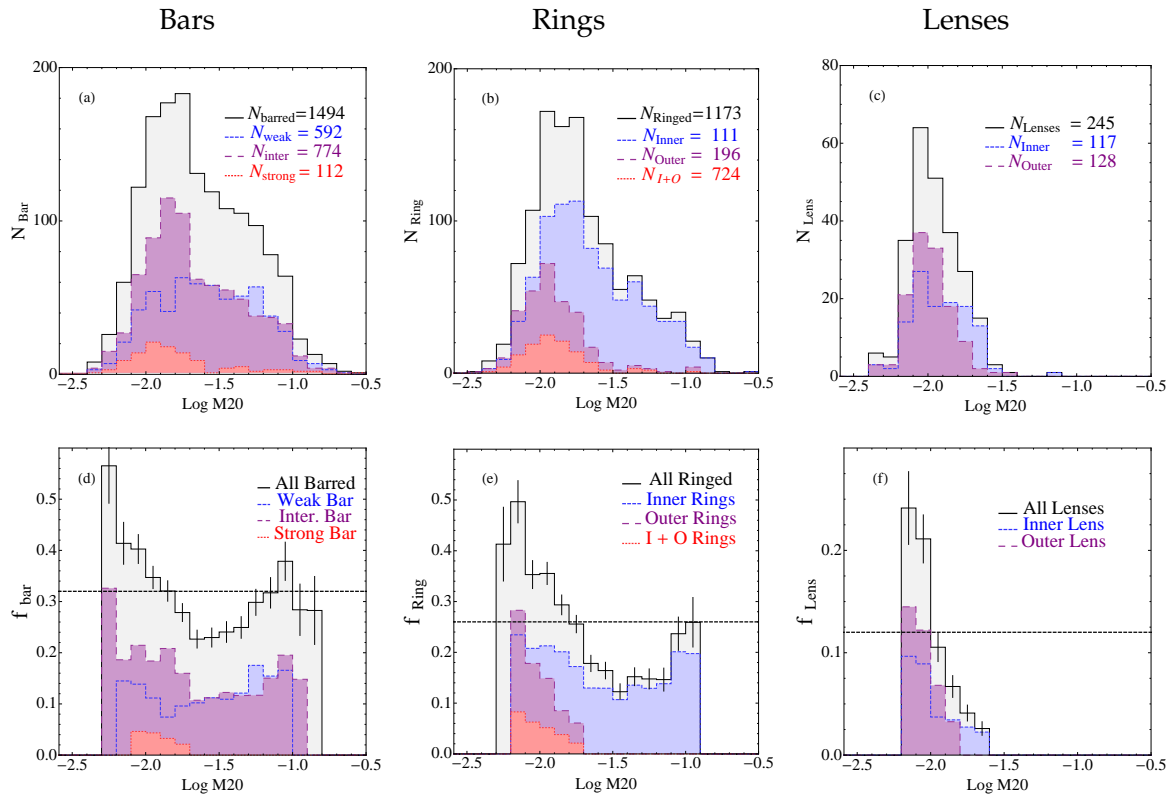


Figure 6.16: **Top:** M20 Histograms for (a) Bars, (b) Rings and (c) Lenses in face-on disks. **Bottom :** Fractional histogram per T-Type for (d) Bars, (e) Rings and (f) Lenses. The distributions of each fine type are shown : Bars(blue), Rings (Purple), Lenses (Red). The horizontal line in each panel is the average total fine-fraction.

color. We expect the high M20 peak to correspond to low mass, blue galaxies and the low M20 peak to correspond to high mass, red galaxies. Figure 6.17 shows this to be case. Thus high M20 galaxies ($\text{LogM20} > -1.48$) which we have seen from Figure 3.28 in Chapter 3 are dominated by Sb to Sd spiral galaxies are the major population in the blue peak.

6.6 Implications

6.6.1 Redshift evolution of bars

We are finally able to identify the cause for the disparate results regarding the evolution of bar fraction with redshift. Abraham et al. (1999), van den Bergh et al. (2002) and Sheth et al. (2008) were all probing high mass galaxies with $\text{LogM} > 10$ in their studies of the evolution of bar fraction with redshift. SE08 conclusively showed that bar fractions in massive galaxies are hierarchical with bars forming in the oldest, red galaxies first before forming in less massive, red galaxies. Thus the decrease in bar fraction with redshift is understandable as intermediate

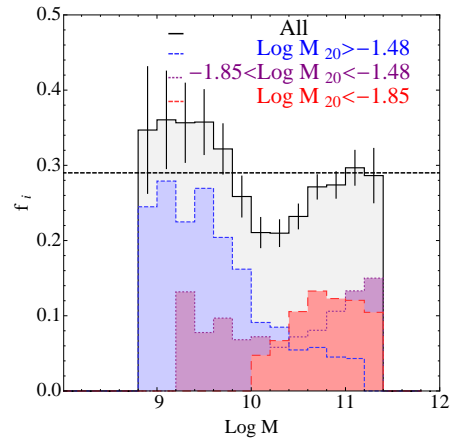


Figure 6.17: Bar fraction as a function of Mass keyed to $\text{Log } M_{20}$ in three quantile bins. Blue indicates the lowest quantile, purple the intermediate range and red the highest quantile. For improved statistics we use $b/a > 0.4$ and restrict the sample to non-AGNs.

mass galaxies have not had enough time to form their bars at high redshifts. Elmegreen et al. (2004) in their analysis of barred galaxies stated that the bar fractions were roughly constant with redshift given their error bars. In fact they find bar fractions decrease from $z \sim 0$ to $z \sim 0.7$ and then increase slightly at higher redshifts. This is the range in which low mass (Elmegreen & Elmegreen 2005) ‘clumpy-bar’ galaxies and ‘barred clump-cluster’ galaxies start to dominate as seen in Figure 11 of Elmegreen et al. (2004). Jogee et al. (2004) were probing to fainter magnitudes in their redshift studies and hence to lower masses. They were thus averaging over the bimodal distribution of bars. However this combined two different forms of bars, created by possibly different processes. As we have already said, low mass bars are most likely formed by some form of external trigger like a minor interaction as they are gas rich and unstable. Old, red and dead galaxies are gas poor and hence it is unclear if the same trigger will work. It is possible that a major merger could cause an instability leading to bar formation. Though currently not possible, it would be interesting to understand how bar fraction in low mass $\text{Log } M < 10$ galaxies evolve with redshift. At higher redshifts these would be the galaxies that dominate the luminosity function. Elmegreen et al. (2004) have already seen a higher bar fraction in their $z > 1$ bin where clump cluster galaxies start to dominate.

6.7 Summary

In conclusion we find the following major results:

1. Bar fraction are bimodal with mass and color.

2. The origins of bars at the low and high mass end are likely different.
3. There is a very strong dependence between bars, rings and lenses. It is unclear if bars are triggering rings or rings are destroying bars.
4. Quantitative morphological quantities show interesting trends with fine fraction. In particular M_{20} , the second order moment of the brightest 20% flux in a galaxy, is bimodal in bar and ring fractions. M_{20} , concentration and gini are good quantitative measures to distinguish inner ring dominated low mass galaxies.

Chapter 7

Role of AGN

7.1 Introduction

In the previous chapter we have established that bar fractions are bimodal with respect to mass and color, with the transition occurring at $\text{Log}M \sim 10.2$ and $g - r \sim 0.55$. This is the transition regime where galaxy properties move from the blue cloud to the red sequence. In addition, we find the dependence of bar fraction on central concentration varies above and below this transition mass. In this chapter we go on to investigate the possible influence of AGN on bar fractions as well as on rings and lenses. Kauffmann et al. (2003a) find Type 2 AGN reside almost exclusively in galaxies more massive than $\text{Log}M \sim 10$, with their fraction decreasing strongly at stellar masses below $10^{10} M_{\odot}$. This mass threshold is similar to that at which we find bar fractions are bimodal. Thus AGN may be connected with the bimodality of bar fractions. However, it should be noted that the determination of AGN fractions at lower masses and bluer colors may be underestimated due to biases in defining what constitutes an AGN. The effect of higher metallicities and recent star formation may mask the signal of an AGN especially LINERs. In this work we predominantly focus on high mass and redder systems.

The influence of AGN on bars is a contentious area of research. Many works have shown no significant difference in bar fractions between active and non-active galaxy samples in the optical (Hunt et al. 1999a; Ho et al. 1997; Moles et al. 1995). However recent works in the infrared (Laine et al. 2002; Knapen et al. 2000; Laurikainen et al. 2004), where bars are more easily detected have found active galaxies are more likely to host bars than inactive galaxies. There is better consensus with rings where Hunt et al. (1999a) find AGN have a higher fraction of rings than normal galaxies, specifically LINERs have a higher frequency of inner rings while seyferts have a higher frequency of outer rings. Arsenault (1989) also find AGN have a higher preponderance of either a bar or a ring (57.8%) versus normal galaxies which have a

fine fraction¹ of 38.9%. In our sample we find bar fractions are $\sim 30\% \pm 1\%$ in both active and non-active galaxies, lenses are $5\% \pm 1\%$ for both cases, while rings are $20\% \pm 1\%$ in non-active galaxies and $25\% \pm 1\%$ in active galaxies. Thus bars and lenses show no overall dependence on AGN while rings do show a weak dependence on AGN activity. As we have seen in the previous section, averaging over too many physical properties causes us to miss important physical relationships like the bimodal nature of bar fractions. Thus it is very important to study the variation of fine fraction in active and non-active galaxies subdivided by the physical properties of the galaxies. We will also investigate the variation of AGN fraction with physical and quantitative morphological properties and compare them with the variation of fine fractions.

7.2 Influence of AGN on fine fractions

7.2.1 Fraction of Bars, Rings and Lenses with T-Type

Figure 7.1 shows the number counts and fractional distributions for galaxies with either a bar, ring or lens as a function of Hubble type. We show the distribution for (a) the entire face on disk sample, (b) the face-on sample without an AGN and (c) the face-on sample with an AGN. The dashed line shows the average fine fraction in each case. With respect to T-Type it is apparent that the average fine fractions are similar for all three cases where objects without AGN have a fine fraction of $42\% \pm 1\%$, objects with AGN have an average fine fraction of $45\% \pm 1\%$ and the total AGN fraction is $43\% \pm 1\%$. Thus the overall fine class fraction depends only slightly on the presence of an AGN. Considering each fraction individually, bar fractions are 29.5%, 29% and 30% for all, normal and AGN only galaxies; rings are 21%, 20%, 25% and lenses are $\sim 5\%$ for all, normal and AGN hosting galaxies. However the trends with T-Type are of more interest.

In galaxies with AGN the bar fraction falls from $40\% \pm 3\%$ for Sc's to $20\% \pm 4\%$ for Sa's. In the non-AGN case, bar fractions are lower for Sc/Scd galaxies at $30\% \pm 2\%$, increase suddenly for Sbc galaxies to $38\% \pm 2\%$ and gradually decrease to 28% for S0a galaxies. It is clear that the decrease of bar fraction from Sb galaxies to S0a galaxies is much sharper for galaxies with AGN than for galaxies without AGN. The 10% increase in bar fraction for Sc galaxies with AGN is surprising. It may well be that the process of formation of an AGN helps drive bars most efficiently in galaxies with small bulges. The lack of bulge-less disk galaxies in our sample will not affect these results which are seen for T-Types Sc and earlier.

¹Fine fraction is defined as the fraction of galaxies with either a bar, ring or lens component

7.2.2 Optical fraction of Bars, Rings and Lenses with Sersic Index n

Figure 7.2 shows the sersic distributions of bars, rings and lenses for (a/d) the complete face-on disk sample, (b/e) the non-AGN face-on disk sample and (c/f) the AGN face-on disk sample. Distributions of bar fractions are similar for AGN and non-AGN. However interesting trends are seen with the ringed galaxy population. There are more ringed galaxies at lower n for galaxies with AGN (predominantly LINERS) than galaxies without. Hunt & Malkan (1999) have also found that LINERS have a higher frequency of inner rings with Seyferts having a higher frequency of outer rings. We find LINERS, with low n specifically, show 2 - 3 times higher frequency of rings than non-active galaxies. Thus rings in low n systems are a sign of AGN activity. As a system becomes more bulge dominated the bar and ring fraction starts to increase. However in $3 < n < 5$ galaxies, bar and ring fractions are actually lower in objects with AGN than objects without an AGN component. Thus although AGN appear to enhance the probability of finding a ring in disk systems, the presence of an AGN actually reduces the probability of finding a bar or a ring in more bulge dominated systems. This result is valid for

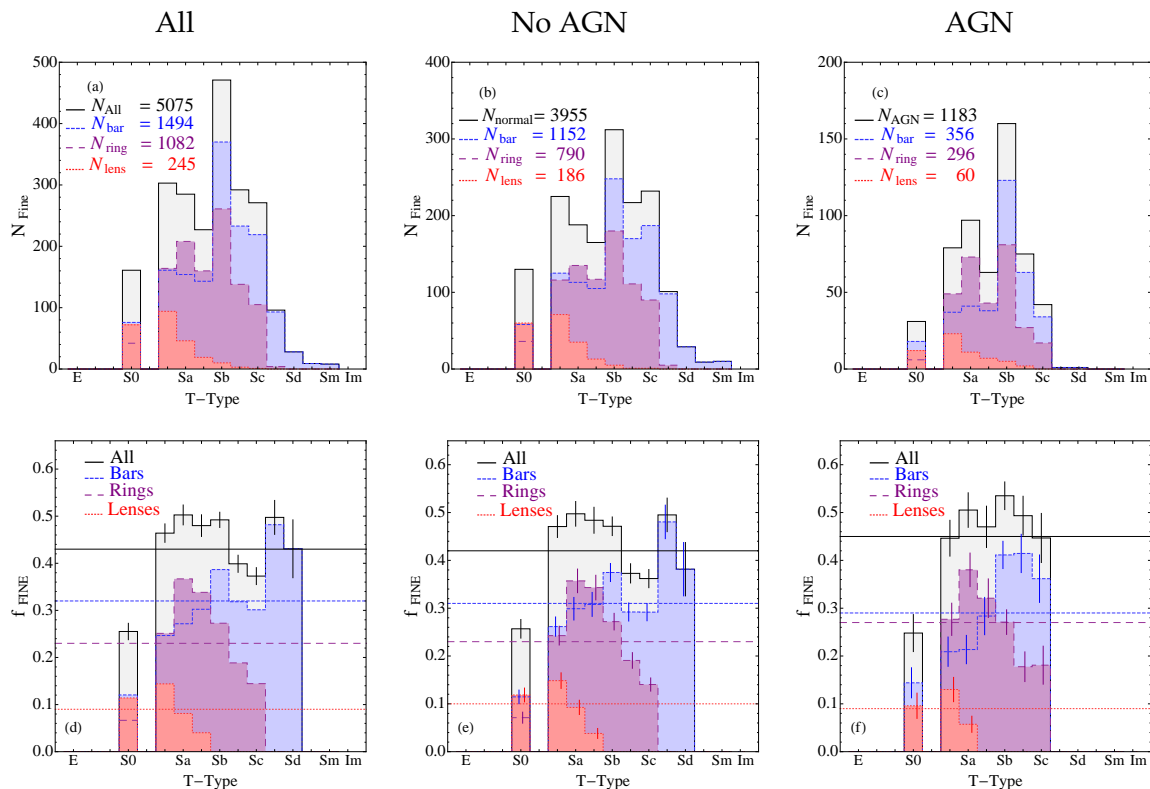


Figure 7.1: Fractional distribution of galaxies with fine features (Bars or Rings or Lenses) against T-Type for (a) face-on sample of disk galaxies (b) face-on sample of disk galaxies with no AGN (c) face-on sample of disk galaxies with AGN. The fractional histograms of each fine type are shown : Bars(blue), Rings (Purple), Lenses (Red). The horizontal line in each panel is the average fine-fraction.

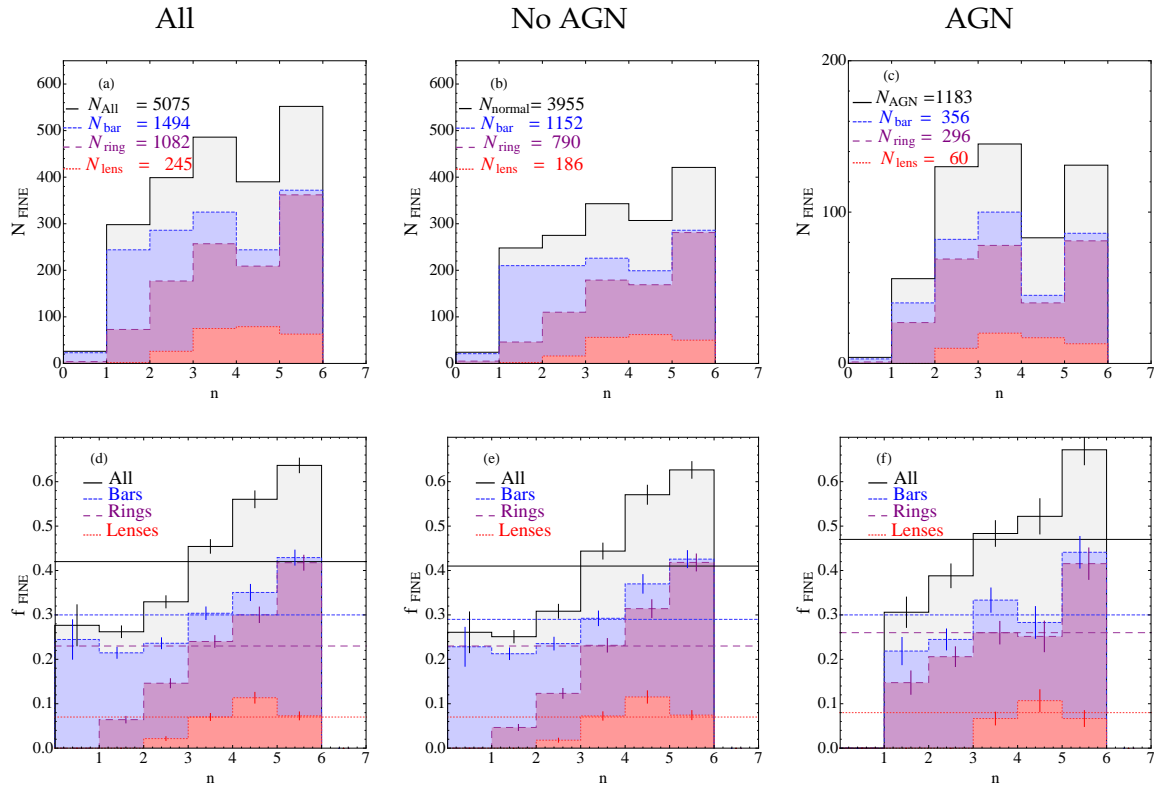


Figure 7.2: Fractional distribution of galaxies with fine features (Bars or Rings or Lenses) against sercic index for (a) face-on sample of disk galaxies (b) face-on sample of disk galaxies with no AGN (c) face-on sample of disk galaxies with AGN. The fractional histograms of each fine type are shown: Bars (blue), Rings (Purple), Lenses (Red). The horizontal line in each panel is the average fine-fraction.

LINERs and given the results obtained by Hunt & Malkan (1999) may not be valid for galaxies with Seyferts. There is no difference in the lens fractions in active vs. non-active galaxies.

7.2.3 Optical fraction of Bars, Rings and Lenses with Mass

Figure 7.3 shows the number count histogram and fractional distribution as a function of mass for galaxies with either a bar, ring or lens. We show the distribution for (a/d) the entire face on disk sample, (b/e) the face-on sample without an AGN and (c/f) face-on sample with an AGN. As has been noted in the previous chapter for non-AGN objects in the low mass peak, as mass increases the bar fraction decreases while the ring fraction increases. For galaxies more massive than $LogM \sim 10$, bar and ring fraction both increase. Thus the presence of an AGN is not responsible for the break in the bar fraction vs mass relation. Figure 7.3 (c) shows there are no galaxies hosting AGN with masses below $LogM \sim 10$. The bar and ring fractions peak at $LogM \sim 10.4$ and then drop off for ringed galaxies but are nearly constant for barred galaxies. The lens fraction is nearly constant or decreases slightly with mass. It is interesting to note that

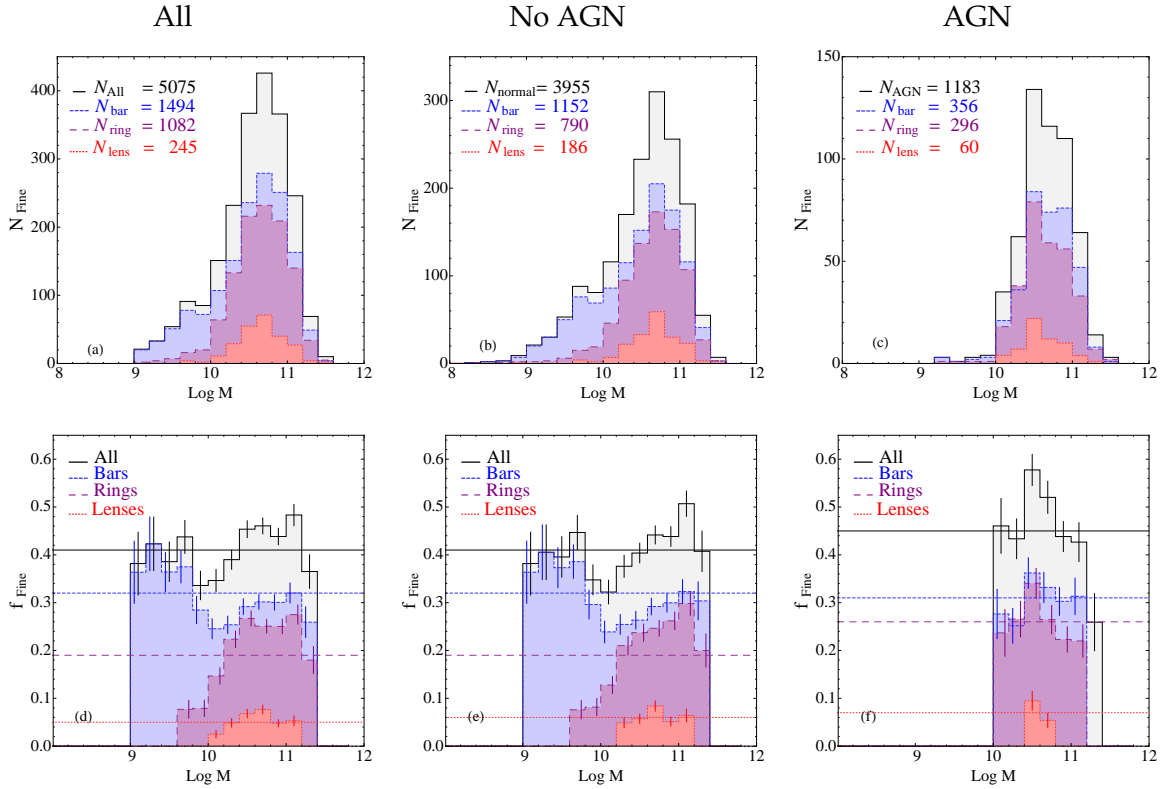


Figure 7.3: Fractional distribution of galaxies with fine features (Bars or Rings or Lenses) against Mass for (a) face-on sample of disk galaxies (b) face-on sample of disk galaxies with no AGN (c) face-on sample of disk galaxies with AGN. The fractional histograms of each fine type are shown : Bars(blue), Rings (Purple), Lenses (Red). The horizontal line in each panel is the average fine-fraction.

the overall variation of fine fractions with mass for objects with an AGN are different than for objects without an AGN. For example, a $10^{10}M_{\odot}$ galaxy with an AGN is 50% more likely to have fine structure than its non-AGN counterpart. When broken down further, the trends are even more striking. A $10^{10}M_{\odot}$ galaxy with an AGN is three times more likely to have a ring than is a non-AGN hosting galaxy of the same mass. The total fine fraction in galaxies without an AGN gradually increases by 18% from $\text{Log } M \sim 10$ to $\text{Log } M \sim 11.2$. In the same mass range for galaxies with AGN, we see an initial break in the fine fraction and then a decrease from 58% at $\text{Log } M \sim 10.4$ to 43% at $\text{Log } M \sim 11.2$.

7.2.4 Optical fraction of Bars, Rings and Lenses with Luminosity

Figure 7.4 shows the number count histogram and fractional distribution as a function of absolute magnitude for all three fine features for active and non active galaxies. The color coding is the same as Figure 7.1. Clearly the fine fractions of galaxies as a function of luminosity are different in the AGN and non-AGN samples. For objects with AGN we find the bar-fraction

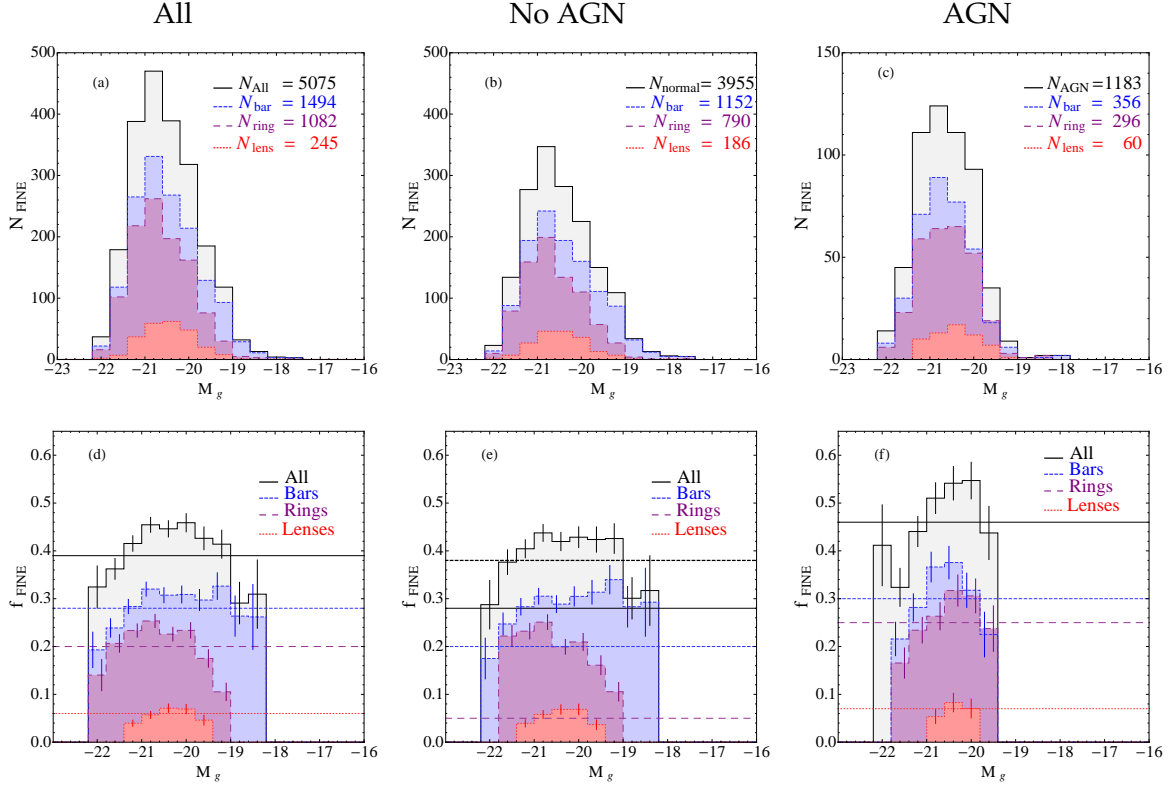


Figure 7.4: Fractional absolute magnitude distribution of galaxies with fine features (Bars or Rings or Lenses) against T-Type for (a) face-on sample of disk galaxies (b) face-on sample of disk galaxies with no AGN (c) face-on sample of disk galaxies with AGN. The fractional histograms of each fine type are shown : Bars (blue), Rings (Purple), Lenses (Red). The horizontal line in each panel is the average fine-fraction.

and ring fraction peaks at $M_g \sim -20$ and falls off at both brighter and fainter ends. The decrease in bar fraction with decreasing luminosity is almost certainly due to the absence of lower mass galaxies with AGN. However the bar and ring fractions do fall faster by 15% with increasing luminosity ($-22 < M_g < -20.5$) in AGN than in normal non-active galaxies where the bar fraction only starts dropping for galaxies brighter than $M_g < -21$ and drops by a factor of $\sim 6\%$. In addition ring fraction are seen to increase from 10% for $M_g \sim -19$ to 24% for $M_g \sim -21$ while in AGN the ring fractions reach a peak at $M_g \sim -20$ and start to decrease around $M_g < -20.6$. Thus the fine fractions of galaxies as a function of luminosity are definitely influenced by AGN activity.

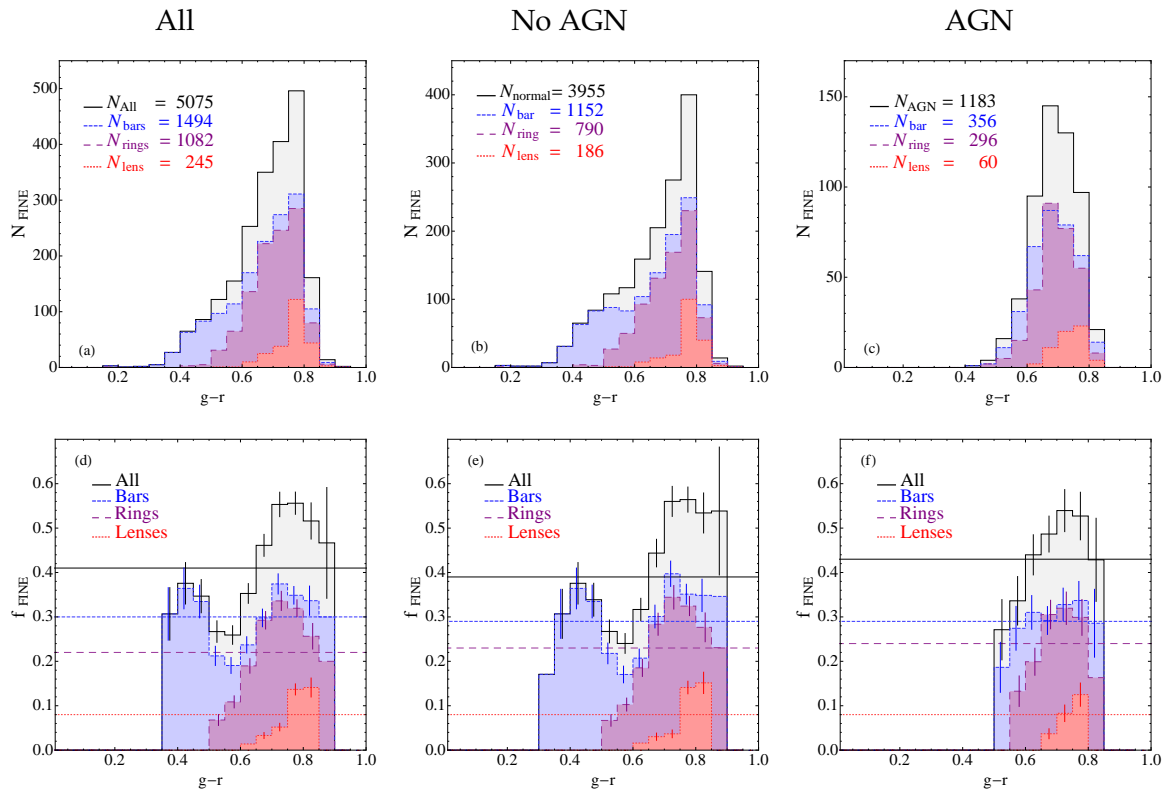


Figure 7.5: Fractional color distribution of galaxies with fine features (Bars or Rings or Lenses) against color for (a) face-on sample of disk galaxies (b) face-on sample of disk galaxies with no AGN (c) face-on sample of disk galaxies with AGN. The fractional histograms of each fine type are shown : Bars(blue), Rings (Purple), Lenses (Red). The horizontal line in each panel is the average fine-fraction.

7.2.5 Optical fraction of Bars, Rings and Lenses with Color

Figure 7.5 shows the number histogram and fractional distribution as a function of color for galaxies with either a bar, ring or lens. The color coding is the same as Figure 7.1. As with mass, we find the bimodality of bar fraction with color is not due to the presence of AGN. We find no objects with AGN in the blue peak as has been noted in previous works (Kauffmann et al. 2003a).

For very blue, non-AGN objects (ignoring the first 2 data points which have a small sample size) the bar fraction decreases as galaxies become redder. At the same time, the ring fraction starts to increase. Beyond the transition both ring fraction and bar fractions increase as the galaxies become redder. They peak at $g-r \sim 0.7$ and then decrease again. For the AGN sample Figure 7.5 (c), we find the bar and ring fraction gradually increase as objects become redder and plateau at 30% with the ring fractions reaching their peak fractions at redder colors. Thus, although the bimodality in color is not due to AGN, we find the behavior of ring and bar fractions are different in the AGN case where the bar fractions and ring fractions are higher

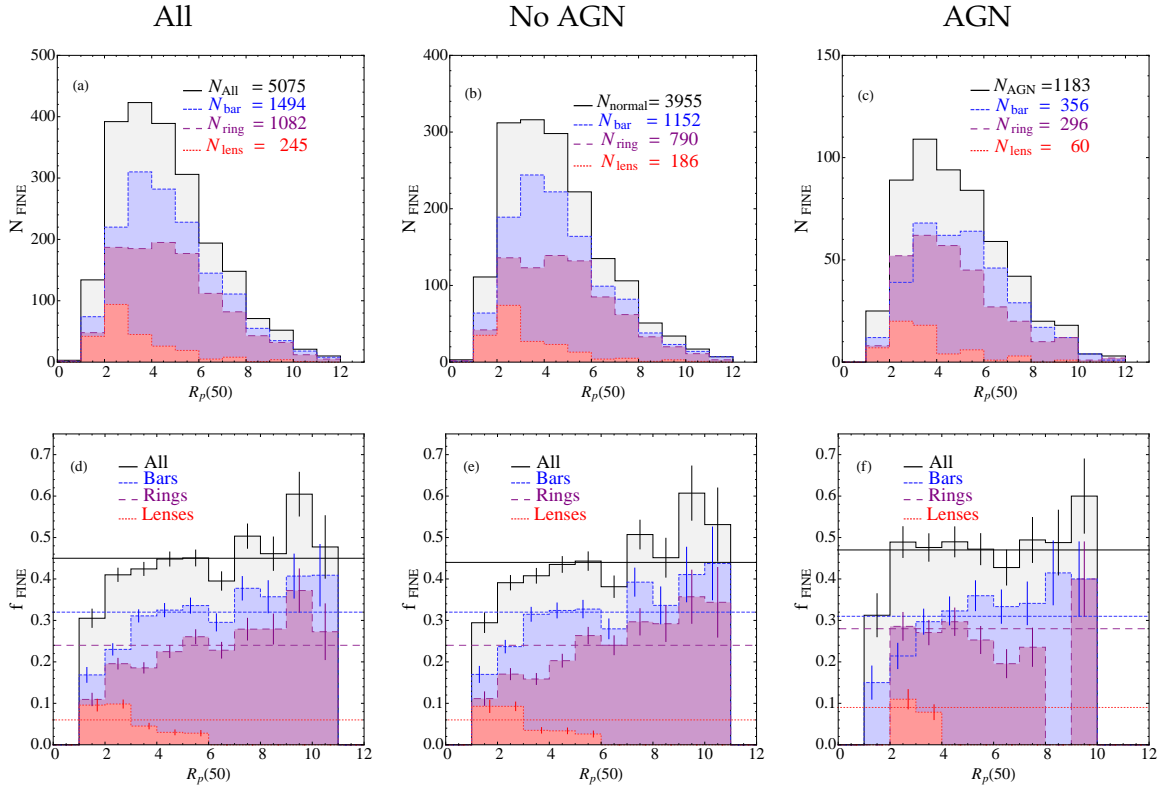


Figure 7.6: Fractional size distribution of galaxies with fine features (Bars or Rings or Lenses) against size for (a) face-on sample of disk galaxies (b) face-on sample of disk galaxies with no AGN (c) face-on sample of disk galaxies with AGN. The fractional histograms of each fine type are shown : Bars(blue), Rings (Purple), Lenses (Red). The horizontal line in each panel is the average fine-fraction.

for $0.5 < g - r < 0.6$ than in the non-AGN case.

7.2.6 Optical fraction of Bars, Rings and Lenses with Size

Figure 7.6 shows the number counts histogram and fractional distribution as a function of petrosian half light sizes for all three fine types for the AGN and non-AGN case. The color coding is the same as Figure 7.1. We find a surprisingly strong dependence of fine fraction properties on the size of a galaxy and the presence of an AGN. In galaxies without AGN the overall fine fraction increases with size while in galaxies with AGN, the total fine fraction is nearly constant. This is predominantly due to ringed galaxies. The ring fraction steadily increase from 10% for $R_p50 \sim 1kpc$ to 30% for $R_p50 \sim 11kpc$ for galaxies without an AGN. In galaxies with an AGN, the ring fraction initially rises, peaks at $R_p50 \sim 4kpc$ and then decreases as size increases. Bar fraction in the non-AGN case appears to gradually increase with size, though given the error bars it is consistent with no variation beyond $R_p50 > 3kpc$. In galaxies

with an AGN the bar fraction is nearly constant at 30% for $R_{p50} > 3kpc$. Lens fractions are nearly the same on both cases. Thus in normal galaxies, the ring fraction grows as galaxies get bigger but this is not the case for galaxies which host AGN. In addition, the overall fine fraction is larger in the presence of an AGN predominantly because the fine fraction at smaller sizes $R_{p50} < 6kpc$ is on average higher in the AGN case than in the non-AGN case.

7.2.7 Summary

We find the presence of an AGN appears to alter the frequency of fine types (bars, rings and lenses) as a function of galaxy properties. With some properties like T-Type the difference is subtle, an increase in the bar fraction of Sc galaxies. With sersic index, there is an over abundance of rings at low n . Luminosity, mass and size show the strongest variation, where the direction of dependence for the fraction of rings changes. Thus accounting for AGN is important to any analysis of disk galaxies.

7.3 AGN Fraction Statistics

Thus far we have only looked at the role of AGN in terms of how their presence influences barred, ringed or lensed galaxies. It is not clear if fine fractions are changing because of a variation in the AGN fraction or because of a change in the strength of AGN with physical properties. In this section we focus on the variation of AGN fractions with physical properties and compare it with the variation of fine fractions over the same range. Previous work looking at AGN fractions have predominantly been focused on the effect of environment or galaxy morphology as defined by concentration (Kauffmann et al. 2003a). In addition, the limited work studying the variation of AGN fraction as a function of the presence of different fine types have been restricted to barred seyfert galaxies (Ho et al. 1997).

7.3.1 Dependence of AGN fractions on T-Types

Ho et al. (1997) looked at a sample of 319 spiral galaxies to understand the influence of barred galaxies on AGN. They found the AGN fraction was stronger in classical spirals ($T < 5$) than in late type spirals ($T > 4$) in both barred and unbarred galaxies. In addition, they found AGN fractions in barred late type spirals were lower than in unbarred late type spirals. No difference was seen in AGN fractions between barred and unbarred galaxies for early type spirals. Due to the low number statistics involved the trends carried no formal statistical significance, although each trend was stronger when considering strongly barred galaxies only. The trends were attributed to the morphological composition of the sample and not to influence of the

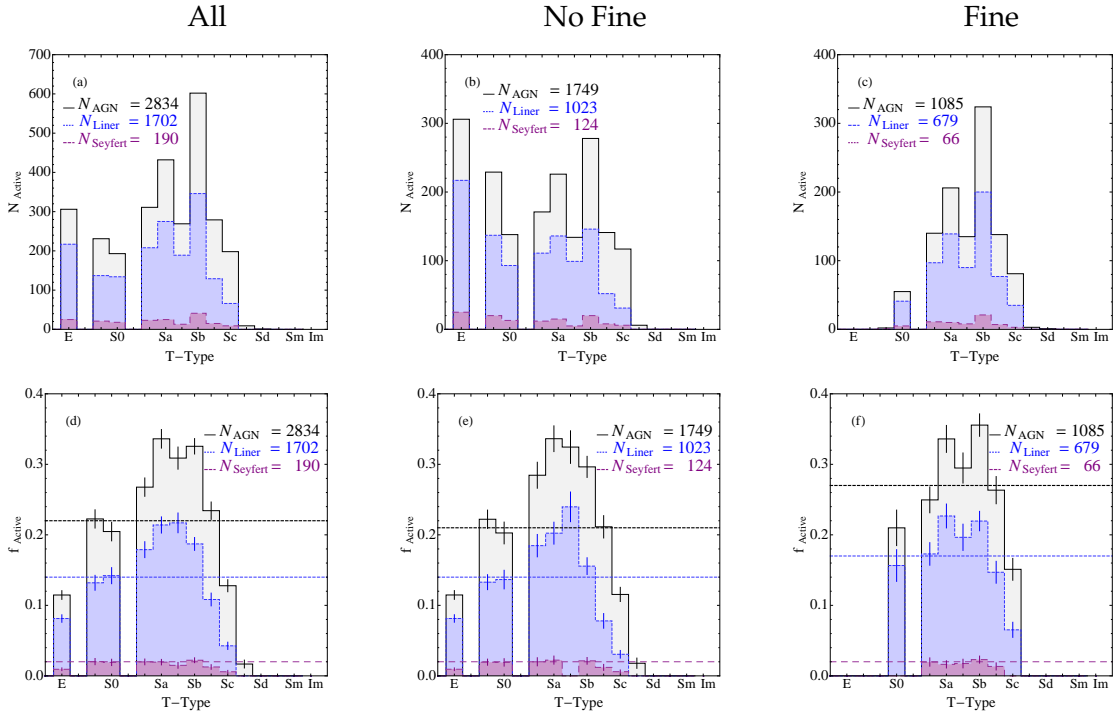


Figure 7.7: **Top Row:** Histogram of T-Type for (a) all galaxies with AGN, (b) AGN galaxies without fine components and (c) AGN galaxies with fine components. **Bottom Row :** AGN fraction vs T-Type for (a) all galaxies, (b) galaxies without fine components and (c) galaxies with fine components.

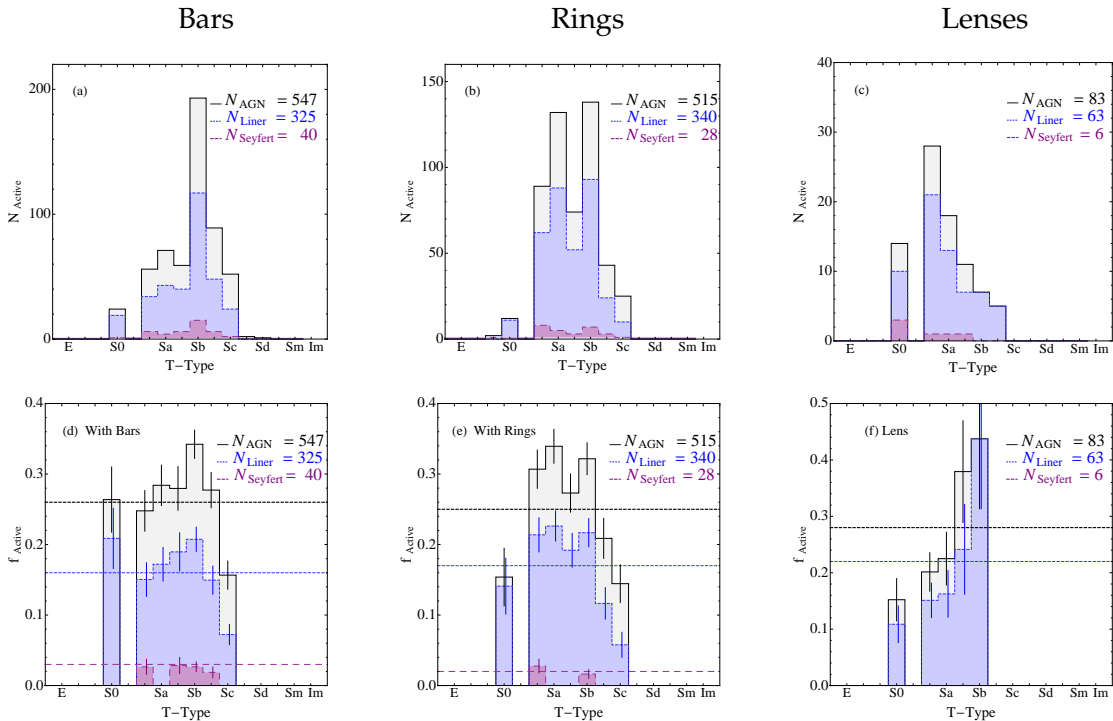


Figure 7.8: **Top Row:** Histogram of T-Type for AGN in galaxies with (a) Bars, (b) Rings and (c) Lenses. **Bottom Row :** AGN fractions vs T-Type for galaxies with (a) Bars, (b) Rings and (c) Lenses.

bar (see §2.2 in Ho et al. 1997).

Using our much larger sample we study the AGN fraction dependence on T-Type and fine components in Figures 7.7 and 7.8. Figure 7.7 shows the variation of AGN distribution and fraction as a function of T-Type for (a/e) all galaxies in our sample, (b/e) galaxies without any fine components and (c/f) galaxies with fine components. Objects classified as pure Seyferts are shown in purple and objects classified as pure LINERs in blue². We find the AGN fraction is strongly dependent on the T-Type of the galaxy with very few objects with AGN below type Sc. Considering objects without fine structures we find the AGN fraction rises sharply from 12% for Sc galaxies to peak at 34% for Sa galaxies beyond which it falls. The decrease is more apparent in LINER only galaxies. Seyfert galaxies show no dependence on T-Type. Considering all AGN we find the AGN fraction in non-fine component galaxies may be constant between T-Types S0a and Sb (within the error bars). For objects with a fine component, the LINER fraction is nearly constant (within error bars) between Sa to Sb galaxies unlike in the case for non-fine component galaxies. The total AGN fraction shows larger variation but can be consistent with constant given the error bars. The presence of fine structure increases the probability of finding a LINER in Sbc/Sc galaxies by a factor of 2 although the total AGN fraction is similar for both fine and non-fine component galaxies. Thus the presence of a bar or ring may possibly help turn on LINERs in disk dominated systems by funneling gas into the centers of galaxies.

Figure 7.8 shows the dependence of AGN fractions on bars, rings and lenses separately. The average AGN fraction is higher in all three fine types compared to normal galaxies. Compare this with Figure 7.1(f) we find the bar and ring fraction for Sbc/Sc galaxies are higher for galaxies with an AGN. Thus it seems the presence of one reinforces the other in late type galaxies. We find bar fractions decrease slowly as galaxies become more bulge dominated though S0 galaxies are 50% more likely to host an AGN in the presence of a bar than without, Figure 7.8(d). Over this same interval in T-Type where AGN fraction is falling off, the bar fraction decreases by $\sim 20\%$ again implying a positive feedback between bars and AGN. AGN fraction in ringed galaxies, Figure 7.8(e), are nearly constant with T-Type (as opposed to decreasing with T as in non-fine structure galaxies). The ring fraction over the same range is increasing again possibly implying a positive feedback between AGN and rings. AGN fraction in galaxies with lenses, Figure 7.8(f), strongly decreases as a galaxy gets more bulge dominated while the fraction of lensed galaxies strongly increases in the same range. Thus lenses and AGN are negatively correlated. As stated earlier in Chapter 3, lenses are normally classified as rings in RC3 and not as distinct structures. The difference in behavior of lenses and rings implies this

²From Kauffmann et al. (2003a) pure Seyferts are galaxies with $[OIII]/H\beta > 3$ and $[NII]/H\alpha > 0.6$ while LINERs have $[OIII]/H\beta < 3$ and $[NII]/H\alpha > 0.6$.

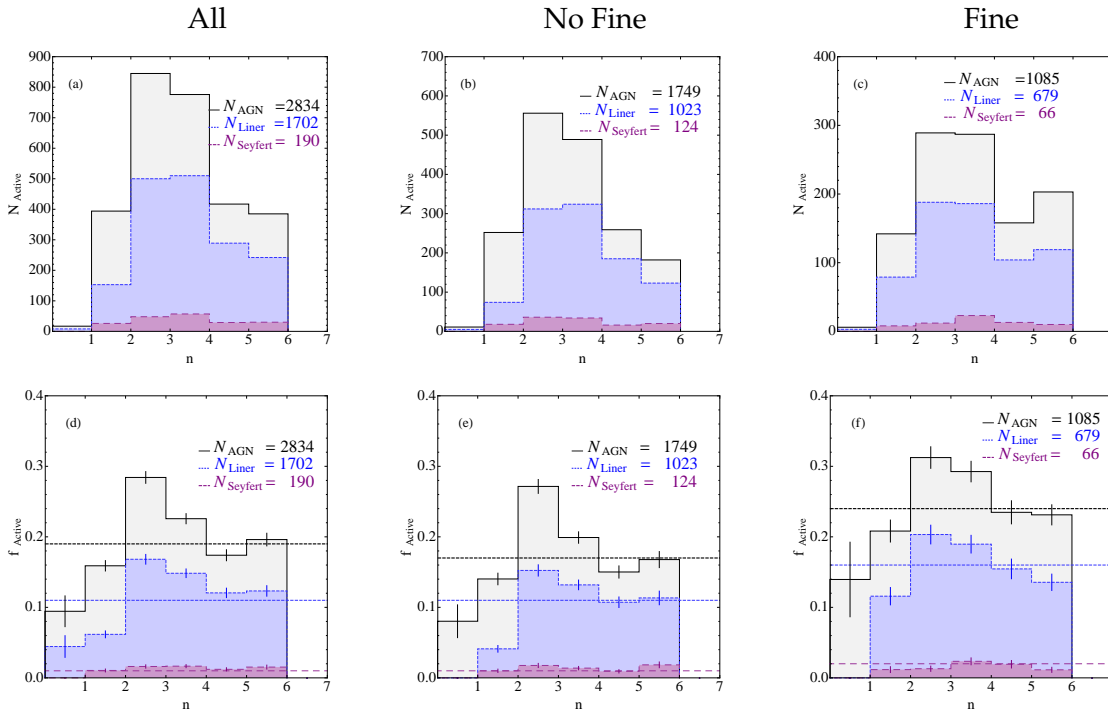


Figure 7.9: **Top Row**: Histogram of sersic index for (a) all galaxies with AGN, (b) AGN galaxies without fine components and (c) AGN galaxies with fine components. **Bottom Row** : AGN fraction vs sersic index for (a) all galaxies, (b) galaxies without fine components and (c) galaxies with fine components.

is not the correct approach. The creation of a lens appears to inhibit AGN unlike the creation of a ring.

In summary, there seems to be a positive correlation between AGN fraction and bar/ring fractions with respect to T-Type and a negative correlation with lens formation. The fine structure may not be directly influencing the AGN but the process causing its formation may be influencing the AGN. However the presence of any fine structure causes an increase in the overall AGN fraction and vice versa possibly implying that fine structures are more effective at keeping the AGN on.

7.3.2 Dependence of AGN fractions on sersic indices

Figure 7.9 shows the variation of AGN fraction as a function of sersic index for objects with and without fine components. The color coding is the same as in Figure 7.7. The shape of the distribution is similar for galaxies with or without fine components with the peak at $n \sim 3$ but the normalization is higher for galaxies with a bar, ring or lens.

To understand which fine feature is contributing to the overall increase in AGN fraction and how it influences sersic indices, Figure 7.10 shows the AGN fraction for each fine type individually. We find the AGN fraction is highest for ringed galaxies (panel e), especially for

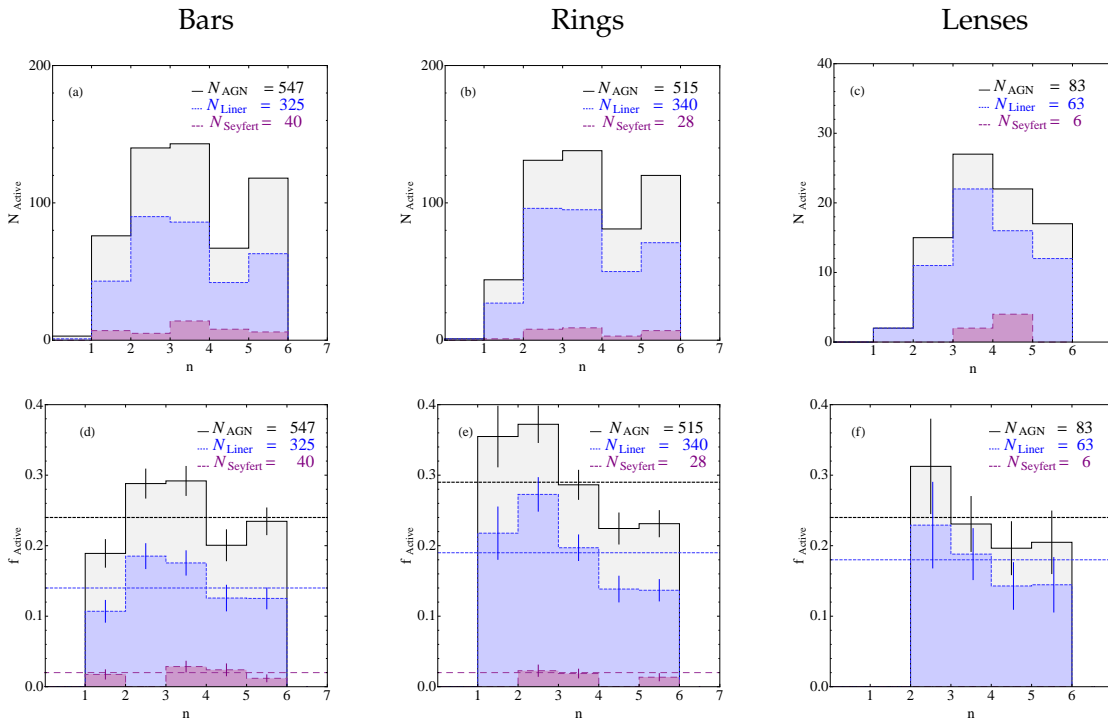


Figure 7.10: **Top Row:** Histogram of sersic index for AGN in galaxies with (a) Bars, (b) Rings and (c) Lenses. **Bottom Row :** AGN fractions vs sersic index for galaxies with (a) Bars, (b) Rings and (c) Lenses.

low n galaxies mirroring the trend of higher ring fraction in low n galaxies seen in Chapter 6. Comparing Figure 7.10 with Figure 7.2(f) we find the bar and ring fractions for AGN host galaxies increases steadily as n increases to $n \sim 3$ beyond which the AGN fraction in galaxies with fine structure decreases. Thus with respect to sersic index AGN fractions are not directly correlated with bar and ring fractions as we found with T-Type. The lens fraction in AGN host galaxies and the AGN fraction in lensed galaxies is nearly constant. The main problem in interpreting this result is that the sersic indices used here are not a true measure of bulge-to-total ratio as they are based on single component fits. Profile fitting of all the galaxies in our sample is currently beyond the scope of this thesis and will be carried out in future work. It should be noted that from sersic index of 1 to 4 the AGN fraction rises. As bulges are normally fit by an $n=4$ profile and disks with $n \sim 2$ this would follow the trend seen with T-Type. Sersic indices greater than 4, if binned with $n=4$, will not change this result.

7.3.3 Dependence of AGN fractions on mass

Kauffmann et al. (2003a) have already shown that galaxies with Type 2 AGN are predominantly massive with the peak of the distribution at around $LogM \sim 11$ and a peak AGN fraction of $\sim 20\%$ (see Figure 5 in Kauffmann et al. 2003a). Figure 7.11 shows the variation of AGN fraction with the mass of the galaxy for objects with and without fine components. The

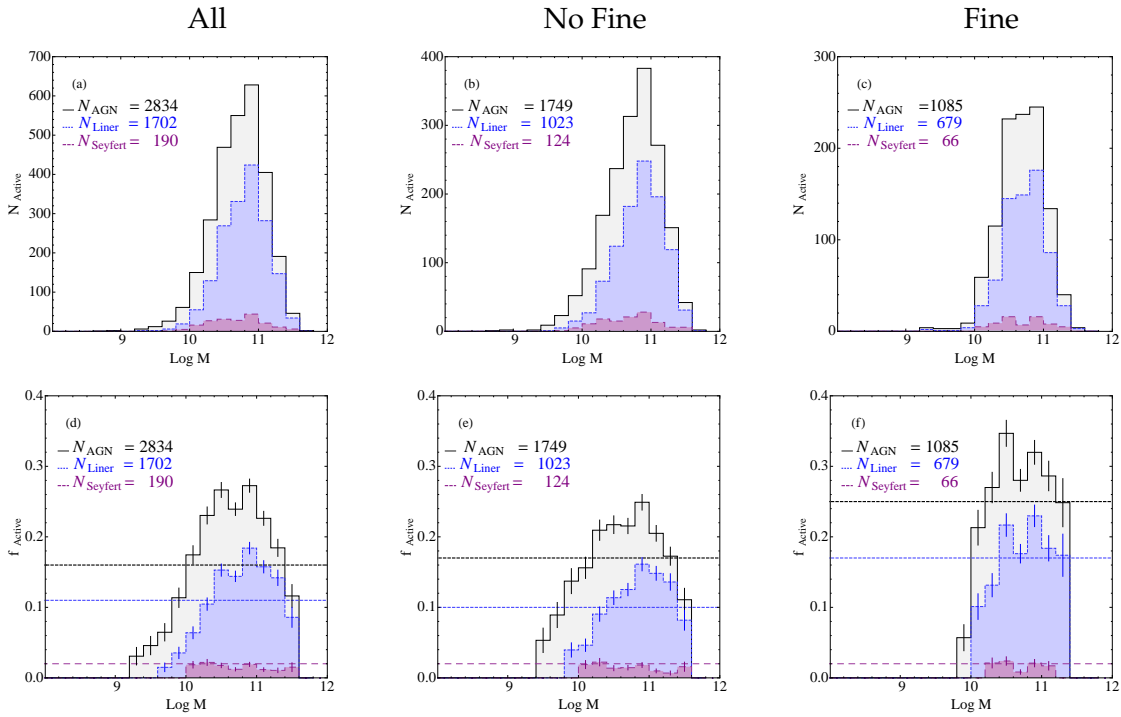


Figure 7.11: **Top Row:** Histogram of Mass for (a) all galaxies with AGN, (b) AGN galaxies without fine components and (c) AGN galaxies with fine components. **Bottom Row :** AGN fraction vs Mass for (a) all galaxies, (b) galaxies without fine components and (c) galaxies with fine components.

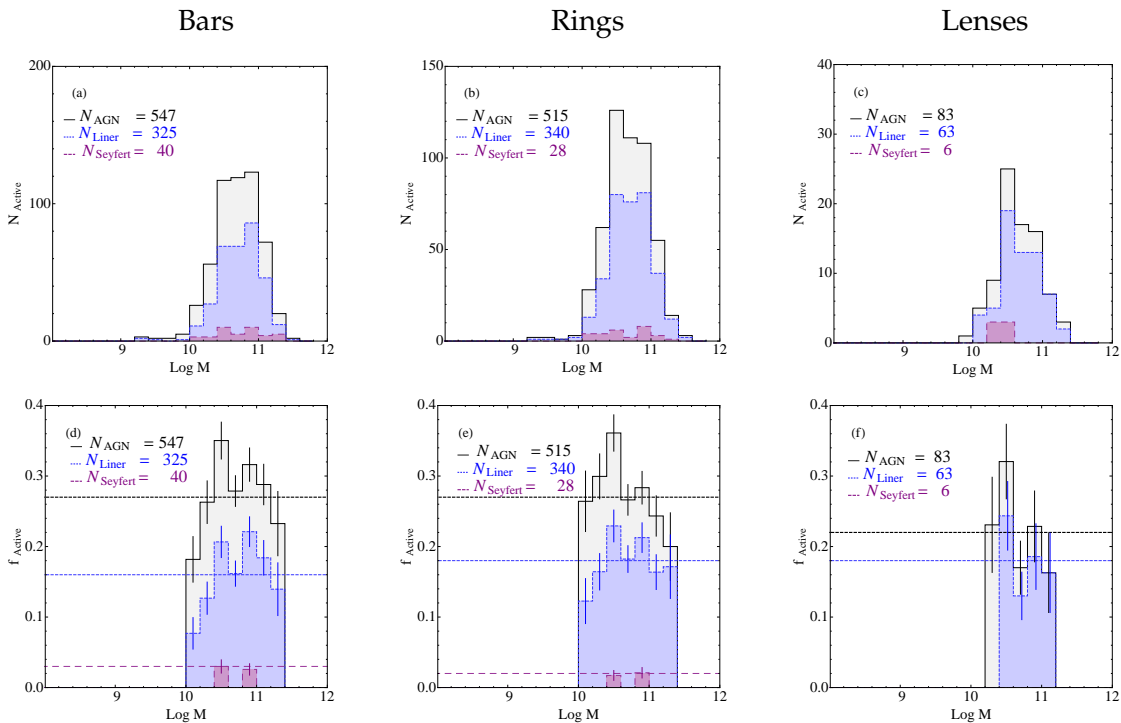


Figure 7.12: **Top Row:** Histogram of Mass for AGN in galaxies with (a) Bars, (b) Rings and (c) Lenses. **Bottom Row :** AGN fractions vs Mass for galaxies with (a) Bars, (b) Rings and (c) Lenses.

color coding is the same as in Figure 7.7. It is apparent that the presence of fine components increases the AGN fraction implying some reinforcing feedback mechanism. Considering objects with fine components only (panel f), we find the AGN fraction is significantly higher with an average percentage of 26% versus 17% in objects without a fine component. We find very few AGN with masses less than $\text{Log}M \sim 10$. The decrease in AGN fraction with mass at high masses is not as great as in the non-fine sample.

Figure 7.12 shows the dependence of AGN fraction on each fine type individually. We find bars and rings both follow the overall distribution of fine component galaxies though the decrease of AGN fraction with mass at high masses is more clear. The average AGN fraction in bars and rings is 27% with the AGN fraction in lenses at 22%. Ringed galaxies show a much stronger decrease of AGN fraction with increasing mass for $\text{Log}M > 10.4$ whereas barred galaxies show a weaker dependence of AGN fraction on mass for $\text{Log}M > 10.2$. We have too few Seyferts for any comment to be made.

Comparing the AGN fractions in Figure 7.12 with the behavior of fine fraction in the same mass range shown in Figure 7.3 (f) we find as AGN fraction decreases with increasing mass, the fine fraction in galaxies with AGN also decreases with increasing mass over the same range. The decrease is most noticeable for the ring fraction whereas the bar fraction drops off more slowly, just as the AGN fraction for barred galaxies drops off more slowly in comparison to ringed galaxies. Lens fraction decreases with increasing mass as does the AGN fraction in galaxies with lenses, though it should be noted that the error bars are very large. Thus, as with T-Type, we find changes in bar and ring fractions are positively correlated with AGN fractions.

7.3.4 Dependence of AGN fractions on magnitude

Figure 7.13 shows the histogram and fractional distribution of AGN as a function of absolute g-band magnitude for (a/e) all galaxies in our sample, (b/e) galaxies without any fine components and (c/f) galaxies with fine components. The color coding is the same as in Figure 7.7. The normalization and shape of the distribution with respect to absolute magnitude is different for objects with a fine component. The presence of either a bar, ring or lens appears to allow brighter objects to continue hosting an AGN. Figure 7.14 shows the dependence of AGN fraction on each fine type individually. We find the LINER fraction for bars, rings and lenses are nearly constant for $M_g < -20$ within the error bars. However the total AGN fraction decreases as galaxies get brighter if a ring or lens is present. This could indicate that the behavior of bars and rings may be different in AGN of different strengths.

Comparing the AGN fraction in Figure 7.14 with the fine fraction in Figure 7.4(f) we find in objects with AGN, bar fractions decrease as galaxies get brighter although the AGN fraction stays constant. The ring fraction also decreases as a galaxy gets brighter while the total AGN

fraction in ringed galaxies decreases. The LINER fraction stays constant for all fine types. Thus rings and AGN are more closely correlated than bars.

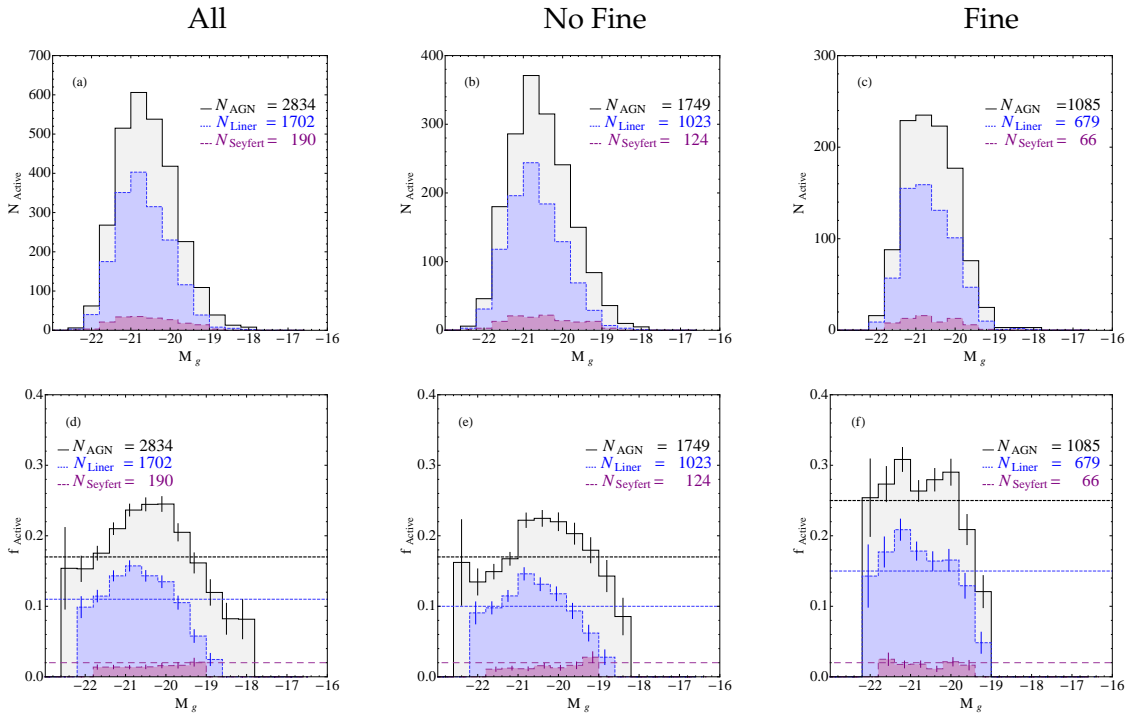


Figure 7.13: **Top Row:** Histogram of Magnitude for (a) all galaxies with AGN, (b) AGN galaxies without fine components and (c) AGN galaxies with fine components. **Bottom Row :** AGN fraction vs Magnitude for (a) all galaxies, (b) galaxies without fine components and (c) galaxies with fine components.

7.3.5 Dependence of AGN fractions on color

Figure 7.15 shows the histogram and fractional distribution of AGN as a function of $g-r$ color for (a/e) all galaxies in our sample, (b/e) galaxies without any fine components and (c/f) galaxies with fine components. The color coding is the same as in Figure 7.7. Mirroring the trend seen with mass, we find AGN are predominantly restricted to the red peak in the color distribution (Kauffmann et al. 2003a). The AGN fraction peaks at $g-r \sim 0.65$ for objects with or without a fine component. LINERS follow the overall trend while Seyferts show a peak around $g-r \sim 0.7$. Objects with a fine component have a similar distribution to those without, though the average AGN fraction is higher.

Figure 7.16 shows the dependence of AGN fraction on each fine type individually. We find AGN fraction increases for barred galaxies as it does in the overall distribution and peaks at $\sim 40\%$ for galaxies with $g-r \sim 0.6$. It then falls off to 20% for the reddest galaxies. Ringed galaxies follow a similar distribution. The LINER fraction in ringed and barred galaxies follow the overall distribution. AGN fraction in lensed galaxies fall off sharply from 45% for $g-r \sim$

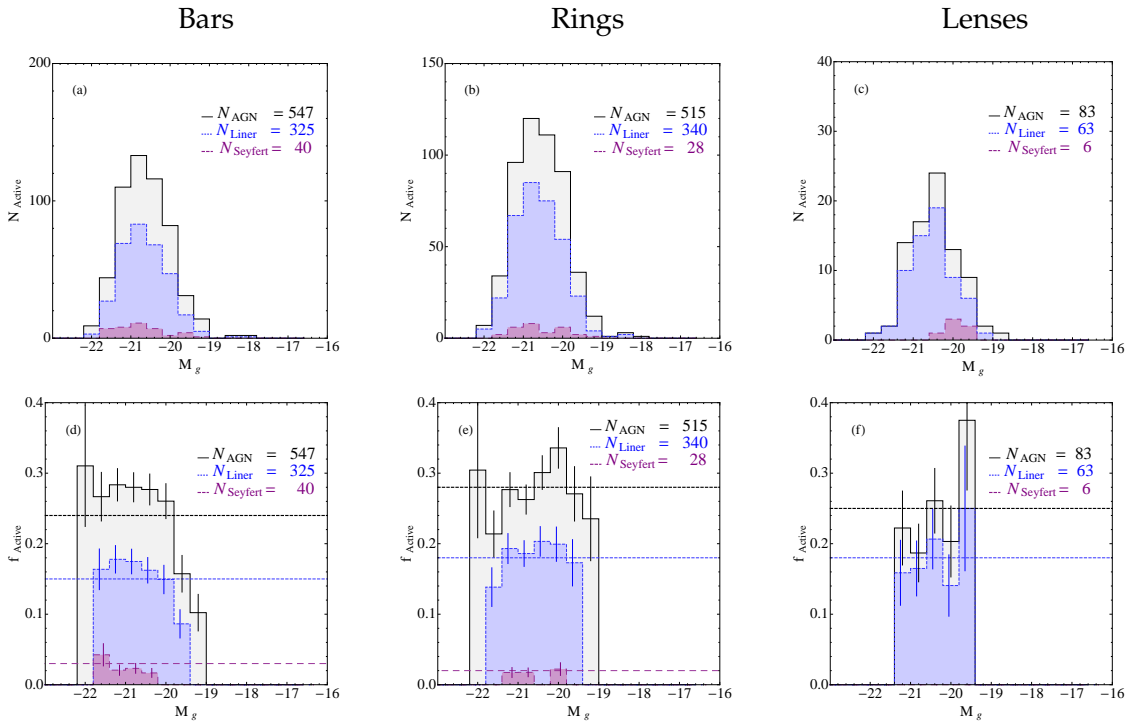


Figure 7.14: **Top Row:** Histogram of Absolute g-band Magnitude for AGN in galaxies with (a) Bars, (b) Rings and (c) Lenses. **Bottom Row :** AGN fractions vs Magnitude for galaxies with (a) Bars, (b) Rings and (c) Lenses.

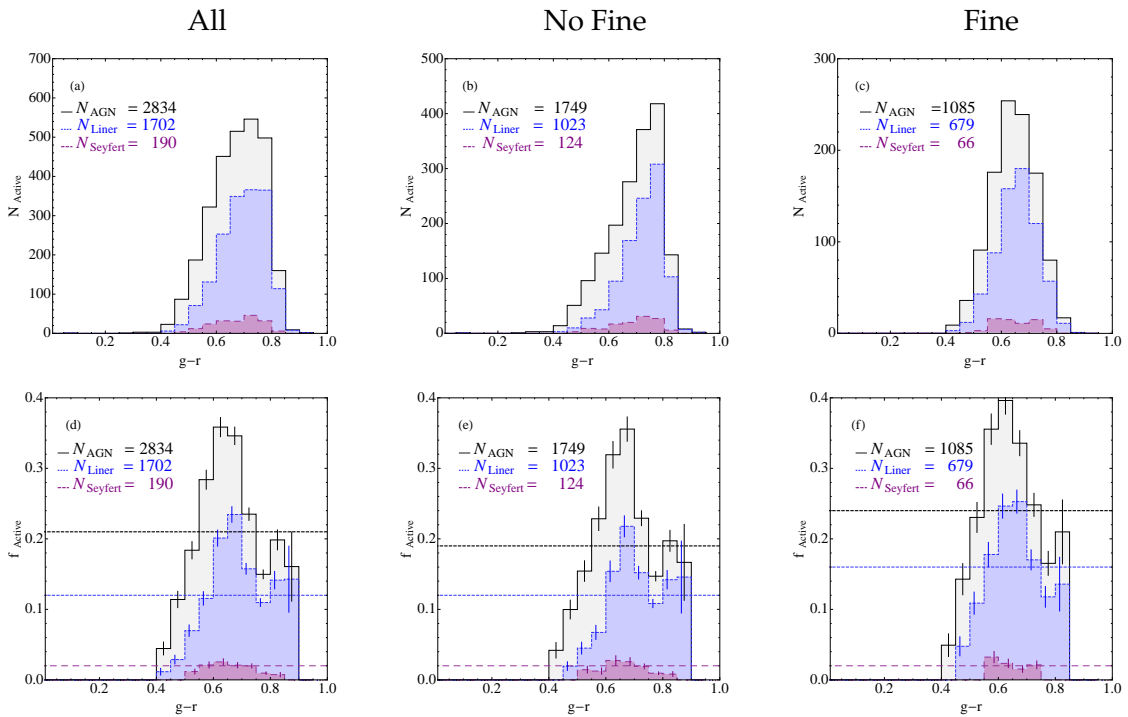


Figure 7.15: **Top Row:** Histogram of Color for (a) all galaxies with AGN, (b) AGN galaxies without fine components and (c) AGN galaxies with fine components. **Bottom Row :** AGN fraction vs Color for (a) all galaxies, (b) galaxies without fine components and (c) galaxies with fine components.

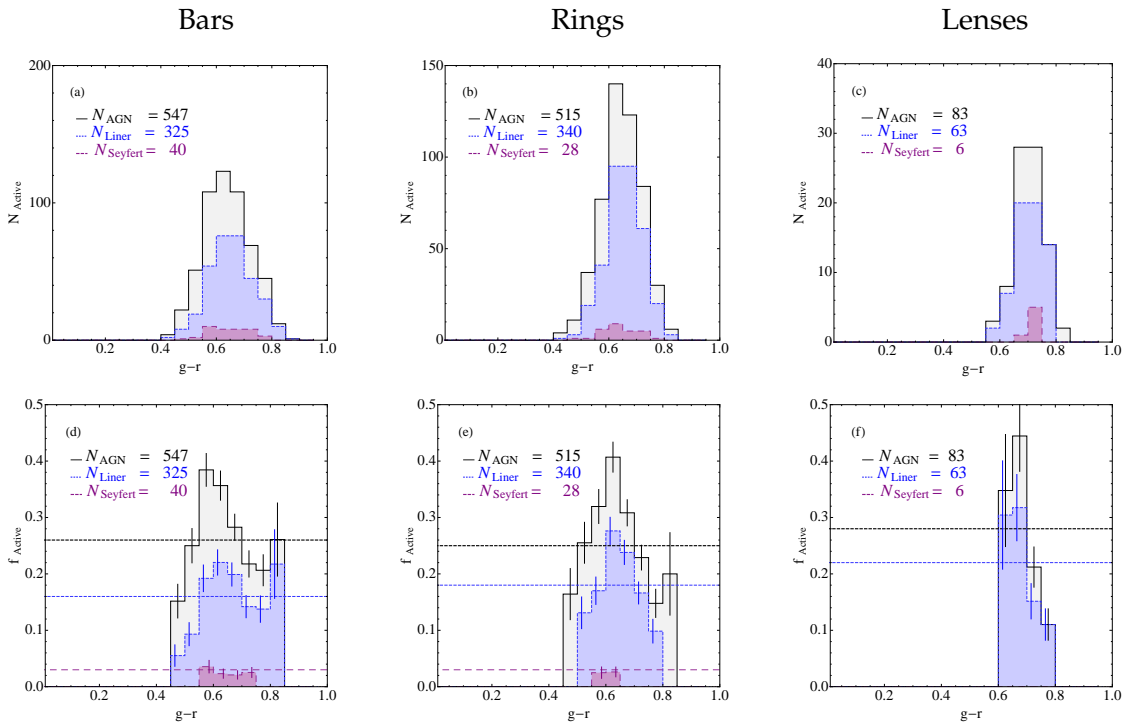


Figure 7.16: **Top Row:** Histogram of Color for AGN in galaxies with (a) Bars, (b) Rings and (c) Lenses. **Bottom Row :** AGN fractions vs Color for galaxies with (a) Bars, (b) Rings and (c) Lenses.

0.7 to 10% $g-r \sim 0.8$. Thus the overall effect of bars, rings and lenses is to support AGN activity in red, luminous, massive, bulge dominated systems. In addition ringed galaxies also support AGN activity in diskier systems.

Comparing AGN fractions in Figure 7.16 with fine fractions in Figure 7.5 we find as bar fractions increase from blue to red objects, the AGN fraction also increases. Beyond $g-r \sim 0.65$, the AGN fraction in barred galaxies decreases although the bar fraction is constant. The variation of ring fractions on the other hand follows the variation of the AGN fraction in ringed galaxies. Lens fractions increase as a galaxy becomes redder over the same range where AGN fraction in lensed galaxies decreases. Thus we see a positive correlation between variation in AGN fraction and ring fraction with color.

7.3.6 Dependence of AGN fractions on size

Figure 7.17 shows the variation of AGN fraction as a function of the petrosian half light radius of the galaxy for (a/e) all galaxies in our sample, (b/e) galaxies without any fine components and (c/f) galaxies with fine components. The color coding is the same as in Figure 7.7. Considering objects with no fine components, there is no dependence of AGN fraction on size. Considering objects with either a bar, ring or lens, we find a surprisingly strong dependence of AGN fraction on size. The results hold when restricting our analysis to the face on sample

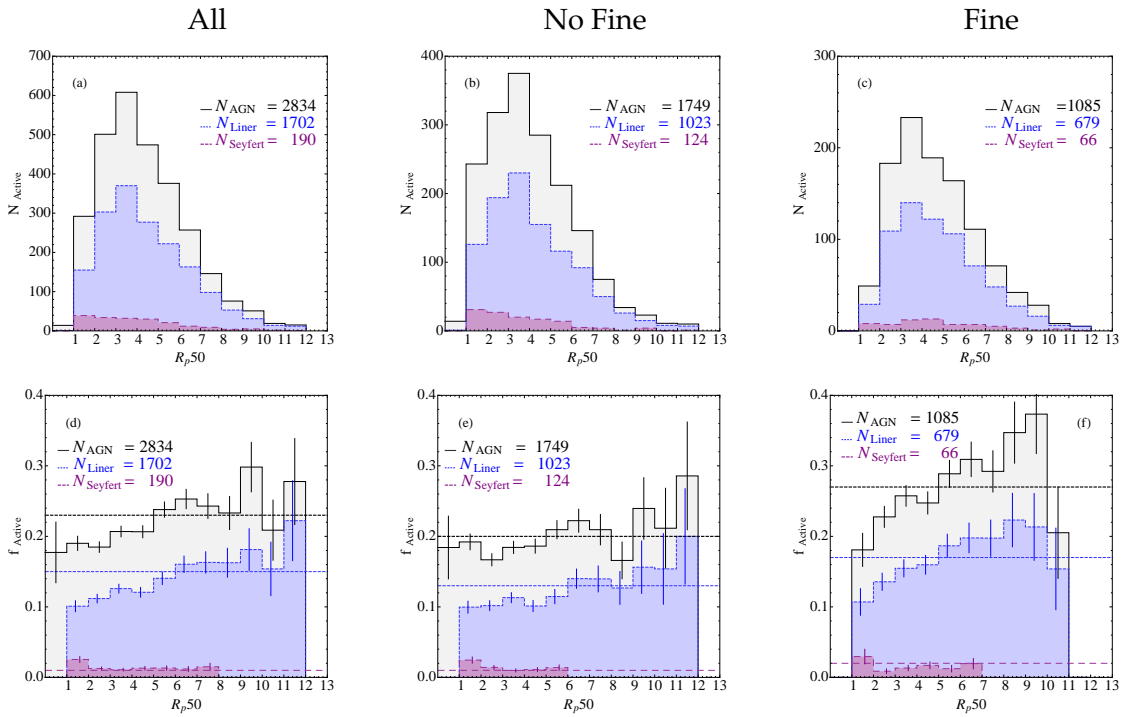


Figure 7.17: **Top Row:** Histogram of Size for (a) all galaxies with AGN, (b) AGN galaxies without fine components and (c) AGN galaxies with fine components. **Bottom Row :** AGN fraction vs Size for (a) all galaxies, (b) galaxies without fine components and (c) galaxies with fine components.

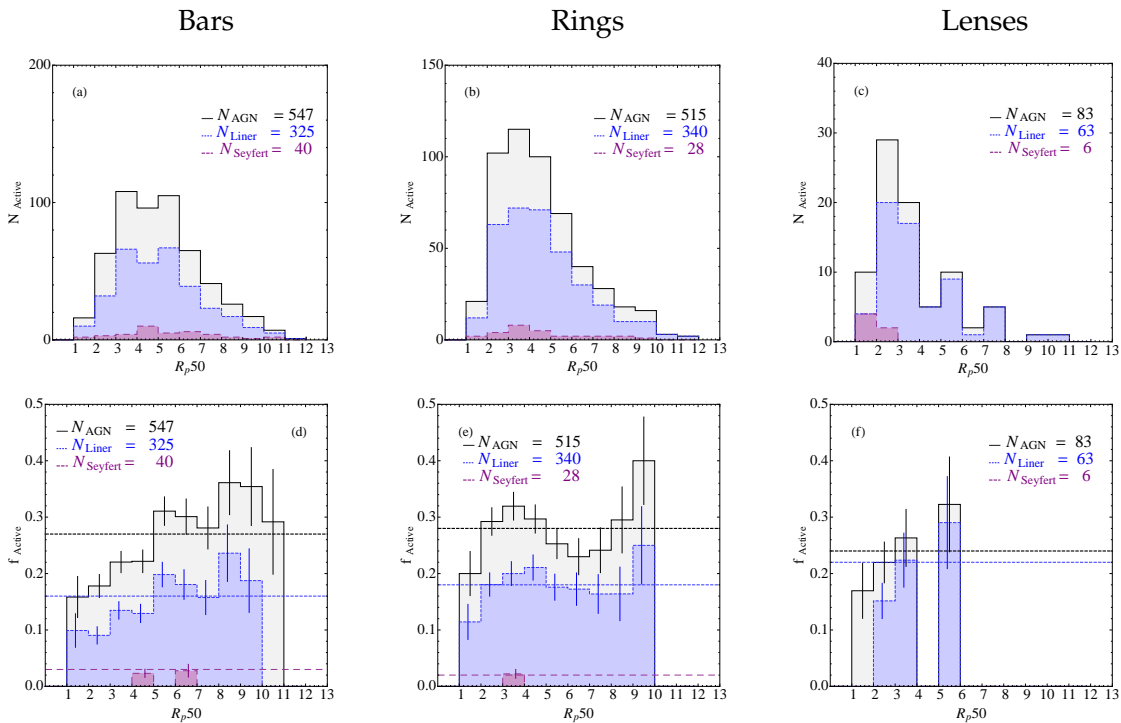


Figure 7.18: **Top Row:** Histogram of Size for AGN in galaxies with (a) Bars, (b) Rings and (c) Lenses. **Bottom Row :** AGN fractions vs Size for galaxies with (a) Bars, (b) Rings and (c) Lenses.

($b/a > 0.6$) as well as when using the semi-major axis measure of size, which properly accounts for the ellipticity of a galaxy. LINERs follow the overall trend as expected as they are the dominant group in our sample. Seyferts show a higher fraction for smaller half light radii $R < 2kpc$ but are nearly constant for $R > 2kpc$ within the error bars.

Figure 7.18 shows the dependence of AGN fraction on each fine type individually. We find the AGN fraction increases with size for barred galaxies and lenses. For ring galaxies, the behavior is peculiar. The AGN fraction initially rises from 20% for $R \sim 1kpc$ to 30% for $R \sim 4kpc$ beyond which the AGN fraction drops to 24% for $R \sim 6kpc$. For objects with $R > 6kpc$ the AGN fraction increases again but is consistent with no change given the size of the error bars. Using semi-major axis as a measure of size we find the AGN fraction stays constant beyond $R > 6kpc$. These trends are followed by the LINER-only class but are not as strong for ringed galaxies.. We have too few Seyferts for any comment to be made. Thus the AGN fraction is very sensitive to the size of a fine-component galaxy and the fine type present. It may be that the size of a galaxy with a fine component may be related to the frequency, size or strength of the fine feature. We cannot ascertain the influence of size or strength of the fine feature in the current work but we can look at how the frequency of a fine component affects the AGN fraction.

Comparing AGN fractions in Figure 7.18 with fine fractions in Figure 7.6, we find in objects with an AGN the total fine fraction is nearly constant with size. However the bar fraction gradually increases with size while the ring fraction initially increases and then decreases with size, following the same trend seen with AGN fraction in objects with a fine component. Lens fractions decrease with size while AGN fractions in lensed galaxies increase with size though it should be noted that the error bars are very large and so there is a large uncertainty in this result. Overall we find a surprisingly close connection between the variation of ring and bar fraction in galaxies with AGN with the variation of the AGN fraction in ringed and barred galaxies. Big galaxies are much more likely (70%) to be AGN if they have fine structure. Why the tiny black hole at the center of a galaxy is so strongly affected by (or affects) structure on such large scales is surprising and mysterious.

7.3.7 Summary

We have found interesting correlations between the variation of AGN fraction and fine fraction as a function of different physical properties. With T-Type, mass, and size, variations in bar and ring fractions positively correlate with variations in AGN fractions. With sersic index, magnitude and color the trends are not as clear though the presence of a fine type does increase the AGN fraction. The difficulty in interpreting the results is because many galaxies have more than one fine component and their effects on the AGN may be competing. In addition there

are different types of rings, lenses and bars. Their scale and strength may also be expected to influence(/or be influenced by) the AGN and its strength. We have no measure of the scale or strength of the fine features and will postpone a study of their relation to AGN properties for the future. The effect of missing large scale bars or rings, not including nuclear rings or bars and missing low luminosity LINERs based on the strict line ratio signal-to-noise cuts implemented by Kauffmann et al. (2003a) all further complicate the result.

7.4 Implications

It is clear that to understand the formation and growth of galaxies the effect of AGN and fine types must be investigated further. Any theory of galaxy formation must be able to account for the effect of AGN and reproduce the trends observed as a function of physical properties and fine types. One of the most interesting trends is with mass where we find no AGN in the low mass peak and a change of the dependence of fine fraction with mass in galaxies with AGN such that fine fraction decreases with mass for high mass galaxies. We also find that in this same mass regime, the AGN fraction is decreasing though the overall fraction is higher than in non-fine type galaxies. It is unclear if the fine fraction is decreasing because the AGN fraction is decreasing or vice versa or if both are decreasing due to some other process. It is also unclear if only the presence of an accreting super-massive black hole is required to influence large scale properties or if the strength of the AGN accretion is playing a determining role in fine fraction statistics in high mass galaxies. Most of our work has focused on LINERs which are more dominant in the local universe. The results cannot be extended to seyferts or quasars which are much more actively accreting especially in the high redshift universe. It is also unclear in what direction the trends will continue though there may be hints from recent results by Sheth et al. (2008) and simulations by Wang & Kauffmann (2008).

Very few AGN have been detected in low mass disk galaxies (Kauffmann et al. 2003a) though the effect of bias in methodology for detection cannot be ruled out (Ferrarese & Ford 2005). However as things stand, the sharp drop in AGN fraction below $\text{Log} M \sim 10$ or $g ? r \sim 0.5$ can be accounted for if the transition from the blue cloud to the red sequence is associated with the formation of a super-massive black hole (SMBH) in the centers of galaxies. Wang & Kauffmann (2008), using simulations, note that SMBHs in ellipticals and other massive early type galaxies must have formed at high- z as they are no longer growing. The process which forms the black hole seed must be different in high mass versus low mass galaxies. The authors note that if major mergers are responsible for the initial seed then the AGN dependence on mass (that they lie mainly in galaxies with $\text{Log} M > 9.8$) can be understood. Working with this assumption the high redshift results of Sheth et al. (2008) (SE08) may be understood.

From SE08, bar fractions exhibit downsizing such that bar fractions are highest in the highest mass disk galaxies in their highest redshift bin $z \sim 1$. In SE08's intermediate redshift bin, the bar fraction for slightly lower mass galaxies have increased implying that whatever process prevented their formation at higher z is no longer in effect. As noted by Wang & Kauffmann (2008), black hole formation and AGN activity also exhibit downsizing with the most massive galaxies having already formed their SMBH at higher redshifts. So at $z \sim 1$ while very massive galaxies may not be actively accreting and hence may not have very powerful AGN, the slightly lower mass galaxies might still be actively accreting. Thus the downsizing of AGN activity may be the process responsible for the downsizing of bar fractions. If AGN and fine features are controlled by the same process then this would help explain the high mass trend of fine fractions in the presence of an AGN. Although we have established a connection between AGN fractions and fine fractions at low- z , the details are still unknown. The AGN may not directly influence the formation of a bar. It could be that AGN activity prevents buckling instabilities or their accretion rate may need to be low enough for bars to start to form. Correlations between AGN fraction and fine fraction as a function of redshift need to be measured to further understand their relation. No work has been done on the evolution of ring fraction with redshift. Given how strongly they are correlated with AGN activity this needs to be investigated. In addition, studying the evolution of bar fraction in low mass galaxies is also essential though more challenging.

7.5 Summary

In conclusion we find the following major results:

1. We have shown that AGN and fine structures like bars/rings seem to influence each other.
2. Ringed galaxies are very frequent in AGN especially in low-sersic index galaxies.
3. AGN appear influence the overall fine fraction variation of galaxies. As opposed to normal galaxies, those with AGN appear to have decreasing fine fractions with increasing mass and luminosity. In addition ring frequencies decrease with size in galaxies with AGN.
4. AGN fractions show very interesting trends with T-Type and other physical properties that are also dependent on the presence of fine component. In the presence of a fine feature, most often rings, the AGN fraction is higher in early type, bulge dominated, more massive and red galaxies.

5. AGN fractions in objects with fine structures seem to be dependent on the size of the galaxy, with the fraction increasing as size increases.
6. It is unclear if bar fractions are significantly higher in AGN but it is clear that AGN fractions are much higher in objects with fine types (bars, rings or lenses). It should be kept in mind that our bar and fine fractions will actually be much higher if we were to include weak bars and partial rings which we currently miss. Thus the bar fraction in objects with AGN are more likely lower limits. The AGN fraction in fine featured galaxies are also likely lower limits as the S/N requirement for line emissions required for identification of an AGN are stringent and likely to miss LINERs.
7. The variation of fine fractions and AGN fractions are intimately related. With the exception of sersic index, ring fractions correlate positively with variations in AGN fraction. The bar fraction variation is more complicated where it positively correlates with AGN fraction changes with some physical properties, like mass, and not with others. This most probably is because fine fraction properties are bimodal with mass and color.
8. Lens fraction may be negatively correlated with the variation of AGN fraction in lensed galaxies, though the error bars are large in this result. It implies that lenses should probably not be grouped with rings which exhibit positive correlations with AGN fraction.

Chapter 8

Conclusions

Galaxy formation and evolution involves many different astrophysical processes, each of which has its own time scales. It is important to consider large scale structure, environment, dynamics of stellar and gaseous components, masses, ages, luminosities, star formation rates, metallicities, AGN, fine structure, feedback, merging, dark matter and many others. Consequently understanding the process of galaxy formation, and developing a theory for such, is a complicated task. Astronomers in general are forced to consider a handful of properties at any given time but unfortunately this can lead to loss of information, as has been shown in this thesis. Even here we have limited our analysis to groups of properties but have identified areas of further research. However, It is clear that the signature of the formation history of a galaxy is imprinted in its morphology.

This thesis has created a large detailed morphological catalog which can be used to gain a better understanding of the low redshift universe and extend it to higher redshifts. The major results of this work are:

- We have visually classified ~ 14000 galaxies including fine structure and present our catalog of parameters available to the public.
- Galaxies exhibit a continuum of features and there is no single concentration or sersic index cut that can select out early or late type galaxies without missing a significant number due to the tail of the distribution.
- We find many of the observed trends of physical properties with T-Type are due to variations in mass with other physical properties, i.e. mass appears to be a defining characteristic of a galaxy. The break in most correlations seen in the local universe occurs due to a lack of massive late type galaxies. van den Bergh (2008) has suggested that ‘reconciling the conclusion that galaxies are essentially a one parameter family defined by

their initial mass is challenging in the context of hierarchical merging scenario'. This in fact may not be the case as it appears galaxy properties depend on their current mass. Merging may lead to the quick build up of galaxies and may account for some variation seen within T-Types but it may bode well that the wide variety of galaxy interactions does not, to first order, influence overall properties. However the role of AGN is bound to complicate this.

- Color is most strongly related to T-Type but with a slight dependence on mass to light ratio, mass and surface mass density.
- We find S0 galaxies exhibit properties (size, luminosity) intermediate to ellipticals and Sa galaxies in low mass galaxies. It is only in the top 30% mass quantile range where S0 galaxies are smaller and less luminous than either ellipticals or Sa galaxies. The environment of the galaxies may be unduly influencing S0 galaxies more so than Sa galaxies or, ellipticals expand and grow more in cluster environments.
- We find elliptical galaxies exhibit strikingly different size-mass relationships as a function of central concentration, strongly suggesting a non-homologous population of objects. Over the whole mass range, the size-mass relationship for the most centrally concentrated objects are displaced to lower masses and sizes.
- We find the previously undiscovered result that bar fractions are bimodal with respect to mass and color. The origins of bars at low and high masses are likely different as illustrated by their differing dependences on central concentration.
- There may be a very strong correlation between bars, rings and lenses although it is important to not include lenses with rings. The variation of frequency of lenses with respect to physical quantities does not follow that of rings.
- Rings are more frequent in galaxies with AGN, especially in low-sersic index galaxies.
- The presence of a fine component increase AGN fraction in comparison to 'non-fine' galaxies.
- AGN activity influences variations in the overall fine structure fraction of galaxies.
- There may be a positive correlation between AGN fractions and fine (bar/ring/lens) fractions. As opposed to normal galaxies, those with AGN appear to have a decreasing fine fraction with increasing mass and luminosity. In the same range, AGN fractions actually decrease as mass increases, implying a positive correlation between their numbers.

- AGN fraction shows a strong dependence on the size of a galaxy in the presence of a fine structure. Ring frequencies decrease with size in galaxies with AGN while bar frequencies increase.

8.1 Future Work

In this section we briefly outline several future projects based on this work.

8.1.1 Study of Quantitative Morphology

Although visual morphological classifications have proved useful, it is impossible for independent observers to come up with the exact same classification. This is because visual classification is essentially qualitative so although each classifier will be self consistent, there will be large variations between different observers (Naim et al. 1995). For example, what should a galaxy with tight spiral arms like an Sa but small bulge like an early Sc be called? If anything, visual classification has shown that morphology is not discrete but continuous, even when excluding fine structure components. In addition, in the current era of large surveys, visually classifying millions of galaxies is not possible, though the work by Galaxy Zoo (Lintott et al. 2008), which involves the contributions of the general public, has made broad classifications of large data sets easier. Aside from the problems associated with the classification process, the Hubble scheme in its current form is not suited to low luminosity galaxies. It also cannot be extended to higher redshifts where a large portion of the galaxies at high- z end up classified as irregular. However, a non-arbitrary, quantitative system would be the ideal solution. Tremendous efforts have been made over the past decade to quantify the variation in morphology though the disappointing truth is that, at present, state-of-the-art automated galaxy classification is only capable of delivering crude classifications, albeit very quickly. These classifications have proved useful in their appropriate context, but they have been neither as accurate nor as comprehensive as visual classifications made by a trained observer. Until this thesis, the most fundamental difficulty has been the lack of a good, complete, digital sample of classifications nearby galaxies. This has limited the morphological type and luminosity range in most digital surveys of local galaxies conducted so far, which in turn has limited our knowledge of the basic properties that characterize distant galaxies. The catalog presented in this thesis rectifies this deficiency. Our lack of low redshift late type galaxies can be overcome by including the galaxies in RC3 which have been imaged by SDSS. A preliminary comparison of the catalog has shown they are dominated by late type nearby ($z < 0.04$) galaxies. With this final catalog we can conduct a detailed study of the ability and usefulness of non-parametric quantitative classification schemes.

In this thesis we restricted our quantitative analysis to the variations of single parameters as a function of physical properties, AGN fractions and fine fractions. We have found that the quantitative parameters concentration, gini, and M20 all correlate well with T-Type but we have not looked at how a combination of different parameters can be used to distinguish between T-Types. With our current catalog we intend to study the variation of morphology in multi-parameter space with the goal of determining what are the minimum number of parameters required to determine morphology. Is it possible to distinguish objects with fine structures in morphology space? In addition we have calculated morphological terms for a large subset of galaxies in all sloan bands and GALEX nuv and fuv bands. Preliminary results are presented in Abraham et al. (2007). We intend to quantify the systematic variation of quantitative terms with waveband, luminosity, signal-to-noise, resolution and redshift. (The code created for this purpose MORPHEUS by Prof. Roberto Abraham and myself will be made public at a future date.) In doing so we hope to quantify the morphological properties of CFHT Legacy Survey wide fields and the COSMOS fields which achieve greater depth as well as extending our analysis to SDSS DR7.

8.1.2 Quantification of fine parameters

Our results from Chapters 6 and 7 further emphasize the importance of bar, rings and lenses in the evolution of galaxies. The results were based on the presence or absence of fine structures. As we have already noted in Chapter 3, our visual classification scheme only identifies strong bars. Weak bars and partial rings are not as easily identified. We need to incorporate them to gain a full understanding of their relation to AGN activity. Much work has been done in automating and quantifying the strength of fine structure (Laurikainen & Salo 2002; Laurikainen et al. 2007; Marinova & Jogee 2007; Barazza et al. 2008; Buta et al. 2004). We would like to quantify the detection of fine structures, their strengths and sizes and understand their importance to triggering AGN.

8.1.3 Bulge-Disk decomposition

We used a one-parameter model to determine sersic index. Ideally we would like to fit for the bulge and disk separately to determine the influence of central concentration on galaxy evolution. Public codes such as GIM2D (Simard & Pritchett 1998) or GALFIT (Peng et al. 2002) can be used to calculate sersic indices and scale radii for the bulge and disk component to understand the growth of each.

8.1.4 Further extensions

The role of environment on the physical properties, morphology transformation and AGN activity needs to be better understood. Although measures of environment have been made available by the NYU group (Blanton et al. 2005b), they are currently only for the SDSS DR2 release. Ideally we would like to conduct such an analysis on a volume limited sample of galaxies over a large enough area with sufficient depth to allow classification. The wide component of the multi-band CFHT Legacy Survey provides an ideal sample with a survey area of 170 sq. degrees in four fields and a depth of 26.6 in g' . Half of this area is covered by SDSS and hence redshift measurements, metallicities and mass estimates are available. Classifications have already been carried out for a significant fraction of the galaxy sample as a part of this thesis. This study will help to nail down bar and ring fractions as a function of environment, and T-Type. Using this sample, we can also investigate the local morphology density relation as a function of mass and the size function of galaxies with respect to cluster center radii.

8.1.5 Spectroscopic follow-up

It is clear that our understanding of the interactions of bars, rings and lenses with AGN cannot progress without understanding the importance of dark matter and gas. Ideally full characterization of the 2D velocity fields using either an IFU or a Fabry Perot interferometer can provide much more information which would allow the study of :

- (a) the nature of the velocity fields in the sample of galaxies; are they dominated by ordered or chaotic motions, gas inflow or outflows?
- (b) the influence of bars and rings?
- (c) the stellar populations (ages and metallicities) in different components of the galaxy.
- (d) the variation of M/L as a function of radius.
- (e) the connection of these results to global, pixel-by-pixel and fine structure morphology.

Overall, a study of the redshift evolution of a well defined sample of galaxies of varying morphological T-Types in different environments, where the metallicities gradients, age gradients and the rotation curves are known is necessary. A volume limited sample centered on CFHTLS wide fields and COSMOS would be ideal. Currently, given the infancy of the field, investigations of galaxies with IFUs have been restricted to small samples of early type galaxies (Bacon et al. 2001; de Zeeuw et al. 2002) and very few late type galaxies (Ganda et al. 2006).

8.1.6 Other work

There are multiple avenues of research possible with this catalog. As stated in Chapter 3 we have not considered arm structures in the current analysis though we have classified them. In addition we have not studied very disturbed galaxies which do not fit into a T-Type classification scheme, for example collisional rings. An IFU study of rings can help understand these systems which are expected to increase in frequency at higher redshifts. Comparison with models to understand time scales of activity need to be conducted. Our comparison of fine fractions and AGN fractions needs to be extended to higher redshifts as well as an accounting for the differing influences of the strength of the AGN.

8.1.7 Outlook

Deciphering the clues to formation in the variation of the structure of galaxies and the causes for such is one of the biggest challenges facing observers. We are at the cusp of an era where we can look at the evolution of galaxies in multi-parameter space and in fine detail. With the advent of larger surveys like PanStarrs, LSST and new instruments and telescopes (TMT, Herschel), we will be provided many opportunities for further exciting research.

Bibliography

Abazajian, K., Adelman-McCarthy, J. K., Agüeros, M. A., Allam, S. S., Anderson, K., Anderson, S. F., Annis, J., Bahcall, N. A., Baldry, I. K., Bastian, S., Berlind, A., Bernardi, M., Blanton, M. R., Bochanski, J. J., Boroski, W. N., Briggs, J. W., Brinkmann, J., Brunner, R. J., Budavári, T., Carey, L. N., Carliles, S., Castander, F. J., Connolly, A. J., Csabai, I., Doi, M., Dong, F., Eisenstein, D. J., Evans, M. L., Fan, X., Finkbeiner, D. P., Friedman, S. D., Frieman, J. A., Fukugita, M., Gal, R. R., Gillespie, B., Glazebrook, K., Gray, J., Grebel, E. K., Gunn, J. E., Gurbani, V. K., Hall, P. B., Hamabe, M., Harris, F. H., Harris, H. C., Harvanek, M., Heckman, T. M., Hendry, J. S., Hennessy, G. S., Hindsley, R. B., Hogan, C. J., Hogg, D. W., Holmgren, D. J., Ichikawa, S.-I., Ichikawa, T., Ivezić, Ž., Jester, S., Johnston, D. E., Jorgensen, A. M., Kent, S. M., Kleinman, S. J., Knapp, G. R., Kniazev, A. Y., Kron, R. G., Krzesinski, J., Kunszt, P. Z., Kuropatkin, N., Lamb, D. Q., Lampeitl, H., Lee, B. C., Leger, R. F., Li, N., Lin, H., Loh, Y.-S., Long, D. C., Loveday, J., Lupton, R. H., Malik, T., Margon, B., Matsubara, T., McGehee, P. M., McKay, T. A., Meiksin, A., Munn, J. A., Nakajima, R., Nash, T., Neilsen, E. H., Newberg, H. J., Newman, P. R., Nichol, R. C., Nicinski, T., Nieto-Santisteban, M., Nitta, A., Okamura, S., O'Mullane, W., Ostriker, J. P., Owen, R., Padmanabhan, N., Peoples, J., Pier, J. R., Pope, A. C., Quinn, T. R., Richards, G. T., Richmond, M. W., Rix, H.-W., Rockosi, C. M., Schlegel, D. J., Schneider, D. P., Scranton, R., Sekiguchi, M., Seljak, U., Sergey, G., Sesar, B., Sheldon, E., Shimasaku, K., Siegmund, W. A., Silvestri, N. M., Smith, J. A., Smolčić, V., Snedden, S. A., Stebbins, A., Stoughton, C., Strauss, M. A., SubbaRao, M., Szalay, A. S., Szapudi, I., Szkody, P., Szokoly, G. P., Tegmark, M., Teodoro, L., Thakar, A. R., Tremonti, C., Tucker, D. L., Uomoto, A., Berk, D. E. V., Vandenberg, J., Vogeley, M. S., Voges, W., Vogt, N. P., Walkowicz, L. M., Wang, S., Weinberg, D. H., West, A. A., White, S. D. M., Wilhite, B. C., Xu, Y., Yanny, B., Yasuda, N., Yip, C.-W., Yocum, D. R., York, D. G., Zehavi, I., Zibetti, S., & Zucker, D. B. 2004, *The Astronomical Journal*, 128, 502

Abraham, R. G. 1999, *Galaxy Interactions at Low and High Redshift*, 186, 11

Abraham, R. G., Merrifield, M. R., Ellis, R. S., Tanvir, N. R., & Brinchmann, J. 1999, *Monthly Notices*, 308, 569

- Abraham, R. G., Nair, P., McCarthy, P. J., Glazebrook, K., Mentuch, E., Yan, H., Savaglio, S., Crampton, D., Murowinski, R., Juneau, S., Borgne, D. L., Carlberg, R. G., Jørgensen, I., Roth, K., Chen, H.-W., & Marzke, R. O. 2007, *The Astrophysical Journal*, 669, 184
- Abraham, R. G., Tanvir, N. R., Santiago, B. X., Ellis, R. S., Glazebrook, K., & van den Bergh, S. 1996a, *Monthly Notices of the Royal Astronomical Society*, 279, L47
- Abraham, R. G., Valdes, F., Yee, H. K. C., & van den Bergh, S. 1994, *Astrophysical Journal*, 432, 75
- Abraham, R. G., van den Bergh, S., Glazebrook, K., Ellis, R. S., Santiago, B. X., Surma, P., & Griffiths, R. E. 1996b, *Astrophysical Journal Supplement v.107*, 107, 1
- Abraham, R. G., van den Bergh, S., & Nair, P. 2003, *The Astrophysical Journal*, 588, 218
- Adelman-McCarthy, J. K., Agüeros, M. A., Allam, S. S., Anderson, K. S. J., Anderson, S. F., Annis, J., Bahcall, N. A., Baldry, I. K., Barentine, J. C., Berlind, A., Bernardi, M., Blanton, M. R., Boroski, W. N., Brewington, H. J., Brinchmann, J., Brinkmann, J., Brunner, R. J., Budavári, T., Carey, L. N., Carr, M. A., Castander, F. J., Connolly, A. J., Csabai, I., Czarapata, P. C., Dalcanton, J. J., Doi, M., Dong, F., Eisenstein, D. J., Evans, M. L., Fan, X., Finkbeiner, D. P., Friedman, S. D., Frieman, J. A., Fukugita, M., Gillespie, B., Glazebrook, K., Gray, J., Grebel, E. K., Gunn, J. E., Gurbani, V. K., de Haas, E., Hall, P. B., Harris, F. H., Harvanek, M., Hawley, S. L., Hayes, J., Hendry, J. S., Hennessy, G. S., Hindsley, R. B., Hirata, C. M., Hogan, C. J., Hogg, D. W., Holmgren, D. J., Holtzman, J. A., Ichikawa, S.-I., Ivezić, Ž., Jester, S., Johnston, D. E., Jørgensen, A. M., Jurić, M., Kent, S. M., Kleinman, S. J., Knapp, G. R., Kniazev, A. Y., Kron, R. G., Krzesinski, J., Kuropatkin, N., Lamb, D. Q., Lampeitl, H., Lee, B. C., Leger, R. F., Lin, H., Long, D. C., Loveday, J., Lupton, R. H., Margon, B., Martínez-Delgado, D., Mandelbaum, R., Matsubara, T., McGehee, P. M., McKay, T. A., Meiksin, A., Munn, J. A., Nakajima, R., Nash, T., Neilsen, E. H., Newberg, H. J., Newman, P. R., Nichol, R. C., Nicinski, T., Nieto-Santisteban, M., Nitta, A., O'Mullane, W., Okamura, S., Owen, R., Padmanabhan, N., Pauls, G., Peoples, J., Pier, J. R., Pope, A. C., Pourbaix, D., Quinn, T. R., Richards, G. T., Richmond, M. W., Rockosi, C. M., Schlegel, D. J., Schneider, D. P., Schroeder, J., Scranton, R., Seljak, U., Sheldon, E., Shimasaku, K., Smith, J. A., Smolčić, V., Snedden, S. A., Stoughton, C., Strauss, M. A., SubbaRao, M., Szalay, A. S., Szapudi, I., Szokody, P., Tegmark, M., Thakar, A. R., Tucker, D. L., Uomoto, A., Berk, D. E. V., Vandenberg, J., Vogeley, M. S., Voges, W., Vogt, N. P., Walkowicz, L. M., Weinberg, D. H., West, A. A., White, S. D. M., Xu, Y., Yanny, B., Yocum, D. R., York, D. G., Zehavi, I., Zibetti, S., & Zucker, D. B. 2006, *The Astrophysical Journal Supplement Series*, 162, 38

- Allen, P. D., Driver, S. P., Graham, A. W., Cameron, E., Liske, J., & de Propris, R. 2006, *Monthly Notices of the Royal Astronomical Society*, 371, 2
- Arsenault, R. 1989, *Astronomy and Astrophysics* (ISSN 0004-6361), 217, 66
- Athanassoula, E. 1980, *Astronomy and Astrophysics*, 88, 184
- . 2002, *The Astrophysical Journal*, 569, L83
- Athanassoula, E., Lambert, J. C., & Dehnen, W. 2005, *Monthly Notices of the Royal Astronomical Society*, 363, 496
- Bacon, R., Copin, Y., Monnet, G., Miller, B. W., Allington-Smith, J. R., Bureau, M., Carollo, C. M., Davies, R. L., Emsellem, E., Kuntschner, H., Peletier, R. F., Verolme, E. K., & de Zeeuw, P. T. 2001, *Monthly Notices of the Royal Astronomical Society*, 326, 23
- Baldry, I. K., Balogh, M. L., Bower, R., Glazebrook, K., & Nichol, R. C. 2004a, *The New Cosmology: Conference on Strings and Cosmology; The Mitchell Symposium on Observational Cosmology*, 743, 106
- Baldry, I. K., Balogh, M. L., Bower, R. G., Glazebrook, K., Nichol, R. C., Bamford, S. P., & Budavari, T. 2006, *Monthly Notices of the Royal Astronomical Society*, 373, 469
- Baldry, I. K., Glazebrook, K., Brinkmann, J., Ivezić, Ž., Lupton, R. H., Nichol, R. C., & Szalay, A. S. 2004b, *The Astrophysical Journal*, 600, 681
- Barazza, F. D., Jogee, S., & Marinova, I. 2008, *The Astrophysical Journal*, 675, 1194
- Bender, R. 1988, *Astronomy and Astrophysics* (ISSN 0004-6361), 193, L7
- Bershady, M. A., Jangren, A., & Conselice, C. J. 2000, *The Astronomical Journal*, 119, 2645
- Blanton, M. R., Eisenstein, D., Hogg, D. W., Schlegel, D. J., & Brinkmann, J. 2005a, *The Astrophysical Journal*, 629, 143
- Blanton, M. R., Hogg, D. W., Bahcall, N. A., Baldry, I. K., Brinkmann, J., Csabai, I., Eisenstein, D., Fukugita, M., Gunn, J. E., Ivezić, Ž., Lamb, D. Q., Lupton, R. H., Loveday, J., Munn, J. A., Nichol, R. C., Okamura, S., Schlegel, D. J., Shimasaku, K., Strauss, M. A., Vogeley, M. S., & Weinberg, D. H. 2003, *The Astrophysical Journal*, 594, 186
- Blanton, M. R., Schlegel, D. J., Strauss, M. A., Brinkmann, J., Finkbeiner, D., Fukugita, M., Gunn, J. E., Hogg, D. W., Ivezić, Ž., Knapp, G. R., Lupton, R. H., Munn, J. A., Schneider, D. P., Tegmark, M., & Zehavi, I. 2005b, *The Astronomical Journal*, 129, 2562

- Blumenthal, G. R., Faber, S. M., Flores, R., & Primack, J. R. 1986, *Astrophysical Journal*, 301, 27
- Bournaud, F., Combes, F., & Semelin, B. 2005, *Monthly Notices RAS Letters*, 364, L18
- Brinchmann, J., Abraham, R., Schade, D., Tresse, L., Ellis, R. S., Lilly, S., Fevre, O. L., Glazebrook, K., Hammer, F., Colless, M., Crampton, D., & Broadhurst, T. 1998, *Astrophysical Journal* v.499, 499, 112
- Brinchmann, J., Abraham, R., Schade, D., Tresse, L., Ellis, R. S., Lilly, S. J., Fevre, O. L., Glazebrook, K., Hammer, F., Colless, M., Crampton, D., & Broadhurst, T. 1997, eprint arXiv, 12060
- Brinchmann, J., Charlot, S., White, S. D. M., Tremonti, C., Kauffmann, G., Heckman, T., & Brinkmann, J. 2004, *Monthly Notices of the Royal Astronomical Society*, 351, 1151
- Bruzual, G. & Charlot, S. 2003, *Monthly Notices of the Royal Astronomical Society*, 344, 1000
- Bundy, K., Georgakakis, A., Nandra, K., Ellis, R. S., Conselice, C. J., Laird, E., Coil, A., Cooper, M. C., Faber, S. M., Newman, J. A., Pierce, C. M., Primack, J. R., & Yan, R. 2008, *The Astrophysical Journal*, 681, 931
- Buta, R. 1990, (Galactic models; Proceedings of the 4th Florida Workshop on Nonlinear Dynamics, 596, 58
- . 1995, *Astrophysical Journal Supplement Series* (ISSN 0067-0049), 96, 39
- Buta, R. & Combes, F. 1996, *Fundamentals of Cosmic Physics*, 17, 95
- Buta, R., Laurikainen, E., & Salo, H. 2004, *The Astronomical Journal*, 127, 279
- Conselice, C. J., Bershady, M. A., & Jangren, A. 2000, *The Astrophysical Journal*, 529, 886
- Curir, A., Mazzei, P., & Murante, G. 2008, *Astronomy and Astrophysics*, 481, 651
- Damjanov, I., McCarthy, P. J., Abraham, R. G., Glazebrook, K., Yan, H., Mentuch, E., Borgne, D. L., Savaglio, S., Crampton, D., Murowinski, R., Juneau, S., Carlberg, R. G., Jorgensen, I., Roth, K., Chen, H.-W., & Marzke, R. O. 2008, eprint arXiv, 0807, 1744
- Davies, R. L., Efstathiou, G., Fall, S. M., Illingworth, G., & Schechter, P. L. 1983, *Astrophysical Journal*, 266, 41
- de Vaucouleurs, G. 1959a, *Handbuch der Physik*, 53, 275
- . 1959b, *Handbuch der Physik*, 53, 311
- . 1963, *Astrophysical Journal Supplement*, 8, 31

- de Vaucouleurs, G. & Buta, R. 1980, *Astronomical Journal*, 85, 637
- de Vaucouleurs, G., de Vaucouleurs, A., & Corwin, J. R. 1976, *Second reference catalogue of bright galaxies*, 0
- de Zeeuw, P. T., Bureau, M., Emsellem, E., Bacon, R., Carollo, C. M., Copin, Y., Davies, R. L., Kuntschner, H., Miller, B. W., Monnet, G., Peletier, R. F., & Verolme, E. K. 2002, *Monthly Notices of the Royal Astronomical Society*, 329, 513
- Debattista, V. P. & Sellwood, J. A. 1998, *Astrophysical Journal Letters* v.493, 493, L5
- . 2000, *The Astrophysical Journal*, 543, 704
- Disney, M. J., Romano, J. D., Garcia-Appadoo, D. A., West, A. A., Dalcanton, J. J., & Cortese, L. 2008, *Nature*, 455, 1082
- Djorgovski, S. & Davis, M. 1987, *Astrophysical Journal*, 313, 59
- Dressler, A. 1980, *Astrophysical Journal*, 236, 351
- Dubinski, J., Gauthier, J.-R., Widrow, L., & Nickerson, S. 2008, eprint arXiv, 0802, 3997
- Elmegreen, B. G. & Elmegreen, D. M. 1985, *Astrophysical Journal*, 288, 438
- . 1989, *Astrophysical Journal*, 342, 677
- . 1990a, *Astrophysical Journal*, 355, 52
- . 2005, *The Astrophysical Journal*, 627, 632
- Elmegreen, B. G., Elmegreen, D. M., & Hirst, A. C. 2004, *The Astrophysical Journal*, 612, 191
- Elmegreen, D. M. & Elmegreen, B. G. 1982, *Royal Astronomical Society*, 201, 1021
- . 1987, *Astrophysical Journal*, 314, 3
- . 1990b, *Astrophysical Journal*, 364, 412
- Elmegreen, D. M., Elmegreen, B. G., Rubin, D. S., & Schaffer, M. A. 2005, *The Astrophysical Journal*, 631, 85
- Fall, S. M. & Efstathiou, G. 1980, *Royal Astronomical Society*, 193, 189
- Fan, X., Hennawi, J. F., Richards, G. T., Strauss, M. A., Schneider, D. P., Donley, J. L., Young, J. E., Annis, J., Lin, H., Lampeitl, H., Lupton, R. H., Gunn, J. E., Knapp, G. R., Brandt, W. N., Anderson, S., Bahcall, N. A., Brinkmann, J., Brunner, R. J., Fukugita, M., Szalay, A. S., Szokoly, G. P., & York, D. G. 2004, *The Astronomical Journal*, 128, 515

- Fan, X., Narayanan, V. K., Lupton, R. H., Strauss, M. A., Knapp, G. R., Becker, R. H., White, R. L., Pentericci, L., Leggett, S. K., Haiman, Z., Gunn, J. E., Ivezić, Ž., Schneider, D. P., Anderson, S. F., Brinkmann, J., Bahcall, N. A., Connolly, A. J., Csabai, I., Doi, M., Fukugita, M., Geballe, T., Grebel, E. K., Harbeck, D., Hennessy, G., Lamb, D. Q., Miknaitis, G., Munn, J. A., Nichol, R., Okamura, S., Pier, J. R., Prada, F., Richards, G. T., Szalay, A., & York, D. G. 2001, *The Astronomical Journal*, 122, 2833
- Fan, X., Strauss, M. A., Richards, G. T., Hennawi, J. F., Becker, R. H., White, R. L., Diamond-Stanic, A. M., Donley, J. L., Jiang, L., Kim, J. S., Vestergaard, M., Young, J. E., Gunn, J. E., Lupton, R. H., Knapp, G. R., Schneider, D. P., Brandt, W. N., Bahcall, N. A., Barentine, J. C., Brinkmann, J., Brewington, H. J., Fukugita, M., Harvanek, M., Kleinman, S. J., Krzesinski, J., Long, D., Neilsen, E. H., Nitta, A., Snedden, S. A., & Voges, W. 2006, *The Astronomical Journal*, 131, 1203
- Fan, X., White, R. L., Davis, M., Becker, R. H., Strauss, M. A., Haiman, Z., Schneider, D. P., Gregg, M. D., Gunn, J. E., Knapp, G. R., Lupton, R. H., Anderson, J. E., Anderson, S. F., Annis, J., Bahcall, N. A., Boroski, W. N., Brunner, R. J., Chen, B., Connolly, A. J., Csabai, I., Doi, M., Fukugita, M., Hennessy, G. S., Hindsley, R. B., Ichikawa, T., Ivezić, Ž., Loveday, J., Meiksin, A., McKay, T. A., Munn, J. A., Newberg, H. J., Nichol, R., Okamura, S., Pier, J. R., Sekiguchi, M., Shimasaku, K., Stoughton, C., Szalay, A. S., Szokoly, G. P., Thakar, A. R., Vogeley, M. S., & York, D. G. 2000, *The Astronomical Journal*, 120, 1167
- Ferrarese, L. & Ford, H. 2005, *Space Science Reviews*, 116, 523
- Ferrarese, L. & Merritt, D. 2000, *The Astrophysical Journal*, 539, L9
- Friedli, D. & Benz, W. 1993, *Astronomy and Astrophysics* (ISSN 0004-6361), 268, 65
- Fukugita, M., Nakamura, O., Okamura, S., Yasuda, N., Barentine, J. C., Brinkmann, J., Gunn, J. E., Harvanek, M., Ichikawa, T., Lupton, R. H., Schneider, D. P., Strauss, M. A., & York, D. G. 2007, *The Astronomical Journal*, 134, 579
- Gadotti, D. A. 2008, *Monthly Notices of the Royal Astronomical Society*, 384, 420
- Gadotti, D. A. & de Souza, R. E. 2004, *The Interplay among Black Holes*, 222, 423
- Ganda, K., Falcón-Barroso, J., Peletier, R. F., Cappellari, M., Emsellem, E., McDermid, R. M., de Zeeuw, P. T., & Carollo, C. M. 2006, *Monthly Notices of the Royal Astronomical Society*, 367, 46

- Gebhardt, K., Bender, R., Bower, G., Dressler, A., Faber, S. M., Filippenko, A. V., Green, R., Grillmair, C., Ho, L. C., Kormendy, J., Lauer, T. R., Magorrian, J., Pinkney, J., Richstone, D., & Tremaine, S. 2000, *The Astrophysical Journal*, 539, L13
- Genzel, R., Pichon, C., Eckart, A., Gerhard, O. E., & Ott, T. 2000, *Monthly Notices of the Royal Astronomical Society*, 317, 348
- Gini, C. 1912, *Memorie di Metodologia Statistica*
- Groot, H. 1925, *Monthly Notices of the Royal Astronomical Society*, 85, 535
- Gunn, J. E., Carr, M., Rockosi, C., Sekiguchi, M., Berry, K., Elms, B., de Haas, E., Ivezić, Ž., Knapp, G., Lupton, R., Pauls, G., Simcoe, R., Hirsch, R., Sanford, D., Wang, S., York, D., Harris, F., Annis, J., Bartozek, L., Boroski, W., Bakken, J., Haldeman, M., Kent, S., Holm, S., Holmgren, D., Petravick, D., Prosapio, A., Rechenmacher, R., Doi, M., Fukugita, M., Shimasaku, K., Okada, N., Hull, C., Siegmund, W., Mannery, E., Blouke, M., Heidtman, D., Schneider, D., Lucinio, R., & Brinkman, J. 1998, *The Astronomical Journal*, 116, 3040
- Gunn, J. E. & Gott, J. R. 1972, *Astrophysical Journal*, 176, 1
- Ho, L. C., Filippenko, A. V., & Sargent, W. L. W. 1997, *Astrophysical Journal* v.487, 487, 591
- Holmberg, E. 1958, *Lund Medd. Astron. Obs. Ser. II*, 136, 1
- Hubble, E. P. 1925, *The Observatory*, 48, 139
- . 1926, *Astrophys. J.*, 64, 321
- . 1927, *The Observatory*, 50, 276
- Hunt, L. K. & Malkan, M. A. 1999, *The Astrophysical Journal*, 516, 660
- Hunt, L. K., Malkan, M. A., Moriondo, G., & Salvati, M. 1999a, *The Astrophysical Journal*, 510, 637
- Hunt, L. K., Malkan, M. A., Rush, B., Bica, M. D., Nelson, B. O., Stanga, R. M., & Webb, W. 1999b, *The Astrophysical Journal Supplement Series*, 125, 349
- Jogee, S., Barazza, F. D., Rix, H. W., Davies, J., Heyer, I., Barden, M., Beckwith, S. V. W., Bell, E. F., Borch, A., Caldwell, J. A. R., Conselice, C., Haussler, B., Heymans, C., Jahnke, K., Knapen, J. H., Laine, S., Lubell, G. M., Mobasher, B., McIntosh, D. H., Meisenheimer, K., Peng, C. Y., Ravindranath, S., Sanchez, S. F., Shlosman, I., Somerville, R. S., Wisotzki, L., & Wolf, C. 2004, arXiv, astro-ph

- Jogee, S., Kenney, J. D. P., & Smith, B. J. 1999, *The Astrophysical Journal*, 526, 665
- Kauffmann, G. & Haehnelt, M. 2000, *Monthly Notices of the Royal Astronomical Society*, 311, 576
- Kauffmann, G., Heckman, T. M., Tremonti, C., Brinchmann, J., Charlot, S., White, S. D. M., Ridgway, S. E., Brinkmann, J., Fukugita, M., Hall, P. B., Ivezić, Ž., Richards, G. T., & Schneider, D. P. 2003a, *Monthly Notices of the Royal Astronomical Society*, 346, 1055
- Kauffmann, G., Heckman, T. M., White, S. D. M., Charlot, S., Tremonti, C., Brinchmann, J., Bruzual, G., Peng, E. W., Seibert, M., Bernardi, M., Blanton, M., Brinkmann, J., Castander, F., Csábai, I., Fukugita, M., Ivezić, Z., Munn, J. A., Nichol, R. C., Padmanabhan, N., Thakar, A. R., Weinberg, D. H., & York, D. 2003b, *Monthly Notice of the Royal Astronomical Society*, 341, 33
- Kauffmann, G., Heckman, T. M., White, S. D. M., Charlot, S., Tremonti, C., Peng, E. W., Seibert, M., Brinkmann, J., Nichol, R. C., SubbaRao, M., & York, D. 2003c, *Monthly Notice of the Royal Astronomical Society*, 341, 54
- Knapen, J. H., Beckman, J. E., Heller, C. H., Shlosman, I., & de Jong, R. S. 1995, *Astrophysical Journal* v.454, 454, 623
- Knapen, J. H., Shlosman, I., & Peletier, R. F. 2000, *The Astrophysical Journal*, 529, 93
- Kormendy, J. 1979, *Astrophysical Journal*, 227, 714
- Kormendy, J. & Bender, R. 1996, *Astrophysical Journal Letters* v.464, 464, L119
- Kormendy, J. & Djorgovski, S. 1989, IN: *Annual review of astronomy and astrophysics*. Volume 27 (A90-29983 12-90). Palo Alto, 27, 235
- Kormendy, J. & Kennicutt, R. C. 2004, *Annual Review of Astronomy & Astrophysics*, 42, 603
- Kormendy, J. & Richstone, D. 1995, *Annual Review of Astronomy and Astrophysics*, 33, 581
- Laine, S., Shlosman, I., Knapen, J. H., & Peletier, R. F. 2002, *The Astrophysical Journal*, 567, 97
- Laurikainen, E. & Salo, H. 2002, *Monthly Notice of the Royal Astronomical Society*, 337, 1118
- Laurikainen, E., Salo, H., & Buta, R. 2004, *The Astrophysical Journal*, 607, 103
- . 2005, *Monthly Notices of the Royal Astronomical Society*, 362, 1319
- Laurikainen, E., Salo, H., Buta, R., & Knapen, J. H. 2007, *Monthly Notices of the Royal Astronomical Society*, 381, 401

- Lindblad, B. 1963, *Stockholms observatoriums annaler* ; bd. 22, 5
- Lindblad, P. O. 1960, *Stockholms observatoriums annaler* ; bd. 21, 4
- Lintott, C. J., Schawinski, K., Slosar, A., Land, K., Bamford, S., Thomas, D., Raddick, M. J., Nichol, R. C., Szalay, A., Andreescu, D., Murray, P., & van den Berg, J. 2008, arXiv, astro-ph
- Lotz, J. M., Primack, J., & Madau, P. 2004, *The Astronomical Journal*, 128, 163
- Lundmark, K. 1926, *Astrophys. J.*, 63, 67
- Lupton, R. H., Ivezić, Z., Gunn, J. E., Knapp, G., Strauss, M. A., & Yasuda, N. 2002, *Survey and Other Telescope Technologies and Discoveries*. Edited by Tyson, 4836, 350
- Lynden-Bell, D. 1969, *Nature*, 223, 690
- Marconi, A. & Hunt, L. K. 2003, *The Astrophysical Journal*, 589, L21
- Marinova, I. & Jogee, S. 2007, *The Astrophysical Journal*, 659, 1176
- Martinez-Valpuesta, I., Shlosman, I., & Heller, C. 2006, *The Astrophysical Journal*, 637, 214
- Miyoshi, M., Moran, J., Herrnstein, J., Greenhill, L., Nakai, N., Diamond, P., & Inoue, M. 1995, *NATURE* V.373, 373, 127
- Moles, M., Marquez, I., & Perez, E. 1995, *Astrophysical Journal*, 438, 604
- Moore, B., Katz, N., Lake, G., Dressler, A., & Oemler, A. 1996, *Nature*, 379, 613
- Morgan, W. W. 1958, *Publications of the Astronomical Society of the Pacific*, 70, 364
- . 1959, *Publications of the Astronomical Society of the Pacific*, 71, 394
- Morgan, W. W. & Mayall, N. U. 1957, *Publications of the Astronomical Society of the Pacific*, 69, 291
- Naim, A., Lahav, O., Buta, R. J., Corwin, H. G., de Vaucouleurs, G., Dressler, A., Huchra, J. P., van den Bergh, S., Raychaudhury, S., Sodre, L., & Storrie-Lombardi, M. C. 1995, *Monthly Notices of the Royal Astronomical Society*, 274, 1107
- Nieto, J.-L., Capaccioli, M., & Held, E. V. 1988, *Astronomy and Astrophysics (ISSN 0004-6361)*, 195, L1
- Nilson, P. 1973, *Acta Universitatis Upsaliensis. Nova Acta Regiae Societatis Scientiarum Upsaliensis - Uppsala Astronomiska Observatoriums Annaler*

- Ostriker, J. P. & Hausman, M. A. 1977, *Astrophysical Journal*, 217, L125
- Peng, C. Y., Ho, L. C., Impey, C. D., & Rix, H.-W. 2002, *The Astronomical Journal*, 124, 266
- Petrosian, V. 1976, *Astrophysical Journal*, 209, L1
- Pier, J. R., Munn, J. A., Hindsley, R. B., Hennessy, G. S., Kent, S. M., Lupton, R. H., & Ivezić, Ž. 2003, *The Astronomical Journal*, 125, 1559
- Regan, M. W., Thornley, M. D., Vogel, S. N., Sheth, K., Draine, B. T., Hollenbach, D. J., Meyer, M., Dale, D. A., Engelbracht, C. W., Kennicutt, R. C., Armus, L., Buckalew, B., Calzetti, D., Gordon, K. D., Helou, G., Leitherer, C., Malhotra, S., Murphy, E., Rieke, G. H., Rieke, M. J., & Smith, J. D. 2006, *The Astrophysical Journal*, 652, 1112
- Reynolds, J. H. 1920, *Monthly Notices of the Royal Astronomical Society*, 80, 746
- . 1925, *Monthly Notices of the Royal Astronomical Society*, 85, 1014
- . 1927, *The Observatory*, 50, 185
- Romero-Gómez, M., Athanassoula, E., Masdemont, J. J., & García-Gómez, C. 2007, *Astronomy and Astrophysics*, 472, 63
- Sakamoto, K., Okumura, S. K., Ishizuki, S., & Scoville, N. Z. 1999, *The Astrophysical Journal*, 525, 691
- Sandage, A. 1961, Washington: Carnegie Institution
- Sandage, A. & Bedke, J. 1994, Washington
- Sandage, A. & Tammann, G. A. 1981, Washington: Carnegie Institution
- Sanders, R. H. & Huntley, J. M. 1976, *Astrophysical Journal*, 209, 53
- Schwarz, M. P. 1981, *Astrophysical Journal*, 247, 77
- . 1984, *Astronomical Society of Australia*, 5, 464
- . 1985, *Astronomical Society of Australia*, 6, 202
- Seigar, M. S., Bullock, J. S., Barth, A. J., & Ho, L. C. 2006, *The Astrophysical Journal*, 645, 1012
- Seigar, M. S., Kenefick, D., Kenefick, J., & Lacy, C. H. S. 2008, arXiv, astro-ph
- Sellwood, J. A. & Wilkinson, A. 1993, *Reports on Progress in Physics*, 56, 173

- Shapley, H. 1941, *Proceedings of the National Academy of Sciences of the United States of America*, 27, 440
- Shapley, H. & Paraskevopoulos, J. S. 1940, *Proceedings of the National Academy of Sciences of the United States of America*, 26, 31
- Shen, J. & Sellwood, J. A. 2004, *The Astrophysical Journal*, 604, 614
- Shen, S., Mo, H. J., White, S. D. M., Blanton, M. R., Kauffmann, G., Voges, W., Brinkmann, J., & Csabai, I. 2003, *Monthly Notice of the Royal Astronomical Society*, 343, 978
- Sheth, K., Elmegreen, D. M., Elmegreen, B. G., Capak, P., Abraham, R. G., Athanassoula, E., Ellis, R. S., Mobasher, B., Salvato, M., Schinnerer, E., Scoville, N. Z., Spalsbury, L., Strubbe, L., Carollo, M., Rich, M., & West, A. A. 2008, *The Astrophysical Journal*
- Sheth, K., Vogel, S. N., Regan, M. W., Thornley, M. D., & Teuben, P. J. 2005, *The Astrophysical Journal*, 632, 217
- Silk, J. & Rees, M. J. 1998, *Astronomy and Astrophysics*, 331, L1
- Simard, L. & Pritchett, C. J. 1998, *The Astrophysical Journal*, 505, 96
- Smith, J. A., Tucker, D. L., Kent, S., Richmond, M. W., Fukugita, M., Ichikawa, T., Ichikawa, S.-I., Jorgensen, A. M., Uomoto, A., Gunn, J. E., Hamabe, M., Watanabe, M., Tolea, A., Henden, A., Annis, J., Pier, J. R., McKay, T. A., Brinkmann, J., Chen, B., Holtzman, J., Shimasaku, K., & York, D. G. 2002, *The Astronomical Journal*, 123, 2121
- Stoughton, C., Lupton, R. H., Bernardi, M., Blanton, M. R., Burles, S., Castander, F. J., Connolly, A. J., Eisenstein, D. J., Frieman, J. A., Hennessy, G. S., Hindsley, R. B., Ivezić, Ž., Kent, S., Kunszt, P. Z., Lee, B. C., Meiksin, A., Munn, J. A., Newberg, H. J., Nichol, R. C., Nicinski, T., Pier, J. R., Richards, G. T., Richmond, M. W., Schlegel, D. J., Smith, J. A., Strauss, M. A., SubbaRao, M., Szalay, A. S., Thakar, A. R., Tucker, D. L., Berk, D. E. V., Yanny, B., Adelman, J. K., Anderson, J. E., Anderson, S. F., Annis, J., Bahcall, N. A., Bakken, J. A., Bartelmann, M., Bastian, S., Bauer, A., Berman, E., Böhringer, H., Boroski, W. N., Bracker, S., Briegel, C., Briggs, J. W., Brinkmann, J., Brunner, R., Carey, L., Carr, M. A., Chen, B., Christian, D., Colestock, P. L., Crocker, J. H., Csabai, I., Czarapata, P. C., Dalcanton, J., Davidsen, A. F., Davis, J. E., Dehnen, W., Dodelson, S., Doi, M., Dombeck, T., Donahue, M., Ellman, N., Elms, B. R., Evans, M. L., Eyer, L., Fan, X., Federwitz, G. R., Friedman, S., Fukugita, M., Gal, R., Gillespie, B., Glazebrook, K., Gray, J., Grebel, E. K., Greenawalt, B., Greene, G., Gunn, J. E., de Haas, E., Haiman, Z., Haldeman, M., Hall, P. B., Hamabe, M., Hansen, B., Harris, F. H., Harris, H., Harvanek, M., Hawley, S. L., Hayes, J. J. E., Heckman, T. M., Helmi, A., Henden, A., Hogan,

- C. J., Hogg, D. W., Holmgren, D. J., Holtzman, J., Huang, C.-H., Hull, C., Ichikawa, S.-I., Ichikawa, T., Johnston, D. E., Kauffmann, G., Kim, R. S. J., Kimball, T., Kinney, E., Klaene, M., Kleinman, S. J., Klypin, A., Knapp, G. R., Korienek, J., Krolik, J., Kron, R. G., Krzesiński, J., Lamb, D. Q., Leger, R. F., Limmongkol, S., Lindenmeyer, C., Long, D. C., Loomis, C., Loveday, J., MacKinnon, B., Mannery, E. J., Mantsch, P. M., Margon, B., McGehee, P., McKay, T. A., McLean, B., Menou, K., Merelli, A., Mo, H. J., Monet, D. G., Nakamura, O., Narayanan, V. K., Nash, T., Neilsen, E. H., Newman, P. R., Nitta, A., Odenkirchen, M., Okada, N., Okamura, S., Ostriker, J. P., Owen, R., Pauls, A. G., Peoples, J., Peterson, R. S., Petravick, D., Pope, A., Pordes, R., Postman, M., Prosapio, A., Quinn, T. R., Rechenmacher, R., Rivetta, C. H., Rix, H.-W., Rockosi, C. M., Rosner, R., Ruthmansdorfer, K., Sandford, D., Schneider, D. P., Scranton, R., Sekiguchi, M., Sergey, G., Sheth, R., Shimasaku, K., Smee, S., Snedden, S. A., Stebbins, A., Stubbs, C., Szapudi, I., Szkody, P., Szokoly, G. P., Tabachnik, S., Tsvetanov, Z., Uomoto, A., Vogeley, M. S., Voges, W., Waddell, P., Walterbos, R., Wang, S., Watanabe, M., Weinberg, D. H., White, R. L., White, S. D. M., Wilhite, B., Wolfe, D., Yasuda, N., York, D. G., Zehavi, I., & Zheng, W. 2002, *The Astronomical Journal*, 123, 485
- Strauss, M. A., Weinberg, D. H., Lupton, R. H., Narayanan, V. K., Annis, J., Bernardi, M., Blanton, M., Burles, S., Connolly, A. J., Dalcanton, J., Doi, M., Eisenstein, D., Frieman, J. A., Fukugita, M., Gunn, J. E., Ivezić, Ž., Kent, S., Kim, R. S. J., Knapp, G. R., Kron, R. G., Munn, J. A., Newberg, H. J., Nichol, R. C., Okamura, S., Quinn, T. R., Richmond, M. W., Schlegel, D. J., Shimasaku, K., SubbaRao, M., Szalay, A. S., Berk, D. V., Vogeley, M. S., Yanny, B., Yasuda, N., York, D. G., & Zehavi, I. 2002, *The Astronomical Journal*, 124, 1810
- Toomre, A. 1969, *Astrophysical Journal*, 158, 899
- . 1977, In: *Annual review of astronomy and astrophysics*. Volume 15. (A78-16576 04-90) Palo Alto, 15, 437
- . 1981, In: *The structure and evolution of normal galaxies; Proceedings of the Advanced Study Institute*, 111
- Tremaine, S., Gebhardt, K., Bender, R., Bower, G., Dressler, A., Faber, S. M., Filippenko, A. V., Green, R., Grillmair, C., Ho, L. C., Kormendy, J., Lauer, T. R., Magorrian, J., Pinkney, J., & Richstone, D. 2002, *The Astrophysical Journal*, 574, 740
- Tremonti, C. A., Heckman, T. M., Kauffmann, G., Brinchmann, J., Charlot, S., White, S. D. M., Seibert, M., Peng, E. W., Schlegel, D. J., Uomoto, A., Fukugita, M., & Brinkmann, J. 2004, *The Astrophysical Journal*, 613, 898
- Trujillo, I., Burkert, A., & Bell, E. F. 2004a, *The Astrophysical Journal*, 600, L39

- Trujillo, I. & Pohlen, M. 2005, *The Astrophysical Journal*, 630, L17
- Trujillo, I., Rudnick, G., Rix, H.-W., Labbé, I., Franx, M., Daddi, E., van Dokkum, P. G., Schreiber, N. M. F., Kuijken, K., Moorwood, A., Röttgering, H., van de Wel, A., van der Werf, P., & van Starckenburg, L. 2004b, *The Astrophysical Journal*, 604, 521
- Tucker, D. L., Kent, S., Richmond, M. W., Annis, J., Smith, J. A., Allam, S. S., Rodgers, C. T., Stute, J. L., Adelman-McCarthy, J. K., Brinkmann, J., Doi, M., Finkbeiner, D., Fukugita, M., Goldston, J., Greenway, B., Gunn, J. E., Hendry, J. S., Hogg, D. W., Ichikawa, S.-I., Ivezić, Ž., Knapp, G. R., Lampeitl, H., Lee, B. C., Lin, H., McKay, T. A., Merrelli, A., Munn, J. A., Neilsen, E. H., Newberg, H. J., Richards, G. T., Schlegel, D. J., Stoughton, C., Uomoto, A., & Yanny, B. 2006, *Astronomische Nachrichten*, 327, 821
- Tully, R. B. & Fisher, J. R. 1977, *Astronomy and Astrophysics*, 54, 661
- van den Bergh, S. 1960a, *Astrophysical Journal*, 131, 558
- . 1960b, *Astrophysical Journal*, 131, 215
- . 1960c, *Publications of the David Dunlap Observatory*, 2, 159
- . 1976, *Astrophysical Journal*, 206, 883
- . 1998, *Galaxy morphology and classification / Sidney van den Bergh*. Cambridge ; New York : Cambridge University Press
- . 2007, *The Astronomical Journal*, 134, 1508
- . 2008, eprint arXiv, 0808, 3601
- van den Bergh, S., Abraham, R. G., Whyte, L. F., Merrifield, M. R., Eskridge, P. B., Frogel, J. A., & Pogge, R. 2002, *The Astronomical Journal*, 123, 2913
- Wang, L. & Kauffmann, G. 2008, *Monthly Notices of the Royal Astronomical Society*, 391, 785
- Weinberg, M. D. 1985, *Royal Astronomical Society*, 213, 451
- White, S. D. M. & Rees, M. J. 1978, *Royal Astronomical Society*, 183, 341
- Widrow, L. M., Pym, B., & Dubinski, J. 2008, *The Astrophysical Journal*, 679, 1239
- Wozniak, H. 2007, *Astronomy and Astrophysics*, 465, L1

- York, D. G., Adelman, J., Anderson, J. E., Anderson, S. F., Annis, J., Bahcall, N. A., Bakken, J. A., Barkhouser, R., Bastian, S., Berman, E., Boroski, W. N., Bracker, S., Briegel, C., Briggs, J. W., Brinkmann, J., Brunner, R., Burles, S., Carey, L., Carr, M. A., Castander, F. J., Chen, B., Colestock, P. L., Connolly, A. J., Crocker, J. H., Csabai, I., Czarapata, P. C., Davis, J. E., Doi, M., Dombeck, T., Eisenstein, D., Ellman, N., Elms, B. R., Evans, M. L., Fan, X., Federwitz, G. R., Fiscelli, L., Friedman, S., Frieman, J. A., Fukugita, M., Gillespie, B., Gunn, J. E., Gurbani, V. K., de Haas, E., Haldeman, M., Harris, F. H., Hayes, J., Heckman, T. M., Hennessy, G. S., Hindsley, R. B., Holm, S., Holmgren, D. J., hao Huang, C., Hull, C., Husby, D., Ichikawa, S.-I., Ichikawa, T., Ivezić, Ž., Kent, S., Kim, R. S. J., Kinney, E., Klaene, M., Kleinman, A. N., Kleinman, S., Knapp, G. R., Korienek, J., Kron, R. G., Kunszt, P. Z., Lamb, D. Q., Lee, B., Leger, R. F., Limmongkol, S., Lindenmeyer, C., Long, D. C., Loomis, C., Loveday, J., Lucinio, R., Lupton, R. H., MacKinnon, B., Mannery, E. J., Mantsch, P. M., Margon, B., McGehee, P., McKay, T. A., Meiksin, A., Merelli, A., Monet, D. G., Munn, J. A., Narayanan, V. K., Nash, T., Neilsen, E., Neswold, R., Newberg, H. J., Nichol, R. C., Nicinski, T., Nonino, M., Okada, N., Okamura, S., Ostriker, J. P., Owen, R., Pauls, A. G., Peoples, J., Peterson, R. L., Petravick, D., Pier, J. R., Pope, A., Pordes, R., Prosapio, A., Rechenmacher, R., Quinn, T. R., Richards, G. T., Richmond, M. W., Rivetta, C. H., Rockosi, C. M., Ruthmansdorfer, K., Sandford, D., Schlegel, D. J., Schneider, D. P., Sekiguchi, M., Sergey, G., Shimasaku, K., Siegmund, W. A., Smee, S., Smith, J. A., Snedden, S., Stone, R., Stoughton, C., Strauss, M. A., Stubbs, C., SubbaRao, M., Szalay, A. S., Szapudi, I., Szokoly, G. P., Thakar, A. R., Tremonti, C., Tucker, D. L., Uomoto, A., Berk, D. V., Vogeley, M. S., Waddell, P., i Wang, S., Watanabe, M., Weinberg, D. H., Yanny, B., & Yasuda, N. 2000, *The Astronomical Journal*, 120, 1579
- Zamojski, M. A., Schiminovich, D., Rich, R. M., Mobasher, B., Koekemoer, A. M., Capak, P., Taniguchi, Y., Sasaki, S. S., McCracken, H. J., Mellier, Y., Bertin, E., Aussel, H., Sanders, D. B., FÈVRE, O. L., Ilbert, O., Salvato, M., Thompson, D. J., Kartaltepe, J. S., Scoville, N., Barlow, T. A., Forster, K., Friedman, P. G., Martin, D. C., Morrissey, P., Neff, S. G., Seibert, M., Small, T., Wyder, T. K., Bianchi, L., Donas, J., Heckman, T. M., Lee, Y.-W., Madore, B. F., Milliard, B., Szalay, A. S., Welsh, B. Y., & Yi, S. K. 2007, *The Astrophysical Journal Supplement Series*, 172, 468